CPPM-T-2012-007

Aix-Marseille Université

Faculté des Sciences

University of Science and Technology of China

Department of Modern Physics

THÈSE DE DOCTORAT

Physique et Sciences de la Matière

Mention : *Physique des Particules et Astroparticules*

présentée par

Shu LI

pour l'attention du titre de docteur en science de l'Université d'Aix-Marseille

et University of Science and Technology of China

Mesure de la production W^+W^- dans les collisions proton-proton à $\sqrt{s} = 7$ TeV avec le détecteur ATLAS au LHC

soutenue le 2 Novembre 2012 devant le jury composé de

Prof.	S. Chen	Examinateur
Dr.	E. Kajfasz	Président du jury
Prof.	Y. Liu	Directeur de thèse
Dr.	E. Monnier	Directeur de thèse
Dr.	M.-A. Pleier	Rapporteur
Prof.	X. Shen	Rapporteur
Prof.	Z. Zhao	Directeur de thèse




USTC-MPHY-2012-007

University of Science and Technology of China

Department of Modern Physics

Aix-Marseille Université

Faculté des Sciences

Ph.D THESIS

Physics and Material Science

Major : *Particle Physics and Nucleus Physics*

presented by

Shu LI

for the title of Ph.D of University of Science and Technology of China

and Aix-Marseille Université

Measurement of W^+W^- production in Proton-Proton Collisions at $\sqrt{s} = 7$ TeV with the ATLAS Detector at the LHC

to be defended on November 2^{nd} 2012 before the committee comprised of

Prof.	S. Chen	Examiner
Dr.	E. Kajfasz	President of the jury
Prof.	Y. Liu	Supervisor
Dr.	E. Monnier	Supervisor
Dr.	M.-A. Pleier	Reviewer
Prof.	X. Shen	Reviewer
Prof.	Z. Zhao	Supervisor

To my family, my supervisors, my colleagues and friends in ATLAS, and to all those who once helped me.

ACKNOWLEDGEMENTS

For more than three years, I have been opening the ATLAS bible as a HEP Ph.D candidate. To work for such a huge collaboration has naturally led to a charming experience full of astonishing and innocent excitements, heroic and tireless efforts, workaholic and touching moments, enthusiastic and encouraging inspiration, unitive and efficient teamwork, etc. Along with all of these precious and unforgetable memories, I would like to show my great appreciations to all the friends and colleagues in the ATLAS collaboration who used to work together with me, offer me the guidance and altruistic support and eventually make this thesis work happen. My dedications go for all the brilliant, ethusiastic, heroic and innocent HEP physicists of ATLAS with special thanks given to the following people.

First of all, I would like to thank my supervisors. Prof. Zhengguo Zhao and Dr. Emmanuel Monnier, I will never forget your encouragements in various aspects of my thesis and also the great personal friendships after work. Thanks to all of your financial and academic supports which have guaranteed my thesis to carry on. I would also like to thank my second supervisor in China, Prof. Yanwen Liu, executively mentoring my thesis, for all his experienced and wise physics advices, technical and financial supports, harsh but pertinent criticism and finally his great personalities which influenced me so much in physics researches.

Besides, I would like to give the special gratitudes to Dr. Oliver Simard, who used to help me out in person when I was once at the edge of giving up two years ago. I will never forget all the inspirations that I used to buy from you as a heroic and affirmative HEP physicist and all the brilliant ideas and great helps that your brought to me during my service task.

My dedicated sincere gratitudes also go to Dr. Marc-Andre Pleier and Dr. Matthias Schott who have been working together with me as not only the analysis group convenors but also my actual external advisors. Thanks to all your help and experienced advice on my analysis work, without which this dissertation would never come into being. Your open-minded, equal-opportunity and tireless coordinations in our analysis group will be memorized by everyone forever. I would also like to thank

Prof. Bing Zhou and Dr. Jianbei Liu from Michigan and Prof. Zhiqing Zhang from LAL, who used to help and advise me so much in the analysis work as the external advisors. And thanks to Dr. Oldrich Kepka, Johannes Ebke, Alberto Belloni and Shih-Chieh Hsu, to whom I have always felt lucky to work together with.

I would like to thank my senior colleagues at CPPM, Fabrice hubaut, Pascal Pralavorio, Laurent Vacavant, Steve Muanza, Yann Coadou, Mossadek Talby, and Emmanuel Le Guirriec. Thanks to all your supportive adivice and technical helps for my thesis. I would also like to thank all my friends in USTC, CPPM and Michigan, without anyone of you, my career would never be so delighted. Thanks to Yusheng Wu and Hulin Wang, I will forever feel lucky to have you as my close friends. Thanks for all the helps that I had from you to make my work carry on and all the hikings, parties and starbucks that we used to enjoy. Thanks to Chao Xu, Salvotore Galata, Julien Maurer and Crosme Adrover Pacheco, only you guys could get my jokes as always. Thanks to Jerome Odier, Elisabeth Petit and Nancy Tannoury for all the interesting discussions that we had and all the kind help that you offered me (Good luck with your new careers :)).

Last but not least, I would like to thank my family who have been always lovingly supporting my career.

Résumé

Le détecteur ATLAS, auprès du Grand collisionneur de hadrons (LHC), est un détecteur polyvalent destiné à la découverte de nouvelle physique et de phénomènes nouveaux, tout en fournissant également une bonne occasion de comprendre le comportement à haute énergie du Modèle Standard (MS), cadre théorique bien établi qui décrit les particules élémentaires et leurs interactions sauf la gravité.

Le LHC est le plus grand accélérateur de particule au monde conçu pour fournir des collisions frontales proton-proton à l'énergie encore jamais obtenue de 14 TeV dans le centre de masse pour une luminosité crête de 10^{34} cm^{-2}s^{-1}. Le LHC fonctionne aussi en mode ion lourd avec des collisions de noyaux de plomb d'une énergie de 574 TeV (92.0 J) par nucléon (2.76 TeV par paire de nucléon) et une luminosité de 10^{27} cm^{-2}s^{-1}. Le LHC et ATLAS fonctionnent superbement bien depuis 2008. En 2011, l'expérience ATLAS a recueillie 4.7 fb^{-1} de données de collision pp à 7 TeV et prévois d'enregistrer encore 25 fb^{-1} de données à 8 TeV d'ici la fin de l'année 2012.

Cette thèse présente le mesure des sections efficaces de production W^+W^- MS et la détermination des couplages triples (TGCs) correspondants en utilisant ces 4.7 fb^{-1} de données 2011 de collision pp. Ces mesures permettent un test contraignant du secteur électrofaible non abélien $SU(2) \times U(1)$ du Modèle Standard; donnent l'opportunité de sonder la nouvelle physique à travers les couplages triples anormaux de bosons de jauge (aTGCs) qui seront observés dans la distribution des variables cinématiques des W^+W^- produits ou de leurs produits de désintégration finaux dans le secteur de haute énergie; et permettent d'avoir une bonne compréhension du bruit de fond irréductible dans la recherche du boson de Higgs dans le canal de désintégration $H \to W^+W^-$.

Ces mesures de la production W^+W^- sont basées sur l'analyse des canaux de désintégration purement leptoniques avec les états finals $e\nu e\nu$, $e\nu\mu\nu$ and $\mu\nu\mu\nu$. Les principaux bruits de fond au signal W^+W^- sont Z+jets, W+jets, top et les autres productions dibosoniques que sont, WZ, ZZ et W/Z+γ. Les bruits de fond Z+jets, W+jets et top sont estimés en utilisant des techniques dédiées et orientées données tandis que les bruits des autres canaux di-bosoniques sont estimés à partir de simulation Monte-

Carlo. Un total de 1325 candidats sont sélectionnés avec un bruit de fond total estimé à 368.5 ± 60.9. La section efficace correspondante mesurée est 51.9 $\pm$2.0 (stat) $\pm$3.9 (syst) $\pm$0.9 (lumi) pb. Ce résultat est compatible avec la prédiction Next-to-Leading Order (NLO) du Modèle Standard de $44.7^{+2.1}_{-1.9}$ pb et surpasse la précision des résultats des expériences auprès de l'accélérateur Tevatron. Les sections efficaces fiducielles de chaque canal sont également mesurées et une première distribution différentielle en impulsion transverse du lepton dominant est extraite.

Finalement, les TGCs des vertex WWZ et WWγ sont explorés en comparant le spectre en impulsion transverse observé dans le signal W^+W^- pour le lepton dominant aux prédictions théoriques incluant les couplages triples anormaux. Pour une coupure $\Lambda = 6$ TeV, une limite de confiance à 95% est donnée sur Δk_Z et λ_Z dans les intervalles $[-0.061, 0.093]$ et $[-0.062, 0.065]$, respectivement (`Equal Coupling Scenario`). Ces limites sont plus strictes que celles données par les expériences auprès de l'accélérateur Tevatron et compétitives avec celles données par les expériences auprès de l'accélérateur LEP.

Ce travail de thèse donne un base solide pour les mesures à venir de la production W^+W^- avec les $\sim$25 fb^{-1} de luminosité intégrée de données à 8 TeV prévue pour la fin 2012, qui conduiront vers une amélioration de la précision et des limites plus strictes sur les aTGCs.

ABSTRACT

The ATLAS detector is a general purpose detector at the Large Hadron Collider (LHC) aimed at the discovery of new physics phenomena as well as improving our understanding of the high energy behavior of the Standard Model (SM), the well established theoretical framework which describes the elementary particles and their interactions except gravity.

The LHC is the world's largest hadron collider designed to provide head on proton proton (pp) collisions at 14 TeV center-of-mass (c.m.) energy and 10^{34} cm^{-1}s^{-1} peak luminosity. The LHC also runs in heavy ion mode with lead nuclei collisions at an energy of 574 TeV per nucleus (2.76 TeV per nucleon-pair) at the luminosity of 10^{27} cm^{-2}s^{-1}. Both LHC and ATLAS are performing excitingly well since 2009. In 2011, the ATLAS experiment collected a 4.7 fb^{-1} pp collisions data at 7 TeV and is expecting to record another 25 fb^{-1} of pp collisions at 8 TeV by the end of 2012.

This thesis presents a measurement of the SM W^+W^- production cross section and the determination of the corresponding limits on anomalous triple gauge boson couplings (aTGCs), using the 2011 4.7 fb^{-1} pp collisions data at 7 TeV collected in 2011. The measurement allows for a stringent test of the non-Abelian $SU(2) \times U(1)$ SM electroweak sector and probes new physics that could manifest itself through aTGCs that may alter the observed production cross section or kinematic distributions. This measurement also provides a good understanding of the irreducible background in searches for the Higgs boson through the $H \to W^+W^-$ decay channel.

The measurement of the W^+W^- production is based on the analysis of the purely leptonic decay channels with the final states of $e\nu e\nu$, $e\nu\mu\nu$ and $\mu\nu\mu\nu$. The main background processes to the W^+W^- signal are Z+jets, W+jets, top quarks, and other diboson production, such as WZ, ZZ and $W/Z+\gamma$. The Z+jets, W+jets and top background processes are estimated using dedicated data-driven techniques while the other diboson background is estimated from Monte-Carlo (MC) simulation. A total of 1325 signal candidates are selected from data with an overall estimated background of 368.5 ± 60.9. The corresponding measured total cross section is 51.9 ± 2.0 (stat) ± 3.9 (syst) ± 0.9 (lumi) pb. This

result is compatible with the Standard Model Next-to-Leading Order (NLO) prediction of $44.7^{+2.1}_{-1.9}$ pb and has surpassed the precision of results from experiments at the Tevatron accelerator. The fiducial cross section for each channel is also measured and a first differential distribution of the leading lepton transverse momentum spectrum is extracted.

Finally, the TGCs of the WWZ and WWγ vertices are studied by comparing the observed leading lepton transverse momentum spectrum of the W^+W^- signal to the theoretical predictions with aTGCs included. For a cutoff scale of $\Lambda = 6$ TeV, 95% Confidence Limits are set on Δk_Z and λ_Z in the intervals $[-0.061, 0.093]$ and $[-0.062, 0.065]$, respectively for `Equal Coupling Scenario`. These are more stringent limits than those from experiments at the Tevatron accelerator and are competitive with results from experiments at the LEP accelerator.

This thesis work has laid a solid foundation for further measurements of the W^+W^- production with the $\sim$25 fb^{-1} integrated luminosity 8 TeV recorded data expected by the end of 2012, which will further improve the precision and yield more stringent limits on the aTGCs.

TABLE OF CONTENTS

CHAPTER 1. THEORY INTRODUCTION

1.1 Introduction to the Standard Model

As the matured framework of quantized field theory for modern elementary particles and interactions, the Standard Model (SM) theory has been developed since the early 20^{th} century, and is theorectically solid and has been experimentally widely verified. It is the foundation of the "Universe mechanics" in predicting the dynamics and properties of microscopic particles. In principle, all known elementary particles and three out of four known fundamental interactions are included in the SM description: strong, weak and electromagnetic interactions excluding the gravitation which is described by the general relativity theory.

Although several issues not explained by the SM, such like the hierarchy problem and the strong CP violation, which may indicate the remaining unexplained properties, the SM theory is still considered to be self-consistent and complete for the major aspects of it. In this chapter the SM theory will be illustrated in a general way but with the electroweak sector highlighted, which will provide the basis and motivation for the thesis.

1.1.1 Elementary particles and objects in the Standard Model

The world is in principle made of elementary particles and their antiparticle partners. The fundamental particles described in SM can be basically sorted into 2 major categories: bosons with their intrinsic angular momenta of integral multiples of $\hbar$ and fermions with $\frac{1}{2}\hbar$ as their intrinsic spin.

All the known matter in our universe is made of fermions while the bosons play the roles of force carriers which mediate the interactions of fermions. The dark matter is not accounted for in the SM theory despite some of its properties are deduced from cosmological observations.

SM fermions are further categorized into 12 elementary particles of spin $\frac{1}{2}$ including six quarks and six leptons, each of which has its antiparticle partner with almost exactly the same properties except for the opposite charges. Those fundamental particles together with bosons as the force carriers can be grouped into 3 generations as shown in Figure 1.1.

Table 1.1 shows in each generation of given leptons or quarks, the charges hold while the masses are way different among different generations.

Table 1.1 SM fermions: Quarks and Leptons. [2]

	Generations			Charge [e]
	1st generation	2nd generation	3rd generation	
Quarks	u(Up) m_u = 1.7 - 3.3 MeV	c(Charm) m_c = 1.27 GeV	t(Top) m_t = 171.2 GeV	$\frac{2}{3}$
	d(Down) m_d = 4.1 - 5.8 MeV	s(Strange) m_s = 101 MeV	b(Bottom) m_b = 4.2 GeV	$-\frac{1}{3}$
Leptons	ν_e $m_{\nu_e} < 2 \times 10^{-6}$ MeV	ν_μ $m_{\nu_\mu} < 0.19$ MeV	ν_τ $m_{\nu_\tau} < 18.2$ MeV	0
	e m_e = 0.511 MeV	μ m_μ = 105.7 MeV	τ m_τ = 1.777 GeV	-1

Fermions, including both leptons and quarks, can interact via the unified electroweak force while only quarks which carry color charges are subject to the strong interaction mediated by the strong force carrier gluons. Quarks are the elementary composition of hardrons, which can be further divided into 2 different categories: Baryons are composed of three confined quarks or antiquarks while Mesons are of a pair of quark-antiquarks, both with integer electric charges and neutral color charges.

Both Baryons and Mesons are colorless and no separate particles have ever been detected to have colored states. The known color charges are $R(Red)$, $G(Green)$ and $B(Blue)$ and their anti-color charges $\bar{R}(Cyan)$, $\bar{G}(Magenta)$ and $\bar{B}(Yellow)$. The eight gluons carry color charges and act as the medium of the strong interactions but never show up outside the particles that are created in strong interactions 1.1.2.

Apart from fermions, we have a total of 12 gauge bosons which can be either neutral massless ones (e.g. photons and gluons) or neutral/charged massive ones(e.g. $W^{\pm}$ and Z bosons). They play the roles of the carriers of fundamental forces to mediate the interactions including strong, weak

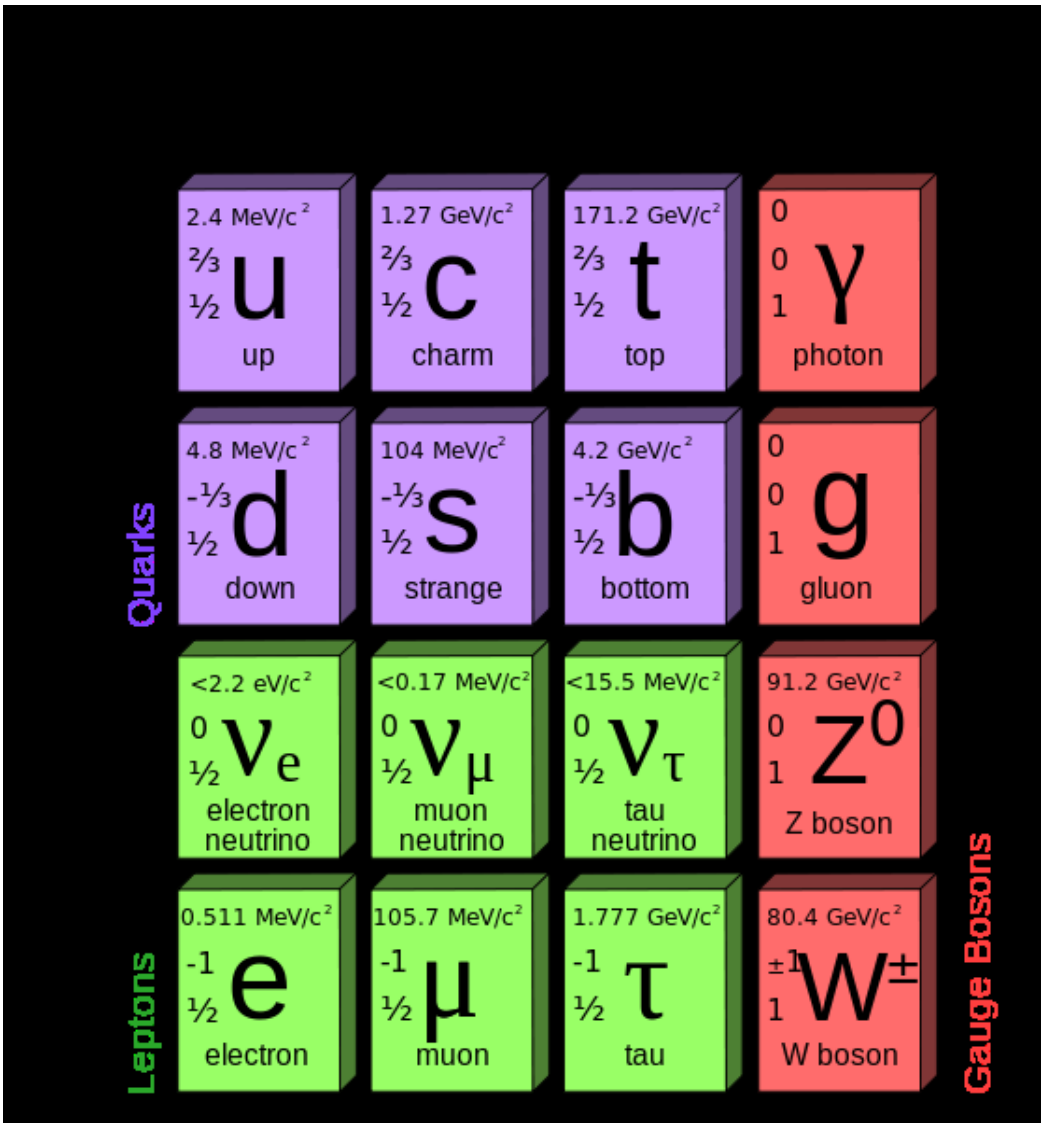

Figure 1.1 The elementary particles in SM including fermions and gauge bosons. Fermions are grouped in 3 generations in the first 3 columns splitted into quarks and leptons. [1]

and electromagnetic interactions except for gravitation which is not included in SM. The detailed information of each gauge boson and the interaction it corresponds to can be found in Table 1.2

All gauge bosons have spin 1 in SM. Due to the integer spins and the symmetric wave functions, they are not restricted by the "`Pauli exclusion principle`" which fermions obey. Hence, there are no theoretically limited spatial densities (i.e. any number of gauge bosons can occupy the same quantum state).

The only SM boson which is predicted in Higgs mechanism but has not yet been convincingly discovered is the Higgs boson. It is a massive scalar elementary boson with no intrinsic spin, which was predicted by R. Brout, F. Englert, P. Higgs, G. Guralnik, C. R. Hagen, and T. Kibble in 1964. [3]

On July 4th, 2012, the two major general purpose experiments ATLAS and CMS announced independent observations of a neutral boson with a mass of 126 GeV and compatible with the SM Higgs boson in terms of its productions and decays at the Large Hadron Collider(LHC) at CERN. However, it still needs some more work to confirm whether or not it is indeed the Higgs Boson in SM.

Table 1.2 List of gauge bosons and corresponding interactions in SM. [2]

Gauge Boson	Mass [GeV]	Charge [e]
gluon(g_i, i=1,...,8)	0	0
Photon(γ)	0	0
W^+(weak boson)	80.4	+1
W^-(weak boson)	80.4	-1
Z(weak boson)	91.2	0
Graviton(hypothetical)		

1.1.2 Quantum Field Theory and the SM interactions

In SM, the interactions between elementary particles are subject to the local gauge symmetries and formulated as a relativistic quantum field theory framework Quantum Field Theory (QFT). QFT is a theory that provides the natural quantitative basis for elementary particle physics and is what several fundamental quantum theories originate from, such as Quantum Electrodynamics (QED) and Quantum Chromodynamics (QCD). In each quantum field based theory, there is always a specific field for each elementary particle and dedicated term that describe the interactions between the particles:

- QED has two fields for electrons and photons, respectively. Developped in the 1940s, it gives a relativistic description of the electrodynamics of light and matter interaction. It also by now provides the most accurate predictions of quantities in quantum electromagnetic interactions such as the anomalous magnetic moment of the electrons, Lamb shift, etc. at the precision of 10 out of 1 billion. The interaction is only subject to charged particles mediated by photons. The corresponding coupling constant is: $g_e = \sqrt{4\pi\alpha}$, where:

$$\alpha = \frac{e^2}{\hbar c} \simeq \frac{1}{137} \tag{1.1}$$

. Due to the massless force carrier photon, the electromagnetic interaction is guaranteed to be effective for long range and hence the most dominant one macroscopically apart from the gravitation.

- QCD is a non-Abelian gauge theory inheriting from QFT framework, which interprets the strong interactions that exist between color-charged quarks and confines them within hadrons. There are in principle 2 features of QCD that have been both theorectically and experimentally evidenced ever since the 20th century:

  - Confinement, which consistently explains why the free quark searches have never really succeeded because of the infinite amount of energy required to separate quarks bound by the strong force that does not diminish. Although it is not analytically proved, this property is still well accepted and experimentally supported as well as being successfully demonstrated in lattice QCD.

  - Asymptotic freedom, which suggests the quark and gluon interactions get weaker as soon as the higher energy scales are reached. Hence, it indicates the confinement is restricted to be dominant at only the low-energy scale. The asymptotic freedom was discovered by D. Politzer, F. Wilczek and D. Gross in 1970s though there is no clear phase-transition line between the asymptotic freedom and confinement.

– In order to elaborate this feature, the running strong coupling constant is presented as:

$$\alpha_s(q^2) \propto \frac{1}{ln(q^2/\lambda_s^2)}, \quad for|q^2| \gg \lambda_s^2. \tag{1.2}$$

, where the q refers to the mediator momentum. The QCD scale cutoff, λ_s is introduced to avoid the divergence in the perturbative calculation of the strong coupling and is of the order of 200 MeV. As a result, $g_s = \sqrt{4\pi\alpha_s}$ indicates that as the q^2 increases, the strong force decreases and eventually leads to the asymptotic freedom or vice versa can lead to the confinement.

Besides the electromagnetic and strong interactions, the third one that exists in SM is the weak interaction, of which the W and Z bosons are the force carriers. The W and Z bosons are massive gauge bosons, which are unlike the photons that mediate their interactions in long range, but instead characterize the weak interaction to be a short range interaction($\sim 10^{-18}$ m) with weaker field strength which is several orders of magnitude less than both strong and electromagnetic interactions. Table 1.3 helps to illustrate the comparison among different SM interactions taking gravitation as reference to suggest the big gap existing between them. The charged W bosons or better to say $W^{\pm}$ bosons to be precise are the only gauge boson mediators in SM that change the lepton and quark flavors by means of charged current interaction. On the contrary, the neutral massive gauge boson Z is the weak force carrier which only appears in neutral current interaction with neither lepton nor quark flavor changes. In the SM, $W^{\pm}$ and Z bosons have non-zero couplings to almost all the elementary particles except gluons.

Table 1.3 The fundamental forces in the universe.

Interaction	Mediators	coupling constant	Relative strength	Long-distance behavior	Range [m]
Electromagnetic	Photon (γ)	$\sim 10^{-2}$	10^{36}	$\frac{1}{r^2}$	∞
Weak	$W^{\pm}$,Z	$\sim 10^{-7}$	10^{25}	$\frac{1}{r}e^{-m_{W,Z}r}$	10^{-18}
Strong	Gluon (g)	~ 1	10^{38}	1	10^{-15}
Gravitation	Gravition (hypo)	$\sim 10^{-45}$	1	$\frac{1}{r^2}$	∞

1.1.3 The electroweak sector of the Standard Model

In late 1970s, two of the three fundamental interactions in SM: electromagnetism and the weak interaction were unified successfully by S. Weinberg, A. Salam and S. Glashow(GWS). [4] Therefore the two forces can be unified as one electroweak force above the unification energy $\sim$ 100 GeV, which was predicted to be consistent with the 10E15 K Universe temperature after the Big Bang. This section will briefly introduce the GWS model of the electroweak unification theory and some key topics in electroweak section of SM.

Theoretically, the electroweak force unification is achieved by means of $SU(2)_L \times U(1)_Y$ gauge symmetry. In reality, the $W^{\pm}$, Z^0 bosons and photons(γ) all there as soon as the spontaneous breaking of electroweak symmetry is introduced, which originate from $SU(2)_L$($W^{\pm}$ and W^0) and $U(1)_Y$ B^0 boson. After the spontaneous symmetry breaking, the W^0 and B^0 bosons are transformed into new gauge bosons Z^0 and γ:

$$\begin{pmatrix} \gamma \\ Z^0 \end{pmatrix} = \begin{pmatrix} cos\theta_W & sin\theta_W \\ -sin\theta_W & cos\theta_W \end{pmatrix} \begin{pmatrix} B^0 \\ W^0 \end{pmatrix} \tag{1.3}$$

, where θ_W stands for the weak mixing angle while γ and Z^0 refer to photon and neutral weak field respectively, which leads to that the new gauge field representing the actual neutral particles are rotated by an angle θ_W in the plane of (W^0, B^0) through the neutral currents and therefore also results in that Z^0 boson mass is slightly different from $W^{\pm}$ bosons as presented in the formula: $M_Z = \frac{M_W}{cos\theta_W}$.

The $U(1)_{em}$ is generated from the new generator Q which is the linear combination of the third weak isospin generator I_3 of $SU(2)_L$ and the weak hypercharge generator Y of $U(1)_Y$ in the formula: $Q = \frac{Y}{2} + I_3$. In Higgs mechanism, $U(1)_{em}$ does not interact with the Higgs boson which is the eigenstate of both Y and I_3. Therefore $U(1)_{em}$ is not broken and eventually leads to the distinction between electromagnetic and weak interactions.

After the electroweak symmetry breaking and the vacuum expectation value of Higgs boson is acquired, the corresponding Lagrangian obtains a more complex form than the usual case without the breaking: $L_{EW} = L_K + L_N + L_C + L_H + L_{HV} + L_{WWV} + L_{WWVV} + L_Y$. Hence, the kinetic term is

given by:

$$\begin{aligned} L_K = &\sum_f \bar{f}(i\partial\!\!\!/ - m_f)f - \frac{1}{4}A_{\mu\nu}A^{\mu\nu} - \frac{1}{2}W^+_{\mu\nu}W^{-\mu\nu} \\ &+ m_W^2 W^+_\mu W^{+\mu} - \frac{1}{4}Z_{\mu\nu}Z^{\mu\nu} + \frac{1}{2}m_Z^2 Z_\mu Z^\mu \\ &+ \frac{1}{2}(\partial^\mu H)(\partial_\mu H) - \frac{1}{2}m_H^2 H^2 \end{aligned} \tag{1.4}$$

, where all relevant gauge boson fields given in a universal way as:

$$X_{\mu\nu} = \partial_\nu X_\nu - \partial_\nu X_\mu + g f^{abs} X^b_\mu X^c_\nu \tag{1.5}$$

and f^{abs} represents the structure constants of a given gauge group. (Note that $W^+_{\mu\nu} \equiv (W^-_{\mu\nu})\dagger$). The neutral and charged current terms and given as:

$$L_N = eJ^{em}_\mu A^\mu + \frac{g}{cos\theta_W}(J^3_\mu - sin^2\theta_W J^{em}_\mu)Z^\mu \tag{1.6}$$

$$L_C = -\frac{g}{\sqrt{2}}[\bar{u}_i\gamma^\mu\frac{1-\gamma^5}{2}M^{CKM}_{ij}d_j + \bar{\nu}_i\gamma^\mu\frac{1-\gamma^5}{2}e_i]W^+_\mu + h.c. \tag{1.7}$$

, where we have the electromagnetic and weak neutral currents:

$$\begin{aligned} J^{em}_\mu &= \sum_f q_f \overline{f}\gamma_\mu f \\ J^3_\mu &= \sum_f I^3_f \overline{f}\gamma_\mu \frac{1-\gamma^5}{2} f \end{aligned} \tag{1.8}$$

(q_f: electric charge of a given fermion; I^3_f: weak isospin of a given fermion.)

The charged and neutral current interactions occurs when $W^\pm$ and Z^0 bosons are absorbed or emitted by quarks or leptons and coherently the up-down type quarks conversion or the rapid decay of

the gauge bosons such as:

$$\begin{aligned} d &\rightarrow u + W^- \\ d + W^+ &\rightarrow u \\ W^- &\rightarrow e^- + \bar{\nu}_e \\ W^+ &\rightarrow e^+ + \nu_e \end{aligned} \tag{1.9}$$

corresponding to charged currents which can be attributed to a beta decay as in the example shown in Figure 1.2. Neutral current interactions are similar with decays such as:

$$\begin{aligned} e^- &\rightarrow e^- + Z^0 \\ Z^0 &\rightarrow b + \bar{b} \end{aligned} \tag{1.10}$$

or a simple Z^0 decaying through a di-electron diagram as shown in Figure 1.3.

In the previous chapter, it is already suggested that in SM, only charged current interactions allow the flavors of quarks and leptons to be changed. Hence, in each generation, the quark and lepton pairs are linked while the quark triplets can be mixed by transforming from the mass eigenstates(d, s and b) to the weak eigenstates($d\prime$, $s\prime$ and $b\prime$). This came first from quark inter-generation interactions such as the $u - s$ interactions in $K^+ \rightarrow \mu^+\nu_\mu$ process, where the Cabibbo angle θ_C was introduced to get a rotation of the 2 generation quark doublets:

$$\begin{pmatrix} \psi'_d \\ \psi'_s \end{pmatrix} = \begin{pmatrix} cos\theta_C & sin\theta_C \\ -sin\theta_C & cos\theta_C \end{pmatrix} \begin{pmatrix} \psi_d \\ \psi_s \end{pmatrix} \tag{1.11}$$

This methodology has been further generalized to be a 3 × 3 matrix, which was developed by Kobayashi and Maskawa and later known as the "CKM Matrix", parametrizing the mixing of the quarks in 3 generations in Equation 1.12 and can be further interpreted as 3 angles and 1 complex phase, the latter one of which is introduced so that the CP violation is permitted since the CKM Matrix elements will show up with their complex conjugates as soon as the CP transformation is applied on

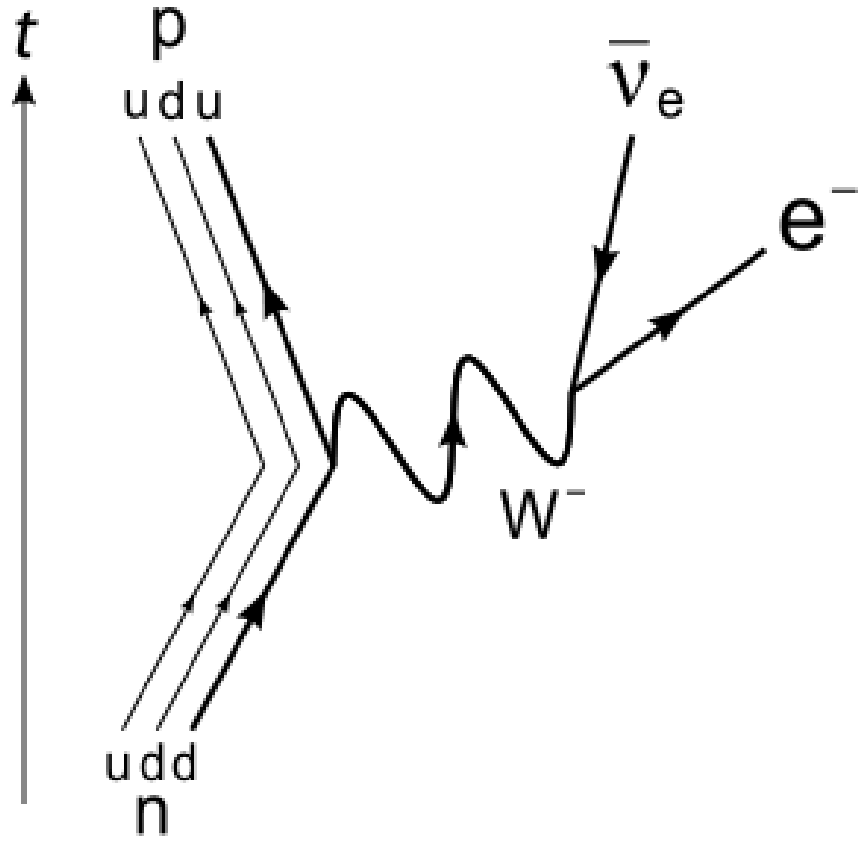

Figure 1.2 An example of charged current interaction in beta decay of a neutron to a proton with an W^- boson emitted and decayed into an electron and an electron anti-neutino.

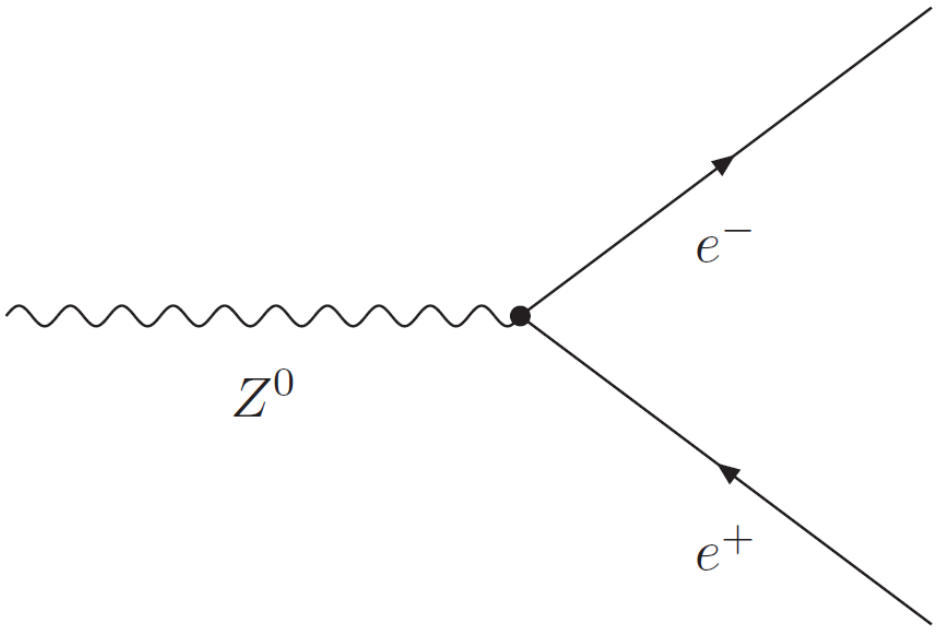

Figure 1.3 A neutral current interaction instance of Z boson decaying into an electron and a positron .

the matrix.

$$\begin{pmatrix} \psi'_d \\ \psi'_s \\ \psi'_b \end{pmatrix} = V_{CKM} \begin{pmatrix} \psi_d \\ \psi_s \\ \psi_b \end{pmatrix} = \begin{pmatrix} V_{ud} & V_{us} & V_{ub} \\ V_{cd} & V_{cs} & V_{cb} \\ V_{td} & V_{ts} & V_{tb} \end{pmatrix} \begin{pmatrix} \psi_d \\ \psi_s \\ \psi_b \end{pmatrix} \tag{1.12}$$

The CP violation was first found to be a big surprise because for a long time, scientists all believe that the law of nature gives perfect symmetries in the "mirror reflection" (e.g. by reversing the axes of all spatial dimensions). The parity conservation law is well accepted as a universal law of Natural because by the mid-20^{th} century, gravitation, electromagnetism and the strong interactions were found to all respect it. C.N.Yang and T.D.Lee proposed the theoretical possibility for parity violation in weak interactions after they carefully reviewed the existing data. This possibility that the P parity was violated in weak interaction was supported by C.S. Wus experimental results of beta decays in Cobalt-60 nuclei. In addition, in the 1960s, the combined CP symmetry is discovered to be broken in kaon decays by J. Cronin and V. Fitch, as well as soon after in certain weak decays of B mesons. However, CP violation occurs in much rarer cases than P violation. Nevertheless, it is widely considered by the scientific community that it could be a valid explanation for the matter anti-matter asymmetry of our universe.

To summarize, the unified electoweak theory has been successfully developed through the 20th century and has well interpreted the electromagnetism and the weak interactions as different aspects of the electroweak interaction unified at the high energy scale. It allowed building up a solid SM theory. Together with the Quantum Chromo Dynamics theory and the Higgs mechanism, it contributes to the matured SM theory although several issues need to be verified such like the Higgs boson itself, theoretically introduced through the so called Higgs mechanism to add masses to the weak bosons as well as to all the other massive elementary particles.

1.2 SM W^+W^- production and Anomalous Triple-Gauge-Boson Couplings

1.2.1 SM Diboson production

One of the crucial foundations of the SM is the principle of the gauge-invariance. In SM electroweak interactions, the gauge bosons have very specific couplings due to the interactions which obey a non-

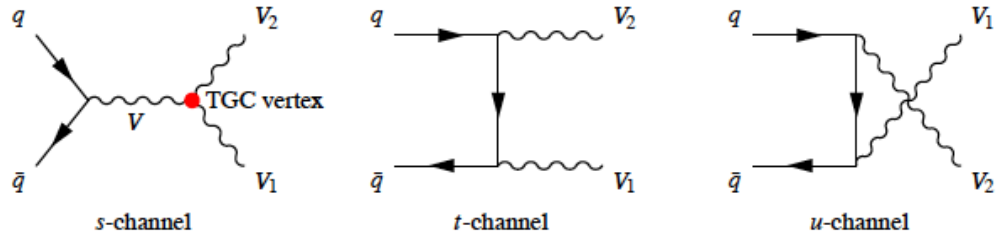

Figure 1.4 The generic SM tree-level Feynman diagrams for diboson production at hadron colliders; V,V1,V2 = W,Z,γ. The s-channel diagram, on the left, contains the trilinear gauge boson vertex.

Abelian gauge group $SU(2)_L \times U(1)_Y$. A good understanding of the Diboson production(W^+W^-, $W^\pm Z$, ZZ, $W^\pm\gamma$ and $Z\gamma$, see Figure 1.4) in high energy experiment is an effective and important way to verify the SM theory, especially its high energy behavior in electroweak interactions. Precision measurements of diboson production are probing the triple gauge-boson vertices such like WWZ and $WW\gamma$. New physics may potentially manifest its non-SM signatures by modifying the vector boson self-interactions, in particular the triple gauge-boson vertices. The results can therefore be interpreted as anomalous (non-SM) vertices. Last but not least, some of the diboson processes such as the SM ZZ and WW, share the same final states with Higgs to diboson decay channels as well as other new phenomena, thus they are also an irreducible background for quite a few new physics searches.

The cross sections of all the SM diboson processes are summarized in Figure 1.5 to be compared with other SM processes among different experiments at different collider center-mass-energy scales.

1.2.2 SM W^+W^- production

One of the major Diboson processes in LHC experiments is the W^+W^- production. It is not only an important test of the electroweak sector of the SM theory but also a probe of new physics through charged aTGCs (anomalous triple gauge-boson couplings). The W^+W^- production mainly originates from the quark-antiquark annihilation. The corresponding tree-level Feymann diagrams are shown in Figure 1.6, the 3rd one refers to the s-channel and directly involves the WWZ and $WW\gamma$ TGC vertices. Another 3% non-negligible production of W^+W^- arises from gluon-gluon fusion which is shown in Figure 1.7.

The SM predicted cross section calculated with MCFM [7] and CT10 [8] PDFs is $44.7^{+2.1}_{-1.9}$ pb

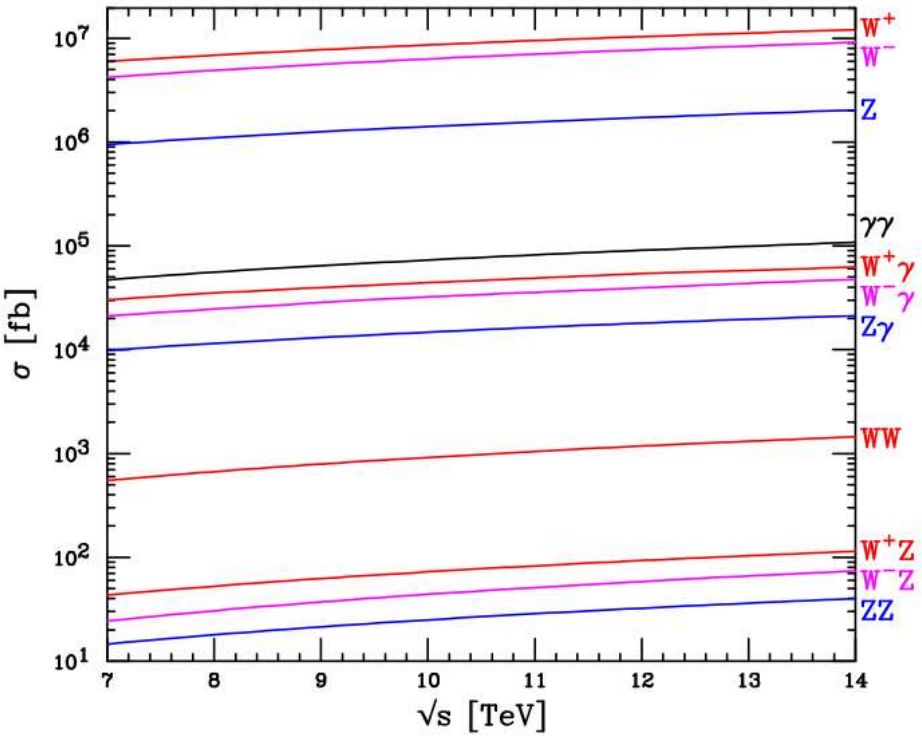

Figure 1.5 NLO boson production in pp-collisions. The decay branching ratios of the Ws and Zs into one species of leptons are included. For $\gamma\gamma$ and $V\gamma$ we apply p_T cuts of 25 and 10 GeV to photons respectively. [5]

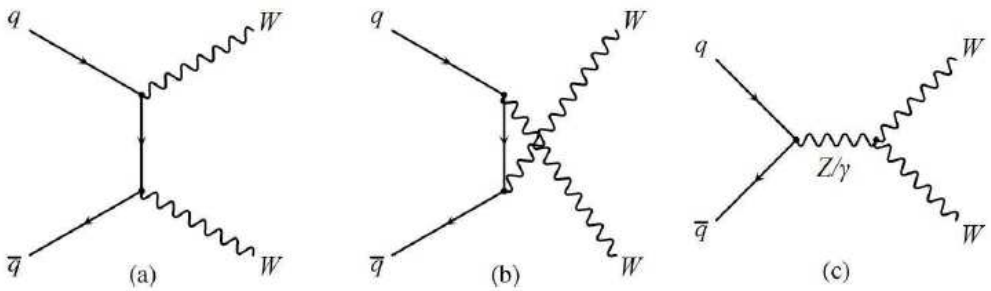

Figure 1.6 The generic SM tree-level Feynman diagrams for W^+W^- production through quark-antiquark initial state.

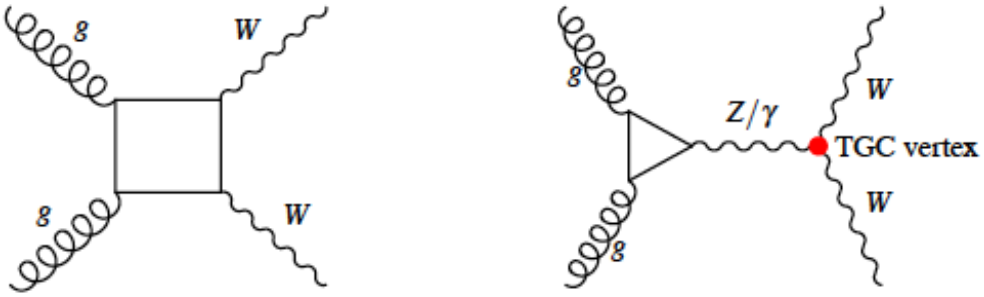

Figure 1.7 SM Feynman diagrams for W^+W production through gluon-gluon fusion in hadron colliders. Please note that the Z-exchange triangle diagrams cancel when summed over massless up- and down-type contributions. [6]

including a 1.3 pb contribution from gluon-gluon fusion. A cross-checked with MC@NLO [9] and CT10 PDFs gives a 45.1 pb cross section. For completeness, there is also ∼0.1% contribution to the W^+W^- signal from Double-Parton-Scattering(DPS). As it is negligible compared to the two major sources through single-parton-scattering, it will not be accounted for in this analysis.

One of the major interests in a precise measurement of the SM WW cross section is due to the fact that the SM production of W^+W^- plays a major role as the irreducible background for $Higgs$ searches in $H \rightarrow W^+W^-$ channels, particularly in the measurement of the fully leptonic decays of W boson pairs. Practically, in $H \rightarrow W^+W^-$ searches, the SM W^+W^- background is estimated from a SM WW control region by giving up $Higgs$ topology selections but with a high dilepton invariant mass which is complementary to the low mass $Higgs$ signal region.

The TGC vertices corresponding to W^+W^- processes are WWZ and $WW\gamma$ which were shown in both Figure 1.6 and Figure 1.7. Any anomalous TGCs(aTGCs) could potentially increase the W^+W^- production rate especially in high p_T or high transverse mass region. The most general and effective Lagrangian that conserves C and P symmetries separately for charged triple gauge boson interactions is:

$$L/g_{WWV} = ig_1^V(W^*_{\mu\nu}W^\mu V^\nu - W_{\mu\nu}W^{*\mu}V^\nu) + ik_V W^*_\mu W_\nu V^{\mu\nu} + \frac{\lambda_V}{M_W^2}W^*_{\rho\mu}W^\mu_\nu V^{\nu\rho} \tag{1.13}$$

, where V can be either γ or Z boson, and $X_{\mu\nu} = \partial_\mu X_\nu - \partial_\nu X_\mu$. Note that W^μ refers to the W^- field. The overall coupling constants can be either:

$$g_{WW\gamma} = -e \tag{1.14}$$

or:

$$g_{WWZ} = -ecot\theta_W \tag{1.15}$$

, where e stands for the absolute value of electron charge.

In the SM, all those TGC parameters have their own fixed values: $g_1^V = k_V = 1$ and $\lambda_V = 0$. Hence, aTGCs will result in a non-zero deviation of TGC parameters with respect to the SM predictions. As a result, the aTGC parameters are defined as:

$$\Delta g_1^Z \equiv g_1^Z - 1, \Delta k_\gamma \equiv k_\gamma - 1, \Delta k_Z \equiv k_Z - 1, \lambda_Z, \lambda_\gamma. \tag{1.16}$$

while $g_1^\gamma \equiv 0$ is always required in order to mantain the electromagnetic gauge invariance. Note that the non-SM coupling parameters will result in an increase of the amplitutes of WW production as energy grows which will lead to the tree-level unitarity violation. This is avoided by introducing a cutoff form factor Λ in the form of:

$$\Delta k(\hat{s}) = \frac{\Delta k}{(1 + \hat{s}/\Lambda^2)^2}, \tag{1.17}$$

where $\hat{s}$ stands for the squared invariant mass of WW. Therefore, as soon as the mass scale of Λ is reached, the new phenomenon which is responsible for the aTGCs is expected to be observed. This will be dicussed in detail in the aTGC section 3.10.

This analysis will be focusing on the precise measurement of the SM W^+W^- cross section and the limit setting on the aTGCs associated with WWZ and $WW\gamma$.

CHAPTER 2. THE ATLAS EXPERIMENT AT THE LARGE HADRON COLLIDER

The Large Hadron Collider(LHC) and the ATLAS experiment, which produced and recorded the analyzed collision data, will be introduced in this chapter. The collider will be briefly introduced in Section 2.1, including the overview of the main ring, infrastructure, general services, beam condition and different subsystems. An illustration of the ATLAS experiment will be given in Section 2.2 by introducing piece by piece the general purposes of the experiment, the different components of the detector, its performances and the physics object reconstruction, the latter of which will be discussed again in the analysis section.

2.1 LHC: The Large Hadron Collider

The LHC is the world's largest particle accelerator with the highest center of mass energy. It is located at the France-Switzerland border hosted by the European Organization for Nuclear Research(CERN). This giant project was approved by CERN Council in the 1990s and financially supported by both member and non-member states. The accelerator was proposed to test the modern quantum theory of particle phycis especially at high energy scale, and theorectical predictions of the elementary interactions and properties of fundamental particles as well as to potentially discover new physics and particles that are predicted by the frontier theories such as supersymmetry and the Higgs theory.

LHC lies in a 27 km tunnel spanning the border of France and Switzerland near the city of Geneva, which was upgraded from the one that used to house the Large Electron-Positron Collider(LEP). The design center-of-mass energy for LHC is $\sqrt{s} = 14$ GeV (7 TeV per beam). It ran at $\sqrt{(s)} = 7$ GeV during 2010 and 2011 and is now increased to $\sqrt{s} = 8$ GeV in 2012. The LHC will be shut down in

2013 for approximately 2 years and to achieve the full energy operation by the end of 2014.

The proton beams are first accelerated in an accelerator complex made of a linear accelerator (LINAC 2), a Proton Synchrotron Booster (PSB), a Proton Synchrotron (PS) and a Super Proton Synchrotron (SPS) and then by the LHC at an unprecedented high center-of-mass energy and luminosity. Protons are generated and accelerated to $\sim$ 50 MeV by LINAC 2 and fed to Proton Synchrotron Booster(PSB) before being futher accelerated to $\sim$ 1.4 GeV and injected to PS. The 26-GeV beam goes out of PS and is injected to SPS, in which the energy can be further increased to 450 GeV and is finally injected into the main ring. Proton bunches are accumulated and accelerated to the peak energy in the LHC main ring and collide at the four intersection points as shown in 2.1.

The collision rate of LHC(per second) can be give by:

$$N_{event} = L \times \sigma_{event} \tag{2.1}$$

, in which the L represents the luminosity of the machine while σ_{event} stands for the cross section of the considered process. The luminosity of LHC, which depends on the beam parameters, can be written for a Gaussian beam distribution as [10]:

$$L = \frac{N_b^2 n_b f_{rev} \gamma_r}{4\pi \epsilon_n \beta^\star} F \tag{2.2}$$

each of the parameters are defined as:

- N_b: number of particles per bunch
- n_b: number of bunches per beam
- f_{rev}: the revolution frequency
- γ_r: the relativistic γ factor
- ϵ_n: the normalized transverse beam emittance
- $\beta^\star$: the beta function at the collision point
- F: the geometric luminosity reduction factor due to the crossing angle at the interaction point (IP):

$$F = 1/\sqrt{1 + (\frac{\theta_c \sigma_z}{2\sigma^\star})^2}, \tag{2.3}$$

- θ_c: the full crossing angle at the IP
- σ_z: the RMS bunch length
- $\sigma^\star$: the transverse RMS beam size at the IP

There are six detectors constructed at the LHC intersection points underground:

- ATLAS: A Toroidal LHC Apparatus
- CMS: Compact Muon Solenoid
- LHCb: LHC-beauty
- ALICE: A Large Ion Collider Experiment
- TOTEM: TOTal Elastic and diffractive cross section Measurement
- LHCf: LHC-forward

Out of the 6 major experiments in LHC, ALTAS (A Toroidal LHC Apparatus) and CMS (Compact Muon Solenoid) experiments are the 2 high luminosity experiments. The peak luminosity of $L = 10^{34} cm^{-2} s^{-1}$ is expected for both of them. Each are based on a general-purpose detector. Mainly working during the LHC proton collision running phase, they investigate at the TeV energy scale a wide range of known and hypothetical physics processes. Many frontier physics searches are the essential motivation of the two experiments such like the Higgs boson hunting and the search fornew physics phenomena such as SUSY, dark matter particles and extra dimentions. In addition to these 2 general-purpose experiments, there are four other experiments at LHC:
LHCb is a dedicated experiment for B-physics research, particularly the measurment of CP violation parameters via the interactions of b-hadrons, which is the one of the most straightforward way to probe the Matter-Antimatter asymmetry in our universe. The expected luminosity peaks at $L = 10^{32} cm^{-2} s^{-1}$.

ALICE is optimized as a heavy ion detector operated during the Pb-Pb nuclei collision running phase of LHC with a center-of-mass energy of 2.76 TeV per nucleon. The motivation is to produce the quark-gluon plasma, in which quarks and gluons are deconfined, mimicing the state of the early

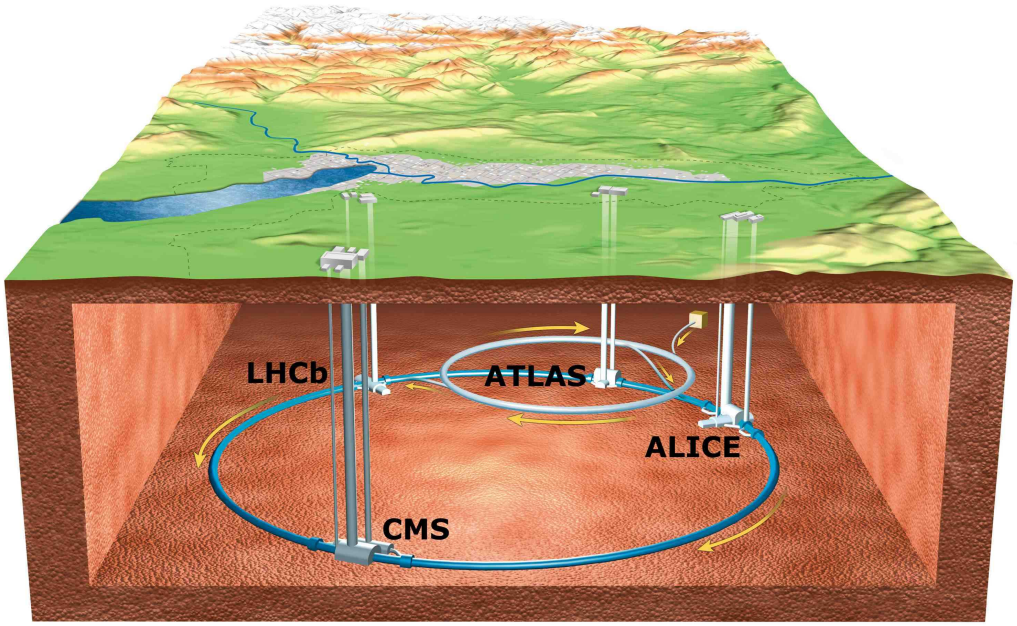

Figure 2.1 The layout of Large Hadron Collider and four major detectors. [10]

Universe after the Big Bang. The evolvement of quark-gluon plasma such like the cooling and expanding will help to visualize the picture how the particles which consistitute the Universe today come into being. The expected luminosity peaks at $L = 10^{27} cm^{-2} s^{-1}$.

TOTEM and LHCf are much smaller experiments compared to the other four. The goal of TOTEM experiment is to detect the protons from elastic scattering at small angles and measure the total cross section, elastic scattering and diffractive processes. LHCf is motivated to investigate the origin of ultra-high-energy cosmic rays by measuring the numbers and energy of neutral pions generated in the forward region of the collisions.

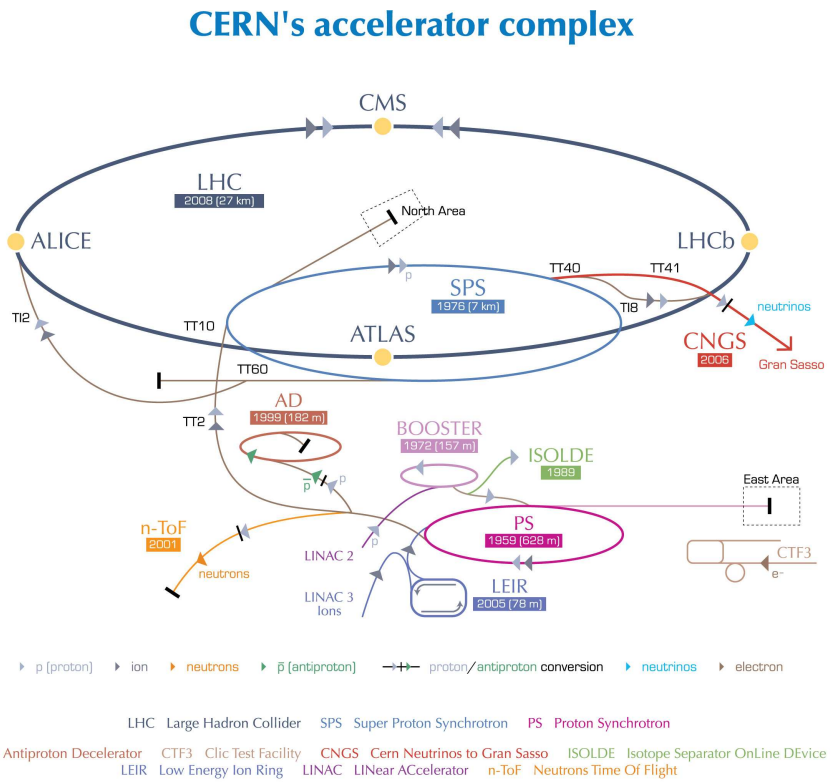

Figure 2.2 The accelerator chain for the LHC at CERN. [10]

2.2 The ATLAS Detector

ATLAS, which is constructed in the experimental cavern at Point 1 at CERN, is one of the two general-purpose detectors at LHC. Due to the extreme LHC characteristics mentioned in section 2.1, the design of the ATLAS detector has to cope with the high interaction rates, high energy deposits, high particle multiplicities and high radiation doses. In addition, the main constraints due to the physics requirements for the ATLAS detector design are:

1) The total production rate of inelastic events from LHC pp collisions are 10^9 per second, which corresponds to an inelastic proton-proton cross-section of 80 mb. As a result, every candidate event of new physics processes approximately has 23 inelastic events per bunch-crossing accompanying it.

2) jet production cross-sections from QCD processes dominate most of the rare new physics processes and is a great challenge to the object-identification capabilities of the detector.

3) the resolution of lepton measurement and charge identification is challenged by the experimental signature of various physics processes such like high p_T leptons decayed from the heavy vector bosons $W\prime$ and $Z\prime$ at TeV scale.

4) Out of all the physics motivations, the search for the SM higgs boson is definitely the hotspot which hence gives the benchmark for the requirements. The natural width of low-mass higgs boson would be ∼MeV scale and it is restricted by the instrumental resolution which defines the observed width.

Hence, the general requirements of the ATLAS detector given by the physics motivations are therefore the following:

1) Fast, radiation-hard electronics and sensor elements are required to match with the extreme experimental conditions.

2) High granularity of the detector is mandatory to avoid as much as possible events overlapping with each other.

3) Good resolution of charged-particle momentum and reconstruction efficiency are crucial for inner tracking as well as good capability of observation of secondary vertices used to tag the τ-leptons and b-jets is required.

4) The capability of electromagnetic calorimeter to identify the electrons and photons and the performance of muon spectrometer for muon identification and momentum resolution are essentially required.

5) Full-coverage hadronic calorimetry for the accurate measurement of jet and missing transverse energy, which are the experimental signatures and many interesting processes and new physics phenomena, is essentially demanded.

6) The allowed trigger rate is limited at low p_T region which has enormarous background domination. Hence, the efficient triggering of low p_T objects with high background rejection is essentially required.

LHC was running pp collisions at $\sqrt{s} = 7$ TeV in 2011 with 5.25 fb^{-1} integrated luminosity recorded by ATLAS detector (4.64 fb^{-1} after general data quality requirement) and peak instaneous luminosity in stable beams reaching $10^{32} \sim 10^{33} cm^{-2} s^{-1}$. Currently, the centre-of-mass energy of LHC has been ramped up to 8 TeV in 2012 pp collision runs with the peak instaneous luminosity in stable beams increased to $7 \times 10^{33} cm^{-2} s^{-1}$. The Cumulative integrated luminosity of ATLAS versus days in 2011 and 2012 are shown in Figure 2.3.

Given all the technical restriction, high-level requirement and great challenges, the ATLAS detector is still well developed and successfully constructed and commisioned by the large collaboration of thousands of physicists and engineers after 15 years of heroic hard work and devotion. The principle layout of the ATLAS detector is shown in Figure 2.5 with the general particle identification picture visualied in Figure 2.4. The different compartments of the detector can be classified and categorized as three sub-systems: Inner Detectors(ID), Calorimeters and Muon Spectrometers(MS).

2.2.1 Inner detector

ATLAS inner detector system is responsible for the inner tracking measurement to cope with the extemely large track density from approximately 1000 particles from LHC collisions every 25 or 50 ns

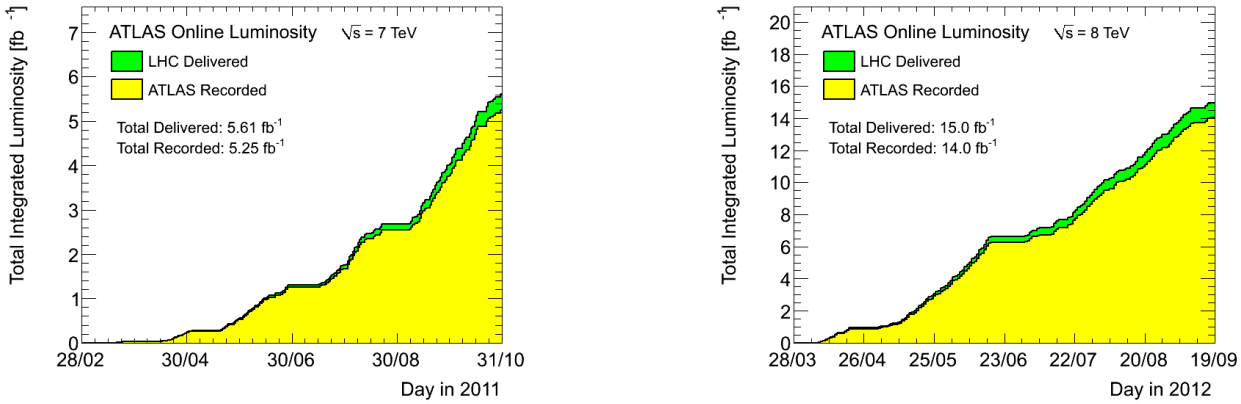

Figure 2.3 Cumulative luminosity versus day delivered to (green), and recorded by ATLAS (yellow) during stable beams and for pp collisions at 7(8) TeV centre-of-mass energy in 2011(2012). The delivered luminosity accounts for the luminosity delivered from the start of stable beams until the LHC requests ATLAS to turn the sensitive detector off to allow a beam dump or beam studies. Given is the luminosity as determined from counting rates measured by the luminosity detectors. These detectors have been calibrated with the use of the van-der-Meer beam-separation method, where the two beams are scanned against each other in the horizontal and vertical planes to measure their overlap function. [11]

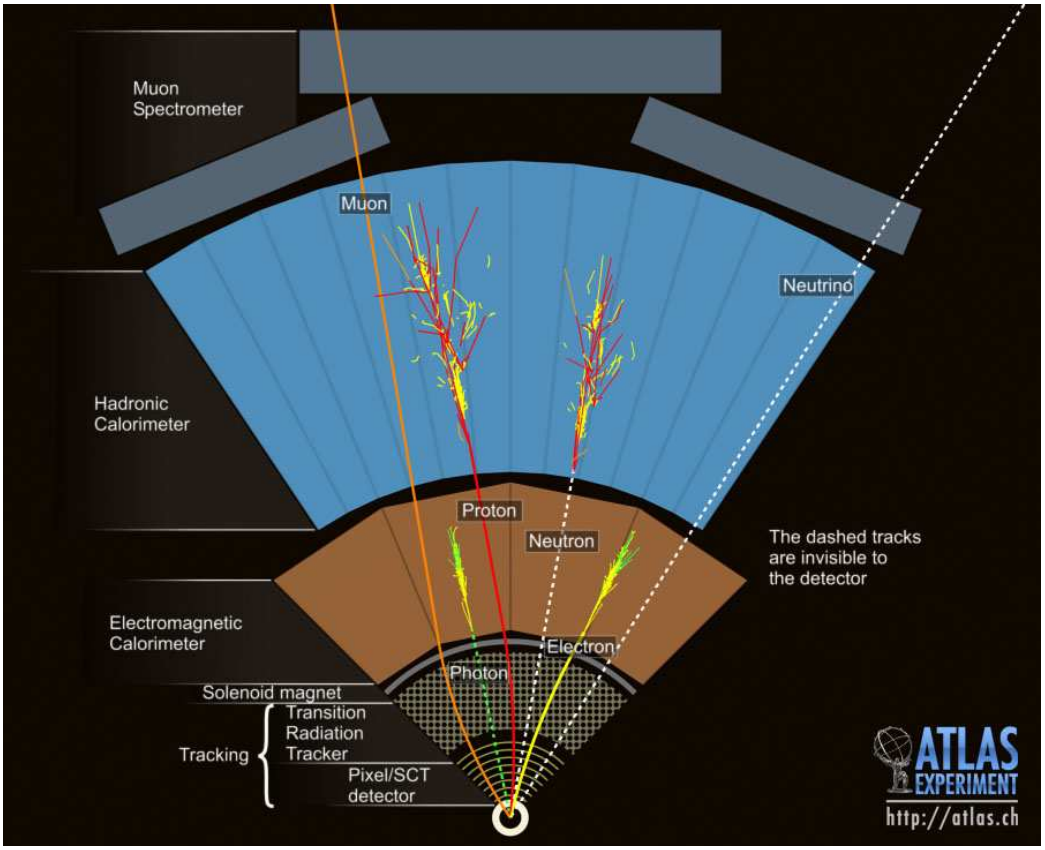

Figure 2.4 Particle identification at ATLAS. [12]

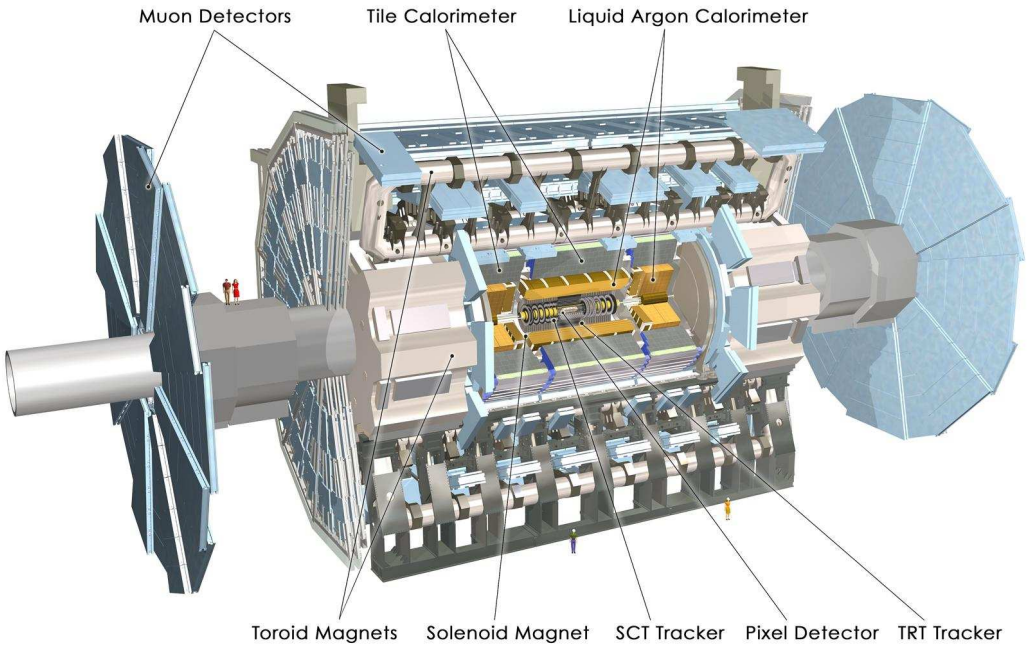

Figure 2.5 Layout of the ATLAS detector. [13]

within $|\eta| < 2.5$ geometry restriction. The precise measurement and good resolution of track quantities including the momenta, impact parameters and primary/secondary vertices is guaranteed by the high granularity of the Inner Detector so as to fulfill the requirement of detecting most of the interesting benchmark physics processes.

The Inner Detector is made up of three major compartments complementary to each other: the Pixel detector, the Sillicon Microstrip Tracker(SCT) and the Transition Radiation Tracker(TRT). The ID is operated within a 2 T magnetic field of the central solenoid magnet. The coverage of the ID is up to $|\eta| < 2.5$ for the precision tracking detectors(Pixel and SCT). The sub-detectors are designed as concentric cylinders around the beam axis in the barrel and are located on disks in the end-cap. Each sub-detector is shown in the general layout of the ID in Figure 2.6 and illustrated in the following subsections. The performance requirements and geometry parameters of the ID are further detailed in Figure 2.7.

Pixel detector

The sillicon pixel detector is the innermost sub-detector of the ID which has the highest granularity in the vertex region. There are three pixel layers as shown in Figure 2.7 expected to be crossed by

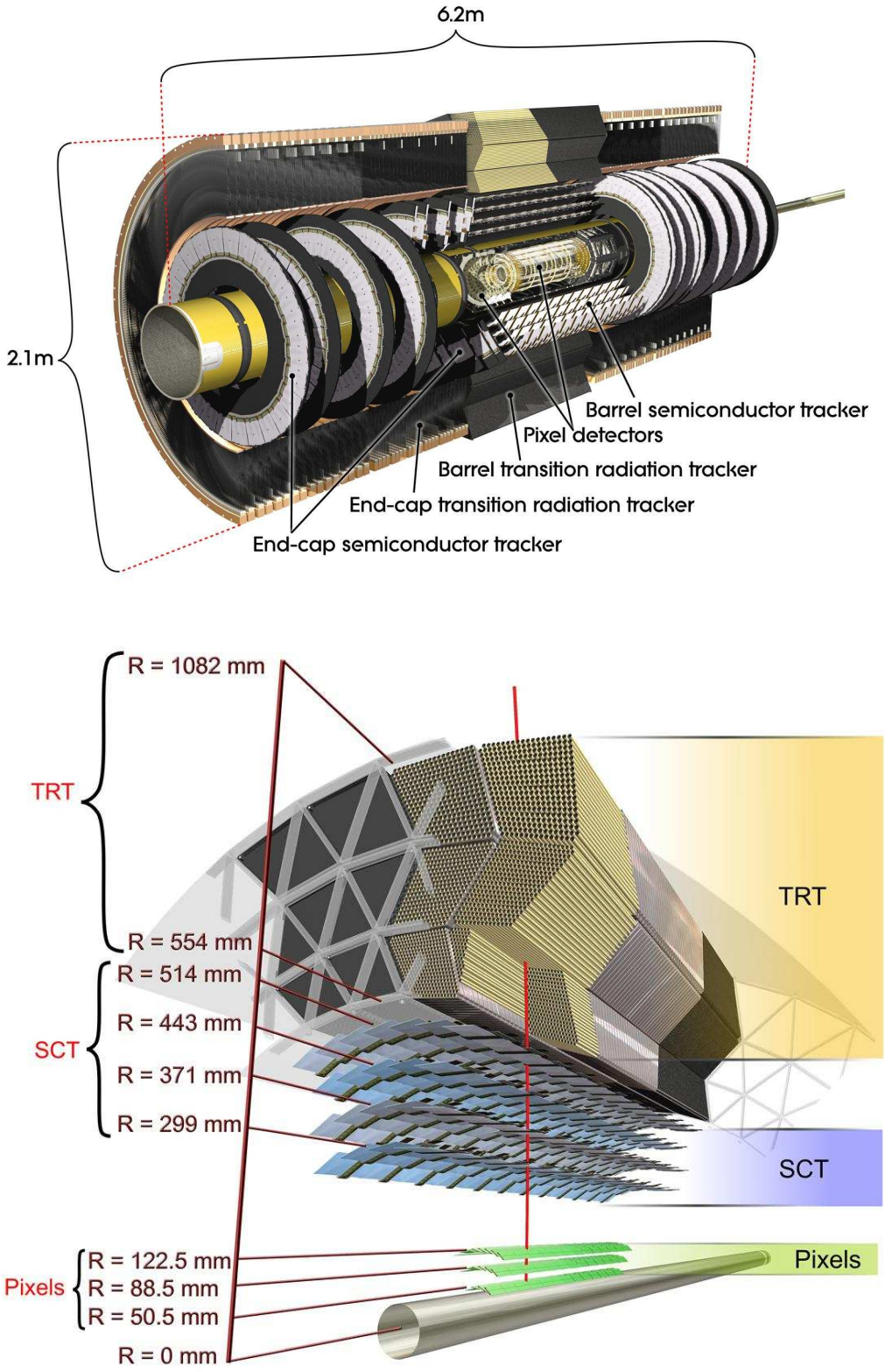

Figure 2.6 The ATLAS Inner Detector. [13]

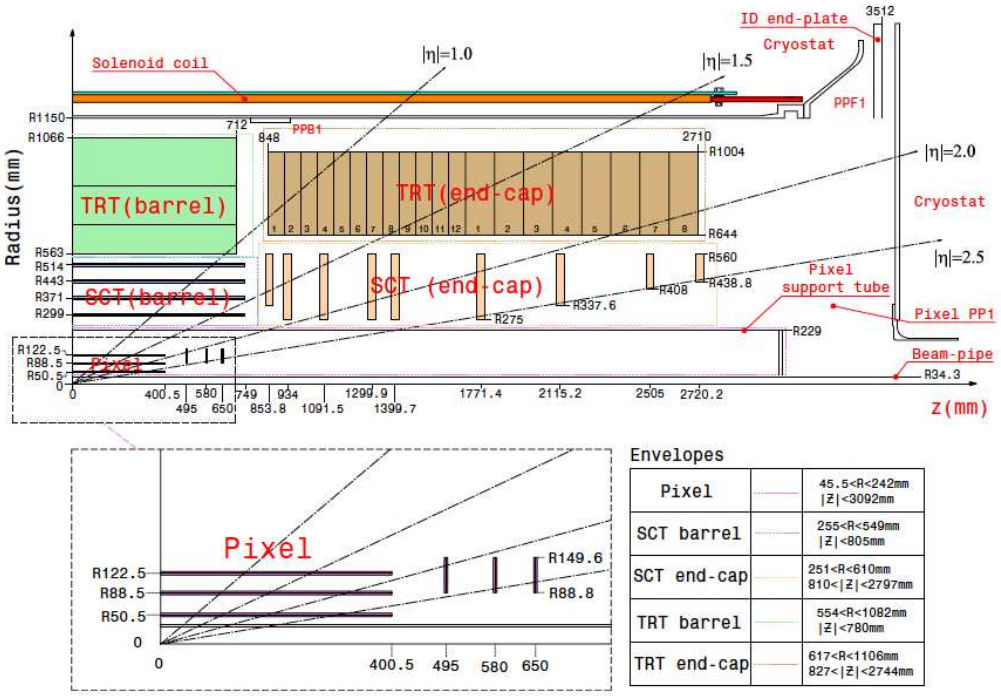

Figure 2.7 Plan view of a quarter-section of the ATLAS inner detector showing each of the major detector elements with its active dimensions and envelopes. The labels PP1, PPB1 and PPF1 indicate the patch-panels for the ID services. [13]

measured tracks. The segmentation is in $R-\phi-z$ coordinate and all pixel sensors are idential to each other with the minimum size of $50 \times 400\mu m^2$ in $R-\phi-z$. The total number of readout channels is ∼80.4 million. The designed intrinsic resolutions of the Pixel detector are 10 μm $(R-\phi)$ and 115 $\mu m(z)$ in the barrel region and 10 μm $(R-\phi)$ and 115 μm (R). There are in total 1744 $19 \times 63mm^2$ sensors in the Pixel detector operating at the temperature $-5°$C to $-10°$C. The design of the Pixel sensors are challenged and restricted by the specification in the high energy hadron collider experiment such as the radiation hardness, occupancy and resolution in the innermost layers. Hence, the sensors are using oxygenated n-type wafers with readout pixels on the n^+-implanted side of the detector with double-side processing involved so as to guarantee good charge-collection efficiency and radiation tolerance. The B-layer which is the innermost layer of the Pixel detector is essentially important in b-jet identification as well as helping to identify electrons from converted photons.

Silicon Strip Tracker

The Silicon Strip Tracker (SCT) is the other precision tracking sub-detector of the ID, with eight strip layers (four space points) that are expected to be crossed by the tracks from collisions. There are ∼6.3 million readout channels and 15912 sensors in all, which use a classic single-sided p-in-n technology with AC-coupled readout strips to guarantee the reasonable cost and reliability. Small-angle stereo strips segmented in $R-\phi$ are installed on each layer parallel to the beam direction in the barrel and radially in the end-cap. The mean pitch of the strips is approximately $80\mu m$ in both the barrel and the end-cap region which are determined by the required digitising precision, granularity, particle occupancy and noise performance. The sensors work at ∼150 V bias voltage initially and then 250 and 350 V after ten years of operation so that the good charge collection efficiency can be guaranteed. The designed intrinsic resolutions determined by the accuracies per module in the barrel are 17 μm $(R-\phi)$ and 580 μm (z) while in the endcap they are 17 μm $(R-\phi)$ and 580 μm (R) respectively.

Transition Radiation Tracker

The outermost Transition Radiation Tracker (TRT) works as a combination of a straw tracker (∼298,000 straws in total) and a transition radiation detector, which consists of 73 layers of staws

interleaved with fibres in the barrel, 160 straw planes intervealed with foils in the end-cap and ∼351000 readout channels in total. The straw tubes have a diameter of 4 mm for each. TRT give the coverage up to $|\eta| < 2.0$ for inner track measurement with 36 hits per track expected by maximum. Each straw in TRT is filled with gass which is a mixture of $Xe - CO_2 - O_2$ and becomes ionized when the tracks of a charged particle crosses it. The Xenon gas is filled so as to increase the number of straws with strong signals from ultra-realivistic charged particles with transition radiation emitted. Unlike Pixel detector and SCT, TRT provides only the $R - \phi$ information which has an intrinsic resolution $\sim 130\mu m$ per straw. TRT provides a very good separation between electrons and hadrons by measuring the transition radiation (TR). In principle, lighter realivistic charged particles such like electrons with a particular energy are supposed to have higher speed and emit the most transition radiations and the measured tracks therefore give larger signals which can be identified from the hadrons which are much heavier. For example, the rejection against charged pions can be achieved by counting the fraction of TRT straws with high-Threshold hits.

2.2.2 Calorimeter

The sampling calorimeters of ATLAS located outside the ID and solenoidal magnet aim to measure the energies of particles using the energy deposit in the calorimeters via the cascaded electromagnetic (EM) processes(electrons and photons) as well as hadronic processes (gluons and quarks reconstructed as "jets"). The ATLAS calorimeter systems contain two sampling calorimeters, the lead-LAr electromagnetic calorimeter and the tile hadronic barrel calorimeter, as shown in in Figure 2.8. The overall pseudorapidity coverage of the calorimeter systems is up to $|\eta| < 4.9$. The fine granularity of the calorimeter systems are essentially demanded so as to fulfill the needs of precise measurement of electrons and photons as well as the reconstruction of jets and missing transverse energies (E_T^{miss}). The detailed parameters of the η coverages, granularities and segmentations in each compartment of the calorimeter systems are summarized in Table 2.1.

One of the most important requirements for calorimeter constructions is to guarantee the sufficient deposition of the EM and hadronic showers to avoid the leakage to the Muon Spectrometers (MS). Hence, the depth of the EM calorimeter was eventually motivated to be designed as >22 radiation lengths (X_0) in the barrel and >24 X_0 in the end-cap. As a result, the approximate interaction

lengths(λ) of active calorimeter are 11 λ including 1.3 λ from the outer services and experimentally verified to be an adequate amount to suppress the punch-through into the MS. Another essential requirement motivated by the LHC physics goal is the fine reconstruction of E_T^{miss} which is one of the most straightforward signature of many interesting physics processes. This can be fulfilled as well, given the thickness mentioned above and the good pseudo-rapidity coverage.

Table 2.1 Main parameters of the calorimeter system.

	Barrel		**End-cap**	
LAr EM Calorimeter				
Number of layers and pseudo-rapidity coverage				
Presampler	1	$\|\eta\| < 1.52$	1	$1.5 < \|\eta\| < 1.8$
alorimeter	3	$\|\eta\| < 1.35$	2	$1.375 < \|\eta\| < 1.5$
C	2	$1.35 < \|\eta\| < 1.475$	3	$1.5 < \|\eta\| < 2.5$
			2	$2.5 < \|\eta\| < 3.2$
Granularity $\Delta\eta \times \Delta\phi$ versus $\|\eta\|$				
Presampler	0.025×0.1	$\|\eta\| < 1.52$	0.025×0.1	$1.5 < \|\eta\| < 1.8$
alorimeter 1st layer	0.025/8×0.1	$\|\eta\| < 1.40$	0.050×0.1	$1.375 < \|\eta\| < 1.425$
	0.025×0.025	$1.40 < \|\eta\| < 1.475$	0.025×0.1	$1.425 < \|\eta\| < 1.5$
			0.025/8×0.1	$1.5 < \|\eta\| < 1.8$
C			0.025/6×0.1	$1.8 < \|\eta\| < 2.0$
			0.025/4×0.1	$2.0 < \|\eta\| < 2.4$
			0.025×0.1	$2.4 < \|\eta\| < 2.5$
			0.1×0.1	$2.5 < \|\eta\| < 3.2$
alorimeter 2nd layer	0.025×0.025	$\|\eta\| < 1.40$	0.050×0.025	$1.375 < \|\eta\| < 1.425$
C	0.075×0.025	$1.40 < \|\eta\| < 1.475$	0.025×0.025	$1.425 < \|\eta\| < 2.5$
			0.1×0.1	$2.5 < \|\eta\| < 3.2$
Calorimeter 3rd layer	0.050×0.025	$\|\eta\| < 1.35$	0.050×0.025	$1.5 < \|\eta\| < 2.5$
Number of readout channels				
Presampler	7808		1536 (both sides)	
Calorimeter	101760		62208 (both sides)	
LAr hadronic end-cap				
$\|\eta\|$ coverage			$1.5 < \|\eta\| < 3.2$	
Number of layers			4	
Granularity $\Delta\eta \times \Delta\phi$			0.1 × 0.1	$1.5 < \|\eta\| < 2.5$
			0.2 × 0.2	$2.5 < \|\eta\| < 3.2$
Readout channels			5632 (both sides)	
LAr forward calorimeter				
$\|\eta\|$ coverage			$3.1 < \|\eta\| < 4.9$	
Number of layers			3	
Granularity $\Delta x \times \Delta y$(cm)			FCal1: 3.0 × 2.6	$3.15 < \|\eta\| < 4.30$
			FCal1:∼four times finer	$3.10 < \|\eta\| < 3.15$,
				$4.30 < \|\eta\| < 4.83$
			FCal2: 3.3 × 4.2	$3.24 < \|\eta\| < 4.50$
			FCal2:∼four times finer	$3:20 < \|\eta\| < 3:24$,
				$4.50 < \|\eta\| < 4.81$
			FCal3: 5.4 × 4.7	$3.32 < \|\eta\| < 4.60$
			FCal3:∼four times finer	$3.29 < \|\eta\| < 3.32$,
				$4.60 < \|\eta\| < 4.75$
Readout channels			3524 (both sides)	
Scintillator tile calorimeter				
	Barrel		Extended barrel	
$\|\eta\|$ coverage	$\|\eta\| < 1.0$		$0.8 < \|\eta\| < 1.7$	
Number of layers	3		3	
Granularity $\Delta\eta \times \Delta\phi$	0.1 × 0.1		0.1 × 0.1	
Last layer	0.2 × 0.1		0.2 × 0.1	
Readout channels	5760		4092 (both sides)	

lead-LAr Electromagnetic Calorimeter

The EM calorimeter constructed in the ATLAS calorimeter system is the lead-LAr calorimeter consisting accordion-shaped kapton electrodes and full-coverage lead absorber plates. It can be further divided into the barrel part ($|\eta| < 1.475$) and two end-cap parts ($1.375 < |\eta| < 3.2$) with separate

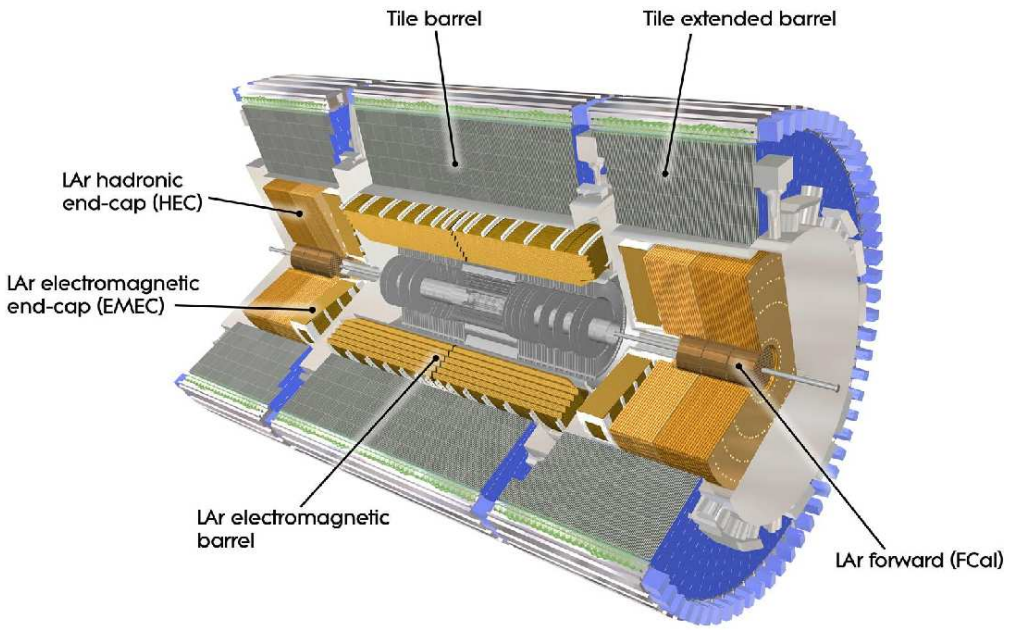

Figure 2.8 The ATLAS Calorimeter. [13]

cryostats. In the barrel region, a 4-mm tiny gap exist at $z = 0$ separating the barrel part into two identcial compartments. Two coaxial wheels with complementary pseudo-rapidity coverages ($1.375 < |\eta| < 2.5$ and $2.5 < |\eta| < 3.2$ for inner and outer wheels respectively) constitute the entire end-cap part of the LAr.

The barrel part of LAr is contained in one barrel cryostat to keep it sufficiently cool at the working temperature while there are two symmetric end-cap cryostats containing the end-cap EM calorimeters (EMEC), the end-cap hadronic calorimeters (HEC) and the forward calorimeters (FCal). The accordion geometry gives the possibility to have multiple active lateral layers, three in the precision-measurement region of $0 < |\eta| < 2.5$ including both the barrel part and the end-cap part in excluding the higher pseudo-rapidity region ($2.5 < |\eta| < 3.2$) where there are two layers only. The EM coverage is also extended to very forward regions ($3.1 < |\eta| < 4.9$) where three layers of FCal are placed closest to the beam.

Besides, an instrumented presampler with only one argon layer and the pseudo-rapidity coverage up to $0 < |\eta| < 1.8$ are installed in front of the barrel and part of the end-cap calorimeters to compensate the measurement of the energy loss right in front of the EM calorimeters so as to correct for the energy

lost by electrons and photons upstream of the calorimeter. The thickness of presampler layer in the barrel (end-cap) is 1.1 cm (0.5 cm).

Choice of the material in LAr Calorimeter Sampling material has been chosen as liquid argon for all these calorimeter compartments due to the intrinsic linear behaviour and radiation-hardness of it and the stability of response over time. The absorber material is chosen as lead and stainless steel with high-density to guarantee the containment of the EM energy depositions.

Geometry and segmentation of LAr Both the absorbers and the electrodes of barrel and end-cap compartments are designed according to an accordion geometry which not only avoids the azimuthal cracks in the ϕ direction but also leads to a great uniformity in terms of linearity and resolution as a function of ϕ. The layout of the signal layers are shown in Figure 2.10 for both barrel and end-cap parts indicating different electrodes in use before folding. The different segmentations of different layers can also be observed that the first and second layers has the finest segmentation along η while the third layer, which only has the residual of the EM showers deposited, is much less segmented. The detailed granularities were shown already in Table 2.1 and can be further visualized in Figure 2.9.

More specifically, in the barrel, LAr is divided into two identical half-barrel parts as mentioned at the very beginning of section 2.2.2 and each half contains 1024 accordion-shaped absorbers interleaved with readout electrodes can be further divided into 16 modules for the ease of construction. Those modules as shown in Figure 2.9 have 3 layers for each, which are the readouts at the low-radius and high-radius sides. The readout granularities are also summarized in Table 2.1. In the end-cap, the EMEC calorimeters are made up of two wheels on two different side of the barrel part and η-coverage ranges in $1.375 < |\eta| < 3.2$. The dedicated regions for precision measurement is $1.5 < |\eta| < 2.5$ on each side of the EMEC and can be longitudinally divided into three layers. Strips are segmented along η direction on the first layer. The second layer has equivalent segmentation as the barrel part while the granularity of the back layer is twice as coarse. The detailed parameters were shown in Table 2.1. Each EMEC wheel, which consists of its own inner wheel and outer wheel parts with a 3 mm boundary locating at $|\eta| = 2.5$, is made up of 768 absorbers on the outer wheel part and 256 absorbers on the inner wheel part. The amount of dead material in front of the EM calorimeter (including the presampler),

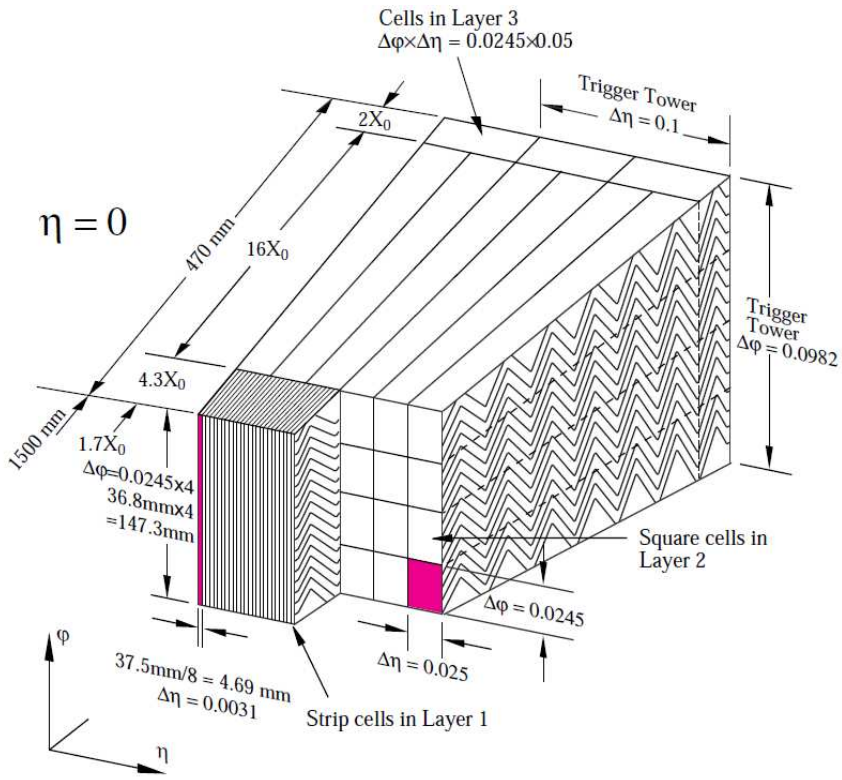

Figure 2.9 A barrel module of the LAr electromagnetic calorimeter showing the cell segmentation. [13]

between the presampler and the innermost layer of the calorimeter as well as the thickness of each calorimeter layer are shown in Figure 2.11 in units of X_0. The total thickness of the EM calorimeter is $> 22X_0$ in the barrel and $> 24X_0$ in the EMEC.

High-voltage distribution The nominal high-voltage (HV) of LAr EM calorimeter is 2 kV while the ones fed to the end-cap are $|\eta|$ dependent. Both side of each electrode are fed with the HV independently for redundancy. Only half of the signal can be collected once one side of the electrodes is not fed or when the HV is tripped. In this and any other non-nominal HV case, the measured energy will have to be re-calibrated so as to handle the non-nominal value measured with the non-nominal HV. For example, 77% of signal will be collected if the HV is fed with half of its nominal value. The collected signal varies as a function of HV is shown in Figure 2.12 which is technically due to the variation of the drift velosity. 32 electrode sectors are powered simutaneously given granularity of the HV as $\Delta\phi \times \Delta\eta = 0.2 \times 0.2$. One thing that needs to be emphasized is that in EMEC, $|\eta|$ dependent

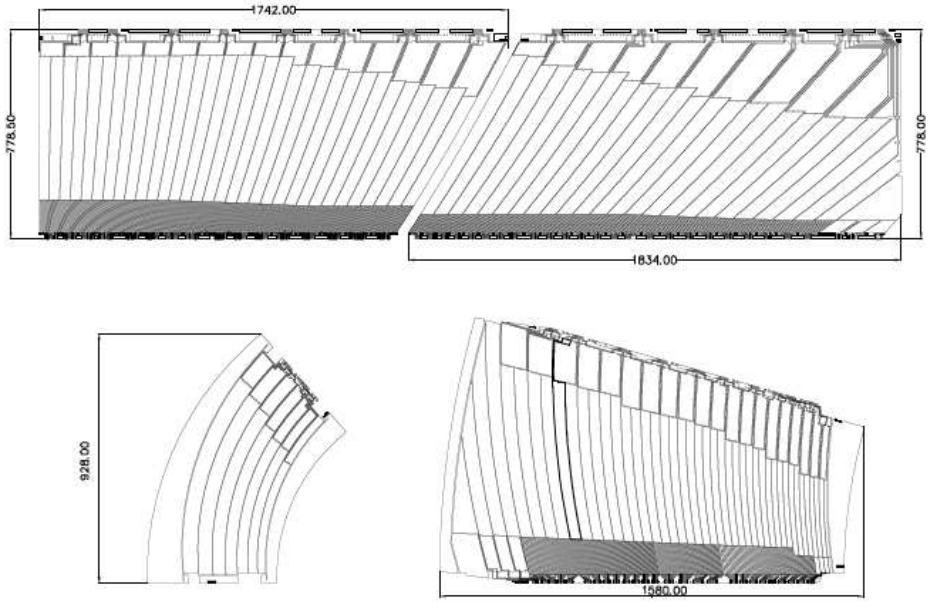

Figure 2.10 Upper two electrodes are for the barrel and the two bottom electrodes are for the end-cap inner (left) and outer (right) wheels. Dimensions are in millimetres. The drawings are all at the same scale. The two or three different layers in depth are clearly visible. [13]

HV are fed to cope with the fact that the drift gap of the EMEC on each side of the electrodes is not constant so as to obtain the uniformity of the detector response. The exact dependence of the HV at EMEC is shown in Figure 2.13.

The nominal resolution of EM calorimeter is $\frac{\sigma_E}{E} = \frac{10\%}{\sqrt{E(GeV)}} \oplus 0.7\%$ over the full coverage.

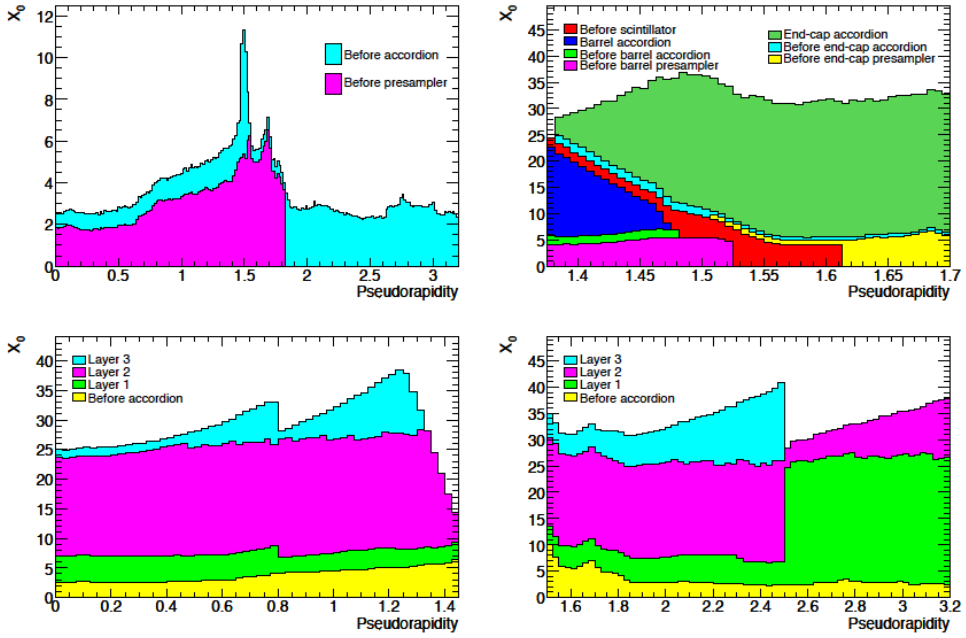

Figure 2.11 Cumulative amounts of material, in units of radiation length X0 and as a function of $|\eta|$, in front of and in the electromagnetic calorimeters. The top left-hand plot shows separately the total amount of material in front of the presampler layer and in front of the accordion itself over the full h-coverage. The top right-hand plot shows the details of the crack region between the barrel and end-cap cryostats, both in terms of material in front of the active layers (including the crack scintillator) and of the total thickness of the active calorimeter. The two bottom figures show, in contrast, separately for the barrel (left) and end-cap (right), the thicknesses of each accordion layer as well as the amount of material in front of the accordion. [13]

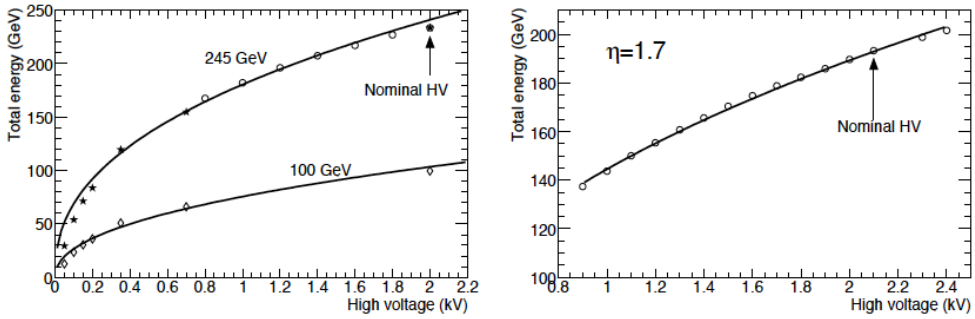

Figure 2.12 Measured electromagnetic cluster energy as a function of the applied high voltage. The results are shown for a barrel module (left), for 245 GeV electrons (open circles), 100 GeV electrons (open diamonds) and for the 100 GeV results at the nominal voltage of 2 kV scaled to the corresponding result at 245 GeV (stars). The results obtained with an end-cap module (right) are shown for 193 GeV electrons. The curves correspond to fits with a functional form $E_{tot} = a \times V^b$. [13]

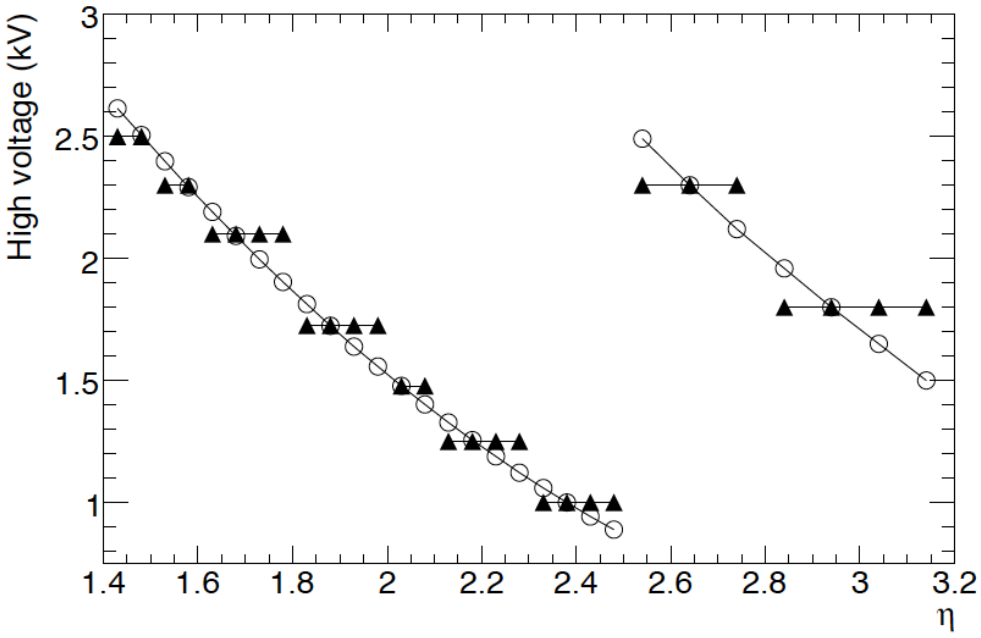

Figure 2.13 High-voltage distribution as a function of $|\eta|$ for the EMEC. A uniform calorimeter response requires a high voltage which varies continuously as a function of $|\eta|$, as shown by the open circles. This has been approximated by a set of discrete values shown as full triangles. [13]

ATLAS 2011 p–p run

Inner Tracking			Calorimeters				Muon Detectors				Magnets	
Pixel	SCT	TRT	LAr EM	LAr HAD	LAr FWD	Tile	MDT	RPC	CSC	TGC	Solenoid	Toroid
99.9	99.8	100	89.0	92.4	94.2	99.7	99.8	99.7	99.8	99.7	99.3	99.0

Luminosity weighted relative detector uptime and good quality data delivery during 2011 stable beams in pp collisions at √s=7 TeV between March 13th and June 29th (in %). The inefficiencies in the LAr calorimeter will partially be recovered in the future. The magnets were not operational for a 3-day period at the start of the data taking.

ATLAS 2011 p–p run

Inner Tracking			Calorimeters				Muon Detectors				Magnets	
Pixel	SCT	TRT	LAr EM	LAr HAD	LAr FWD	Tile	MDT	RPC	CSC	TGC	Solenoid	Toroid
99.9	99.8	100	96.3	98.6	98.9	99.7	99.8	99.8	99.8	99.7	99.3	99.0

Luminosity weighted relative detector uptime and good quality data delivery during 2011 stable beams in pp collisions at √s=7 TeV between March 13th and June 29th (in %).

Figure 2.14 Data taking efficiencies of each ATLAS subdetector system before (upper) and after (bottom) the reprocessing in 2011. [14] LAr has relatively slightly lower efficiency compared to other subdetector systems.

LAr Data Quality The quality of real-time data from LHC *pp* collisions recorded by ATLAS is challenged by the performance of each subdetector system and has important impact on the physics analysis, particularly in various new physics searches. Hence, a good understanding of the data quality (DQ) is not only important for the detector monitoring and performance study but also the crucial warranty of safe and physical analysis results.

LAr calorimeter is the typical subsystem of ATLAS which always plays an essential part in the overall DQ evalution. The data-taking efficiency of LAr calorimeter in 2011 *pp* collision runs are shown in Figure 2.14 and compared with other subdetector systems. The DQ of LAr is evaluated and investigated both online and offline and the typical defects are summarized in Table 2.2.

These typical LAr DQ defects are evaluated and categorized into different levels (OK/WARNING/ERROR) based on the potential physics impacts. All such information has been streamed to event level offline DQ flags as analysis benchmarks. Figure 2.15 shows an example of the distribution of event DQ flags corresponding to different calorimeter partitions.

As shown in Table 2.2, The major LAr defects can be categorized as four different types:

- **Data integrity errors**: such as coverage dropouts or electornics errors. Not recoverable in

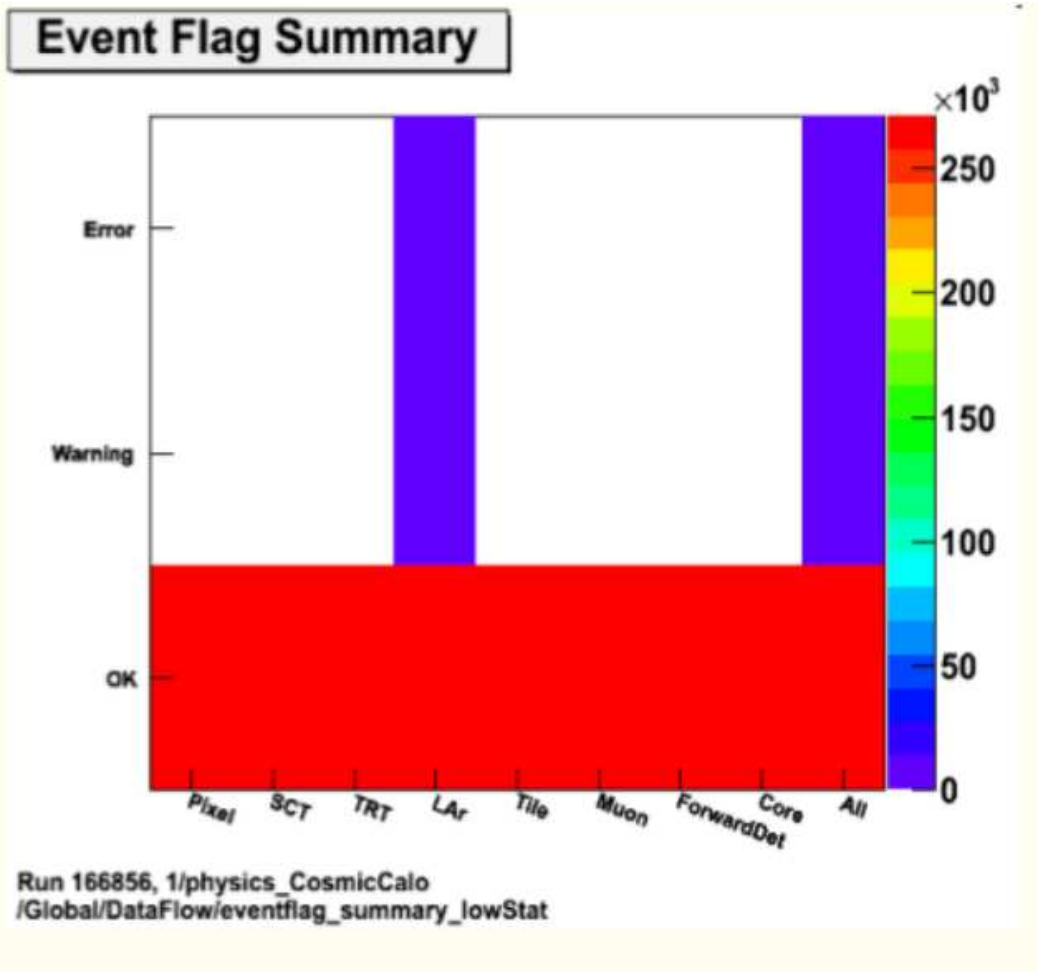

Figure 2.15 Example of typical event summary with LAr DQ flags. [15] EventFlag::ERROR are events with data corruption while EventFlag::WARNING are huge noise bursts.

Table 2.2 Summary of LAr DQ defects which may have impacts on physics analysis results. [15] <PART> refers to different LAr calorimeter partitions.

Defect	Description	Recoverable	Tolerable
LAR_DATACORRUPT	Data integrity problem	NO	NO
LAR_UNCHECKED	Shifter did not look at ES	YES	NO
LAR_BULK_UNCHECKED	Shifter did not look at bulk	YES	YES
LAR_LOWSTAT	Not enough stat for assessment	NO	YES
LAR_<PART>_DISABLED	Partition not included in the run	NO	NO
LAR_<PART>_HVTRIP	LB with HV ramping or off on both sides	NO	NO
LAR_<PART>_HVNONNOMINAL	LB with stable non-nominal HV (Noise not corrected)	YES	NO
LAR_<PART>_HVNONNOM_CORRECTED	LB with stable non-nominal HV (Noise corrected, impact on trigger)	NO	YES
LAR_<PART>_NOISEBURST	LB with minor noise burst	NO	YES
LAR_<PART>_SEVNOISEBURST	LB with severe noise bursts	NO	NO
LAR_<PART>_NOISYCHANNEL	Noisy cell, but harmless	YES	YES
LAR_<PART>_SEVNOISYCHANNEL	Very noisy cell, inducing many clusters	YES	NO
LAR_<PART>_MINORUNKNOWN	Data affected by minor (yet) unknown pathology	MAYBE	YES
LAR_<PART>_SEVUNKNOWN	Data unusable for (yet) unknown reason	MAYBE	NO

re-processing.

- **Noise Bursts**: discarded only when too many noise bursts are found in the same lumiblock. Can be cleaned up at event level.
- **High Voltage Trips**: recoverable at non-nominal stable HV but discarded during the HV trips and rampings. Need more study offline to check the exact impacts in particular regions affected by HV trips.
- **Beam Halo**: usually flagged like noise bursts and big energy deposition is expected. Enormously affecting MET and fake object reconstructions. More studies are desired to understand and quantify the exact contributions from these corresponding events.

More practicle strategies for event and object cleanings will be discussed about in Section 3.4.

Hadronic Calorimeter

The hadronic calorimeters consist of three complementary compartments, Tile calorimeter, LAr hadronic end-cap calorimeter and LAr forward calorimeter. The expected nominal resolution for the Hadronic calorimeters are $\frac{\sigma_E}{E} = \frac{50\%}{\sqrt{E(GeV)}} \oplus 3\%$ for the barrel and end-cap and $\frac{\sigma_E}{E} = \frac{100\%}{\sqrt{E(GeV)}} \oplus 10\%$ for the forward calorimeter.

Tile calorimeter Like the EM calorimeter of LAr, the Tile hadronic calorimeter, which is located right behind the LAr EM calorimeter, is also sampling calorimeter but uses steel as the absorber and

scintillating tiles as the sampling medium. There are 64 modules segmented azimuthally in both the central barrel part ($|\eta| < 1.0$) and the extended barrel part ($0.8 < |\eta| < 1.7$). Radially, there are three layers with the thickness as 1.5, 4.1 and 1.8 interaction lengths (λ) in the central barrel and 1.5, 2.6 and 3.3 λ in the extended barrel.

LAr Hadronic End-Cap calorimeter Like the EMEC, the Hadronic end-cap calorimeters (HEC) of LAr have two independent wheels on each side of the end-cap but right behind the EMEC. They extend the geometry coverage of Tile calorimeter up to $|\eta| < 3.2$ which overlap with the forward calorimeters at around $3.1 < |\eta| < 3.2$ so as to mantain the material density at the transition region. The similar motivation applies to the overlap between HEC and Tile calorimeter at $1.5 < |\eta| < 1.7$. On each side of the HEC wheel, 32 identical wedge-shaped modules are segmented. HEC can be divided into two layers in depth for each wheel and four layers for each side of the HEC.

LAr forward calorimeter The LAr forward calorimeters (FCal) are located on both sides of the end-cap sharing the same end-cap cryostats with the other end-cap calorimeters. The η-coverage of FCal is $3.1 < |\eta| < 4.9$ which overlaps with the HEC as mentioned above. The FCal is motivated to guarantee the hermecity of the detector coverage and suppression of the background level in the MS. The depth of the FCal is approximately 10 interaction length.

2.2.3 Muon spectrometer

The ATLAS muon spectrometer (MS), which is instrumented as four types of chambers: monitored drift tube (MDT) and cathode strip chambers (CSC) for precise tracking, the resistive plate chambers (RPC) and thin gap chambers (TGC) mainly for triggering, is the dedicated tracking system for the reconstruction of the muon trajectories and the measurement of the muon momenta based on the muon tracks deflected in the magnetic field in the R_z panel. The cut-away view and general layout of the MS is shown in Figure 2.16 and Figure 2.17.

The barrel and end-cap superconducting toroid magnets provide the magnetic fields in which the MS operates. In the barrel region, the magnetic bending is provided by the large barrel toroid with eight superconducting toroid magnets for $|\eta| < 1.4$. In the end-cap, the field is provided by two smaller magnets are inserted into the each end of the barrel toroid for $1.6 < |\eta| < 2.7$. The bending in the transition region of $1.4 < |\eta| < 1.6$ is provided by the barrel and end-cap combination. The baseline requirements for the design of the magnetic system of MS are to provide a magnetic field as orthogonal as possible to the muon trajectories and to minimise the resolution degradation due to multiple scattering meanwhile.

According to the numbering of the sectors, the MS can be divided into the Large (odd numbered) sectors and the Small (even numbered) sectors, as shown in Figure 2.19.

The toroid magnets

The magnetic field of MS is provided by three large air-core superconducting toroids for the barrel and two sides of the end-caps. Each toroids contain eight coils with, in the end-caps, the toroid coils rotated by 22.5^o to optimize the bending in the transition between the barrel and the end-caps. The magnetic fied bending power is determined by the field integral as $\int B\dot{d}\ell$ along the infinite-momentum muon trajectory between the innermost and outermost planes of the chambers. The bending power is η-dependent:
1.5 to 5.5 Tm in the barrrel ($|\eta| < 1.4$) and 1 Tm to 7.5 Tm in the end-caps ($1.6 < |\eta| < 2.7$) as shown in Figure 2.18.

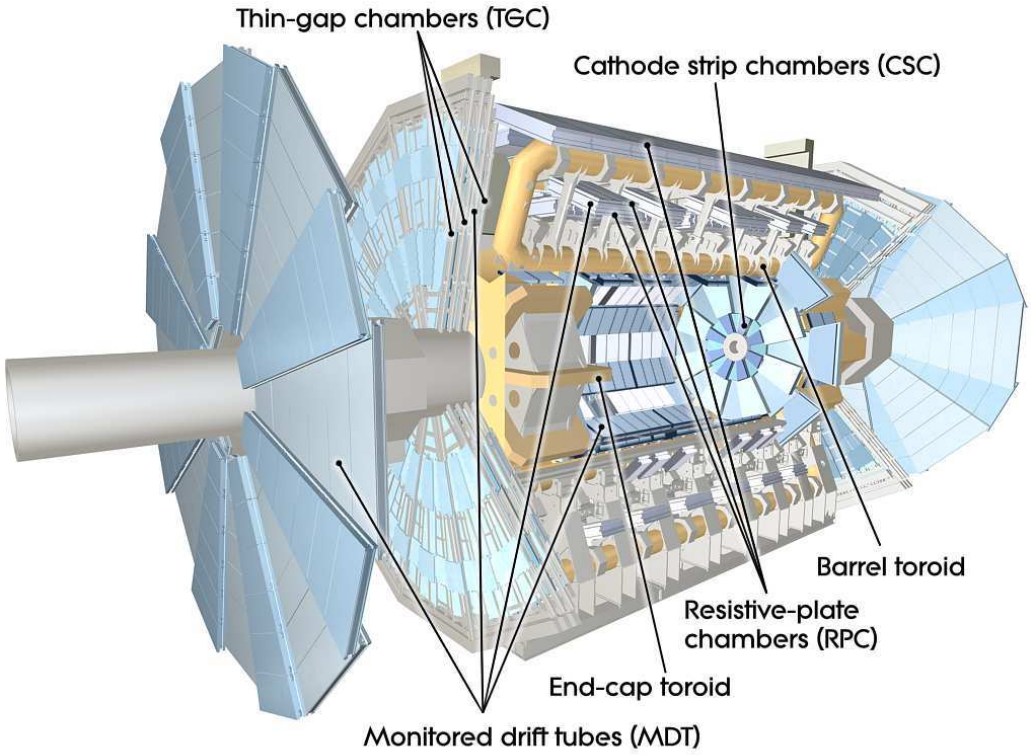

Figure 2.16 The ATLAS Muon Spectrometer cut-away view. [13]

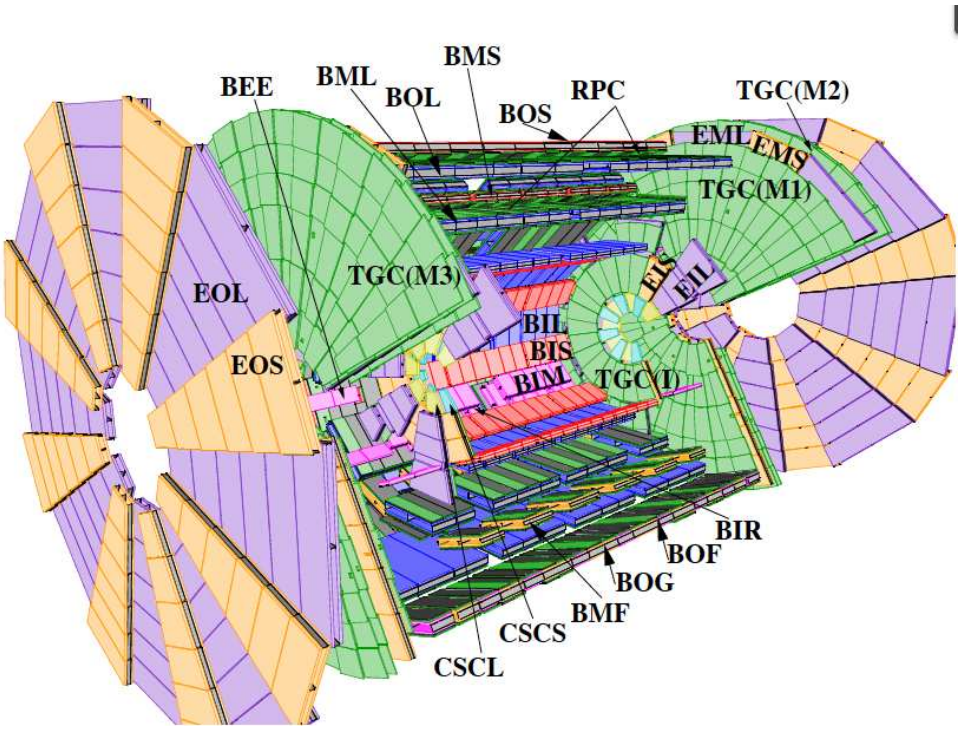

Figure 2.17 The general layout of the ATLAS Muon Spectrometer. [13]

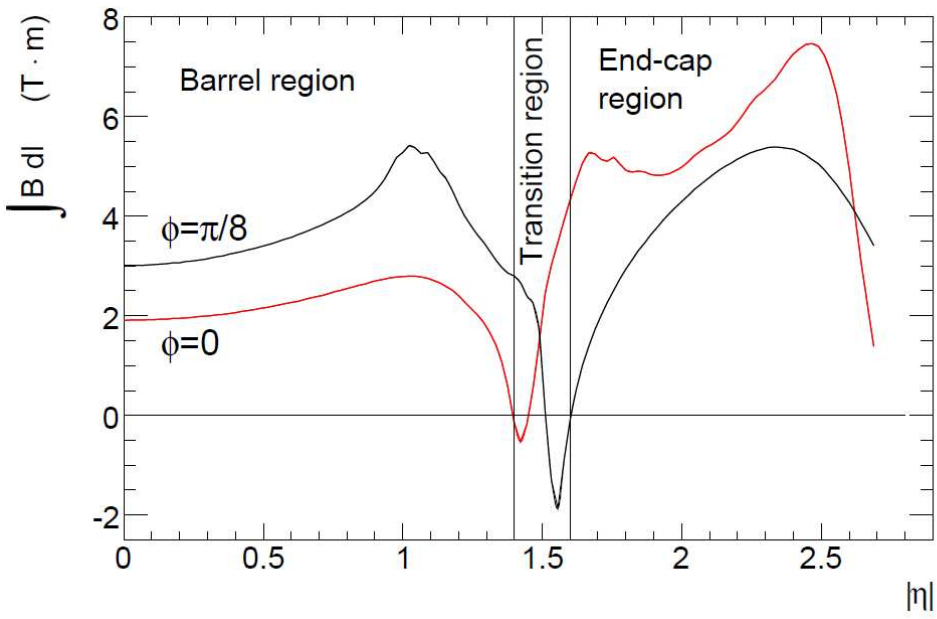

Figure 2.18 Magnetic field performance of the ATLAS Muon Spectrometer. [13]

Precise Tracking chambers: MDT and CSC

MDT and CSC chambers, particularly the MDT, provide a wide η-coverage for precise tracking measurement of muon trajectories.

MDT has an η-coverage up to 2.7 but is restricted to 2.0 for the first layer. There are approximately 1150 MDT chambers and 354000 read-out channels in MDT chamber. The diameter of the tubes are 29.970 mm. A mixture gas of A_r and CO_2 (93:7) are filled. It benifits from the assembling of individual tubes so that the robustness of the chamber can be mostly mantained even when a small number of tubes fail during the operation. However, it is limited due to the radial drift geometry which would result in the long pulse train caused by the track segments far from the tangential point. Therefore, an adjustable dead-time is required to be implemented against the multiple-hit track created by the pulse train. The cross-section of the MDT tubes are shown in Figure 2.20.

CSC, which is the multiwire proportional chambers with cathodes segmented into strips, covers the large pseudorapidities and replaces the MDT chamber in the first layer due to the fact that the particle flux is too high for drift tube chambers in this region. The upper limit of the acceptable counting rate of CSC chamber is expected to be 1000 Hz/cm^2 which is much higher than safe-operation limit of the MDT counting rate of 150 Hz/cm^2.

The nominal spatial resolution of CSC and MDT chambers are 40 μm(in R) and $\sim$35 μm(in z) while CSC also has a nominal resolution (in ϕ) of 5 mm in the non-bending plane.

Trigger chambers: RPC and TGC

The trigger system of MS has a smaller η-coverage up to $|\eta| < 2.4$ compared to the precise tracking chambers one. TGC's are assembled in the end-cap regions complementary to RPC's in the barrel. They play the role of measuring the exact coordinates of muon tracks in the direction orthogonal to those determined by the precise tracking chambers as well as providing bunch-crossing identification and pre-defined pT thresholds for trigger decision. The nominal spatial resolution of RPC is 10 mm (in z) and for TGC, it is 2-6 mm and 3-7 mm in R and ϕ, respectively.

2.2.4 Forward detector

In addition to the three major sub-detectors of ATLAS, three smaller sets of detectors (Figure 2.21) are placed at the very forward region where they play their important roles in luminosity monitoring or measurement and the study of the forward activities:

The LUCID (LUminosity measurement using Cerenkov Integrating Detector), which is a relative luminosity detector dedicated for online luminosity monitoring and diffractive studies.

The ALFA detector (Absolute Luminosity For ATLAS), which is used to determine the absolute luminosity of LHC by measuring elastic scatterings at small angles.

The ZDC detector (zero-degree calorimeters), which aims for detecting forward neutrons in heavy-ion collisions, particularly determing the centrality of those collisions.

2.2.5 Trigger and data acquisition systems

Given the enormous amount of collision events produced at the LHC and the average ATLAS event size, 1.5 MB per events at 40 MHz high rate, it has been a big challenge for data acquisition and storage systems. Therefore, in ATLAS experiment, the collision events are acquired once they manage to fire certain trigger criteria during the run. The trigger criteria are designed to apply real-time pre-selections on the collision events based on the measured qualities and quantities of favored physics objects (e, μ, photon, jet, $E_{\mathrm{T}}^{\mathrm{miss}}$), which will be assembled as a certain combination of trigger selections and defined

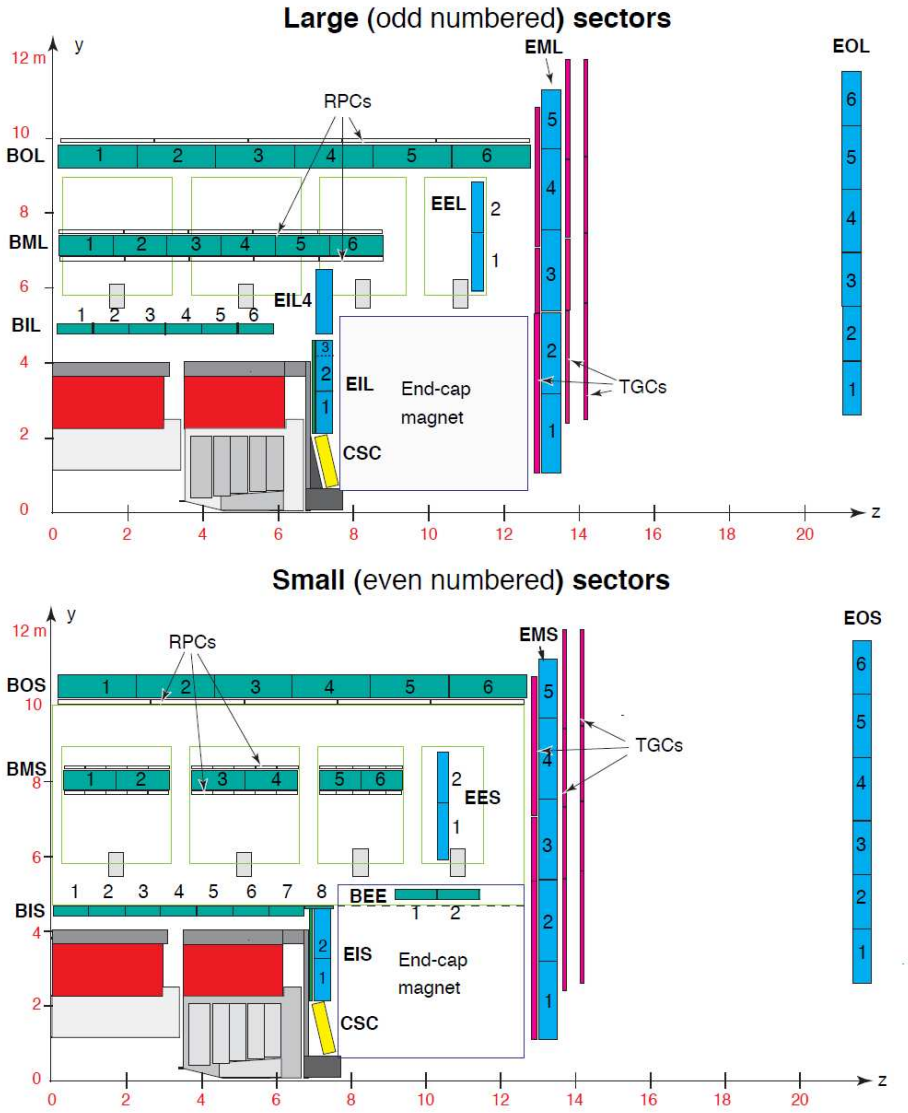

Figure 2.19 The naming the numbering of ATLAS Muon Spectrometer for Large sectors (top) and Small sectors (bottom) separately. [13]

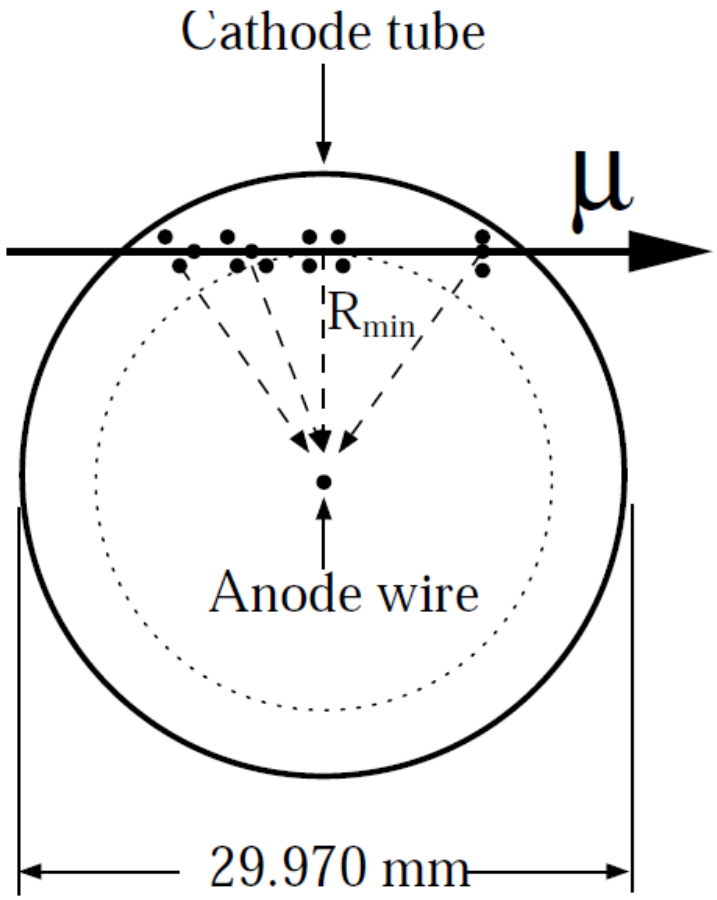

Figure 2.20 The illustration of a monitored drift tube. [13]

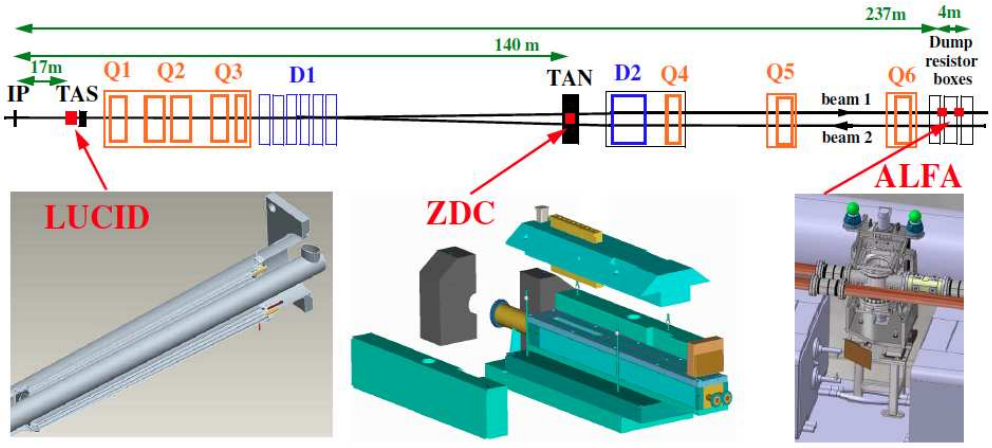

Figure 2.21 Placement of the forward detectors along the beam-line around the ATLAS interaction point (IP). See text for details. [13]

as trigger menu differing between different lumi-blocks. The design of the TDAQ is then motivated to have the most probable candidate events corresponding to interesting physics processes acquired efficiently but with an acceptable rate to be written into the storage for offline physics analysis and performance studies. A brief overview of ATLAS trigger architecture is given in Figure 2.22 and is detailed together with the data acquisition system in Figure 2.23.

The trigger system together with data acquisition system (TDAQ) have each of their partitions assembled with each ATLAS sub-detector system. There are three levels of trigger system in ATLAS.

The L1 trigger

L1 triggers (generic diagram of L1 is shown in Figure 2.24) operate at hardware level and have an acceptable trigger rate of 75 kHz (upgradable to 100 kHz) with a maximum of 2.5μs latency and provide an rejection factor of 500 with respect to the real-time collision rate of ∼40 MHz. It uses the reduced-granularity information from each sub-detectors. For example, the high-p_T muons in muon trigger system RPC and TGC are used while in the calorimeter systems, the EM clusters, jets, $E_{\mathrm{T}}^{\mathrm{miss}}$ and τ-letpons are considered. At L1, one or more Regions-of-Interest (RoI's) are defined in each event, within which the selection process has identified interesting features. The RoI data include information on the type of feature identified and the criteria passed, hence subsequently used by L2 triggers.

The L2 trigger

L2 triggers are seeded by RoIs at software level using the coordinates, energy and type of signatures of the identified trigger objects passing L1 triggers. The event rates can be reduced to be less than 3.5 kHz after L2 triggers.

The Event Filter

Offline analysis procedures are implemented at the 3rd level of the trigger system, the Event Filter (EF) which directly judge whether the events can be stored eventually for offline analysis. The EF operates on fully-constructed events passing L2 and can further reduce the rate to ∼200 Hz. EF together with L2 are also called the High Level Triggers (HLT) which use the full granularity and precision of inner detector, calorimeter and muon systems. (HLT have their tigger decision made upon

the previous levels) Events passing certain sets of EF will eventually be written into specific trigger streams which have essentially certain set of physics signatures which can be assembled such like the Egamma stream, Muon stream and the JetTauEtmiss stream.

The different triggers that are concerned in this analysis related to different reconstructed physics objects are detailed and categorized in Section 3.4.1 and 3.4.2 with the corresponding physics object reconstruction chains ellaborated. The eventual physics EF triggers are illustrated and explained in Section 3.5.1.

Data acquisition

In ATLAS, each sub-detector has its own specific front-end electronics and Readout Drivers (RODs). However, it shares the common definitions of event format, error detection/recovery mechanisms, and the physics interface to the DAQ system, which are all based on general ATLAS rules. At L1, data is preliminarily sorted and stored in local buffers before being processed at L2 and transfered to the event-building system. The EF operates at the final stage to judge whether certain events should be permanently stored at the CERN computer center. Besides, the TDAQ also plays the role of configurating, controling and monitoring of both the hardware and software components.

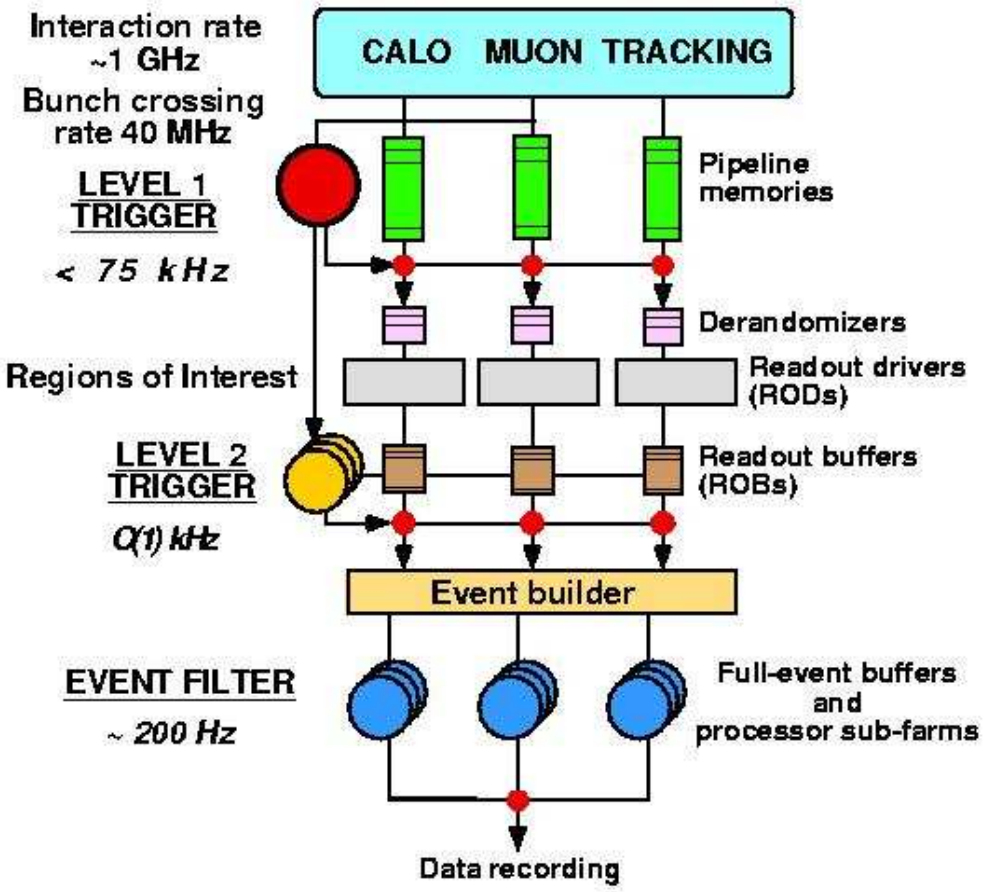

Figure 2.22 A overview of the ATLAS trigger system. [13]

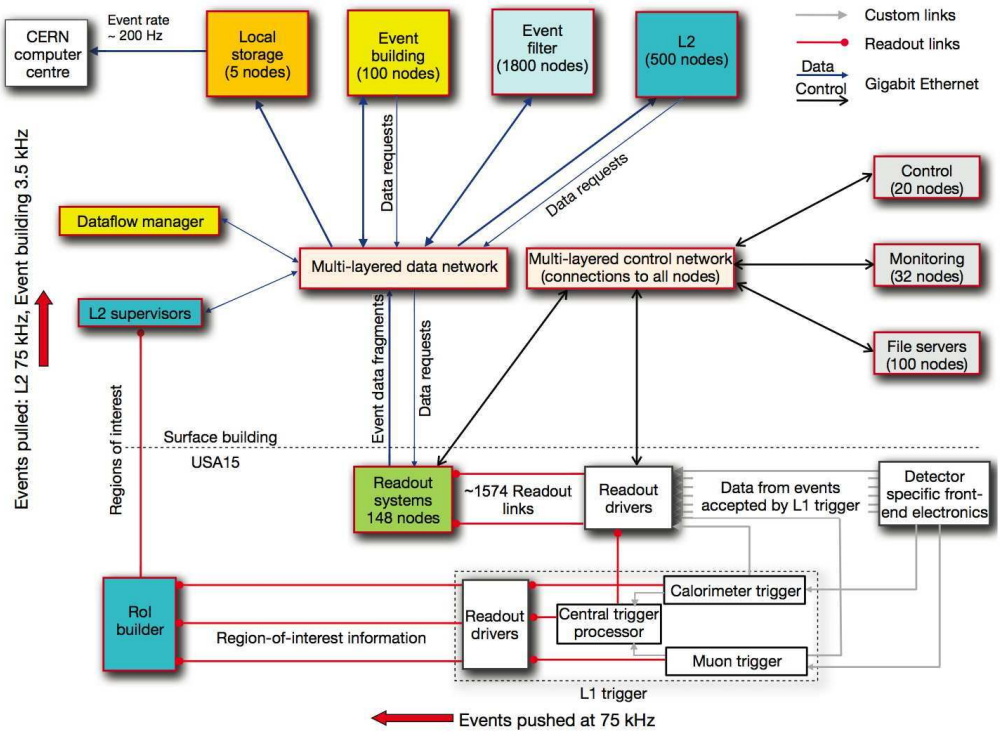

Figure 2.23 A diagram of the ATLAS trigger and data acquisition system. [13]

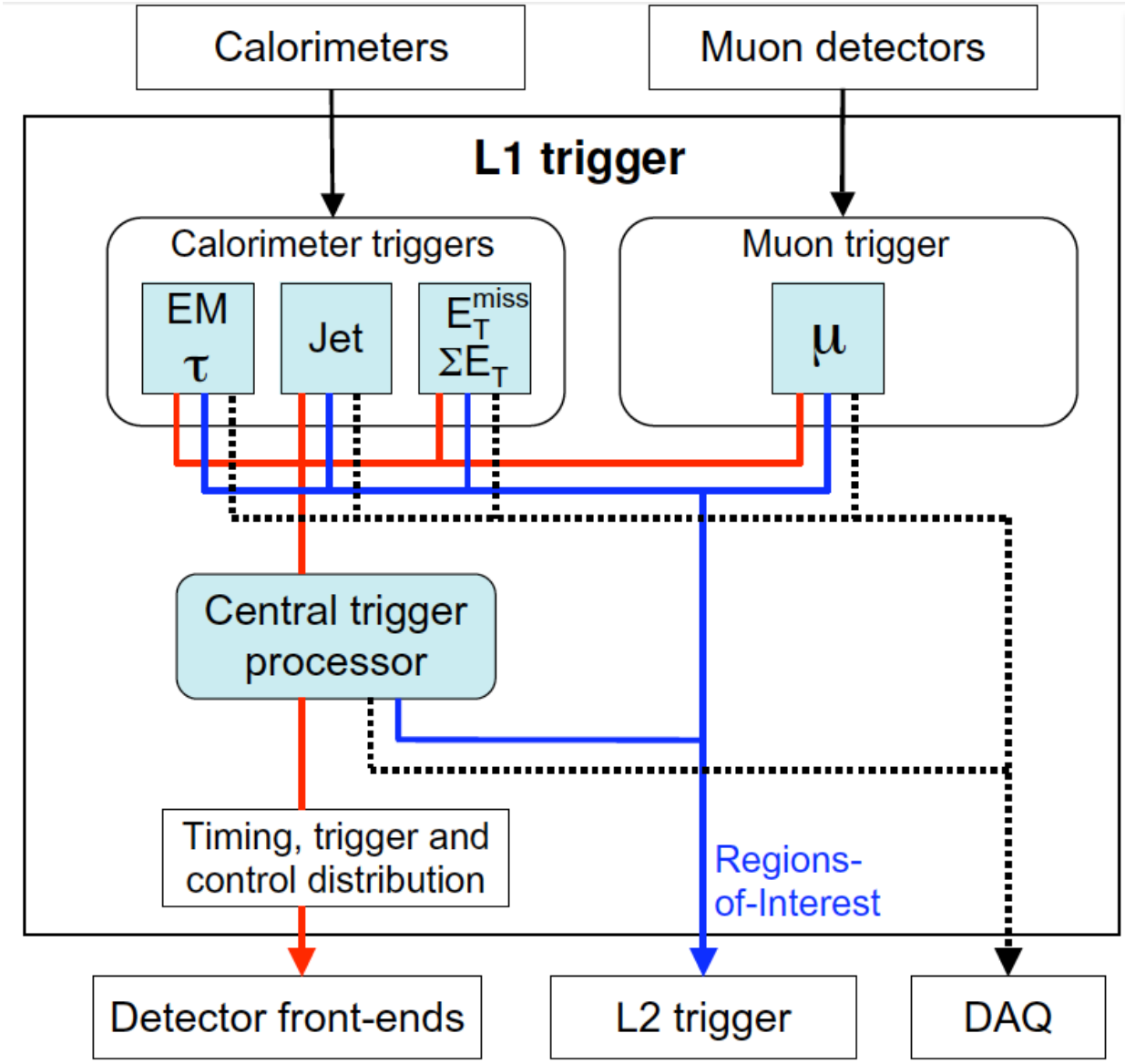

Figure 2.24 A diagram of the ATLAS L1 trigger. [13]

CHAPTER 3. $W^+W^- \to \ell\nu\ell\nu$ MEASUREMENT

3.1 Introduction

As elaborated in Section 1.2, a precise measurement of the $W^+W^- \to \ell^+\nu_\ell\ell^-\bar{\nu}_\ell$ production has its unique motivation in ATLAS experiment, particularly in early physics. It is not only an important test of the electoweak sector of the SM theories but also able to probe the anomalous triple gauge boson interactions resulting from the non-abelian structure of the gauge symmetry group $(SU(2)_L \times U(1)_Y)$ of the SM and other new particles decaying into W boson pairs, in which the production cross section and kinematic distributions may deviate from the SM prediction.

In addition, it can also help with the search of the new phenomena with the W^+W^- as the final state where the SM W^+W^- plays the role of a irreducible background. This is essential for not only the search of $gg \to H + X \to W^+W^- + X$ but also the new phenomena beyond the SM.

In this chapter, the measurement of the total cross section of SM W^+W^- will be detailed and the fiducial cross section and first differential cross section measurement will be also presented. In addtion, the limits on anomalous WWZ and $WW\gamma$ Triple-Gauge Couplings (aTGCs) will be set according to the measured distribution of leading lepton p_T.

The fully leptonic decay channels of $W^+W^- \to \ell\nu\ell\nu$ are considered for the measurement to extract the signal from enormous contamination of various backgrounds. The final state of $\ell\nu\ell\nu$ can be any combination of two e or μ leptons with those cascaded decays from $W \to \tau + X \to e/\mu + X$ leptons included. The neutrinos $(\nu/\bar{\nu})$ are experimentally observed as missing transverse energies $(E_{\mathrm{T}}^{\mathrm{miss}})$ in the detector. The signal processes under consideration include both the quark-antiquark annihilation shown in Figure 1.6, which is the dominant mechanism at leading order, and the W^+W^- coming from the gluon-gluon (gg) fusion in Figure 1.7, which contributes ~3% to the total. Given the fact that the W^+W^- production through vector-boson fusion/scattering and double parton scattering (DPS)

mechanism are even one order of magnitude lower than the gg fusion contribution (0.85 fb for a very heavy Higgs [16, 17, 18], or 1.33 fb for a Higgs mass of 120 GeV, 7 fb through the DPS process [19]), they are not included in the signal simulation.

All the results are based the total integrated luminosity of 4.6 fb^{-1} pp collision data taken by ATLAS in 2011 at the center-mass-energy of $\sqrt{s} = 7$ TeV.

3.2 Signal and background overview

As mentioned in Section 3.1, only the leptonic decay channels of $W^+W^- \to \ell\nu\ell\nu$ are used for the measurement. However, some other physics processes can also have a similar final state and experimental signatures such as $t\bar{t}$ production which can produce two opposite-sign (OS) W bosons which further decay leptonically. In this measurement, top quark pair production is not considered as signal process but vetoed as background by requiring no presence of reconstructed jets.

As predicted by the SM, the overall W^+W^- production rate is way lower than the various background processes which may contaminate the signal purity in the measurement due to the object misidentification, misdetection, and other limitations of the detector performance. Each background has its unique way to mimic or fake the signal, which can be elaborated as follows:

- Z+jets with fake $E_{\mathrm{T}}^{\mathrm{miss}}$ due to the mismeasurement of lepton or jet energies, high pileup condition or undetected particles,
- $t\bar{t}$ and single top production (particularly, Wt) with soft jets of low transverse momenta (p_T) after vetoing the presence of high p_T jets,
- W+jets with one jet misidentified as one e or μ,
- $W + \gamma$ with one γ faking one electron,
- $WZ \to \ell\ell\ell\nu$ due to misdetection of one final state lepton,
- $ZZ \to \ell\ell\nu\nu$ with the dilepton invariant mass off the chosen Z-mass window
- multi-jet QCD backgrounds due to the misidentification of both leptons and the missing transverse energy ($E_{\mathrm{T}}^{\mathrm{miss}}$).

The estimation of each background contribution passing signal selection will be elaborated in dedicated section 3.6.

3.3 Data and MC samples

In this analysis, the complete dataset of pp collision data at a center-mass-energy of $\sqrt{s} = 7$ TeV acquired with ATLAS detector in 2011 is used. The corresponding total integrated luminosity with the data quality requirement applied in this analysis is 4.644 fb^{-1} (determined by the standard ATLAS tool for luminosity calculation [20]).

3.3.1 Monte Carlo samples

The W^+W^- production from quark-antiquark annihalation $q\bar{q} \to W^+W^- \to \ell^+\nu_\ell\ell^-\bar{\nu}_\ell$ followed by purely leptonic decays are modeled with an next-to-leading-order (NLO) Monte Carlo (MC) generator, MC@NLO [9], in which the NLO QCD matrix elements are incorporated to HERWIG/Jimmy [21] parton shower and CT10 as the parton density function. The leptonic decays of τ-leptons from W boson is inlcuded in the MC event generator also with the other possible final states accounted. W-boson width and spin-spin correlations are included in the generator. $gg \to W^+W^- \to \ell^+\nu_\ell\ell^-\bar{\nu}_\ell$ signal processes are modeled by `gg2ww` [22] generator with CT10 as the PDF set. The cross sections are calculated for $q\bar{q} \to W^+W^- \to \ell^+\nu_\ell\ell^-\bar{\nu}_\ell$ with both MC@NLO with CT10 and `MCFM` [7] with MSTW2008 [23] and yield 43.8 pb and 43.6 pb, respectively while for $gg \to W^+W^- \to \ell^+\nu_\ell\ell^-\bar{\nu}_\ell$, the results given by both CT10 and MSTW2008 are 1.3 pb. The final choice of the SM predicted total cross section value is derived from `MCFM` [7] and CT10 PDFs to be consistent with other ATLAS diboson analyses and CMS, yielding $44.7^{+2.1}_{-1.9}$ pb. The uncertainty of $^{+4.8\%}_{-4.2\%}$ consists the variation of renormalisation (μ_R) and factorisation (μ_F) scales by a factor of two ($^{+3.6\%}_{-2.5\%}$) and `CT10` PDF uncertainties ($^{+3.1\%}_{-3.4\%}$), The uncertainties from the scale and pdf are added in quadrature. The result is consistent with the cross section obtained from the generators themselves. All the W^+W^- MC signal samples listed in Table 3.1 and the cross sections shown are based directly on the MC@NLO/gg2ww results in combination with CT10 PDFs.

Major backgrounds for W^+W^- signal detection come from top quark production including $t\bar{t}$ and single top, summarized in Table 3.5, and W/Z+jets which are documented in Tables 3.3, 3.2, and 3.4 with heavy flavour (HF) overlap removal [24] applied.

Process	cross-section [fb]	ϵ_{filter}	N_{MC}	Generator
$q\bar{q}' \to W^+W^- \to e^+\nu e^-\nu$	510.48	1.0	141723	MC@NLO
$q\bar{q}' \to W^+W^- \to \mu^+\nu\mu^-\nu$	510.48	1.0	140628	MC@NLO
$q\bar{q}' \to W^+W^- \to e^+\nu\mu^-\nu$	510.48	1.0	141486	MC@NLO
$q\bar{q}' \to W^+W^- \to \mu^+\nu e^-\nu$	510.48	1.0	141365	MC@NLO
$q\bar{q}' \to W^+W^- \to e^+\nu\tau^-\nu$	510.48	1.0	141466	MC@NLO
$q\bar{q}' \to W^+W^- \to \mu^+\nu\tau^-\nu$	510.48	1.0	141502	MC@NLO
$q\bar{q}' \to W^+W^- \to \tau^+\nu\mu^-\nu$	510.48	1.0	141488	MC@NLO
$q\bar{q}' \to W^+W^- \to \tau^+\nu e^-\nu$	510.48	1.0	141372	MC@NLO
$q\bar{q}' \to W^+W^- \to \tau^+\nu\tau^-\nu$	510.48	1.0	141406	MC@NLO
$gg \to W^+W^- \to e^+\nu e^-\nu$	15.24	.9895	10000	gg2ww
$gg \to W^+W^- \to \mu^+\nu\mu^-\nu$	15.24	.9890	9999	gg2ww
$gg \to W^+W^- \to e^+\nu\mu^-\nu$	15.24	.9899	10000	gg2ww
$gg \to W^+W^- \to \mu^+\nu e^-\nu$	15.24	.9869	10000	gg2ww
$gg \to W^+W^- \to e^+\nu\tau^-\nu$	15.24	.9232	10000	gg2ww
$gg \to W^+W^- \to \mu^+\nu\tau^-\nu$	15.24	.9288	10000	gg2ww
$gg \to W^+W^- \to \tau^+\nu\mu^-\nu$	15.24	.9289	10000	gg2ww
$gg \to W^+W^- \to \tau^+\nu e^-\nu$	15.24	.9219	10000	gg2ww
$gg \to W^+W^- \to \tau^+\nu\tau^-\nu$	15.24	.3269	10000	gg2ww

Table 3.1 The W^+W^- signal production processes, cross-sections and numbers of fully simulated MC events. The MC simulation 'filter' is an event selection at the generator level. The corresponding filter efficiencies are given in the table. We also indicate the MC generators used to produce the MC events and to calculate the cross-sections given in this table. [6]

The generators which are used to produce these MC samples are:

- MC@NLO for $t\bar{t}$ events
- AcerMC for single top events
- ALPGEN for the V+jets background
- PYTHIAB for events with heavy flavor dijets (see Table 3.5)

The diboson processes WZ, ZZ, $W\gamma$ and $W\gamma^*$, which contribute much less to the background of W^+W^- signal compared to those above, are modelled with HERWIG, ALPGEN or MADGRAPH, respectively and are summarized in Table 3.6. A W boson and a massive virtual photon ($\gamma*$) can also mimic experimentally the dilepton plus missing E_T signature when the photon converts 'internally' in vacuum to two OS leptons [25]. In this internal conversion scenario, e^+e^-, $\mu^+\mu^-$ and even $\tau^+\tau^-$ decays occur with substantial probability.

The cross-sections for the different processes, the generator names, the generator level filter efficiencies and total number of events are shown in the tables. Whenever LO event generators are used, the cross-sections are corrected by using k-factors to NLO or NNLO (if available) matrix element calculations [26].

Process	cross-section [pb]	k-factor	ϵ_{filter}	N_{MC}	Generator
ZnunuNp0	3533.76	1.25	0.01	54949	ALPGEN
ZnunuNp1	732.31	1.25	0.61	909848	ALPGEN
ZnunuNp2	222.34	1.25	0.88	169899	ALPGEN
ZnunuNp3	61.96	1.25	0.97	144999	ALPGEN
ZnunuNp4	15.77	1.25	0.99	309849	ALPGEN
ZnunuNp5	4.42	1.25	1.00	84999	ALPGEN
ZeeNp0($M > 40$ GeV)	668.32	1.25	1	6618284	ALPGEN
ZeeNp1($M > 40$ GeV)	134.36	1.25	1	1334897	ALPGEN
ZeeNp2($M > 40$ GeV)	40.54	1.25	1	909999	ALPGEN
ZeeNp3($M > 40$ GeV)	11.16	1.25	1	220000	ALPGEN
ZeeNp4($M > 40$ GeV)	2.88	1.25	1	60000	ALPGEN
ZeeNp5($M > 40$ GeV)	0.83	1.25	1	20000	ALPGEN
ZmumuNp0($M > 40$ GeV)	668.7	1.25	1	6615230	ALPGEN
ZmumuNp1($M > 40$ GeV)	134.1	1.25	1	1334296	ALPGEN
ZmumuNp2($M > 40$ GeV)	40.3	1.25	1	404947	ALPGEN
ZmumuNp3($M > 40$ GeV)	11.2	1.25	1	110000	ALPGEN
ZmumuNp4($M > 40$ GeV)	2.8	1.25	1	30000	ALPGEN
ZmumuNp5($M > 40$ GeV)	0.77	1.25	1	10000	ALPGEN
ZtautauNp0($M > 40$ GeV)	668.4	1.25	1	10613179	ALPGEN
ZtautauNp1($M > 40$ GeV)	134.8	1.25	1	1999491	ALPGEN
ZtautauNp2($M > 40$ GeV)	40.4	1.25	1	404950	ALPGEN
ZtautauNp3($M > 40$ GeV)	11.3	1.25	1	509847	ALPGEN
ZtautauNp4($M > 40$ GeV)	2.8	1.25	1	29999	ALPGEN
ZtautauNp5($M > 40$ GeV)	0.77	1.25	1	45000	ALPGEN
ZeeNp0($10 < M < 40$ GeV)	3051.62	1.22	1	994949	ALPGEN
ZeeNp1($10 < M < 40$ GeV)	87.87	1.22	1	299998	ALPGEN
ZeeNp2($10 < M < 40$ GeV)	41.40	1.22	1	499997	ALPGEN
ZeeNp3($10 < M < 40$ GeV)	8.38	1.22	1	149998	ALPGEN
ZeeNp4($10 < M < 40$ GeV)	1.85	1.22	1	40000	ALPGEN
ZeeNp5($10 < M < 40$ GeV)	0.46	1.22	1	10000	ALPGEN
ZmumuNp0($10 < M < 40$ GeV)	3051.62	1.22	1	999849	ALPGEN
ZmumuNp1($10 < M < 40$ GeV)	87.87	1.22	1	300000	ALPGEN
ZmumuNp2($10 < M < 40$ GeV)	41.45	1.22	1	999995	ALPGEN
ZmumuNp3($10 < M < 40$ GeV)	8.38	1.22	1	150000	ALPGEN
ZmumuNp4($10 < M < 40$ GeV)	1.85	1.22	1	39999	ALPGEN
ZmumuNp5($10 < M < 40$ GeV)	0.46	1.22	1	10000	ALPGEN
ZtautauNp0($10 < M < 40$ GeV)	3055.1	1.22	1	999649	ALPGEN
ZtautauNp1($10 < M < 40$ GeV)	84.93	1.22	1	299999	ALPGEN
ZtautauNp2($10 < M < 40$ GeV)	41.47	1.22	1	498899	ALPGEN
ZtautauNp3($10 < M < 40$ GeV)	8.36	1.22	1	150000	ALPGEN
ZtautauNp4($10 < M < 40$ GeV)	1.85	1.22	1	39999	ALPGEN
ZtautauNp5($10 < M < 40$ GeV)	0.46	1.22	1	10000	ALPGEN

Table 3.2 MC samples/processes used to model Z+jets and Drell-Yan backgrounds. The corresponding cross-sections, generator names, generator level filter efficiencies and total numbers of events are shown in this table. NpX (X=0..5) in the process name refers to the number of additional partons in the final state [6].

Process	cross-section [pb]	k-factor	ϵ_{filter}	N_{MC}	Generator
WenuNp0	6921.6	1.2	1	3358884	ALPGEN
WenuNp1	1304.3	1.2	1	2499645	ALPGEN
WenuNp2	378.3	1.2	1	3768632	ALPGEN
WenuNp3	101.4	1.2	1	1008947	ALPGEN
WenuNp4	25.9	1.2	1	250000	ALPGEN
WenuNp5	7.0	1.2	1	69999	ALPGEN
WmunuNp0	6919.6	1.2	1	3462942	ALPGEN
WmunuNp1	1304.2	1.2	1	2498592	ALPGEN
WmunuNp2	377.8	1.2	1	3768737	ALPGEN
WmunuNp3	101.9	1.2	1	1008446	ALPGEN
WmunuNp4	25.8	1.2	1	254950	ALPGEN
WmunuNp5	6.9	1.2	1	70000	ALPGEN
WtaunuNp0	6918.60	1.2	1	3418296	ALPGEN
WtaunuNp1	1303.20	1.2	1	2499194	ALPGEN
WtaunuNp2	378.18	1.2	1	3750986	ALPGEN
WtaunuNp3	101.51	1.2	1	1009946	ALPGEN
WtaunuNp4	25.64	1.2	1	249998	ALPGEN
WtaunuNp5	7.04	1.2	1	65000	ALPGEN

Table 3.3 MC samples/processes used to model W+X background. The corresponding cross-sections, generator names, generator level filter efficiencies and total numbers of events are shown in this table. NpX (X=0..5) in the process name refers to the number of additional partons in the final state [6].

Process	cross-section [pb]	k-factor	ϵ_{filter}	N_{MC}	Generator
ZeebbNp0	6.57	1.25	1	150000	Alpgen
ZeebbNp1	2.48	1.25	1	100000	Alpgen
ZeebbNp2	0.89	1.25	1	40000	Alpgen
ZeebbNp3	0.39	1.25	1	10000	Alpgen
ZmmbbNp0	6.56	1.25	1	149950	Alpgen
ZmmbbNp1	2.47	1.25	1	100000	Alpgen
ZmmbbNp2	0.89	1.25	1	40000	Alpgen
ZmmbbNp3	0.39	1.25	1	9999	Alpgen
WcNp0	650.0	1.2	1	6498837	Alpgen
WcNp1	205.0	1.2	1	2069646	Alpgen
WcNp2	50.8	1.2	1	519998	Alpgen
WcNp3	11.4	1.2	1	115000	Alpgen
WcNp4	2.8	1.2	1	30000	Alpgen
WbbNp0	47.32	1.2	1	474997	Alpgen
WbbNp1	35.77	1.2	1	205000	Alpgen
WbbNp2	17.34	1.2	1	174499	Alpgen
WbbNp3	6.63	1.2	1	69999	Alpgen
WccNp0	127.53	1.2	1	1264846	Alpgen
WccNp1	104.68	1.2	1	1049847	Alpgen
WccNp2	52.08	1.2	1	524947	Alpgen
WccNp3	16.96	1.2	1	170000	Alpgen

Table 3.4 MC samples/processes used to model Z+X and W+X with heavy quark flavor (b and c) backgrounds. The corresponding cross-sections, generator names, generator level filter efficiencies and total numbers of events are shown in this table. NpX (X=0..5) in the process name refers to the number of additional partons in the final state [6].

Process	cross-section [pb]	k-factor	ϵ_{filter}	N_{MC}	Generator
ttbar	166.8	1	0.543	1499991	MC@NLO
Wt	15.74	1	1	994897	AcerMC
tchan->e	6.97	1	1	99999	AcerMC
tchan->mu	6.97	1	1	999948	AcerMC
tchan->tau	6.97	1	1	199999	AcerMC
schan->e	0.5	1	1	199899	AcerMC
schan->mu	0.5	1	1	199850	AcerMC
schan->tau	0.5	1	1	190000	AcerMC
bbcc_mu10mu10X	2830.0	1	1	296599	PythiaB
bbcc_mu10e10X	4017.0	1	1	795695	PythiaB
bbcc_e10e10X	1693.0	1	1	290995	PythiaB

Table 3.5 MC samples/processes used to model dijet and top backgrounds ($t\bar{t}$ and single top). The corresponding cross-sections, generator names, generator level filter efficiencies and total numbers of events are shown in the table [6].

Process	cross-section [pb]	k-factor	ϵ_{filter}	N_{MC}	Generator
WZ	11.076	1.857	0.30986	999896	Herwig
ZZ	4.5964	1.847	0.21152	249998	Herwig
WγNp0	198.876	1.50	0.323	3198694	Alpgen
WγNp1	48.944	1.50	0.457	999998	Alpgen
WγNp2	17.183	1.50	0.551	499699	Alpgen
WγNp3	5.2981	1.50	0.632	199899	Alpgen
W$\gamma* \rightarrow \ell\nu ee$	4.80130	1.0*	1.0	294999	MadGraph
W$\gamma* \rightarrow \ell\nu\mu\mu$	1.45360	1.0*	1.0	149900	MadGraph
W$\gamma* \rightarrow \ell\nu\tau\tau$	0.21330	1.0*	1.0	50000	MadGraph

Table 3.6 MC samples/processes used to model the diboson backgrounds WZ, ZZ, $W\gamma$, and $W\gamma*$. The corresponding cross-sections, generator names, generator level filter efficiencies and total numbers of events are shown in the table. NpX (X=0..3) in the process name refers to the number of additional partons in the final state. k-factors of 1.0* indicate the value quoted from the generator, while a non-unity k-factor was applied in the analysis (see also Sec. 3.6.4) [6].

3.3.2 Signal Acceptance and Background Modelling

The signal expected from data is modelled with MC simulation while the acceptance and efficiency uncertainties are derived with MC based methods as well as data-driven techniques. Most of the background estimations in this analysis are performed with data-driven or semi-data-driven techniques while the MC samples are mainly used for background estimation cross checks, background control sample subtractions and systematic estimations.

To correct for the mismodeling of experimental resolution and efficiencies in MC simluation, several smearing/scaling corrections are introduced:

Correction	see Section
Lepton trigger efficiency	3.5.1
Electron identification efficiency	3.4.1
Electron isolation efficiency	3.4.1
Electron p_{T} smearing	3.4.1
Electron energy scale (data only)	3.4.1
Muon identification efficiency	3.4.2
Muon isolation efficiency	3.4.2
Muon p_{T} smearing	3.4.2
Pile-up reweighting	3.4.5
Jet Veto efficiency	3.7.1

In the case of correction factors that are run period dependent, the MC events samples are divided into samples reflecting the integrated luminosities in each period and the correction factors relevant to the corresponding period are applied.

3.3.3 Analysis data format

Due to the overwhelmingly high collision rates, complex interactions in the LHC hadron collider and the ATLAS detector and variety of physics analysis interests within the collaboration, the real-time data processing and offline data preparation, storage and replication is one of the biggest challenge, in ATLAS and all the other LHC expriments. There are in general the following different data formats

as result of the data processing sequence to both the collision data and MC:

- **Raw Data**: Data provided by the front-end electronics to the readout buffer. Raw Data is then written into disk/tape and used as the inputs of the reconstruction software.
- **ESD**: Event Summary Data produced from Raw Data. Provides sufficient information to re-run parts of the reconstruction.
- **AOD**: Analysis Object Data. Reduced size output of physics quantities from the reconstruction. May not be enough for the data re-processing as ESD but is sufficient for most of the performance studies and physics analysis.
- **DPD**: Derived Physics Data. The most commonly used data format for physics analysis, which can be further categorized as D1PD, D2PD and D3PD. D3PD is basically the most popular analysis data format which can be generated by the ATLAS official D3PDMaker package and accessed and analyzed in common analysis tool ROOT [27]. Nowadays, D3PDs can be accessed within hours after ESDs or AODs are ready.

In this analysis, a common data production SMWZ D3PD, which is widely used in all electroweak diboson analyses in ATLAS, is chosen as the analysis benchmark data format for both MC and data.

3.4 Object reconstruction and definitions

The performance of the reconstruction of the physics objects is essentially the fundation for physics analysis to start from. As far as the full-leptonic decay channels of $W^+W^- \to \ell^+\nu_\ell\ell^-\bar{\nu}_\ell$ is concerned, prompt and isolated leptons (e or μ) and $E_{\mathrm{T}}^{\mathrm{miss}}$ are the physics signatures which give the baseline for this measurement.

3.4.1 Electrons

The performance of well reconstructed isolated electrons over the full detector acceptance plays a very important role in extracting interesting physics signatures with electrons in their final states from the overwhelming backgrounds of QCD multijets, electrons from heavy flavors and background electrons from Dalitz decays or photon conversions originating from neutral pion decays. A rejection power of at least 10^5 is desired which demands a high and uniform efficiency over the full p_T and η range, good alignment and combination of inner detector and calorimeter, powerful reconstruction software and good understanding of the material interfering with the electron pre-shower in front of the calorimeter.

3.4.1.1 Electron trigger

In addtion to the general overview of the the trigger framework of ATLAS, the electron triggering strategy can be further detailed as follows:

At L1, electron candidates are selected using the calorimeter information with a reduced granularity given by the trigger tower (TT) within a window of $\Delta\eta \times \Delta\phi = 0.1 \times 0.1$, from which the RoIs are formed. The L1 trigger objects are clustered in 4×4 trigger trigger towers with the energy passing the associated thresholds. L2 triggers are seeded by L1 RoIs but with full granularity. The default calorimeter reconstruction works in a similar way as the offline algorithms except for the cluster seed finding technique which is done using the most energetic cell in the second EM layer at L2 while a sliding window algorithm is used for offline reconstruction. Cluster building, calibration and cluster corrections are the same as in the offline reconstruction. For tracking purposes three different tracking algorithms are available: SiTrack, IdScan and TRTSegFinder. The main electron chains use an or

between SiTrack and IdScan. [28]

EF triggers use the electron identification criteria which are very similar to the offline ones but not p_T dependent. The cuts that are implemented are taken from the p_T bin corresponding to the trigger thresholds.

3.4.1.2 Electron reconstruction

In the standard offline reconstruction algorithm, electron objects are formed based on the clusters reconstructed in the EM calorimeter and the associated tracks of charged particles reconstructed in the Inner Detector. The algorithm is optimized aiming for a well reconstructed 4-momentum of electrons for the full p_T and $|\eta|$ range.

The reconstruction starts with a set of seed clusters with energies above 2.5 GeV formed by a sliding window algorithm in a 3×5 cell unit (0.025×0.025 in η and ϕ). Electrons are defined once one or more reconstructed tracks are matched to a seed cluster. The matching is done by extrapolating the tracks from the outermost hits in the inner detector to the 2nd layer of the calorimeter with the η/ϕ coordinates between the two being compatible within a certain threshold. As for the potential that more than one track matches with one, seed cluster, all matched tracks are recorded but ordered depending on their matching quality and the one with the smallest difference of $\Delta R = \sqrt{\Delta\eta^2 + \Delta\phi^2}$ between impact point on the EM calorimeter and the seed cluster is selected. In addition, tracks with more silicon hits have higher priority than those with no hit, which are more likely electrons coming from photon conversions. Converted photons, which can also have tracks matching to the seed, are categorized as both electron candidates and photon candidates as duplicates.

The final EM clusters are re-computed using a $3 \times 7(5 \times 5)$ sliding window in the middle layer cell unit for the barrel (end-cap) region, which is seeded from the 3 seed cluster matched by tracks. The electron 4-momentum is eventually determined using the combined information from both the cluster and the original track matched to the seed cluster. The energy is computed as a weighted average between the cluster energy and the track momentum (*only* the cluster energy is used for offline physics analysis). η/ϕ directions are taken from tracks unless the track has no silicon hits, in which case η is provided by the cluster η-pointing. In cases where the track has only TRT hits, the ϕ position is taken from the track and the η is provided by cluster η-pointing. In the offline physics analysis, the electron

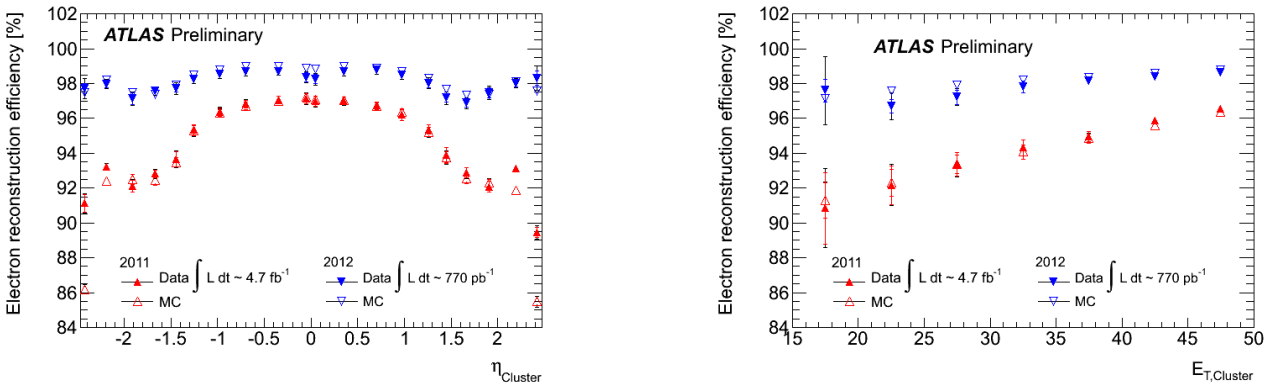

Figure 3.1 The reconstruction efficiency (including the requirements on the track quality, namely that the number of pixel hits and silicon hits the sum of pixel and SCT hits exceed 1 and 7 respectively) is shown as a function of the electron cluster η (left) and transverse energy (right), for data (filled markers) and MC (open markers) from 2011 (red up triangles) and 2012 (blue down triangles). [29]

energy is always taken from the corresponding final reconstructed cluster while the η/ϕ direction is defined by the matched track unless the number of silicon hits are less than four in which case the cluster coordinates will be used.

The offline reconstruction efficiencies are shown in Figure 3.1 as a function of E_T and η of the clusters.

3.4.1.3 Electron identification

In principle, the electron identification criteria and its optimization are driven by the motivation of providing good separation between electrons and fakes (can be either jets or photons). The criteria are created using the information of the inner trackers and the calorimeters as well as the combination of the two. There are three different sets of reference cuts, `loose++`, `medium++` and `tight++`, defined with increasing the rejection power against backgrounds. Shower shape variables of the second calorimeter layer and hadronic leakage variables are used in the `loose++` selection. First calorimeter layer cuts, track quality requirements and track-cluster matching are added at the level of the `medium++` selection. The `tight++` selection adds E/p, b-layer hit requirements and the particle identification potential indicated by the TRT high threshold hit ratio [28]. All of these sets of identification criteria can evolve as long as a better understanding of detector performance and more challenges coming from both experiment conditions (such like the robustness and stability against worse pileup shown in Figure 3.2)

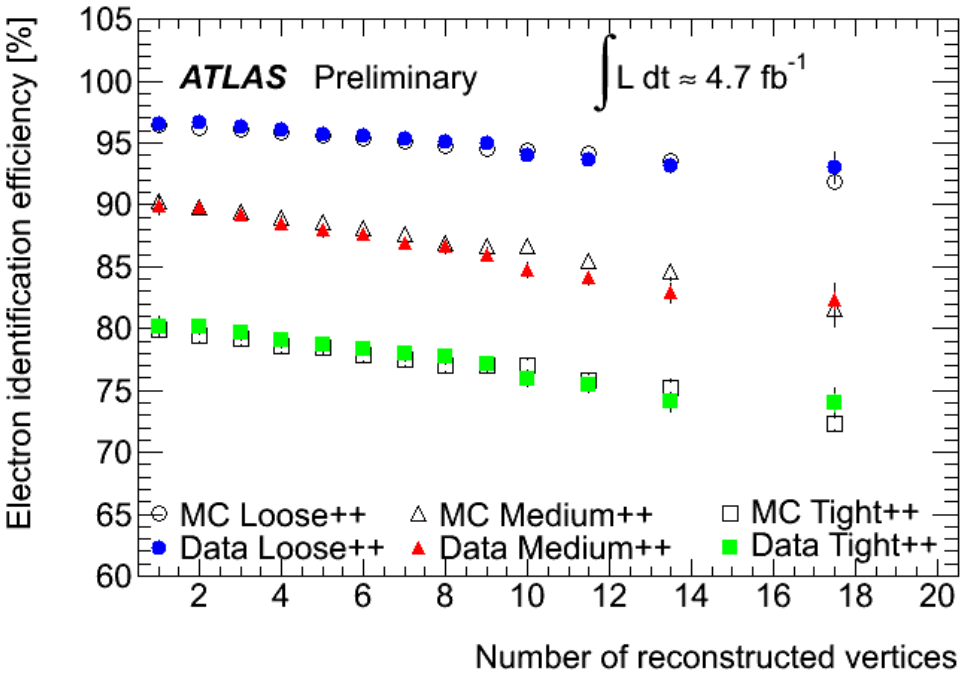

Figure 3.2 Electron identification efficiency dependence on pileup with 2011 full pp collision data set (4.7 fb^{-1}). [29]

and the physics analysis demands.

3.4.1.4 Electron isolation

The electron identifications do not have dedicated isolation cuts because particularly different isolation criteria may be favored in different physics analysis. The most common isolation cuts that are shared among different analysis are basically categorized as two kinds, the calorimeter isolation discriminator and the track isolation discriminator, which are defined as either the reconstructed energy in a cone of half opening angle R_0 around the electron candidate direction excluding the electron itself or the summed scalar p_T of tracks in a cone of R_0 around the electron.

The calorimeter based isolation requires both the discrimation power and the robustness against energy deposition of pileup events. In principle, isolation with a larger cone size should contain more energy in case of misidentified jets and smaller cone size should be less sensitive to pileup. The cone with $R_0 = 0.3$ is mostly favored in this analysis as a compromise of both of the two requirements above. Tracking based isolation is naturally not accounting for the neutral particles but has its advantage of

rejecting tracks from secondary vertices by applying track quality requirement. Experimentally, the isolation criteria may result in certain level of bias in terms of the isolation efficiency between the collision data and MC simulated events. A set of combined scale factors of impact parameter and isolation cut efficiency are derived so as to account for this difference, which are shared among different analysis [28]. (The impact parameter of a track is defined as the (geometrically signed) closest distance in the plane transverse or longitudinal to the beam line.)

3.4.1.5 Electron defintion in WW

The electron selection used in this analysis is listed in Table 3.7.

As mentioned in section 3.4.1.3, the `tight++` identification criterion is a reference set of electron selection requirements that is based on shower shape, track quality, detection of transition radiation, and track-to-calorimeter-cluster matching. The isolation requirement is based on the sum of calorimeter energy in a cone of 0.3, excluding the energy in the electron cluster, and on the sum of track transverse momentum in a cone of 0.3. The calorimeter isolation energy is corrected for the lateral leakage of the electron shower into the isolation cone. A dedicated correction has been made to account for the increased isolation energy due to in-time pileup on the calorimeter isolation. The electron energy scale is corrected in data and smeared in MC using the official `EnergyRescaler` tool [30].

Electron Selection
Reconstructed Electron Candidate
Geometrical Acceptance: $\|\eta\| < 2.47$, outside crack region $1.37 \leq \|\eta\| \leq 1.52$
Object Quality: Outside regions w/LAr readout problems
Kinematic Acceptance: $E_T > 20GeV$
Identification Criteria: `Tight++`
Calorimeter Isolation Requirement: $\sum_{\Delta R<0.3} E_T(i) \; < \; 0.14 \times E_T(e)$
Track Isolation Requirement: $\sum_{\Delta R<0.3} p_T(i) \; < \; 0.13 \times E_T(e)$
Transverse Impact parameter requirement: $\frac{d_0}{\sigma_{d_0}} < 10$
Longitudinal Impact parameter requirement: $\|z_0\| < 1mm$

Table 3.7 Electron definition used in this analysis.

The electron ID efficiency is determined from data using the *tag-and-probe* method on $Z \rightarrow e^+e^-$and $W \rightarrow e\nu$ events [31]. The overall electron selection efficiency in this analysis is about 78% for the central

region ($|\eta| < 0.8$), and decreases to about 64% in the forward region ($2.0 < |\eta| < 2.47$). The statistical uncertainty for these measurements is less than 0.4%. The corresponding systematic uncertainty is 2–5% and is dominated by the uncertainty on the background in the *tag-and-probe* samples.

Scale factors are applied to the MC to correct the efficiency to match that seen in data.

The `tight++` electron identification scale factors are measured in 20 η-bins from -2.47 to 2.47, and include E_T-dependent corrections. The reconstruction and `tight++` identification scale factors are provided by the e/γ performance group, and are found to be between 0.98 to 1.13 depending on the position of the electron cluster in the calorimeter. Scale factors for the additional isolation and impact parameter requirements used in this analysis have been calculated as described in a separate section and are found to be consistent with unity.

The combined electron scale factors are taken to be the standard `tight++` scale factors from the e/γ performance group.

3.4.2 Muons

3.4.2.1 Muon reconstruction, trigger and identification

Due to the large amount of QCD background generated in LHC pp collisions, energetic isolated muons are one of the most straightforward and effective way to extract interesting physics signals. ATLAS is optimized to detect, reconstruct and identify muons with a generally high efficiency ($>$ 95%) and a high momentum resolution $< 3\%$ for wide p_T ranges achieved. Both the inner detector (ID) and the muon spectrometer are responsible for muon momentum measurement. As indicated in section 2.2.3, the precise measurement of muon deflected by the magnetic field of air core toroid system is accomplished with a combination of MDT and CSC chambers, the latter of which works complementary at $2.0 < |\eta| < 2.7$ with 2 layers of MDT in the end-cap. The $|\eta|$ coverage for muon trigger is up to $|\eta| < 2.4$ provided by the combination of TGC ($1 < |\eta| < 2.4$) and RPC ($|\eta| < 1$). In inner detector, the measurement can be achieved up to $|\eta| = 2.5$.

Muon candidates are reconstructed by ATLAS in four different ways, namingly stand-alone muons, combined muons, segment tagged muons, and calorimeter tagged muons.

Stand-alone muon (SA) : The muon trajectory is only reconstructed in the muon spectrometer. The muon momentum measured in muon spectrometer is corrected for the parametrized energy loss of the muon in the calorimeter, to obtain the muon momentum at the interaction point. The direction of flight and the impact parameter of the muon at the interaction point are determined by extrapolating the spectrometer track back to the beam line.

Combined muon (CB) : The momentum of the stand-alone muon is combined with the momentum measured in the inner detector. The muon trajectory in the inner detector also provides information about the impact parameter of the muon trajectory with respect to the primary vertex.

Segment tagged muon (ST) : A trajectory in the inner detector is identified as a muon if the trajectory extrapolated to the muon spectrometer can be associated with track segments in the precision muon chambers.

Calorimeter tagged muon (CT) : A trajectory in the inner detector is identified as a muon if the associated energy depositions in the calorimeters is compatible with the hypothesis of a minimum ionizing particle.

In addtion, there are two independent reconstruction chains as chain 1 (or Staco) and chain 2(or muid), both of which have CB and ST muons implemented and important cross checks of each other as different reconstruction algorithms for early LHC and ATLAS operation. CB Staco muons are chosen as the physics objects in this analysis.

3.4.2.2 Muon trigger

ATLAS muon trigger system is designed based on the general trigger framework elaborated in section 2.2.5 with dedicated muon trigger algorithm for MS and ID trackers to guarantee high trigger efficiency in a wide p_T range. Muon trigger objects carrying estimated p_T information together with the position information of certain region of the detector are passed to HLT by L1 once a certain programmable threshold is fired. HLT selects the events starting from the RoIs defined using the position information given by L1 and goes in parallel to the reconstruction process to judge at each step of the HLT whether the object can be further processes as a muon candidate or discarded. Eventually at EF stage, the full event data is accessible. Both "outside-in" and "inside-out" EF trigger algorithms starting from either ID or MS for the extrapolation are implemented for EF trigger so as to minimises the risk of losing events at the online selection during the commissioning of the ATLAS muon trigger.

3.4.2.3 Muon definition for WW

The muon selection criteria used in this analysis are listed in Table 3.8. For MC, the muon momentum scale and resolution are adjusted based on a Z boson control sample [32].

The MC simulation predicts the muon reconstruction and identification efficiency very well. The muon reconstruction and identification efficiencies are also measured from $Z \rightarrow \mu^+\mu^-$ data with tag-and-probe method which is the same as what is done for electrons. The efficiency is divided into inner detector track matching efficiency and muon reconstruction efficiency in the muon spectrometer. The overall muon data/MC efficiency scale factor [32] is found to be close to 1 with an uncertainty of 1-2%. The muon isolation efficiency is the probability for a combined muon to pass both the calorimeter and

Muon Selection
Reconstructed combined staco muon
Kinematic Acceptance: $p_T > 20$ GeV
nBLayerHits > 0 if BLayerHits are expected
nPixHits + nPixelDeadSensors > 1
nSCTHits + nSCTDeadSensors ≥ 6
nPixHoles + nSCTHoles < 3
(nTRTOutliers+nTRTHits)≥ 6 and nTRTOutliers/(nTRTOutliers+nTRTHits)<0.9 for $\lvert\eta\rvert <1.9$; nTRTOutliers/(nTRTOutliers+nTRTHits)<0.9 for $\lvert\eta\rvert >1.9$ and (nTRTOutliers+nTRTHits)≥ 6
Geometrical Acceptance: $\lvert\eta\rvert < 2.4$
Longitudinal Impact parameter requirement: $\lvert z_0(\mu)\rvert < 1$ mm
Transverse Impact parameter requirement: $\frac{d_0}{\sigma_{d_0}} < 3$
Track Isolation Requirement: $\sum_{\Delta R<0.3} p_T(i) \ < \ 0.15 \times p_T(\mu)$
Calorimeter Isolation Requirement: $\sum_{\Delta R<0.3} E_T(i) \ < \ 0.14 \times p_T(\mu)$

Table 3.8 Muon definition used in this analysis.

the tracker isolation requirements of $p_T(cone30)/p_T(\mu) < 0.15$ and $E_T(cone30)/p_T(\mu) < 0.14$. The probe muon is a muon that passes all default selection cuts except the isolation requirements. The data/MC scale factor for the muon isolation efficiency is $(100.0 \pm 0.5)\%$. Figure 3.3 shows the Muon inner track matching, muon spectrometer matching and isolation efficiency as a function of muon p_T. The efficiencies measured in data and MC simulation together with corresponding scale factors are listed in Table 3.9.

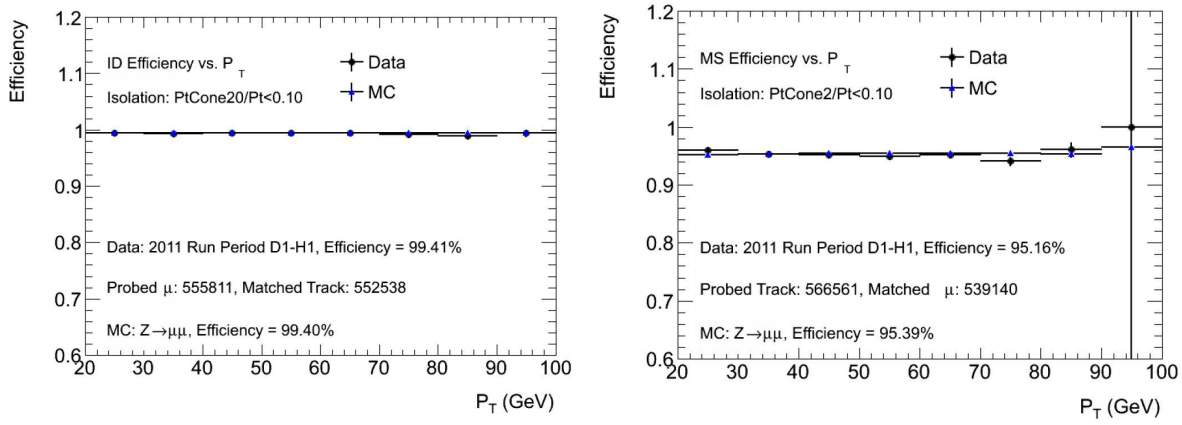

Figure 3.3 Muon inner track matching (left), muon spectrometer matching (right) as a function of muon p_T.

	ID track matching eff	MS track matching eff
Data	$(99.41 \pm 0.08)\%$	$(95.16 \pm 0.50)\%$
MC	$(99.40 \pm 0.00)\%$	$(95.39 \pm 0.02)\%$
Scale factor	1.0001 ± 0.001	0.9975 ± 0.0052

Table 3.9 ID track matching efficiency and MS track matching efficiency measured for data and MC together with the scale factor.

3.4.3 Jets

There are multiple jet reconstruction algorithms implemented for ATLAS fufilling different analysis needs and performance investigation demands, all of which can be used for missing transverse energy reconstruction.

The jets, which are used in this analysis, are reconstructed from 3-dimensional topological calorimeter clusters using the anti-k_{T} algorithm [33, 34] with a resolution parameter of $R = 0.4$ and are calibrated from the electromagnetic (EM) scale to the hadronic energy scale using an E_T and η dependent correction factor (EM+JES) [35, 36] based on Monte Carlo simulation.

Jets are required to satisfy the following criteria:

- $p_{\mathrm{T}} > 25$ GeV and $|\eta| < 4.5$ after calibration to the hadronic energy scale with the latest in-situ jet calibration implemented,
- A "looser bad" criterion [37] is impelemented as general jet quality requirement for both data and MC to reject events with jet energy wrongly measured 3.4.7.

Calibration corrections are propagated per object (using all the jets passing the selection but with a lower threshold $p_{\mathrm{T}} > 20$ GeV) to the MET using the momentum deviation in X and Y direction Jets are identified as b-jets if they have b-tagging weights greater than MV1 85% efficiency operating point [38]. In this analysis, b-tagging is only used in a control sample to extract top backgrounds.

3.4.4 Missing transverse energy $E_{\mathrm{T}}^{\mathrm{miss}}$

The missing transverse energy ($E_{\mathrm{T}}^{\mathrm{miss}}$) is reconstructed from the energies deposited in the calorimeters and the muon momenta measured by the muon spectrometer and inner detector.

$E_{\mathrm{T}}^{\mathrm{miss}}$ used in this analysis in defined as MET_RefFinal, which is measured by the calorimeters as the sum of the transverse energy of calibrated topological clusters. The $|\eta|$ coverage of topological clustering is up to 4.9 allowing nearly all of the transverse energy in an event to be recorded in calibrated topological clusters. The seeds of topological clusters grow from the calorimeter cells which have energy deposition greater than four times of the standard cell noise but then also add in all the neighbouring cells with energy deposition greater than twice of the standard cell noise. finally all neighbouring cells are included regardless of the energy deposition.

3.4.4.1 Relative Missing Energy

In order to carry on with the dedicated background treatment, a further characterized Relative $E_{\mathrm{T}}^{\mathrm{miss}}$ ($E_{\mathrm{T,\ Rel}}^{\mathrm{miss}}$) is defined as follows:

$$E_{\mathrm{T,\ Rel}}^{\mathrm{miss}} = \begin{cases} E_{\mathrm{T}}^{\mathrm{miss}} \times \sin\left(\Delta\phi_{\ell,j}\right) & \text{if } \Delta\phi_{\ell,j} < \pi/2 \\ E_{\mathrm{T}}^{\mathrm{miss}} & \text{if } \Delta\phi_{\ell,j} \geq \pi/2 \end{cases} \tag{3.1}$$

, where $\Delta\phi_{\ell,j}$ is the azimuthal angle difference between $E_{\mathrm{T}}^{\mathrm{miss}}$ and the nearest good lepton or jet passing corresponding nominal object selection. The relative $E_{\mathrm{T,\ Rel}}^{\mathrm{miss}}$ is defined so as to be less sensitive to mis-measured leptons or jets with large momentum/energy uncertainty (e.g. high p_{T} muons or high mass di-muon pairs). Hence, the sensitivity of $E_{\mathrm{T,\ Rel}}^{\mathrm{miss}}$ to the real missing transverse energy carried by neutrinos can be further increased.

3.4.4.2 Missing Energy Smearing

Energy corrections due to the scaling or smearing of certain objects as described in Sections 3.4.2, 3.4.1 and 3.4.3 must be propagated to $E_{\mathrm{T}}^{\mathrm{miss}}$ in X and Y direction, respectively. Any change in the p_{T} of muons passing full identification is added vectorially to the Met_MuonBoy term. Similarly, any change of the p_{T} of electrons passing full identification is added vectorially to the Met_RefEle term.

3.4.5 Vertex and Pileup Reweighting

3.4.5.1 Vertex definition

The primary vertex (vertex with largest $\sum p_T^2$) is required to be reconstructed with at least 3 good associated tracks so as to make sure the selected events correspond to a hard-scattering pp collision.

3.4.5.2 Pileup reweighting

In ATLAS, MC samples are mostly simulated before a certain data taking period. Therefore, only a conservative pileup assumption, which covers a generally wider range of pileup interactions than in actual data-taking, can be preset before the MC production, and during the data analysis MC samples need to be reweighted to the actual pileup conditions in data. The exact quantities concern both in-time pileup (number of interactions in a given bunch crossing) represented by the number of reconstructed vertices and the out-of-time pileup (overlapping signals in the detector from other neighboring bunch crossings) described by the average number of interactions per bunch crossing ($< \mu >$). The data set used for this analysis taken in 2011 by ATLAS were accumulated with 50 ns in-train bunch spacing when collison beams operated with bunch trains, in which out-of-time pileup plays an important role. Consequently, the centrally provided PileupReweighting tool [39] reweights the $< \mu >$ distribution with which the MC was generated to that observed in data.

3.4.6 Object Overlap Removal treatment

Some of the reconstructed objects may originate from the same measurement due to "overlap". Therefore, an "overlap removal" (OR) prescription is introduced so as to avoid the double-counted measurements for: μ/e and e/jet.

The essential effect of the OR procedure takes place for when a jet overlap with a electron, which can happen at an considerably high rate due to the intrinsic "overlap" between the electron and jet reconstruction chains. i.e. any calorimeter cluster associated with a high-p_T electron will also be accounted for in the reconstruction of jet objects. After the OR, any jet inside a cone (η-ϕ plane) of 0.3 around the selected good electron is removed. But the calorimeter isolation for the standard electron selection still includes the corresponding clusters of the jets which are removed.

Although the electron is supposed to affect the reconstruction and scale of additional jets, this non-optimal effects due to e/jet, which hurts the reconstruction of the addition jets, are still quite neglible due to the isolation criteria in use [40].

A muon may have very rare probability to "fake" an electron cluster, due to the effects of bremsstrahlung emission, etc. As a result, an electron object may be constructed very close to the muon. Hence, we introduce the μ/e OR prescription to remove any electron with a cone of 0.1 around a selected muon.

3.4.7 Event Cleaning

In order to get rid of some individual events which are affected by the unacceptable problematic physics objects with their kinematics badly measured by the detector, we introduce the following event cleaning strategies:

- *LAr hole veto:* An event is vetoed if a calorimeter jet with $p_{\mathrm{T}} > 25$ GeV happens to fall into the LAr hole region, which is mainly due to 6 dead FEB's in the EMBA compartment of the LAr calorimeter (4 in layer 2, 2 in layer 3. The 4 FEB's in layer 2 were restored later). The detailed strategy is referring to the Jet/Etmiss prescription [41].

- $E_{\mathrm{T}}^{\mathrm{miss}}$ *cleaning:* Any jet with badly measured energy and directions will also affect the resolution of $E_{\mathrm{T}}^{\mathrm{miss}}$ reconstruction. Hence, a dedicated "looser bad" criteria (defined by Jet/Etmiss combined performance group of ATLAS [37]) is defined to spot those jets with $p_{\mathrm{T}} > 20$ GeV and not overlapping with the selected good leptons. The corresponding events with at least one "looser bad" jet spotted in each are vetoed and therefore the adverse effects on $E_{\mathrm{T}}^{\mathrm{miss}}$ reconstruction can be avoided.

- *LAr Flag:* Events with LAr data integrity errors are vetoed by checking a particular data quality flag with a value greater than 1 given the variable larError which can be directly retrieved and used in the analysis. More details about the data quality issues can be found in the dedicated Section 2.2.2.

3.5 Event Selection and Optimizations

3.5.1 Trigger

We use a combination of single lepton triggers to select WW candidates depending on the decay channel and different data periods. A summary is given in Table 3.10

Channel	Period	Trigger
μ	D-I	mu18_MG
μ	J-M	mu18_MG_medium
e	D-J	e20_medium
e	K	e22_medium
e	L-M	e22vh_medium1

Table 3.10 Trigger requirements for electron and muon stream in the used data-periods.

It is very likely that the $W^+W^- \to \ell^+\nu_\ell\ell^-\bar{\nu}_\ell$ final states which have two isolated and energetic leptons can fire both electron trigger and muon trigger in the $e\mu$ channel. This will result in duplication in the electron and muon data-stream which are streamed from different trigger sets of electron and muon triggers.

To avoid the duplication of events in the electron and muon data-streams, the following procedure is applied: Keep all events at trigger decision level once they manage to fire the muon-trigger so as to keep the muon data-stream. Meanwhile, reject events in electron data-stream. Therefore, events in the electron stream are only selected, if they do not pass the muon-trigger requirement; events in the muon stream are only selected if they pass the muon-trigger requirement.

The lepton trigger efficiencies are measured in both MC and data with a simple tag-and-probe method on $Z/\gamma^* \to \ell\ell$ ($\ell = e, \mu$). The tag leptons which are required to match to the trigger objects provide an unbiased sample for the trigger efficiency measurement together with the probe leptons with looser requirement.

For muons, the trigger efficiency is measured separately in the barrel and endcap region as a function of p_T as shown in Figure 3.4. The electron trigger efficiency is measured as a function of electron η and the efficiencies for data and MC simulation are shown in Fig. 3.5. The single muon trigger efficiency is close to 80% for the barrel region and 90% for the endcap region [42] for muons with $p_T > 20$ GeV.

The single electron trigger efficiency is close to 99% for electrons with $p_T > 25$ GeV.

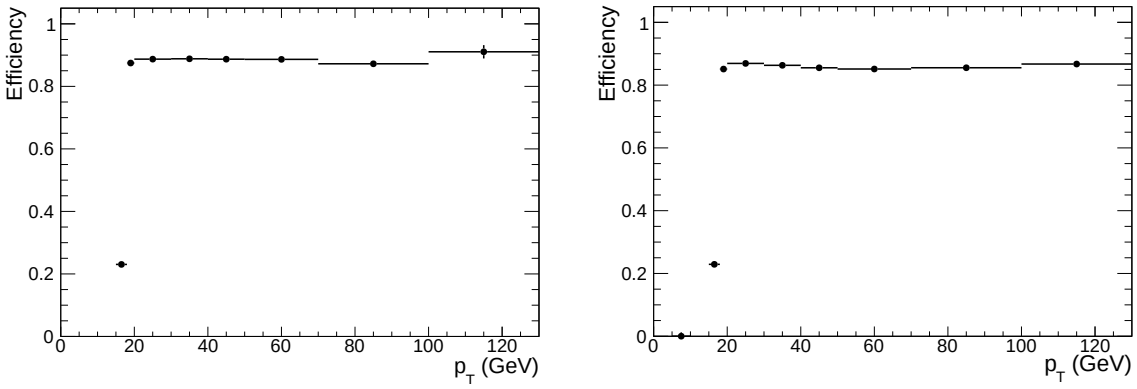

Figure 3.4 Muon trigger efficiency as a function of muon p_{T} for data (left) and MC (right) in the Endcap region. [6]

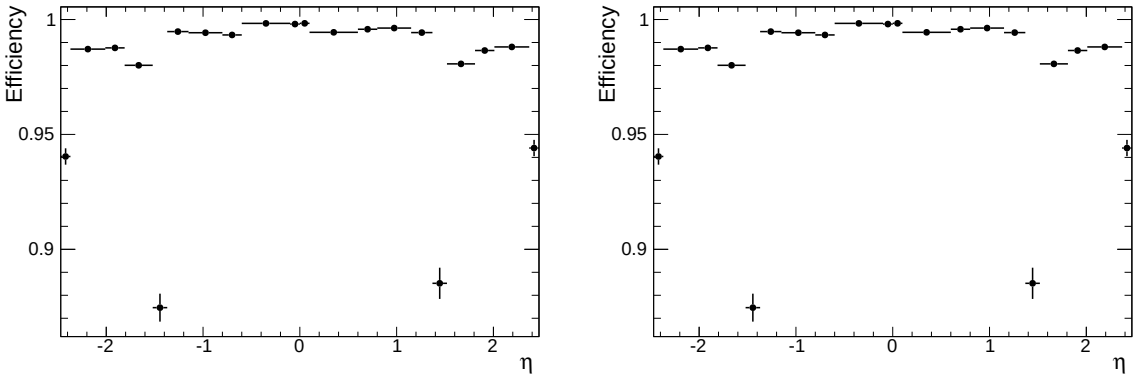

Figure 3.5 Electron trigger efficiency as a function of electron η for data (Left) and MC (Right). [6]

3.5.2 WW event selection criteria

The analysis can be classified by the flavor of leptons in the final state into the three final states $e^+e^-E_{\mathrm{T}}^{\mathrm{miss}}$, $\mu^+\mu^-E_{\mathrm{T}}^{\mathrm{miss}}$ and $e^{\pm}\mu^{\mp}E_{\mathrm{T}}^{\mathrm{miss}}$.

The event selection cuts were optimised by maximising the signal to background significance for WW detection. based on the period dependent lowest p_{T} unprescaled single-lepton signal triggers. This section presents the cuts used in the analysis which are applied on both data and MC, along with the cut-flows and event yields which are compared graphically at different selection stages.

The event selection includes a pre-filter at the stage of converting the AOD events from muon and electron data streams to SMWZ D3PD (see Section 3.3.3) ntuples. The filter cuts are given below.

- At least two leptons (medium electron or tight muon) with $p_T > 10$ GeV.
- Removal of the overlaps for combined muon and electron D3PD datasets.

For the general purpose of identifying the $W^+W^- \rightarrow \ell^+\nu_\ell\ell^-\bar{\nu}_\ell$ signal from the large amout of various background processes mentioned in Section 3.2, the nominal selection criteria are designed as follows:

1. **Data Quality**: Events must be in the *Good-Run-List* (GRL), reflecting luminosity blocks with fully functional sub-detectors during data taking. The GRL is meant to ensure that the given collision data are of adequate quality in terms of the condition or performance of each of the detector subsystems during the data-taking, based on the data quality requirements which are required in a particular performance investigation or physics analysis. In this analysis, we use the centrally provided GRL, common in SM working group of ATLAS.
2. **Object Overlap Removal**: Overlapping objects are removed as described in Section 3.4.6. The summary of the removal criteria is given below:
   - e/e removal: If two electrons overlap within a cone of $\Delta R = 0.1$, remove e with lower $p_T(cluster)$;
   - μ/e removal: If one muon and one electron overlap within a cone of $\Delta R = 0.1$, remove the electron;
   - e/jet removal: If one jet and one electron overlap within a cone of $\Delta R = 0.3$, remove the jet.
3. **Event Cleaning**: Removal of problematic events in data/MC as detailed in Section 3.4.7.
4. **Primary Vertex Selection**: The primary vertex (vertex with largest $\sum p_T^2$) is required to be reconstructed with at least 3 good tracks.
5. **Trigger Selection**: Different single lepton triggers are used in different data periods as detailed in Section 3.5.1. For $e\mu$ events, the triggers used are the "OR" of the electron and muon triggers.

6. **Dilepton Selection**: An event is selected if it has exactly two isolated, oppositely charged leptons of $p_{\mathrm{T}} > 25/20$ GeV for leading/trailing leptons respectively with the lepton selection criteria as described in Section 3.4.

   The electron $p_{\mathrm{T}} > 25$ GeV requirement ensures reaching the trigger plateau region and enables the use of the official trigger scale factors. Requiring leading muon $p_{\mathrm{T}} > 25$ GeV in the $\mu\mu$ channel (where the trigger plateau is reached at 20 GeV) only marginally reduces the signal acceptance wrt. a 20 GeV threshold while strongly reducing W+jets and QCD backgrounds due to the p_{T} dependence of the muon fake rate.

7. **Trigger matching**: At least one lepton has to be matched to a signal lepton trigger (detailed matching criteria are illustrated in [43]). For electrons, the requirement is $p_{\mathrm{T}} > 21$ GeV for $EF\_e20\_medium1$ or 23 GeV for EF_e22_medium and $EF\_e22vh\_medium1$. For muons, the requirement is $p_{\mathrm{T}} > 20$ GeV for both EF_mu18_MG and $EF\_mu18\_MG\_medium$ triggers.

The used trigger and physics objects are introduced in Sections 3.5.1 and 3.4.

After the preselection, the dominant contribution (>99%) to ee and $\mu\mu$ events comes from the inclusive $Z/\gamma* \to \ell^+\ell^-$ process. The WW signal only contributes ~0.065% of the selected events. For the $e\mu$ final state, the WW signal contributes already 10.4%, where the major background contributions come from $t\bar{t}$/single-top (50.3%), $Z \to \tau\tau$ (35.4%) and QCD (W+jet and di-jets) (2.7%). Above numbers are based on MC studies.

Figure 3.9 shows the leading and sub-leading p_T distributions for the dileptons, the $E_{\mathrm{T}}^{\mathrm{miss}}/E_{\mathrm{T,\ Rel}}^{\mathrm{miss}}$ distributions, and the dilepton invariant mass distributions after the preselection detailed above. The MC normalization is done with a total integrated luminosity of 4.6 fb^{-1} using NLO cross-sections as predicted by the SM and introduced in Section 3.3.1.

A good understanding of our backgrounds is evidenced by the agreement shown in these distributions for pre-selected dilepton events. More distributions at preselection level are shown in Figures 3.10 and 3.11. The agreement still holds for the $E_{\mathrm{T,\ Rel}}^{\mathrm{miss}}$ distributions after the Z-veto is applied in same-flavor channels and low mass cut on $M_{\ell\ell}$ in $e\mu$ channel as shown in Figure 3.12.

3.5.3 Cut Optimization and track-based $E_{\mathrm{T}}^{\mathrm{miss}}$ usage

In addition to the preselection, some channel-specific selection cuts are applied to extract the signal out from the large background:

- $M_{\ell^+\ell^-} > 15$ GeV (ee, $\mu\mu$ channels) to suppress multijet QCD and Υ contributions,
  $M_{\ell^+\ell^-} > 10$ GeV ($e\mu$ channel) to suppress the low mass spectrum not modelled in MC,
  $|M_{\ell^+\ell^-} - M_Z| > 15$ GeV (ee, $\mu\mu$ channels) to suppress $Z \to \ell^+\ell^-$,
- $E_{\mathrm{T,\ Rel}}^{\mathrm{miss}} > 45$ GeV for the $\mu\mu$ and ee channel, and $E_{\mathrm{T,\ Rel}}^{\mathrm{miss}} > 25$ GeV for the $e\mu$ channel to suppress $Z \to \ell^+\ell^-$ where ℓ includes e, μ, and τ, and $E_{\mathrm{T,\ Rel}}^{\mathrm{miss}}$
- no jets with $E_{\mathrm{T}} > 25\,\mathrm{GeV}$ and $|\eta| < 4.5$ to reject background arising from top quark production.

Given the current selections listed above, there are still large Z+X contributions which are enhanced due to a bad measurement of reconstructed energies of energetic leptons and jets and worsened MET resolution due to the high pileup conditions in the LHC high luminosity collision runs. At the final stage of the selection illustrated above, $Z + X$ processes still contribute greatly with an expectation at a compatible order of magnitude with estimated WW signal yields as suggested in the first column of Table 3.11.

There are several different approaches which are worth investigating to optimize the event selection aiming for a better signal to background significance $S/\sqrt{S+B}$, where S and B stand for signal and background contributions, respectively .

3.5.4 Usage of missing transverse momentum from tracks $p_{\mathrm{T}}^{\mathrm{miss}}$

One of the possible discriminants to tell the WW signal out from the large Z+jets background is the track-based $E_{\mathrm{T}}^{\mathrm{miss}}$. The missing transverse momentum from tracks, also known as track $E_{\mathrm{T}}^{\mathrm{miss}}$, is reconstructed with tracks (passing certain quality criteria) from the primary vertex (PV) in a given collision event. As long as the track $E_{\mathrm{T}}^{\mathrm{miss}}$ is calculated for the main PV, it is more stable than the calorimeter $E_{\mathrm{T}}^{\mathrm{miss}}$ with respect to pileup, and more correlated to the true $E_{\mathrm{T}}^{\mathrm{miss}}$ of the event. Besides, by applying certain quality cuts on the quality of tracks and PV in the calculation, track $E_{\mathrm{T}}^{\mathrm{miss}}$ is supposedly less affected by cosmics and beam background.

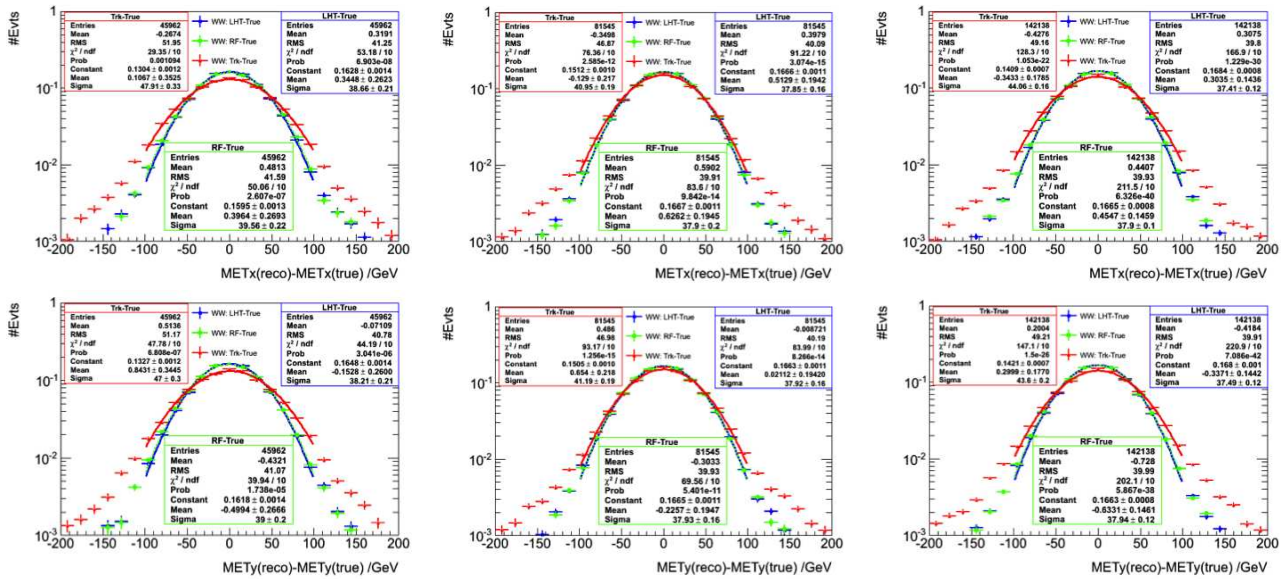

Figure 3.6 Track $E_{\mathrm{T}}^{\mathrm{miss}}$ resolution in X (top) and Y (bottom) direction for WW signal in ee (left), $\mu\mu$ (middle) and $e\mu$ (right) channels.

In the following studies, the $p_{\mathrm{T}}^{\mathrm{miss}}$ is defined as:

$$p_{x,y}^{miss} = -\sum_{Tracks} p_{x,y} \tag{3.2}$$

by summing up inner tracks satisfying the following quality requirements:

- $p_{\mathrm{T}} > 500$ MeV and $|\eta| < 2.5$
- $|d_0| < 1.5$ mm and $|z_0 \times sin\theta| < 1.5$ mm
- At least 1 pixel hit and at least 6 hits in the SCT

The $p_{\mathrm{T}}^{\mathrm{miss}}$ resolution of the WW signal is shown in Figure 3.6, which gives consistent results between the X and Y direction. A data/MC comparison is shown in Figure 3.7, exhibiting a reasonable agreement.

Unlike the calorimeter $E_{\mathrm{T}}^{\mathrm{miss}}$, track $E_{\mathrm{T}}^{\mathrm{miss}}$ (also called $p_{\mathrm{T}}^{\mathrm{miss}}$) uses tracks from the ID only, so neutral particles are not accounted for in its calculation. In addition, it is calculated only within $|\eta| < 2.5$ due to the limitation of the ID coverage. This leads to tails in the $p_{\mathrm{T}}^{\mathrm{miss}}$ distribution which do not allow to cut directly on $p_{\mathrm{T}}^{\mathrm{miss}}$ (see Figure 3.7). Still several prescriptions allow for the use of $p_{\mathrm{T}}^{\mathrm{miss}}$ information:

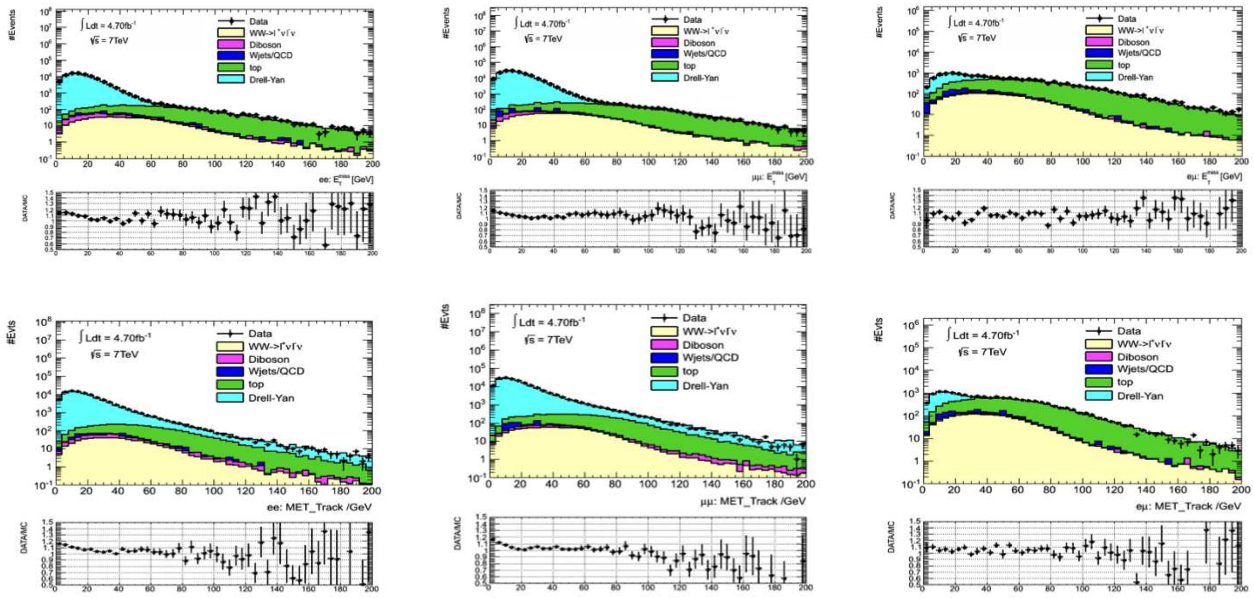

Figure 3.7 Calorimeter(top) and Track(bottom) $E_{\mathrm{T}}^{\mathrm{miss}}$ distribution comparison between data and MC in ee (left), $\mu\mu$ (middle) and $e\mu$ (right) channels.

1) 2-D combination of $E_{\mathrm{T}}^{\mathrm{miss}}$ and $p_{\mathrm{T}}^{\mathrm{miss}}$

2) minimum of $E_{\mathrm{T}}^{\mathrm{miss}}$ and $p_{\mathrm{T}}^{\mathrm{miss}}$

3) $E_{\mathrm{T}}^{\mathrm{miss}} + p_{\mathrm{T}}^{\mathrm{miss}}$

4) $\sqrt{{E_{\mathrm{T}}^{\mathrm{miss}}}^2 + {p_{\mathrm{T}}^{\mathrm{miss}}}^2}$

5) $\Delta\phi(E_{\mathrm{T}}^{\mathrm{miss}}, p_{\mathrm{T}}^{\mathrm{miss}})$, which takes the advantage that $E_{\mathrm{T}}^{\mathrm{miss}}$ and $p_{\mathrm{T}}^{\mathrm{miss}}$ are less relevant for $Z + X$ processes with *only* fake $E_{\mathrm{T}}^{\mathrm{miss}}$ in them

Table 3.11 shows a brief comparison of the evolvement of each signal and background component w.r.t. the different $E_{\mathrm{T}}^{\mathrm{miss}}$ combination choices, where a clear advantage of introducing $p_{\mathrm{T}}^{\mathrm{miss}}$ is demonstrated. Each cut value is tuned to reach an optimal working point at which a best signal to background significance is expected.

A further improvement can be expected by introducing multi variable analysis (MVA) techniques, using the various discriminants mentioned above with the relative $E_{\mathrm{T}}^{\mathrm{miss}}$ and $p_{\mathrm{T}}^{\mathrm{miss}}$ as the input discriminants for training. Several MVA techniques are introduced and the overall performance in terms of the

$E_{\mathrm{T}}^{\mathrm{miss}}$ cut choices	S(Signal)	B(Background)	$S+B$	S/B	$S/\sqrt{B}$	$S/\sqrt{S+B}$	W+jets	Drel-Yan	Top	Diboson
				ee **channel**						
$E_{\mathrm{T}}^{\mathrm{miss}}$	91.7±1.46	104±8.15	196±8.28	0.879	8.98	**6.55**	12.5±4.95	67.9±6.31	15.8±0.957	8.2±1.14
$(p_{\mathrm{T}}^{\mathrm{miss}}, E_{\mathrm{T}}^{\mathrm{miss}})$	125±1.71	86.5±8.78	212±8.94	1.45	13.4	**8.6**	19±6.79	37.5±5.13	17.3±1.01	12.8±1.91
$min(p_{\mathrm{T}}^{\mathrm{miss}}, E_{\mathrm{T}}^{\mathrm{miss}})$	129±1.73	90.2±8.88	219±9.05	1.42	13.5	**8.69**	19±6.79	40.5±5.3	17.8±1.03	12.9±1.91
$p_{\mathrm{T}}^{\mathrm{miss}} + E_{\mathrm{T}}^{\mathrm{miss}}$	127±1.72	88.2±8.67	215±8.84	1.44	13.5	**8.66**	19±6.79	35.5±4.79	18.9±1.05	14.8±2.26
$\sqrt{p_{\mathrm{T}}^{\mathrm{miss}\,2} + E_{\mathrm{T}}^{\mathrm{miss}\,2}}$	125±1.71	114±9.49	239±9.64	1.09	11.7	**8.08**	19.6±6.81	63±6.24	18.7±1.04	13.1±1.89
$\Delta\phi(p_{\mathrm{T}}^{\mathrm{miss}}, E_{\mathrm{T}}^{\mathrm{miss}})$	88±1.43	66.8±6.78	155±6.93	1.32	10.8	**7.08**	12.5±4.95	31.8±4.39	14.7±0.92	7.86±1.13
				$\mu\mu$ **channel**						
$E_{\mathrm{T}}^{\mathrm{miss}}$	142±1.79	99.2±6.14	241±6.39	1.43	14.2	**9.13**	3.64±1.54	63±5.81	20.1±1.06	12.5±0.586
$(p_{\mathrm{T}}^{\mathrm{miss}}, E_{\mathrm{T}}^{\mathrm{miss}})$	221±2.25	82.3±6.12	303±6.51	2.69	24.4	**12.7**	6.53±3.29	31.7±4.96	26±1.22	18.1±0.711
$min(p_{\mathrm{T}}^{\mathrm{miss}}, E_{\mathrm{T}}^{\mathrm{miss}})$	234±2.31	100±6.77	334±7.16	2.33	23.3	**12.8**	7.59±3.37	46.6±5.69	27±1.24	19.1±0.731
$p_{\mathrm{T}}^{\mathrm{miss}} + E_{\mathrm{T}}^{\mathrm{miss}}$	239±2.33	118±7.31	356±7.67	2.03	22	**12.6**	7.69±3.39	61.6±6.31	28.2±1.26	20.3±0.753
$\sqrt{p_{\mathrm{T}}^{\mathrm{miss}\,2} + E_{\mathrm{T}}^{\mathrm{miss}\,2}}$	226±2.27	124±7.54	350±7.88	1.81	20.2	**12.1**	7.69±3.39	69.3±6.58	27.9±1.26	19.4±0.735
$\Delta\phi(p_{\mathrm{T}}^{\mathrm{miss}}, E_{\mathrm{T}}^{\mathrm{miss}})$	192±2.09	172±17	364±17.1	1.11	14.6	**10**	8.84±3.48	125±16.6	22±1.12	16.2±0.671
				$e\mu$ **channel**						
$E_{\mathrm{T}}^{\mathrm{miss}}$	634±3.83	315±14.5	950±15	2.01	35.7	**20.6**	69±12.1	143±7.12	70.2±2.04	33.2±2.84
$(p_{\mathrm{T}}^{\mathrm{miss}}, E_{\mathrm{T}}^{\mathrm{miss}})$	690±3.99	265±14.1	955±14.7	2.61	42.4	**22.3**	72.3±12.4	85.1±5.6	71.7±2.06	35.5±2.93
$min(p_{\mathrm{T}}^{\mathrm{miss}}, E_{\mathrm{T}}^{\mathrm{miss}})$	682±3.97	258±14.2	941±14.8	2.64	42.5	**22.2**	74.3±12.7	76.3±5.33	71.5±2.06	36.2±3.06
$p_{\mathrm{T}}^{\mathrm{miss}} + E_{\mathrm{T}}^{\mathrm{miss}}$	695±4.01	274±14.4	970±15	2.54	42	**22.3**	75.8±12.8	85.2±5.57	75.5±2.12	37.8±3.07
$\sqrt{p_{\mathrm{T}}^{\mathrm{miss}\,2} + E_{\mathrm{T}}^{\mathrm{miss}\,2}}$	695±4.01	295±14.2	991±14.7	2.36	40.5	**22.1**	69±12.1	111±6.3	75.8±2.12	39.5±3.21
$\Delta\phi(p_{\mathrm{T}}^{\mathrm{miss}}, E_{\mathrm{T}}^{\mathrm{miss}})$	678±3.96	361±15.6	1.04e+03±16.1	1.88	35.7	**21**	75.1±12.9	178±7.99	72.9±2.07	35.8±3.06

Table 3.11 Comparison of the evolution of signal and background w.r.t. the different $E_{\mathrm{T}}^{\mathrm{miss}}/p_{\mathrm{T}}^{\mathrm{miss}}$ combination optimised choices. In pratice, both $E_{\mathrm{T}}^{\mathrm{miss}}$ and $p_{\mathrm{T}}^{\mathrm{miss}}$ are recalculated to their relative form based on the definition of $E_{\mathrm{T,\,Rel}}^{\mathrm{miss}}$. The marginal contrition of dijet background are not included due to 0 event yield with MC prediction.

final signal to background significance is slightly higher than the cut-based results shown in Table 3.11 as suggested in Figure 3.8. However, the expected improvement of significance is not so encouraging at this stage.

Moreover, other discriminants such as the transverse momentum $p_T^{\ell\ell}$ or the difference of ϕ angle $\Delta\phi_{\ell\ell}$ of the OS di-lepton in the final state, which can characterize the di-lepton experimental signature of $Z+X$ processes, are also considered and compared with the $p_{\mathrm{T}}^{\mathrm{miss}}$ choices discussed above. The results of different selection choices at the cut-based MVA optimal working points are compared in Table 3.12. As a compromise for simplicity, the 2-D combination of calorimeter $E_{\mathrm{T}}^{\mathrm{miss}}$ and $p_T^{\ell\ell}$ is selected.

3.5.5 Cut Optimization and track-based $E_{\mathrm{T}}^{\mathrm{miss}}$ usage

The **final** WW **channel-specific event selection cuts** are chosen to optimise the signal to background ratio, and are listed below.

1) The invariant mass of the dilepton pair ($M_{\ell\ell}$) must be greater than 15 (10) GeV for $ee/\mu\mu$ ($e\mu$) events to further remove dijet events and the low mass spectrum not modelled by MC.

2) Z-veto: $|M_{\ell_1\ell_2} - M_Z| > 15$ GeV for the ee and $\mu\mu$ channels to remove events from $Z \to \ell^+\ell^-$.

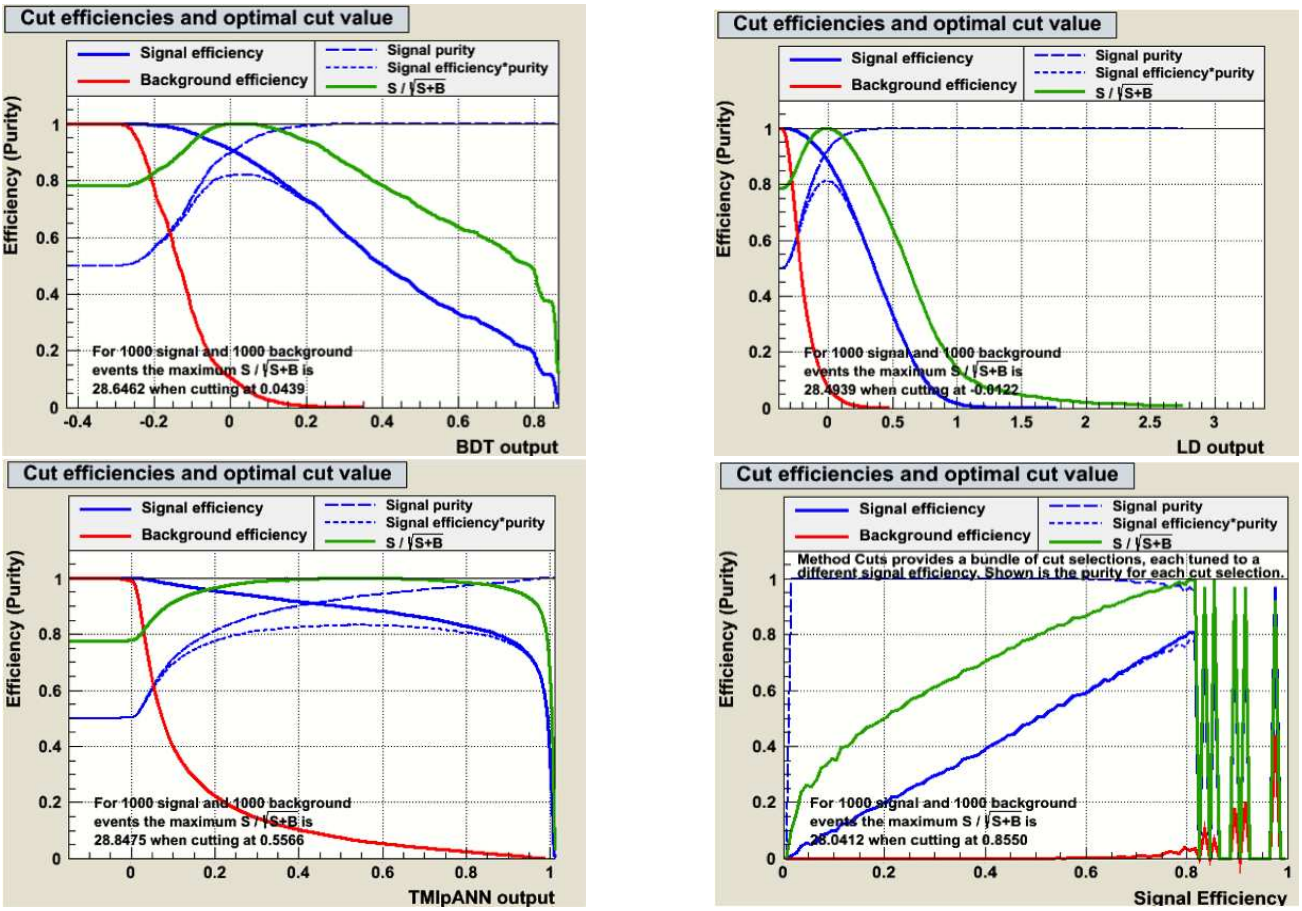

Figure 3.8 Signal to background significance tuning results with various MVA techniques: BDT (upper left), LD (upper right), ANN (bottom left) and cut based tuning(bottom right). [44]

$E_{\mathrm{T}}^{\mathrm{miss}}$ cut choices	S(Signal)	B(Background)	$S+B$	S/B	$S/\sqrt{B}$	$S/\sqrt{S+B}$	W+jets	Drel-Yan	Top	Diboson
ee channel										
nominal	91.7±1.46	104±8.15	196±8.28	0.879	8.98	**6.55**	12.5±4.95	67.9±6.31	15.8±0.957	8.2±1.14
4-D	132±1.77	94.6±7.93	227±8.12	1.4	13.6	**8.78**	15.8±5.49	48.2±5.36	17.4±1	13.2±1.72
3-D	132±1.76	78.8±7.32	211±7.53	1.68	14.9	**9.1**	17±5.55	28.1±4.22	19.4±1.07	14.3±1.96
2-D	132±1.76	79.7±7.34	212±7.55	1.66	14.8	**9.09**	17±5.55	28.8±4.26	19.5±1.07	14.4±1.96
$\mu\mu$ channel										
nominal	142±1.79	99.2±6.14	241±6.39	1.43	14.2	**9.13**	3.64±1.54	63±5.81	20.1±1.06	12.5±0.586
4-D	195±2.11	61.8±3.99	257±4.52	3.16	24.8	**12.2**	3.63±1.54	16.9±3.42	24.7±1.19	16.5±0.679
3-D	230±2.29	148±23.8	378±23.9	1.56	19	**11.9**	6.33±1.96	94.2±23.7	27.5±1.25	19.7±0.739
2-D	193±2.1	63±4.24	256±4.73	3.06	24.3	**12**	5.8±1.89	16.6±3.55	24.1±1.16	16.6±0.675
$e\mu$ channel										
nominal	634±3.83	315±14.5	950±15	2.01	35.7	**20.6**	69±12.1	143±7.12	70.2±2.04	33.2±2.84
4-D	585±3.68	149±11.3	734±11.9	3.92	47.8	**21.6**	53.4±10.7	3.16±1.05	63.5±1.95	29.3±2.78
3-D	720±4.07	290±15.6	1.01e+03±16.1	2.48	42.3	**22.7**	91.6±14.1	78±5.25	79.5±2.18	40.9±3.29
2-D	719±4.07	287±15.5	1.01e+03±16.1	2.5	42.4	**22.7**	91±14.1	76.4±5.19	79.2±2.18	40.8±3.29

Table 3.12 Comparison of the evolution of each signal and background component w.r.t. the various cut choices: "nominal" standing for the standard calo-based $E_{\mathrm{T,\,Rel}}^{\mathrm{miss}}$ cut as shown in Table 3.11, 2-D combination of $E_{\mathrm{T}}^{\mathrm{miss}}$ and $p_T^{\ell\ell}$, 3-D combination of $E_{\mathrm{T}}^{\mathrm{miss}}$, $p_T^{\ell\ell}$ and $\Delta\phi_{\ell\ell}$, 4-D combination of $E_{\mathrm{T}}^{\mathrm{miss}}$, $p_{\mathrm{T}}^{\mathrm{miss}}$, $p_T^{\ell\ell}$ and $\Delta\phi_{\ell\ell}$. The marginal contrition of dijet background is not included due to 0 event yield from MC prediction.

3) $E_{\mathrm{T,\ Rel}}^{\mathrm{miss}} > 45$, 45, 25 GeV for the $\mu\mu$, ee and $e\mu$ channels, respectively. $E_{\mathrm{T,\ Rel}}^{\mathrm{miss}}$ is calculated as follows:

$$\not\!\!E_T^{\mathrm{Rel}} = \not\!\!E_T \times sin(\Delta\phi) \ \ if\ \Delta\phi < \pi/2; \quad \not\!\!E_T^{\mathrm{Rel}} = \not\!\!E_T \ \ if\ \Delta\phi \geq \pi/2,$$

where $\Delta\phi$ is the minimum separation ϕ angle between lepton or jet and $E_{\mathrm{T}}^{\mathrm{miss}}$ detailed in Section 3.4.4.

4) Jet-veto: The number of jets ($E_T > 25$ GeV, $|\eta| < 4.5$) is required to be zero. Figure 3.13 shows the jet multiplicity distributions before the jet veto cut is applied to the selected WW candidate events. This cut removes very effectively inclusive top events with leptonic decay modes.

5) $p_T(\ell\ell) > 30$ GeV for all 3 channels. This cut helps to further reduce Drell-Yan background significantly.

3.5.6 Event selection cut-flow

The WW event selection cut-flow is shown in Table 3.13. A total number of 10395 inclusive $\ell^+\ell^- E_{\mathrm{T}}^{\mathrm{miss}}$ events before jet vetoes are observed which is consistent with the corresponding MC expectation of 9645.1 events for 4.6 fb^{-1} of integrated luminosity. The consistency continues until the final stage, where the total number of observed events is 1325 with expected 1181.6 events including 823.6 expected SM WW events and 358.0 estimated background events.

Cuts	$ee + E_{\mathrm{T}}^{\mathrm{miss}}$	$\mu\mu + E_{\mathrm{T}}^{\mathrm{miss}}$	$e\mu + E_{\mathrm{T}}^{\mathrm{miss}}$
>= 2 leptons (SS+OS)	995273	1706679	16453
2 leptons (OS)	989740	1706493	16453
ℓ $p_{\mathrm{T}} > 25$GeV	979364	1678578	15157
trigger matching	978920	1678539	15063
$M_{\ell\ell^{(\prime)}}$ >15/10 GeV	977327	1674123	15052
Z mass veto	80140	148841	15052
$E_{\mathrm{T,\ Rel}}^{\mathrm{miss}}$ cut	1398	2411	6586
Njet(0,1,2,3,>=4)	(310,285,412,246,145)	(633,535,656,381,206)	(1169,1272,2083,1274,788)
Jet veto	310	633	1169
$p_T(\ell\ell) > 30$ GeV	174	330	821

Table 3.13 Event selection cut flow for data collected in 2011 at 7 TeV for 4.6 fb^{-1} in the three di-lepton channels. SS denotes same-sign and OS denotes opposite-sign lepton charges.

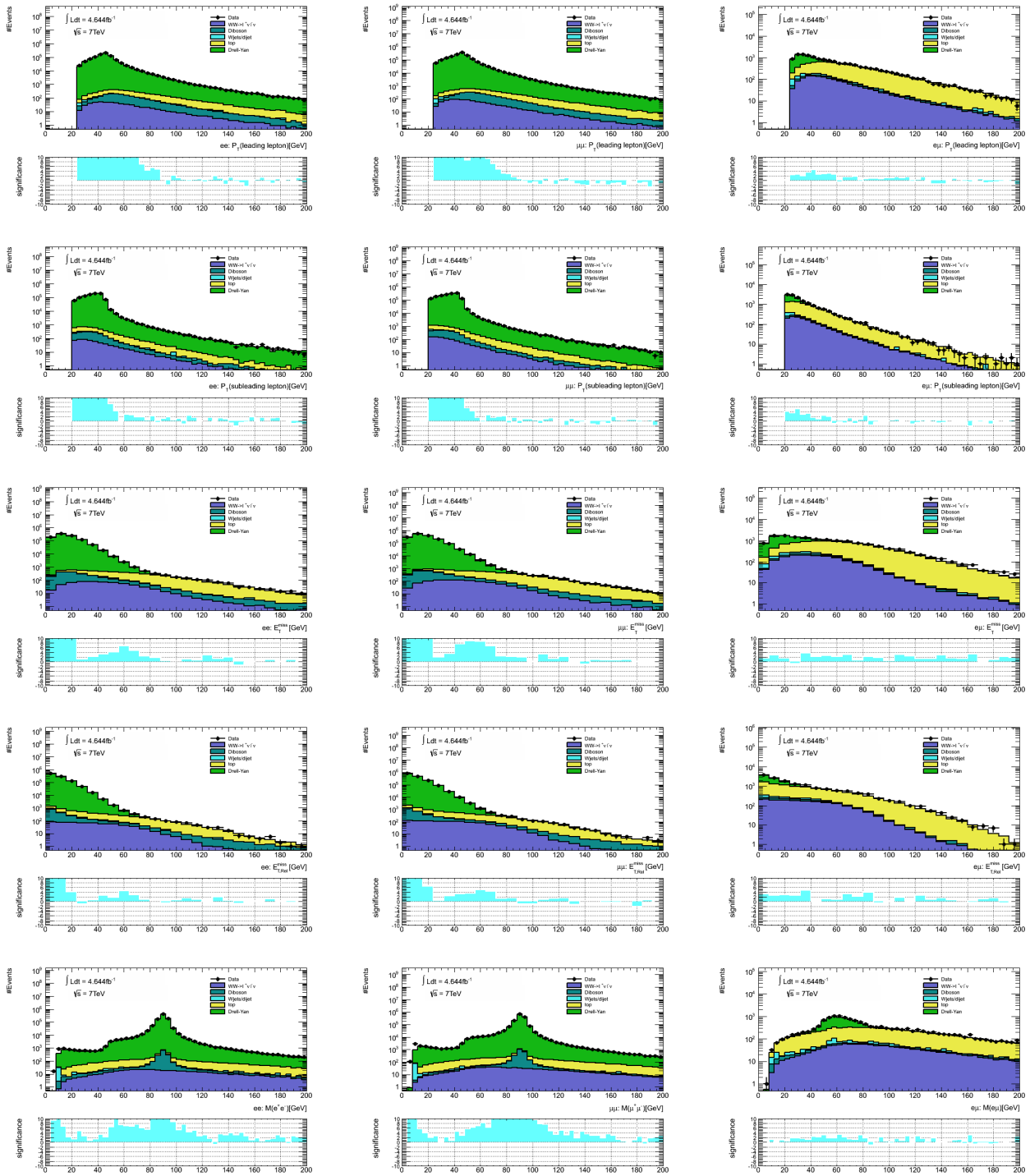

Figure 3.9 Kinematic variable distributions at preselection level (two good opposite sign leptons) where the left column shows the ee channel, the middle column the $\mu\mu$ channel and the right column the $e\mu$ channel. The first row shows the leading lepton p_T, the second row the p_T of the trailing lepton, the third row shows the $E_{\mathrm{T}}^{\mathrm{miss}}$ distributions, the 4th row shows $E_{\mathrm{T,\,Rel}}^{\mathrm{miss}}$ and the 5th row the invariant dilepton mass distributions. The points represent data and the stacked histograms are the MC predictions normalised by SM cross sections to 4.6 fb^{-1}. Scale factors as outlined in Section 3.3.2 are applied to MC.

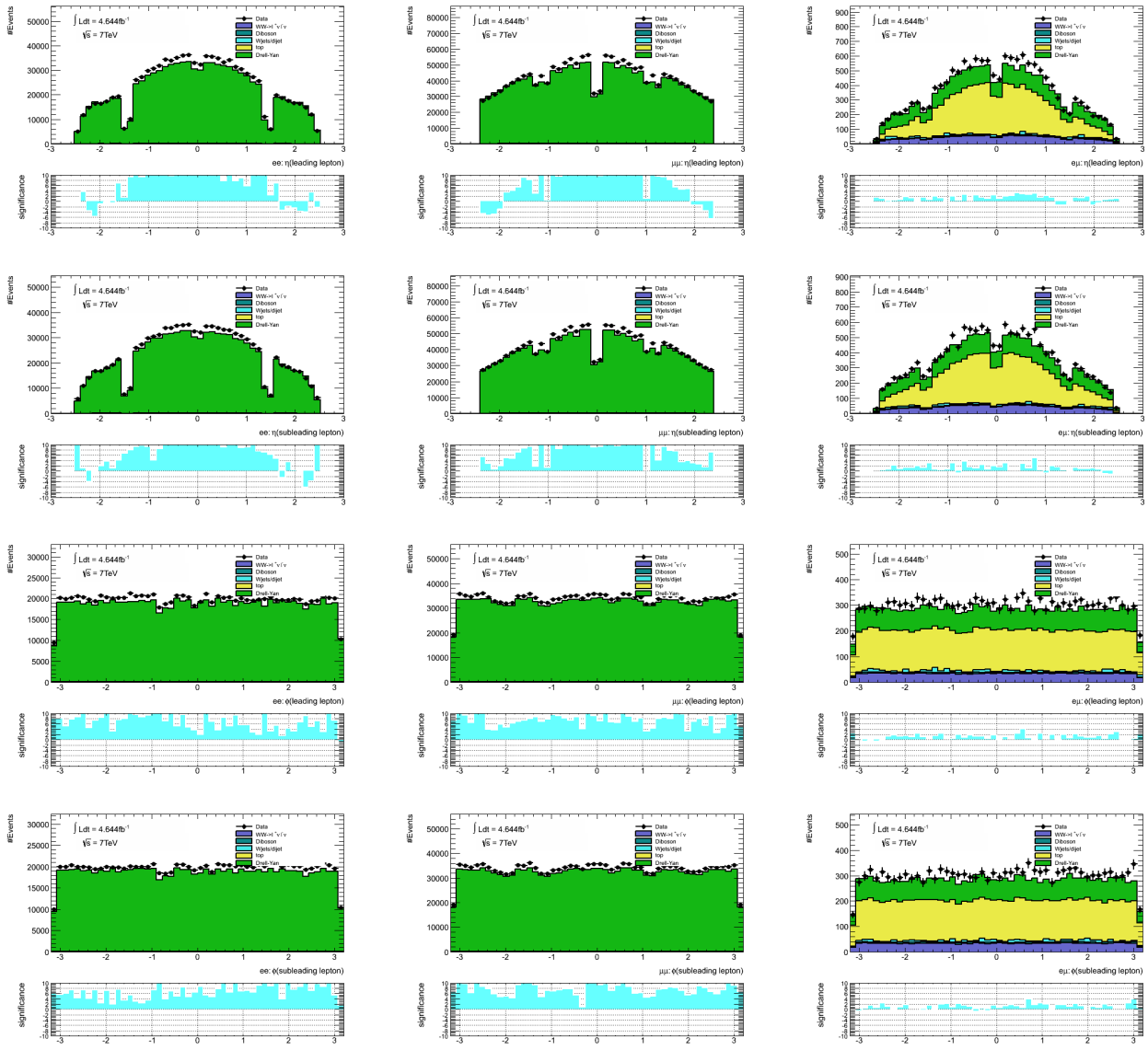

Figure 3.10 Kinematic variable distributions at preselection level (two good opposite sign leptons) where the left column shows the ee channel, the middle column the $\mu\mu$ channel and the right column the $e\mu$ channel. The first row shows the leading lepton η, the second row the η of the trailing lepton, the third row shows ϕ of the leading lepton, and the 4th row shows ϕ of the trailing lepton. The points represent data and the stacked histograms are the MC predictions normalised by SM cross sections to 4.6 fb^{-1}. Scale factors as outlined in Section 3.3.2 are applied to MC.

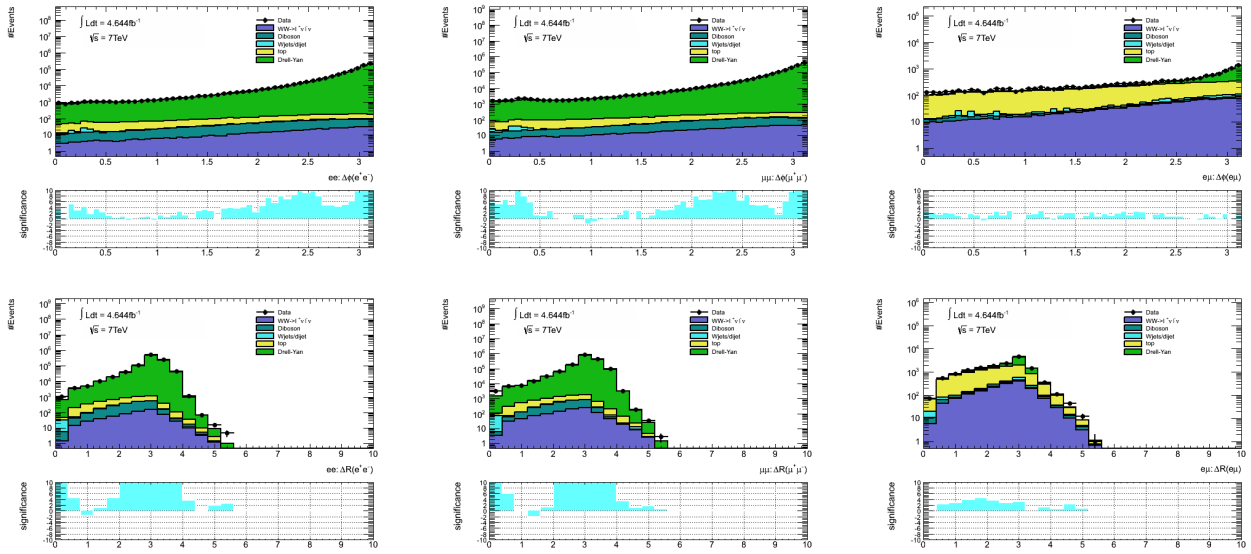

Figure 3.11 Kinematic variable distributions at preselection level (two good opposite sign leptons) where the left column shows the ee channel, the middle column the $\mu\mu$ channel and the right column the $e\mu$ channel. The first row shows $\Delta\phi$ between the leptons, the second row the ΔR between the leptons. The points represent data and the stacked histograms are the MC predictions normalised by SM cross sections to 4.6 fb^{-1}. Scale factors as outlined in Section 3.3.2 are applied to MC.

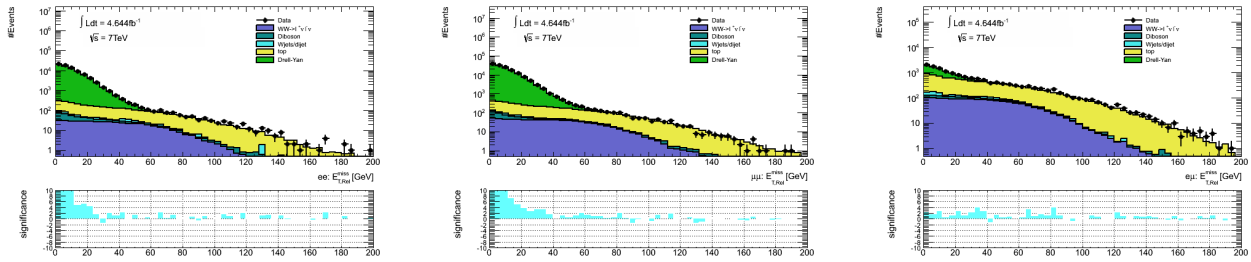

Figure 3.12 $E_{\mathrm{T,\ Rel}}^{\mathrm{miss}}$ distributions (without $E_{\mathrm{T,\ Rel}}^{\mathrm{miss}}$ cut applied) for ee (left), $\mu\mu$ (middle) and $e\mu$ (right) channels after the Z-veto cut. The points represent data and the stacked histograms are the MC predictions. Scale factors as outlined in Section 3.3.2 are applied to MC.

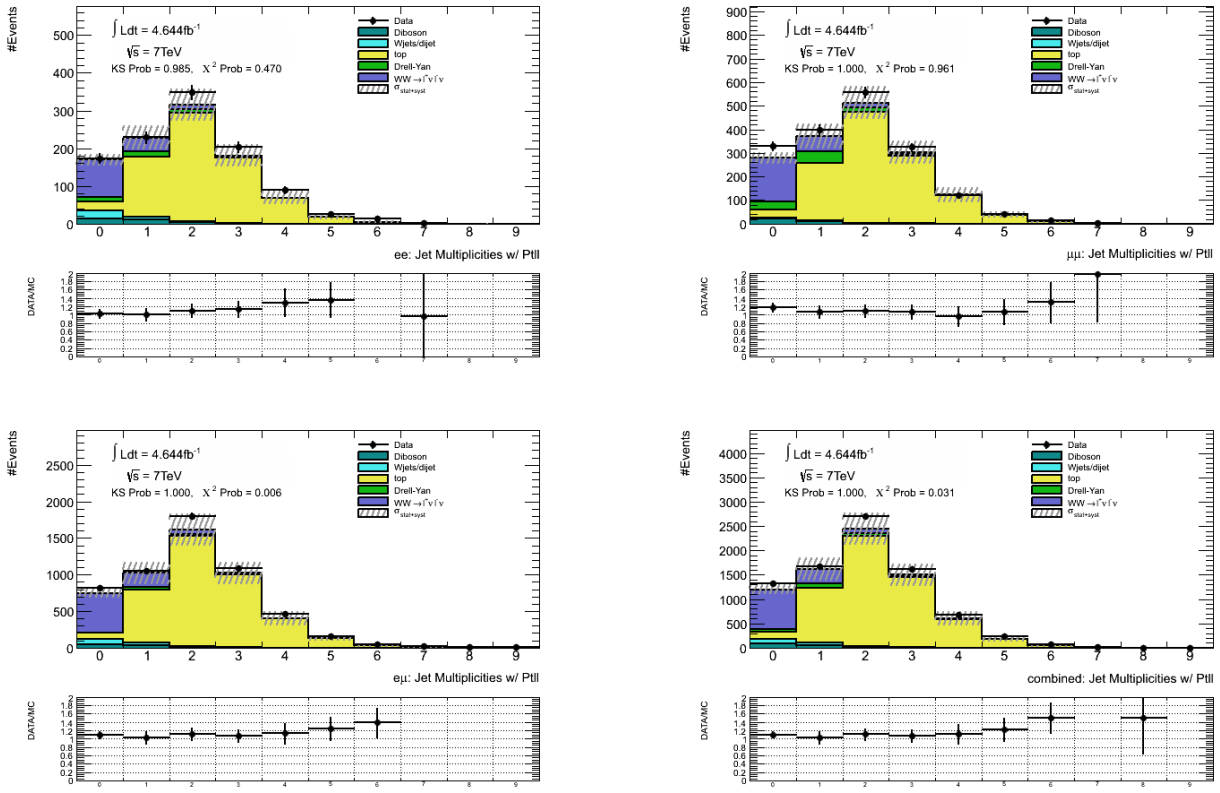

Figure 3.13 Jet multiplicity distributions for the ee and $\mu\mu$ channels (top row plots), and for the $e\mu$ and combined dilepton channels (bottom row plots). All the dilepton events have passed the full WW selection up to the jet veto. The points represent data and the stacked histograms are the MC predictions. Scale factors as outlined in Section 3.3.2 are applied to MC.

3.5.7 Distributions of selected events

Figure 3.14 shows kinematic distributions for WW candidate events after all selection cuts are applied: the first row of plots shows the p_{T} of the leading lepton (left) and trailing lepton (right); the second row shows the transverse momentum distribution of the di-lepton system (left) and the ϕ angle difference between the two leptons (right); the third row shows the transverse mass

$$M_T = \sqrt{(E_T^{\ell_1} + E_T^{\ell_2} + E_{\mathrm{T}}^{\mathrm{miss}})^2 - (\vec{p}_T^{\,\ell_1} + \vec{p}_T^{\,\ell_2} + \vec{E}_T^{miss})^2}$$

for the di-lepton+$E_{\mathrm{T}}^{\mathrm{miss}}$ system (left) and p_{T} for di-lepton+$E_{\mathrm{T}}^{\mathrm{miss}}$ (right). Figure 3.15 shows the η distributions for leading and subleading leptons, dilepton invariant mass and ΔR between the leptons as well as $E_{\mathrm{T}}^{\mathrm{miss}}$ and $E_{\mathrm{T,\ Rel}}^{\mathrm{miss}}$ distributions. In all figures the points represent data and stacked histograms are from MC predictions except for the W+jets/Dijet contribution, derived solely with a data-driven method (see Section 3.6.2). Appendix A shows the same distributions for each channel separately.

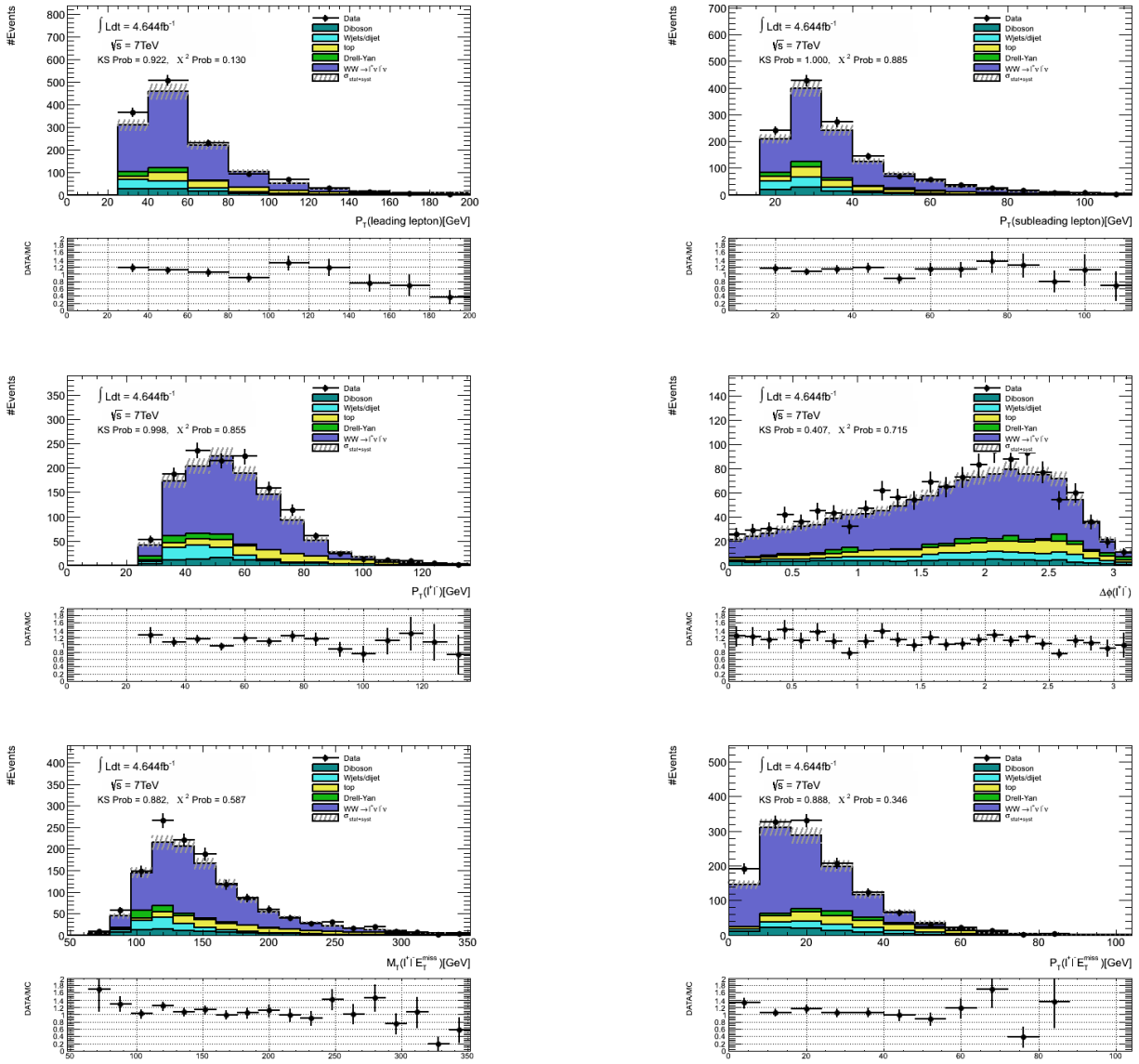

Figure 3.14 Distributions for WW candidates after the $p_T(\ell\ell)$ cut (final selection) for combined ee, $\mu\mu$ and $e\mu$ channels: the first row is the p_{T} of leading lepton (left) and the p_{T} of trailing lepton (right); the second row is the $p_T(\ell\ell)$ (left) and the ϕ angle difference between two leptons (right); the third row is the M_T for di-lepton+$E_{\mathrm{T}}^{\mathrm{miss}}$ system (left) and p_{T} for di-lepton+$E_{\mathrm{T}}^{\mathrm{miss}}$ (right). The points represent data and stacked histograms are from MC predictions except W+jets/Dijet background, obtained from a data-driven method. Scale factors as outlined in Section 3.3.2 are applied to MC. The (stat+syst) uncertainties are shown as the grey bands.

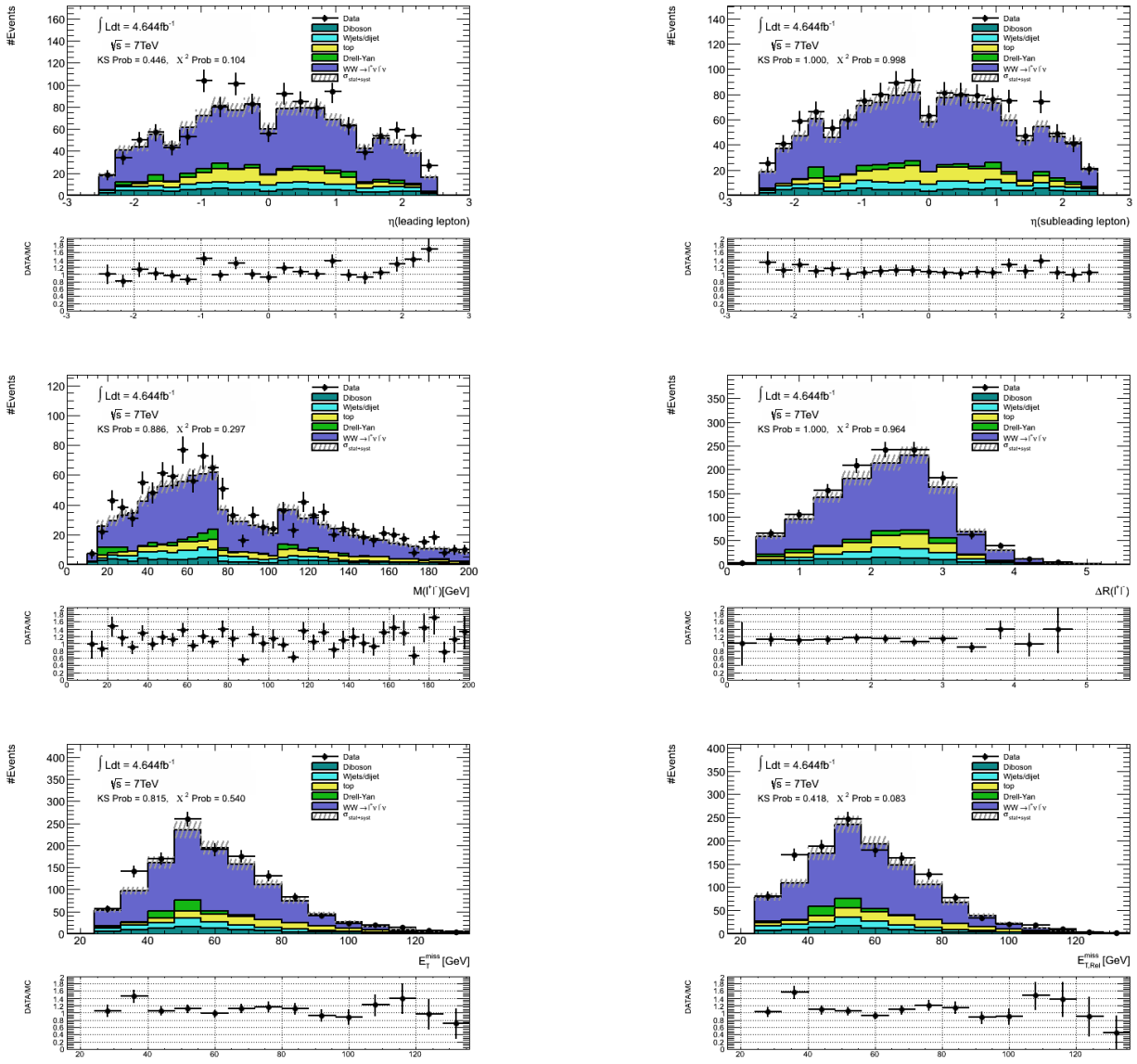

Figure 3.15 Distributions for WW candidates after the $p_T(\ell\ell)$ cut (final selection) for combined ee, $\mu\mu$ and $e\mu$ channels: the first row is the η of the leading lepton (left) and the η of the trailing lepton (right); the second row is the $M(\ell\ell)$ (left) and the ΔR between the leptons (right); the third row is the $E_{\mathrm{T}}^{\mathrm{miss}}$ (left) and $E_{\mathrm{T,\,Rel}}^{\mathrm{miss}}$ (right). The points represent data and stacked histograms are from MC predictions except W+jets/Dijet background, obtained from a data-driven method. Scale factors as outlined in Section 3.3.2 are applied to MC. The (stat+syst) uncertainties are shown as the grey bands.

3.5.8 WW signal event selection cut flow and acceptance

Table 3.14 and Table 3.15 shows the MC WW signal event selection cut flow for the three di-lepton channels and the acceptance at each step. The MC events are normalised to 4.6 fb^{-1} using the NLO SM cross section. The acceptances for prompt electron or muon decays from W bosons are shown separately from $WW \to \tau\nu\ell\nu$, where $\ell = e, \mu, \tau$. The overall acceptances are given in this table as well.

Cuts	ee Channel		$\mu\mu$ Channel		$e\mu$ Channel	
	$e\nu e\nu$	$\tau\nu\ell\nu$	$\mu\nu\mu\nu$	$\tau\nu\ell\nu$	$e\nu\mu\nu$	$\tau\nu\ell\nu$
Total Events (4.6 fb^{-1})	2421.1	922.4	2421.1	922.4	4842.2	1844.9
2 leptons (SS+OS)	562.89	69.58	964.07	108.44	1493.68	173.51
2 leptons (OS)	558.23	69.19	964.07	108.44	1493.68	173.51
ℓ $p_{\mathrm{T}} > 25$GeV	554.78	68.32	954.58	106.45	1475.24	169.36
trigger matching	551.17	67.71	944.83	105.30	1461.02	167.10
$M_{\ell\ell^{(\prime)}}$ >15/10 GeV	548.81	67.59	938.84	104.98	1460.10	167.00
Z mass veto	424.96	49.98	724.75	78.52	1460.10	167.00
$E^{\mathrm{miss}}_{\mathrm{T,\,Rel}}$ cut	154.42	12.91	286.98	24.21	921.08	94.69
Jet veto	97.60	7.03	180.07	14.56	586.40	57.33
$p_T(\ell\ell) > 30$ GeV	93.57	6.68	171.89	13.66	490.71	47.10
WW Acceptance	3.86%	0.72%	7.10%	1.48%	10.13%	2.55%

Table 3.14 WW MC event selection cut flow and overall acceptance. The MC WW signal expectations are normalised to 4.6 fb^{-1} integrated luminosity, using the NLO SM cross section. For the final WW acceptance, the jet veto SF (0.957/0.954/0.956 for $ee/\mu\mu/e\mu$) has already been included.

Table 3.16 shows the observed data WW candidate yields in each channel, compared to the **MC** expectations for WW signal and backgrounds from different sources which are elaborated in Section 3.6.

Cuts	ee Channel		$\mu\mu$ Channel		$e\mu$ Channel	
	$e\nu e\nu$	$\tau\nu\ell\nu$	$\mu\nu\mu\nu$	$\tau\nu\ell\nu$	$e\nu\mu\nu$	$\tau\nu\ell\nu$
Total Events	2421.1	922.4	2421.1	922.4	4842.2	1844.9
2 leptons (SS+OS)	23.25%	7.54%	39.82%	11.76%	30.85%	9.41%
2 leptons (OS)	23.06%	7.50%	39.82%	11.76%	30.85%	9.41%
ℓ $p_{\mathrm{T}} > 25$GeV	22.91%	7.41%	39.43%	11.54%	30.47%	9.18%
trigger matching	22.77%	7.34%	39.03%	11.42%	30.17%	9.06%
$M_{\ell\ell^{(\prime)}}$ >15/10 GeV	22.67%	7.33%	38.78%	11.38%	30.15%	9.05%
Z mass veto	17.55%	5.42%	29.94%	8.51%	30.15%	9.05%
$E^{\mathrm{miss}}_{\mathrm{T,\ Rel}}$ cut	6.38%	1.40%	11.85%	2.62%	19.02%	5.13%
Jet veto	4.03%	0.76%	7.44%	1.58%	12.11%	3.11%
$p_T(\ell\ell) > 30$ GeV	3.86%	0.72%	7.10%	1.48%	10.13%	2.55%

Table 3.15 WW MC event selection cut flow acceptance at each step. The MC WW signal expectations are normalised to 4.6 fb^{-1} integrated luminosity, using the NLO SM cross section. For the final WW acceptance, the jet veto SF (0.957/0.954/0.956 for $ee/\mu\mu/e\mu$) has already been included.

Final State	ee Channel	$\mu\mu$ Channel	$e\mu$ Channel	combined
Observed Events	174	330	821	1325
total MC prediction(S+B)	163.5	278.0	740.0	1181.6
MC WW signal	100.3	185.5	537.8	823.6
Top	23.3	33.7	90.1	147.1
W+jets+QCD	14.6	5.58	63.1	83.3
Drell-Yan	12.6	32.2	4.87	49.7
Diboson	12.70	21.0	44.1	77.9
Total Background	63.2	92.5	202.2	358.0

Table 3.16 Summary of observed data events and MC expected signal and background contributions in the three channels and their combined results. The jet veto SF (0.957/0.954/0.956 for $ee/\mu\mu/e\mu$) has already been applied to the WW MC signal acceptance.

3.6 Background estimation

3.6.1 Drell-Yan background estimation

The $Z + X$ background contaminates the WW signal due to Z+jets with fake $E_{\mathrm{T}}^{\mathrm{miss}}$ due to the mismeasurement of lepton or jet energies, high pileup conditions or particles which exit down the beamline. Given the potentially mismodeled fake $E_{\mathrm{T}}^{\mathrm{miss}}$ in $Z + X$ samples, it is important to validate the background estimation in data using a $Z + X$ control sample defined by reversing only the $p_T^{\ell\ell}$ cut to $p_T^{\ell\ell} < 30$ GeV for all three channels. The control region is thus well dominated by the Z+jets process in the ee and $\mu\mu$ channels and about 50% dominated by Z+jets in the $e\mu$ channel. This is verified by the di-lepton invariant mass distributions in the control region shown in Figure 3.16.

A scale factor is derived to account for the discrepancy of data and Monte Carlo in the control region, which is conservatively assumed to be caused by $Z + X$ background only, as

$$\mathrm{SF} = \frac{N_{Z,\mathrm{CR}}^{\mathrm{data}}}{N_{Z,\mathrm{CR}}^{\mathrm{MC}}} = \frac{N_{\mathrm{CR}}^{\mathrm{data}} - N_{non-Z,\mathrm{CR}}^{\mathrm{MC}}}{N_{Z,\mathrm{CR}}^{\mathrm{MC}}} \tag{3.3}$$

, where $N_{\mathrm{CR}}^{\mathrm{data}}$ is the control region (CR) yield observed in data, $N_{non-Z,\mathrm{CR}}^{\mathrm{MC}}$ is the non-Z+jets event yield in the CR predicted by MC, and $N_{Z,\mathrm{CR}}^{\mathrm{MC}}$ is the Z+jets event yield in the CR predicted by MC. Eventually, the scale factor is then applied to the Z+jets MC prediction in the signal region (SR) to get the final estimation.

The CR yields, scale factors and SR estimates are documented in Table 3.17.

channel	$N_{\mathrm{CR}}^{\mathrm{data}}$	$N_{Z,\mathrm{CR}}^{\mathrm{data}}$	$N_{Z,\mathrm{CR}}^{\mathrm{MC}}$	SF	$N_{Z,\mathrm{SR}}^{\mathrm{MC}}$	$N_{Z,\mathrm{SR}}^{\mathrm{DD}}$
ee	136	125.6 ± 12.1	134.6 ± 8.6	0.933 ± 0.108	12.7 ± 2.9	11.9 ± 3.0
$\mu\mu$	303	288.2 ± 17.7	276.0 ± 12.2	1.044 ± 0.079	32.9 ± 5.0	34.4 ± 5.8
$e\mu$	348	194.5 ± 20.2	173.3 ± 7.7	1.123 ± 0.127	4.6 ± 1.3	5.2 ± 1.6

Table 3.17 Event yields in the Z+jets CR and the WW signal region. All uncertainties shown here are statistical ones only. [6]

The systematic uncertainty of Z+jets background estimation is obtained by varying each relevant systematic term up and down by one standard deviation and quoting the corresponding deviation with respect to the nominal values. The dominating sources are the $E_{\mathrm{T}}^{\mathrm{miss}}$ and jet energy scale/resolution uncertainties. The uncertainties due to the non-Z+jets background subtraction in the control region

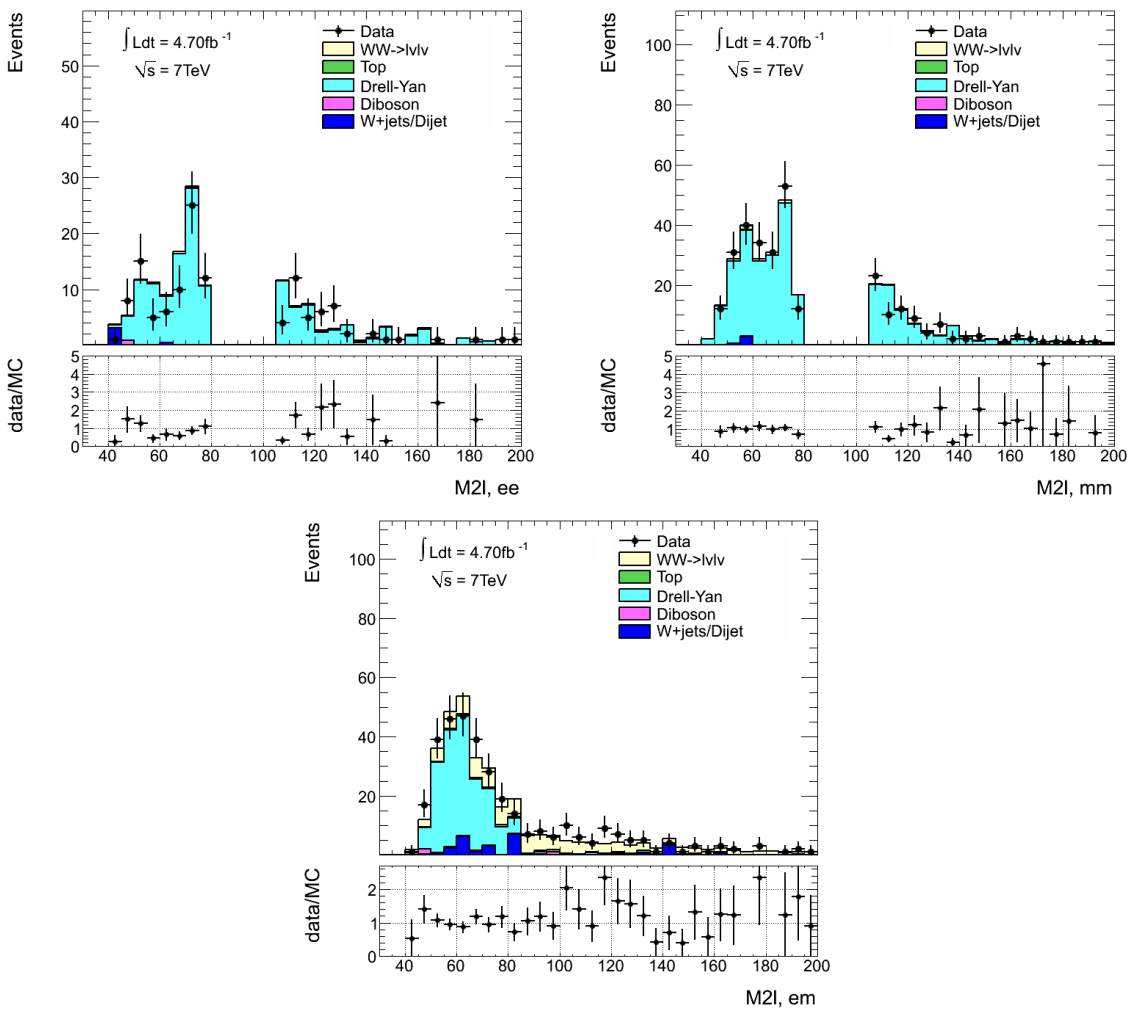

Figure 3.16 The di-lepton invariant mass distribution in the Z+jets control region. [6]

are found to be negligible for the ee and $\mu\mu$ channels. A 5% variation for WW and other diboson processes, 10% for top background and 50% for W+jets and di-jet background are used to assess the the uncertainties due to non-$Z+X$ subtraction, which are verified to be negligible. The systematic uncertainties are summarised in Table 3.18.

Sources	ee	$\mu\mu$	$e\mu$	combined
Electron Energy Scale	6.14%	-	6.11%	0.81%
Electron Energy Resolution	0.82%	-	1.30%	0.31%
Muon p_{T} Scale	-	1.05%	0.60%	0.38%
ID Muon p_{T} Resolution	-	0.29%	0.20%	0.18%
MS Muon p_{T} Resolution	-	0.66%	0.10%	0.45%
Electron recon. SF	0.39%	-	0.60%	0.15%
Electron ID SF	0.01%	-	0.50%	0.05%
Muon ID SF	-	0.04%	0.40%	0.07%
Electron Iso/IP SF	0.04%	-	0.10%	0.01%
Muon Iso/IP SF	-	0.03%	0.01%	0.02%
MET: SoftTerms Reso	10.26%	3.12%	8.42%	3.62%
MET: SoftTerms Scale	14.59%	20.76%	13.73%	18.66%
JES	6.95%	13.80%	6.71%	10.31%
JER	5.75%	13.32%	2.00%	5.24%
non-Z+jets x-section and Lumi.	-	-	7.90%	0.78%
Total uncertainty	20.93%	28.46%	20.27%	22.29%

Table 3.18 The systematics on the Z+jets background estimation. The 1.8% uncertainty on the luminosity has also been included. [6]

The final results for the Z+jets background estimation are shown in Table 3.19.

3.6.2 W+jets background estimation

This method in principle also estimates WW events with one hadronically decaying W, but these events only constitute $\approx 0.1\%$ of the W+jets background.

	ee	$\mu\mu$	$e\mu$	combined
data-driven estimation	$11.9 \pm 3.0(\mathrm{stat}) \pm 2.5(\mathrm{syst})$	$34.4 \pm 5.8(\mathrm{stat}) \pm 9.8(\mathrm{syst})$	$5.2 \pm 1.6(\mathrm{stat}) \pm 1.1(\mathrm{syst})$	$51.4 \pm 6.8(\mathrm{stat}) \pm 11.5(\mathrm{syst})$
MC prediction	$12.7 \pm 2.9(\mathrm{stat})$	$32.9 \pm 5.0(\mathrm{stat})$	$4.6 \pm 1.3(\mathrm{stat})$	$50.3 \pm 5.9(\mathrm{stat})$

Table 3.19 Z+jets background yields in the signal region for three channels. [6]

The W+jet production, which has a much larger inclusive cross section than the WW signal, can mimic the WW signal when the associated jets are misidentified as leptons due to the naturally complicated interaction between jets and the calorimeters as well as the potential interplay between the jet shape and lepton identification algorithms. The rate of QCD jets faking leptons may not be correctly modeled in MC, therefore a data-driven method is required to estimate the background using a fake factor measured directly from a di-jet control sample from data with the jet-rich identification customized in Table 3.20 for both electrons and muons.

jet-rich electron	jet-rich muon
Same pT and η range as identified electron	Same pT and range as identified muon
Nhit (SCT + Pixel) ≥ 4	Same ID track requirement as id-muon
$\|z0\| < 1$mm	$\|z0\| < 1$mm
etcone30(corrected)< 0.3	etcone30(corrected) < 0.3
ptcone30 < 0.13	remove jets in cone 0.3 around the muon
remove identified electrons	remove identified muons

Table 3.20 Definitions of jet-rich electrons and muons for the fake factor measurements (Looser electron/muon isolation and looser electron ID criteria). [6]

The fake factor f_l shown in Equation 3.4, is the rate at which QCD jets pass the the full lepton identification requirements represented by the ratio of the number of jets satisfying the full lepton identification, to those satisfying the jet-rich lepton selection.

$$\mathrm{f}_l \equiv \frac{\mathrm{N}_{\text{identified lepton}}}{\mathrm{N}_{\text{jet-rich lepton}}}. \tag{3.4}$$

The W+jet control sample is then defined from data passing most of the WW signal selection except for the di-lepton selection which is replaced as one fully identified lepton plus one jet passing the "jet-rich" lepton definition. At all the other stage of the control sample selection, the jet is considered as a well identified lepton. The W+jets background to WW is eventually estimated by scaling the control sample ($\mathrm{N}_{\text{lepton ID + Jet-Rich ID}}$) by the measured "fake factor" above:

$$\mathrm{N}_{\text{one id + one fake}} = \mathrm{f}_l \times \mathrm{N}_{\text{one id + one jet-rich}}. \tag{3.5}$$

In the $e-\mu$ channel, there are two terms in the final estimation with contributions by both misidentified electrons and misidentified muons as shown in Equation 3.6.

$$\mathrm{N}^{e\mu\text{-ch}}_{\text{one id + one fake}} = \mathrm{f}_e \times \mathrm{N}_{\text{one id } \mu \text{ + one jet-rich e}} + \mathrm{f}_\mu \times \mathrm{N}_{\text{one id e + one jet-rich } \mu} \tag{3.6}$$

The fake factors of electrons and muons are shown in Figure 3.17. Given the current jet-rich lepton definition, the measured fake factor for muons is much higher than for electrons due to a "tighter" jet-rich definition for muons.

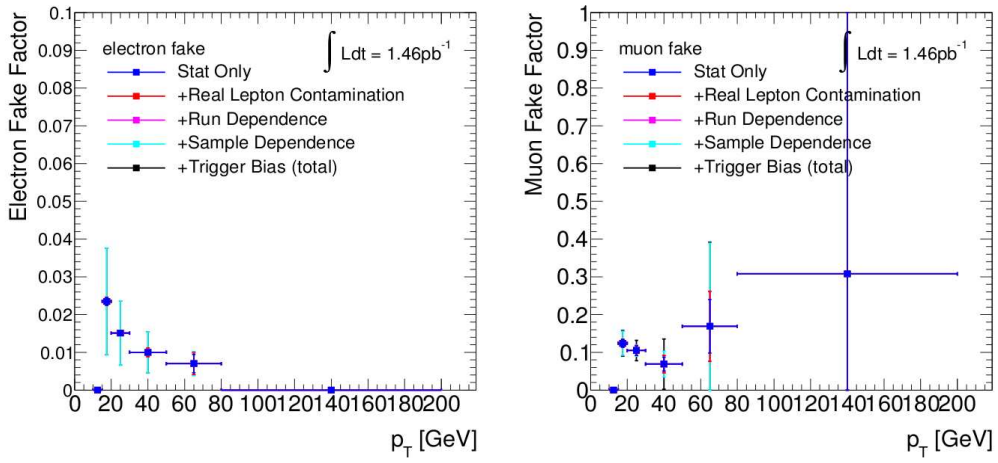

Figure 3.17 W+jets fake factor with systematics from [45]. This fake factor is calculated with very loose (high prescale) trigger EF_g20_etcut, leading to a low effective luminosity. The large systematic uncertainties are sample dependence (dijets vs W+jets) for electrons, and trigger dependence for muons. [6]

The leading and subleading lepton p_T spectra in the W+jets control region are shown in Figure 3.18 for electrons and Figure 3.19 for muons.

In order to test the robustness of the method, we introduce and W+jet control region (CR) by requiring that the leptons in the WW selection are of the same sign (SS) so that the W+jet contributions in it are enriched a lot. The same strategy is implemented in this CR by using the same electron/muon fake factors as in the signal region (SR).

The SS CR yields with W+jet estimations along with the non-W+jet contributions (WW signal and other backgrounds) predicted by MC are presented in Table 3.21. The statistical and systematic uncertainties of the W+jet estimates and the statistical uncertainties of the non-W+jet MC predictions are shown. The leading and sub-leading lepton p_T distributions in the SS region are shown in Figure 3.20, which gives very good agreements between the observations and estimations/predictions in the SS CR in each channel.

The W+jet background in the WW signal region obtained from the fake factor procedure is pre-

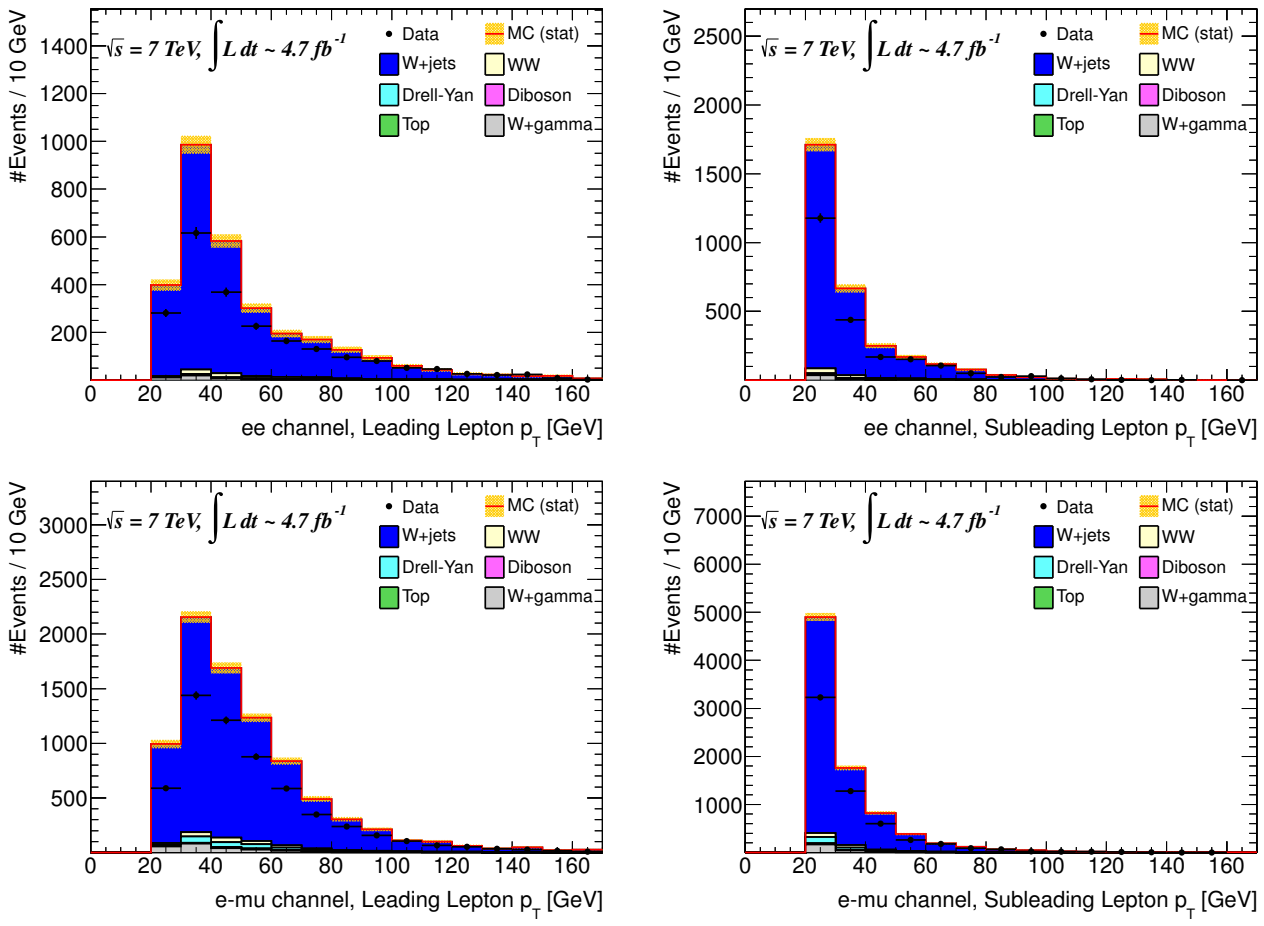

Figure 3.18 Leading and subleading lepton p_T for leptons in the signal region with one identified electron or muon and one jet-rich electron. All Monte Carlo samples including the W+jets simulation are shown, in the method itself the W+jets simulation is not used. The top row shows the distributions for the ee channel, the lower row for the $e\mu$ channel. The W+jets simulation overpredicts the yield in this sideband, indicating that the probability of misidentifying a jet as electron-like is overestimated in simulation. [6]

	$W+\gamma$	di-boson	Drell-Yan	W+jets Prediction	Total	observed
ee channel	8.8 ± 2.3	1.41 ± 0.21	0.32 ± 0.32	$10.84 \pm 0.38 \pm 5.76$	$22.3 \pm 2.4 \pm 5.8$	12
$e\mu$ channel	17.5 ± 2.6	19.37 ± 0.76	1.6 ± 1.0	$29.95 \pm 0.87 \pm 14.90$	$71.5 \pm 3.0 \pm 14.9$	53
$\mu\mu$ channel	1.66 ± 0.27	9.04 ± 0.51	0.0 ± 0.0	$1.25 \pm 0.48 \pm 1.58$	$12.00 \pm 0.75 \pm 1.58$	14
all channels	27.9 ± 3.5	29.8 ± 1.0	1.9 ± 1.0	42.0 ± 1.1	105.8 ± 3.9	79

Table 3.21 Selected and Total Monte Carlo and W+jets data-driven Predictions in the same-sign control region. [6]

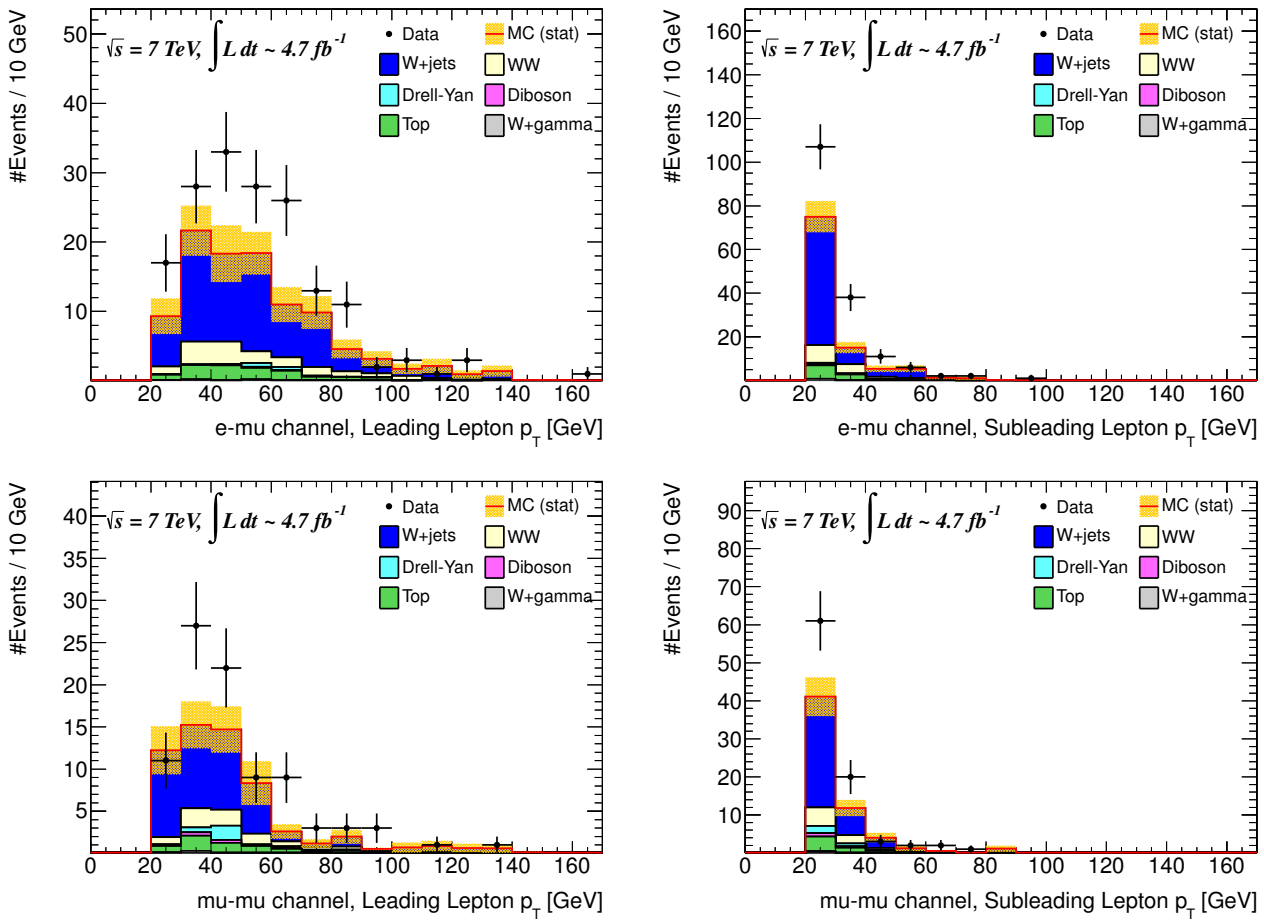

Figure 3.19 Leading and subleading lepton p_T for leptons in the signal region with one identified electron or muon and one jet-rich muon. All Monte Carlo samples including the W+jets simulation are shown, in the method itself the W+jets simulation is not used. The top row shows the distributions for the $e\mu$ channel, the lower row for the $\mu\mu$ channel. The result indicates an underestimate of jet-rich muons in the W+jet simulation. [6]

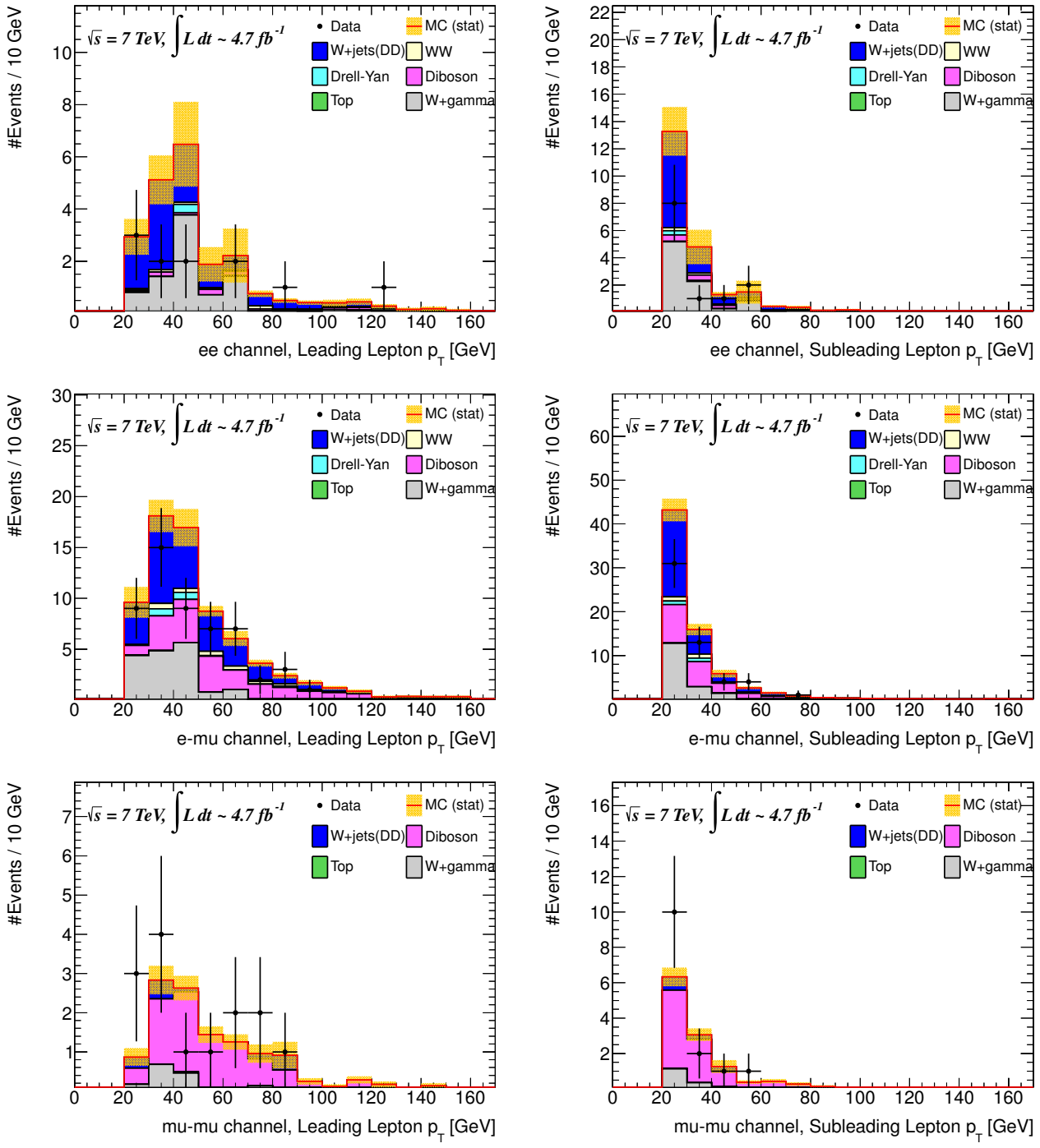

Figure 3.20 Leading and subleading lepton p_T for leptons in the same-sign control region after all cuts compared to predictions. From top to bottom the ee, $e\mu$ and $\mu\mu$ channels are shown. [6]

sented in Table 3.22 The total background is the sum of the W+jet estimation from data and the non-W+jet MC corrections. The total uncertainties are the quadratic sum of the uncertainties on the W+jet prediction from data and the MC corrections. The systematic uncertainties are due to the systematic uncertainty on the measured fake factor. [6]

	ee-ch	eμ-ch	$\mu\mu$-ch	Total
W+jet background (e-fakes)	$21.38 \pm 0.53 \pm 11.34$	$56.25 \pm 0.90 \pm 30.19$	-	$77.6 \pm 1.0 \pm 41.5$
W+jet background (μ-fakes)	-	$13.8 \pm 1.4 \pm 8.1$	$6.56 \pm 0.96 \pm 2.77$	$20.4 \pm 1.7 \pm 10.9$
Total W+jet background	$21.38 \pm 0.53 \pm 11.34$	$70.0 \pm 1.7 \pm 31.3$	$6.56 \pm 0.96 \pm 2.77$	$98.0 \pm 2.0 \pm 42.9$
W+jet MC (comparison)	16.2 ± 4.5	60.1 ± 8.4	5.5 ± 2.1	81.8 ± 9.8

Table 3.22 Summary of the W+Jet background estimates with associated statistical and systematic uncertainties. The W+jets MC prediction is given only for comparison, and is not used in the analysis. [6]

3.6.3 Top background estimation

The decay products from both top-pair ($t\bar{t} \to WbWb$) and single top processes contain WW in the final states. The top events are characterised by hadronic jet activity in the final states. Using a jet-veto cut, the majority of the top background can be removed from the WW event selection. However, some top events containing jets with transverse energy E_T^{jet} less than 25 GeV would still mimic the SM WW events. The top background contribution is estimated using data driven methods. The results are cross checked by using MC predictions. The primary method is based on a template fit method and is described in Section 3.6.3.2 because of the less complicated methodology and less systematic uncertainties. The method to cross-check these results is described in Section 3.6.3.1 and uses b-tagging to estimate the top contribution in the zero jet bin.

3.6.3.1 Jet Veto Scale Factor Method

To estimate the top background after full jet veto (0-jet bin), a data-driven method is introduced so that the jet veto scale factor of MC is corrected with two control samples defined from both data and MC. The first consists of two leptons, $E_{\text{T}}^{\text{miss}}$, and at least one b-jet, tagged at the 85% operating point of the MV1 tagger with $E_T > 25$ GeV and $|\eta| < 2.5$.

An estimate of the jet veto efficiency, $P_1^{\text{Btag,data}}$, is extracted from this control sample, as [46, 47]

$$P_1^{\text{Btag}} = \frac{N_{0j}^{\text{Btag}}}{N_{\text{all}}^{\text{Btag}}}, \tag{3.7}$$

where N_{0j}^{Btag} and $N_{\text{all}}^{\text{Btag}}$ are the number of events with no probing jets and the total number of events of the sample. Probing jets, reconstructed using the same transverse energy threshold in the same η range as other jets, are all jets excluding the b-jet and the distance between the b-jet and a probing jet is required to satisfy $\Delta R > 1$.

The observed numbers of events in the data are compared to MC for the different final states in Table 3.23.

Figure 3.21 shows the jet distributions in data compared to MC in the b-tagged control sample. Figures 3.22-3.24 show similar distributions separately for ee, $\mu\mu$ and $e\mu$ channels. The pseudo-rapidity distribution of the b-tagged jets (top-right plot) shows that their acceptance in pseudo-rapidity is limited to about 2.5. This is different from that of the probing jets which can extend down to 4.5. It is checked, however, that the P_1^{Btag} calculated based on the probing jets has little sensitivity to the acceptance variation of the b-tagged jets. Indeed by varying the acceptance largely from 2.5 to 1.5, the P_1^{Btag} in data decreases only by 7.2% which is fairly described by MC (5.5%). In addition, any remaining difference in the forward pseudo-rapidity region would be taken into account by an uncertainty of 1.5% associated to the closure test (see the third systematic uncertainty listed below). Figure 3.22 indicates that the b-tagging efficiency is higher in data than the top MC prediction in the ee channel. However the difference is mostly within the quadratic sum of the statistical and systematic uncertainties. It should also be pointed out that P_1^{Btag} is not directly sensitive to the normalization difference of the b-tagged samples but to the potential shape difference of the probing jet multiplicity distributions (low-right plot) such that the mismodeling between data and top MC in the 0-jet bin (signal region) can be taken into account.

The jet veto efficiency in the b-tagged sample, defined in Eq.(3.7), is determined for both data and the top MC (for data, the small non-top background contributions shown in Table 3.23 are subtracted from the corresponding observed data events). The full-jet veto efficiency for top events in the signal

Table 3.23 Number of events observed in data in the b-tagged control sample. The first row under the data item ($N_{\text{all}}^{\text{Btag}}$) corresponds to the total number of events observed after the $E_{\text{T}}^{\text{miss}}$ cut and the requirement of at least one b-jet (see text). The second row under the data item (N_{0j}^{Btag}) indicates the number of events observed without a probing jet. The MC expectation for various processes is also given. The results for MC are given in terms of the expected number of events for $4.6\,\text{fb}^{-1}$ of integrated luminosity. The first and second rows under each MC item are defined the same way as for the data. Results are given for the ee, $\mu\mu$, $e\mu$ and their sum.

channel		ee	$\mu\mu$	$e\mu$	all
Data	$N_{\text{all}}^{\text{Btag}}$	845	1288	4371	6504
	N_{0j}^{Btag}	170	304	844	1318
$t\bar{t}$	$N_{\text{all}}^{\text{Btag}}$	656.8	1090.8	3576.8	5324.3
	N_{0j}^{Btag}	129.2	198.7	597.0	924.9
Single top	$N_{\text{all}}^{\text{Btag}}$	61.3	98.3	331.7	491.3
(including Wt)	N_{0j}^{Btag}	33.2	52.0	172.3	257.4
All top	$N_{\text{all}}^{\text{Btag}}$	718.1	1189.1	3908.5	5815.7
	N_{0j}^{Btag}	162.4	250.7	769.2	1182.3
WW	$N_{\text{all}}^{\text{Btag}}$	8.4	16.1	50.6	75.1
	N_{0j}^{Btag}	5.0	9.4	30.3	44.7
W+jets, QCD	$N_{\text{all}}^{\text{Btag}}$	2.6	0	7.6	10.3
	N_{0j}^{Btag}	2.1	0	5.3	7.4
Z+jets	$N_{\text{all}}^{\text{Btag}}$	7.2	23.7	19.6	50.4
	N_{0j}^{Btag}	4.5	12.3	11.1	28.0
Diboson	$N_{\text{all}}^{\text{Btag}}$	2.5	2.7	9.1	14.4
	N_{0j}^{Btag}	1.4	1.7	5.0	8.1
All non-top background	$N_{\text{all}}^{\text{Btag}}$	20.8	42.4	87.0	150.2
	N_{0j}^{Btag}	13.0	23.5	51.7	88.2

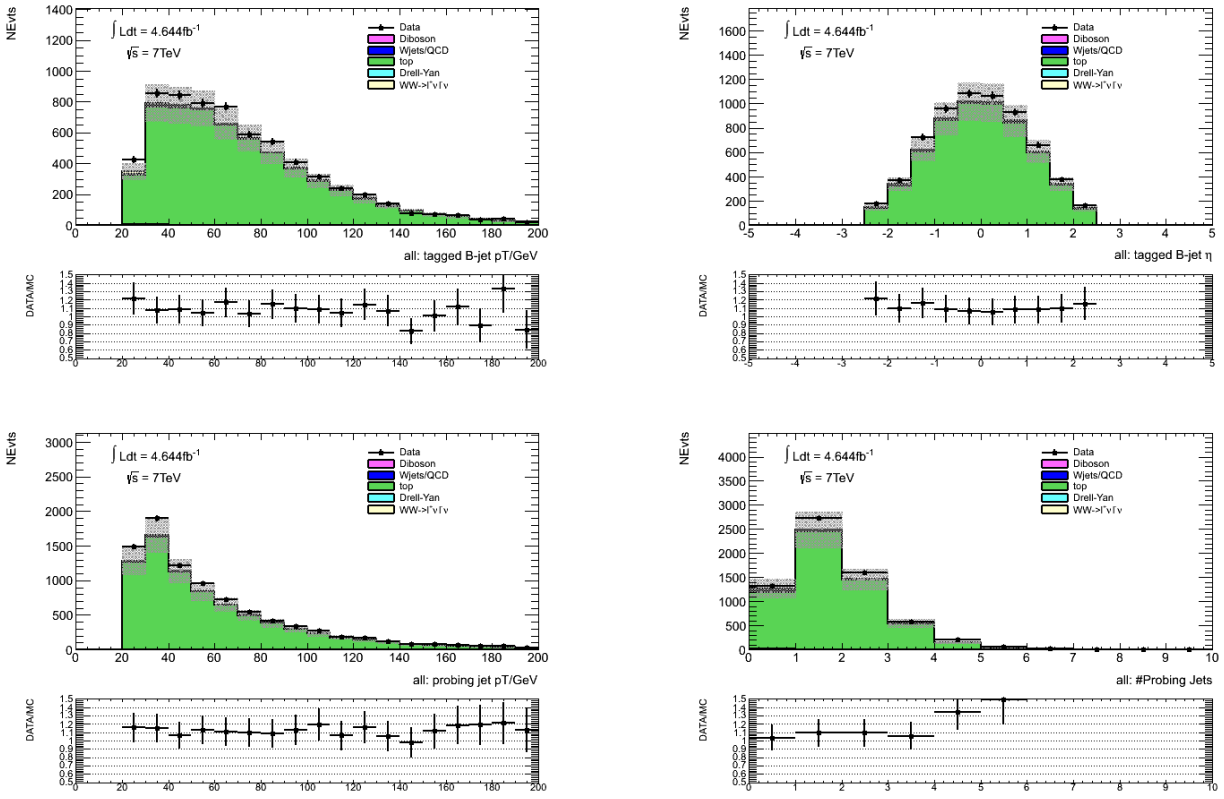

Figure 3.21 Jet distributions in data compared to MC in the b-tagged control sample used to extract the jet veto efficiency for top backgrounds. The upper plots display the transverse momentum (left) and pseudo-rapidity (right) of the tagging b-jets. The lower plots display the transverse momentum (left) and the multiplicity of the probing jets (right). The data is compared with MC corresponding to the most relevant processes (see text).

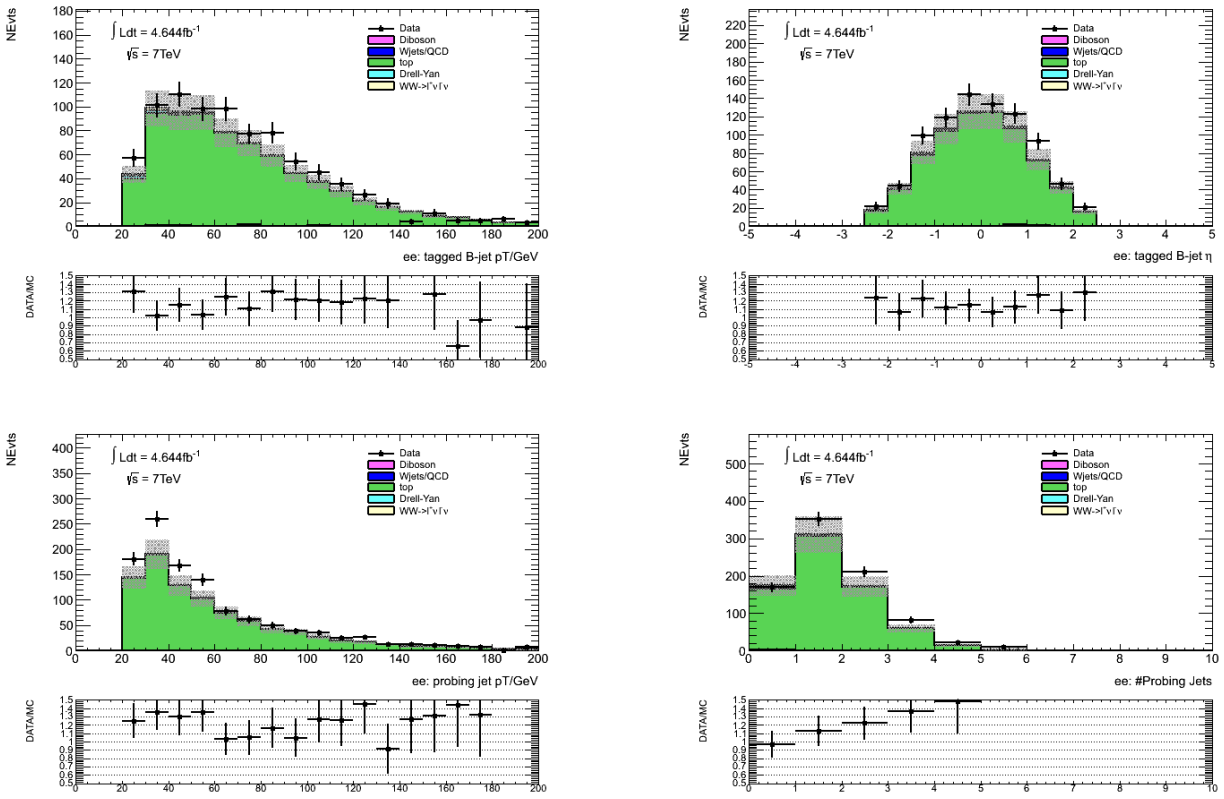

Figure 3.22 Same as Fig. 3.21 for the *ee* channel.

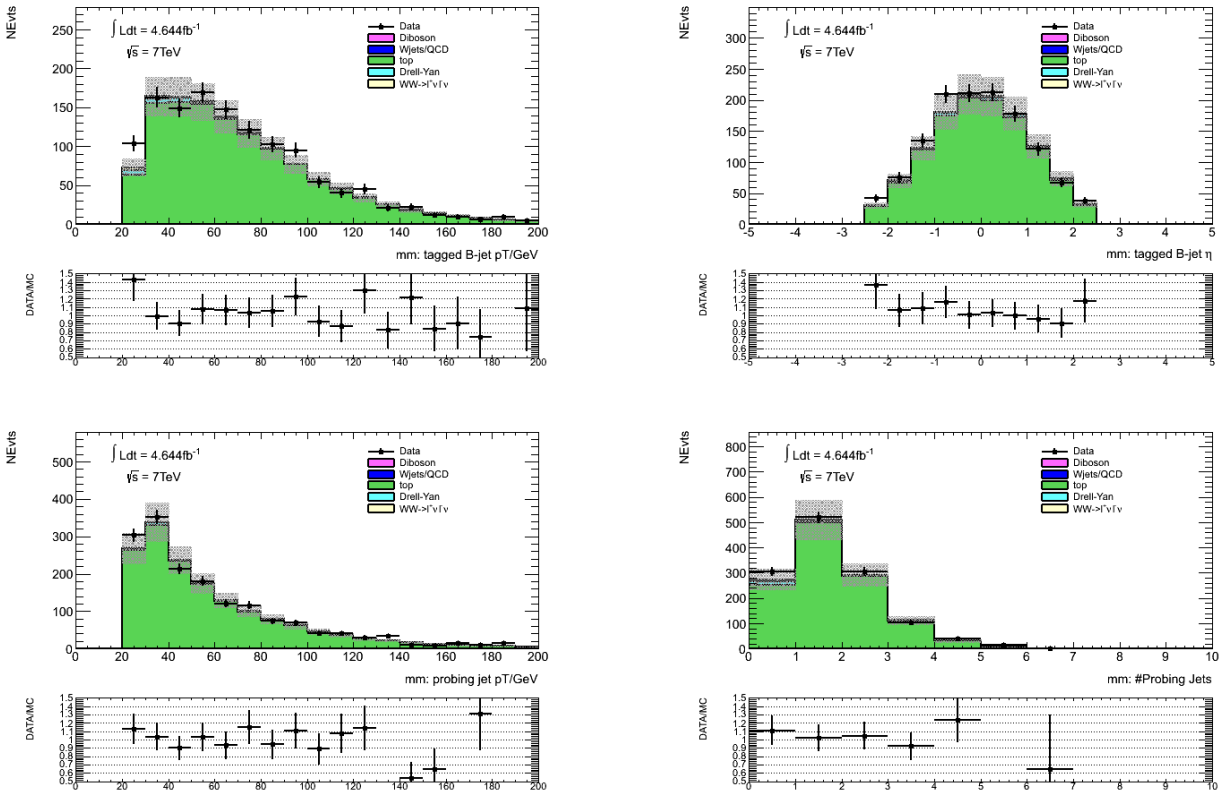

Figure 3.23 Same as Fig. 3.21 for the $\mu\mu$ channel.

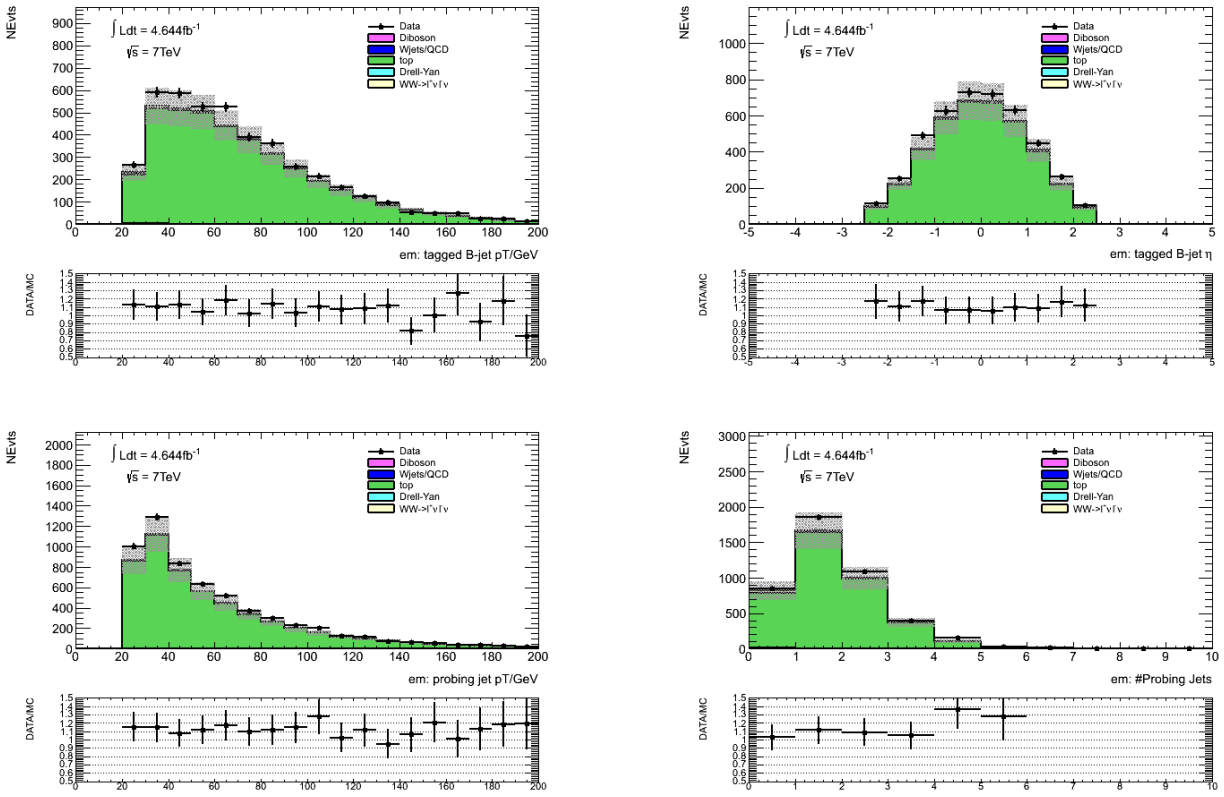

Figure 3.24 Same as Fig. 3.21 for the $e\mu$ channel.

region in data, P_2^{Data}, is estimated from

$$P_2^{\text{Data}} = \left(P_1^{\text{Btag,data}}\right)^2 \times \frac{P_2^{\text{MC}}}{\left(P_1^{\text{Btag,MC}}\right)^2}\,, \tag{3.8}$$

where P_2^{MC} and $P_1^{\text{Btag,MC}}$ are the corresponding quantities in MC. This full-jet veto efficiency P_2^{MC} is derived with the second control sample, which consists of two leptons and $E_{\text{T}}^{\text{miss}}$ with no restrictions on the number of jets (see Table 3.24),

$$P_2^{\text{MC}} = \frac{N_{\text{Top}}^{\text{MC}}(\ell\ell + E_{\text{T}}^{\text{miss}}, 0j)}{N_{\text{Top}}^{\text{MC}}(\ell\ell + E_{\text{T}}^{\text{miss}})}\,, \tag{3.9}$$

with the numerator and the denominator being the number of top background events after the application of a full-jet veto and the total number of top background events without the application of any requirement on the jet multiplicity in the final state, respectively.

Table 3.24 Summary of observed data events and MC expected top and non-top background contributions for the second control sample (full preselection except for jet veto cuts applied) in the three channels and their combined results. The W+jet+QCD contribution is obtained by scaling the corresponding MC prediction with the ratio of the data-driven estimate after the 0-jet and $p_T(\ell\ell)$ cut over the MC prediction with the same cuts. The uncertainties of the non-top processes include both the statistical and systematic uncertainties added in quadrature according to Table 3.50 except for WW which is enlarged to correspond to the measured and NLO prediction cross section difference and for W+jet+QCD which includes both the uncertainties of the data-driven estimate and the uncertainties of the scaling.

Final State	ee Channel	$\mu\mu$ Channel	$e\mu$ Channel	combined
Observed Events	1398	2411	6586	10395
Top	828.7 ± 6.5	1366.1 ± 8.1	4454.8 ± 14.9	6649.7 ± 18.1
WW	167.1 ± 24.4	310.6 ± 45.3	1014.4 ± 148.0	1492.1 ± 217.6
W+jets+QCD	40.2 ± 22.7	14.7 ± 7.7	154.6 ± 71.3	210.9 ± 94.5
Z+jets	205.3 ± 81.0	534.2 ± 193.3	328.4 ± 151.4	1058.4 ± 300.3
Other diboson	34.4 ± 5.4	37.8 ± 4.3	115.8 ± 16.2	187.9 ± 24.9
Total non-top background	447.0 ± 87.8	897.3 ± 198.7	1613.2 ± 224.0	2949.4 ± 383.5

The estimated number of top background events in the signal region in data is

$$N_{\text{Top}}^{\text{Data}}(\ell\ell + E_{\text{T}}^{\text{miss}}, 0j) = N_{\text{Top}}^{\text{Data}}(\ell\ell + E_{\text{T}}^{\text{miss}}) \times P_2^{\text{Data}}\,, \tag{3.10}$$

where $N_{\rm Top}^{\rm Data}(\ell\ell + E_{\rm T}^{\rm miss}) = N_{\rm all}^{\rm Data} - N_{\rm all}^{\rm non-top}$ is the number of top background events observed in data in the second control sample after subtracting the non-top contribution. The non-top background contributions (about 24.5% for the dominant $e\mu$ channel and 28.4% for combined channels) are estimated based on either data driven methods (for W+jet and QCD) or MC predictions (for Z+jets, diboson and WW) shown in Table 3.24. The uncertainty of the WW process corresponds to an enlarged uncertainty of 15.4% covering the difference between the measured cross section value (51.9 pb) and that of the NLO prediction (44.7 pb). The W+jet+QCD contribution is obtained by scaling the corresponding MC prediction with the ratio of the data-driven estimate after the 0-jet and $p_T(\ell\ell)$ cut over the MC prediction with the same cuts. Its uncertainty includes both the uncertainties of the data-driven estimate (Table 3.50) and those involved in the scaling (Secs. 3.8.1 and 3.7.1). The uncertainties of the other processes are taken from Sec. 3.8.1. Table 3.25 summarises the results of the top background extraction. The number of top background events surviving the jet veto cut is estimated to be $161.9 \pm 11.1(\text{stat}) \pm 26.2(\text{syst})$, to be compared with the corresponding MC prediction of 159.5 ± 3.0. After the $p_T(\ell\ell)$ cut, the top background contributions are reduced to $150.1 \pm 10.7(\text{stat}) \pm 24.3(\text{syst})$ and 146.8 ± 2.9 in data and MC, respectively. The statistical uncertainty includes the error propagation of all relevant components

$$\frac{\delta N_{\rm Top}^{\rm Data}}{N_{\rm Top}^{\rm Data}} = \frac{\delta N_{\rm all}^{\rm Data}}{N_{\rm all}^{\rm Data} - N_{\rm all}^{\rm non-top}} \oplus \frac{\delta N_{\rm all}^{\rm non-top}}{N_{\rm all}^{\rm Data} - N_{\rm all}^{\rm non-top}} \oplus 2 \times \frac{\delta P_1^{\rm Btag,data}}{P_1^{\rm Btag,data}} \oplus \frac{\delta\left(\frac{P_2^{\rm MC}}{(P_1^{\rm Btag,MC})^2}\right)}{\frac{P_2^{\rm MC}}{(P_1^{\rm Btag,MC})^2}}. \qquad (3.11)$$

The uncertainties of all these terms are shown explicitly in Table 3.25. Numerically, the dominant contribution in the statistical uncertainty is from the third term which is $2 \times 1.7\%$. The other terms contribute 1.3%, 1.0% and 2.4% for the first, second and last terms, respectively (taking the combined channels as an example). Note that the second term, corresponding to the uncertainty of the non-top background subtraction, includes both statistical and systematic components. For simplicity, its uncertainty is included in the statistical part of the top estimate.

The dominant systematic uncertainties considered are listed below.

- The jet energy scale (JES) and resolution (JER) are varied following the recommendation of the Jet Etmiss working group with an upward and downward relative variation of +2.1%, −0.9% for

Table 3.25 Summary of results for the jet veto efficiencies used for the prediction of the number of top background events after the application of the jet cut. For each channel, the top (bottom) line corresponds to the result before (after) the final $p_T(\ell\ell)$ cut in the signal region (see text). When there are two errors shown, the first is statistical and the second systematic.

Channel	$P_1^{\mathrm{Btag,data}}$	$P_2^{\mathrm{MC}}/(P_1^{\mathrm{Btag,MC}})^2$	$N_{\mathrm{Top}}^{\mathrm{Data}}(\ell\ell + E_{\mathrm{T}}^{\mathrm{miss}})$	$N_{\mathrm{Top}}^{\mathrm{Data}}(\ell\ell + E_{\mathrm{T}}^{\mathrm{miss}}, 0j)$	$N_{\mathrm{Top}}^{\mathrm{MC}}(\ell\ell + E_{\mathrm{T}}^{\mathrm{miss}}, 0j)$
all	0.194 ± 0.005	0.580 ± 0.012	7445.6 ± 396.8	$161.9 \pm 11.1 \pm 26.2$ $150.1 \pm 10.7 \pm 24.3$	159.5 ± 3.0 146.8 ± 2.9
ee	0.190 ± 0.014	0.572 ± 0.030	951.0 ± 95.4	$19.7 \pm 3.1 \pm 3.2$ $19.0 \pm 3.2 \pm 3.1$	24.3 ± 1.2 23.3 ± 1.1
$\mu\mu$	0.225 ± 0.012	0.572 ± 0.025	1513.7 ± 204.7	$43.9 \pm 7.1 \pm 7.1$ $42.6 \pm 7.3 \pm 6.9$	34.7 ± 1.4 33.7 ± 1.4
$e\mu$	0.185 ± 0.006	0.583 ± 0.015	4972.8 ± 238.2	$99.1 \pm 7.1 \pm 16.1$ $88.5 \pm 7.1 \pm 14.3$	100.6 ± 2.4 89.8 ± 2.3

JES and +1.8%, +4.1% for JER on $P_2^{\mathrm{MC}}/(P_1^{\mathrm{Btag,MC}})^2$. The corresponding average variations are therefore ±1.5% and ±2.9%. The relatively small systematic effect can be understood because of the cancellation in the ratio.

- The uncertainties on the b-tagging yield an upward and downward relative variation of -4.8% and 4.8% on $P_2^{\mathrm{MC}}/(P_1^{\mathrm{Btag,MC}})^2$.

- Based on a closure test performed using a MC@NLO $t\bar{t}$ MC11c sample as the MC sample and two Powheg MC11c $t\bar{t}$ AFII samples as test samples, we found a relative shift of $(-0.03 \pm 4.3)\%$ (Powheg+Pythia) and $(-1.5 \pm 4.4)\%$ (Powheg+Jimmy) between the data-driven estimate and the corresponding MC prediction, where the uncertainty is statistical only. We conservatively take the largest shift as a parton shower related systematic uncertainty.

- To take into account possible missing contributions in our current top MC models (e.g. the missing interferences between $t\bar{t}$, single top and non-resonant $W^+W^-b\bar{b}$ in the region of the phase space of interest), we performed in [47] a detailed study on the stability of the ratio $P_2^{\mathrm{MC}}/(P_1^{\mathrm{Btag,MC}})^2$ of the inclusive processes of all $W^+W^-b\bar{b}$ final state in comparison with that of the $t\bar{t}$ process only using the MADGRAPH package in leading order (Table 3.26). Variations of the renormalization and factorization scales were made using MADGRAPH. The ratio sustains variations $\mathcal{O}(1\%)$, consistent with the statistics of the samples used. This is consistent with studies performed by

Table 3.26 Results [47] of jet veto survival probabilities calculated at parton level in leading order using the MADGRAPH package for inclusive $pp \to W^+W^-b\bar{b}$ processes compared with that for $t\bar{t}$ production only at 7 TeV center-of-mass energy. Results are shown for different values of the transverse momentum for the jet veto.

p_T^v	P_2	P_1^{Btag}	$(P_1^{\mathrm{Btag}})^2/P_2$	P_2	P_1^{Btag}	$(P_1^{\mathrm{Btag}})^2/P_2$
[GeV]	inclusive			$t\bar{t}$ only		
20.0	0.005	0.09	1.50	0.003	0.07	1.49
22.5	0.007	0.10	1.45	0.004	0.08	1.58
25.0	0.010	0.12	1.51	0.007	0.10	1.47
27.5	0.013	0.14	1.53	0.010	0.12	1.36
30.0	0.018	0.16	1.46	0.014	0.14	1.44
32.5	0.025	0.18	1.32	0.019	0.16	1.38
35.0	0.032	0.21	1.31	0.026	0.18	1.28
37.5	0.040	0.23	1.32	0.034	0.21	1.24
40.0	0.051	0.26	1.30	0.042	0.23	1.23

N. Kauer. It was felt that the scale variations, although indicative that they are expected to be small, may not be conservative enough. [1] Instead studies were performed on the stability of the ratio in a wide dynamic range of parton transverse momenta. We found the ratio is stable well within 15% for different values (varying between 20 GeV and 40 GeV) of the transverse momentum for the jet veto. We also checked the higher order and hadronisation effects on the ratio by comparing the LO calculation with the NLO implementation for the dominant $t\bar{t}$ process. A conservative uncertainty of 15% is assigned for all these theoretical uncertainties. [2]

- The data-driven top estimate represents the top background contribution after the 0-jet veto. The contribution after the $p_T(\ell\ell)$ cut is obtained by scaling the data-driven estimate with the corresponding top MC predictions.

[1] The Matrix Elements of $WWbb$ at NLO are now available, but are not yet public. In order to reduce the theoretical uncertainty one would have to calculate the change of the ratio when going from LO to NLO.

[2] Note that these uncertainties were derived using top samples with slightly different selection cuts than the one used in the current analysis. The main difference concerns the b-tagging efficiency which was assumed to be 60%. However we have checked that the P_1^{Btag}, because of its fractional ratio (see Eq. 3.7), depends only weakly on the b-tagging efficiency. Again, any residual difference is accounted for by the 1.5% uncertainty on the closure test performed using the exact analysis preselection and ATLAS MC samples. Also all other experimental systematic uncertainties listed above are evaluated under the current experimental conditions.

3.6.3.2 Alternative Template Method

The top-background contribution after full-jet veto (0-jet bin) can be estimated also with a simple template fitting method (further elaborated in [48]). This method gives a consistent result with the other method introduced in Section 3.6.3.1, both of which agree with the MC prediction given the uncertainties estimated.

In this method, three regions are considered for control sample definition. Signal Region 1 (SR1) contains events passing all the cuts in the cutflow presented in Table 3.13 up to the relative missing energy (MEtrel) cut and hence includes all jet multiplicities. Signal Region 2 (SR2) contains events passing all cuts. The Control Region (CR) is a subset of SR1 which contains the events having at least one b-tagged jet with $p_T > 20$ GeV. The Data/MC comparison plots for SR1 and CR are shown in Figure 3.25.

Method

The data-driven top contribution in SR1 is estimated by an extrapolation using the ratio estimated from MC from the b-tagged top CR in data with non-top contribution subtracted. A factor f is introduced to correct for the normalization of the non-top contribution in the CR as given in Equation 3.12. All the terms in Equation 3.12 represent jet multiplicities.

$$\text{Data-Driven Top}^{\text{SR1}} = \frac{\text{MC Top}^{\text{SR1}}}{\text{MC Top}^{\text{CR}}} \cdot \left(\text{Data}^{\text{CR}} - f \cdot \text{MC Non-Top}^{\text{CR}}\right) \tag{3.12}$$

The normalization factor f is also introduced to the non-top normalization in SR1 so that the value is obtained by fitting the data in SR1 with the sum of the data-driven top template of Equation 3.12 and the non-top jet multiplicity template scaled by f, as given in Equation 3.13. The non-top jet multiplicity template is built from MC, and the relative contributions of the different processes are set by their theoretical cross sections. The fit is done via a log-likelihood minimization.

$$\begin{aligned}\text{Data}^{\text{SR1}} &= \text{Data-Driven Top}^{\text{SR1}}(f) + f \cdot \text{MC Non-Top}^{\text{SR1}} \\ &= f \cdot \underbrace{\left(\text{MC Non-Top}^{\text{SR1}} - \frac{\text{MC Top}^{\text{SR1}}}{\text{MC Top}^{\text{CR}}} \cdot \text{MC Non-Top}^{\text{CR}}\right)}_{\text{f-dependent template}} + \underbrace{\frac{\text{MC Top}^{\text{SR1}}}{\text{MC Top}^{\text{CR}}} \cdot \text{Data}^{\text{CR}}}_{\text{f-independent template (fixed in the fit)}}\end{aligned} \tag{3.13}$$

Since SR1 is not yet the final stage of the signal selection, the output fit value only helps to provide the top background estimate in SR1 from the 0 jet bin entry, but before applying the $p_T^{\ell\ell}$ cut (SR2). The final top estimate in SR2 is obtained by scaling the SR1 top estimate with a $p_T^{\ell\ell}$ cut efficiency factor, which is calculated relatively to the $E_{\mathrm{T,\ Rel}}^{\mathrm{miss}}$ cut stage, predicted by top MC. This is illustrated by Equation 3.14.

$$\text{Top Estimate}^{\mathrm{SR2}}\,(\text{bin}\,0) = \text{Data-Driven Top}^{\mathrm{SR1}}(\text{bin}\,0) \cdot \frac{\text{MC Top}^{\mathrm{SR2}}(\text{bin}\,0)}{\text{MC Top}^{\mathrm{SR1}}(\text{bin}\,0)} \tag{3.14}$$

One thing that needs to be emphasized is that the parameter f is meant to correct for a possible difference of the non-top vs. top ratio in data and in MC. Although it could be interpreted as a step towards a simultaneous measurement of the top and non-top cross sections, this interpretation goes beyond the scope that the method we are describing. The only purpose of this method is to provide an estimate of the top contribution, and it is important to verify that the top estimate we obtain is correct.

Results

In order to define the control region, the MV1 85% working point algorithm [49] is used to select the p_T >20 GeV b-jets. The fitting result is $f = 1.07 \pm 0.03$ and shown in Figure 3.26.

Figure 3.27 (left) shows the MC top in the SR1 region together with the data-driven top template in this region, in which the fit output value f has been injected. The ratio of the data-driven top template over the MC top is shown on the right. The structure observed in the ratio distribution suggests that the shape of the jet multiplicity distribution is not well reproduced in Monte Carlo. [6]

The top background estimate in the SR1 region is taken from the data-driven top template. Its value is given in Table 3.27. Its ratio with respect to the Monte Carlo top is found to be 0.94. The cut efficiencies to go from the SR1 region to the SR2 region is 0.94, leading to a top background estimate after all cuts of 141.2 events.

Uncertainties

The absolute statistical uncertainty is calculated from the b-tagged CR data, scaled by the same MC ratio used to construct the top template using Equation 3.15. The relative statistical uncertainty

Table 3.27 Top background estimates in the SR1 region and cut efficiencies to extrapolate them from the SR1 to the SR2 region. The MC Top uncertainty is just statistical, the Data-driven Top Template uncertainty includes a 13% systematic uncertainty.

MC Top in SR1	159.8±16.4
Data-driven Top Template in SR1	150.2±31.7
Data-driven Top / MC Top	0.94±0.22
Cut Efficiency (SR1→SR2)	0.94

is obtained by dividing the result of Equation 3.15 with the data-driven top template in SR1. [6]

$$\sigma_{\text{stat}} = \frac{\text{MC Top}^{\text{SR1}}}{\text{MC Top}^{\text{CR}}} \cdot \sqrt{\text{Data}^{\text{CR}}} \tag{3.15}$$

With the 4.6 fb^{-1} 2011 pp collision data at $\sqrt{s} = 7$ TeV, the statistical uncertainty is 21.1% in the 0-jet bin. The inputs which are used in the statistical uncertainty calculation are documented in Table 3.28.

Table 3.28 Components used in the calculation of the statistical uncertainty.

MC Top in SR1	159.8
MC Top in CR	52.0
MC Top Ratio (SR1/CR)	3.07
MC Non-Top in CR	53.3
f	1.07
Data in CR	106
σ_{stat}	31.7
relative σ_{stat}	21.1

For the systematic uncertainties affecting this measurement of the top background the following procedures have been applied:

- The scale and resolution uncertainty of the lepton and jet energies. These are accessed by varying the corresponding quantity up and down by 1 σ using the ATLAS recommended object scale/resolution uncertainty. The $E_{\text{T}}^{\text{miss}}$ uncertainties are supposedly correlated to the object uncertainties as they are what the $E_{\text{T}}^{\text{miss}}$ are reconstructed from. The estimate obtained with the default $E_{\text{T}}^{\text{miss}}$ RefFinal value is compared with results obtained when the energies of the non-lepton contributions ($E_{\text{T}}^{\text{miss}}$ soft term scale and resolution) are varied. These uncertainties are orthogonal to the pile-up corrections applied in the JES systematic uncertainty, as these involve hard jets.

- The b-tagging weights associated to true $b-$, $c-$ and light-jets are varied within their uncertainties. Uncertainties are also assessed on Monte Carlo using different generators (MC@NLO versus PowHeg) and different hadronization and parton shower implementations (Pythia versus Herwig). The relative $c-$ and light-jet content in WW is also checked (MC@NLO versus Alpgen).

- theory uncertainties are assessed on the interference between single top and $t\bar{t}$, on the top scale and on the effect of initial/final state radiation.

Both the MC top templates (which enter the correction from the CR to the SR1) and the MC non-top templates (used to perform the non-top subtraction in the CR, and in the fit for f in the SR1) are varied accordingly to the variation w.r.t. each systematic source. The full procedure is repeated so that the final results with systematic variations are compared with the central result with the nominal estimate. The itemized systematic uncertainties are shown in Table 3.29. [48].

To test the robustness of our technique, a closure test is performed:
MC simulation is chosen to replace the the real data in SR1 and CR with the jet energy scaled down/up for the top background. The top background estimated in the SR1 and compared with the top yields predicted directly from MC with the jet energy is scaled down/up consistently. A variation of $-0.1\%/-4.6\%$ is observed for down/up variation. Using top MC with nominal JES, the top background estimate agrees with the Monte Carlo prediction within $+0.01\%$.

One of the limitations of this method is due to the poor statistics with 4.6 fb^{-1} data. Therefore, the technique is applied on the combined channels, from which the by-channel estimates are derived using the fractions predicted by MC, taking Table 3.16 as the reference. (15.84% for the ee-channel, 61.25% for the $e\mu$-channel and 22.90% for the $\mu\mu$-channel.) The statistical and systematic uncertainties between all channels are fully correlated. Overall this results in a relative systematic uncertainty of $\sim 13\%$. The final numbers of the top-background estimate are given in Table 3.30. [6]

Table 3.29 All systematic uncertainties. The systematic uncertainties that were specifically re-evaluated for the SM WW analysis are shown in boldface. [6]

	Systematic Uncertainty [%]	
1	Electron Energy Resolution	1
2	Electron Energy Scale	< 0.5
3	ID Muon Momentum Resolution	< 0.5
4	MS Muon Momentum Resolution	< 0.5
5	Muon Momentum Scale	< 0.5
6	Jet Energy Scale	**6**
7	Jet Energy Resolution	**6**
8	MEt Soft-term Scale	**4**
9	MEt Soft-term Resolution	**6**
10	True b-jet Weights	**6**
11	True c-jet Weights	**2**
12	True light-jet Weights	**9**
13	MC Generator	1
14	MC Parton Shower+Had.	3
15	c-jet/light-jet Content	< 0.5
16	Fit Error on f	**3**
17	Single Top-$t\bar{t}$ interference	**3**
18	Top Scale	**1**
19	Initial/Final State Radiation	**3**
TOTAL	Systematics	15
TOTAL	Statistics	21
TOTAL	Systematics + Statistics	26

Table 3.30 Data-driven top background estimates with data-driven template method. The first number states the expected number of events, the second the statistical uncertainty, the third number accounts for the systematic uncertainty. [6]

Channel	ee	$\mu\mu$	$e\mu$	Combined
N_{top}	$22.4 \pm 11.8 \pm 3.4$	$32.3 \pm 14.2 \pm 4.9$	$86.5 \pm 23.3 \pm 13.1$	$141.2 \pm 29.7 \pm 21.5$

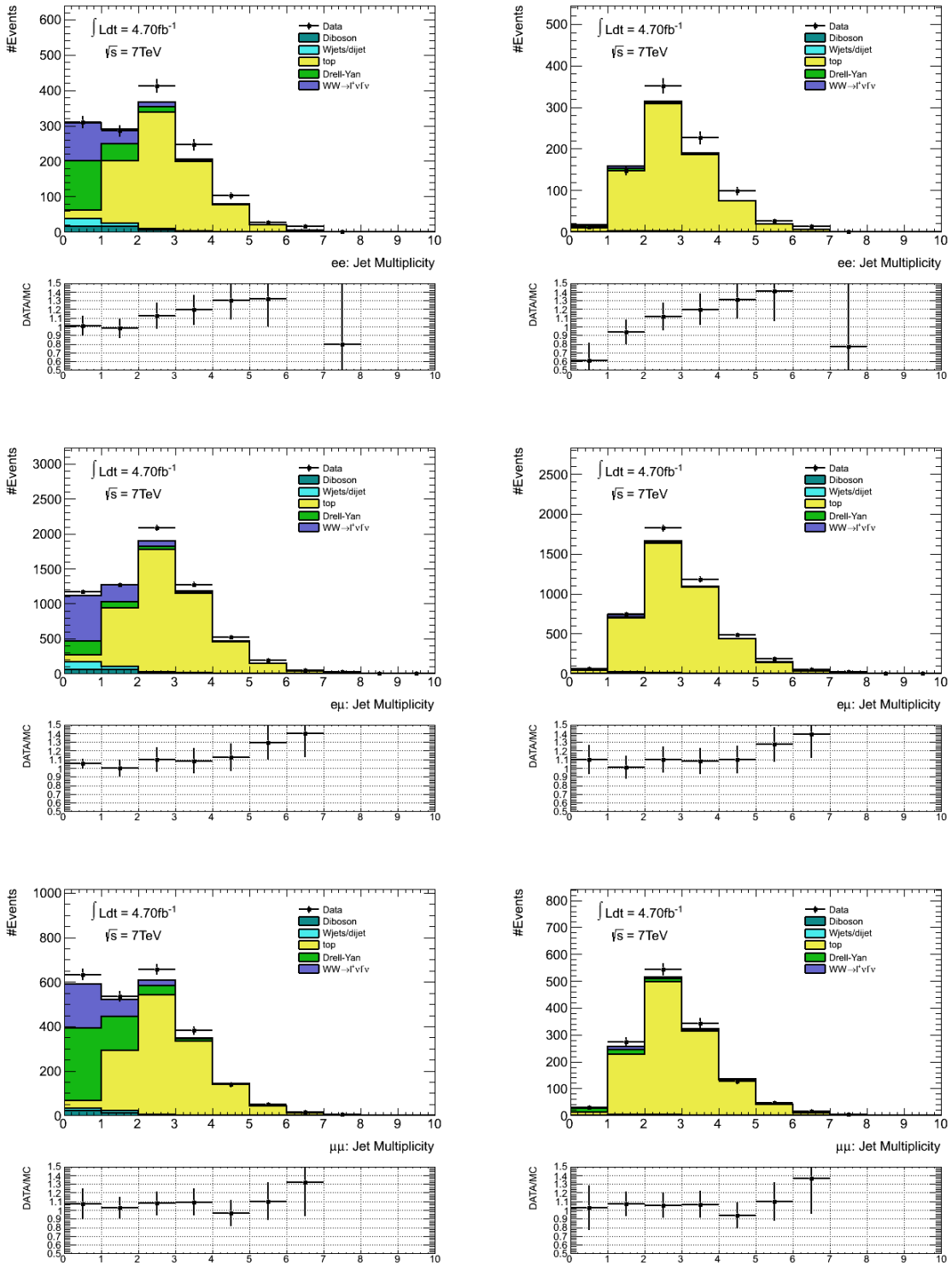

Figure 3.25 Monte Carlo and Data comparison plots for signal region SR1 (left) and control region CR (right) for the electron-electron channel (upper row), the electron-muon channel (middle row) and the muon-muon channel (lower row).

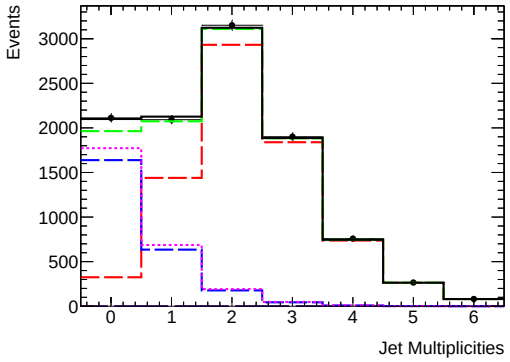

Figure 3.26 Result of the fit to determine the value of the parameter f. The black dots are data in the SR1 region, the red distribution corresponds to the f-independent term in Equation 3.13, the blue distribution corresponds to the f-dependent term, the green distribution is the sum of the red and blue distributions, the magenta distribution is the blue distribution corrected by the output fit value of f and the black solid line distribution is the sum of the red and magenta distributions. The last one should be compared to data. A good agreement is observed.

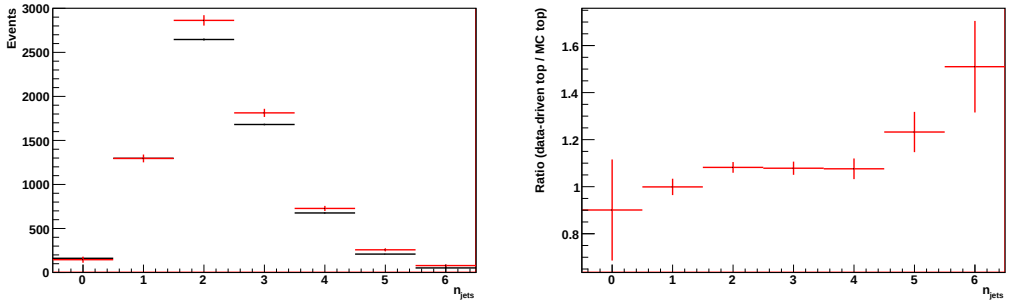

Figure 3.27 MC top (black) and data-driven top template (red) in the SR1 region (left) and their ratio (right).

3.6.4 Diboson background estimation

The contribution of background from other diboson processes including WZ, ZZ, $W\gamma$ and $W\gamma*$ is estimated directly from MC, which is normalised to the integrated luminosity of 4.6 fb^{-1}. The Zγ process is already included in Z+jets samples and hence not considered in our estimation so as to avoid duplication. The $W\gamma$ process is normalized using a $k-$factor derived from a comparison of data and MCFM [7] NLO calculation [50]. This yields a normalization of 1.50 ± 0.10, where the uncertainty is primarily due to the photon identification uncertainty.

As for the $W\gamma*$ contribution, $W\gamma* \to \tau\tau$ yields less than 0.1 event once the full jet veto is applied. A $k-$factor of 1.31 (1.43) for the ee ($\mu\mu$) channel is derived using the ratio between MCFM [7] NLO to MadGraph LO cross section. The factor for $e\mu$ channel is the average from ee and $\mu\mu$. A 16% systematic uncertainty is derived from the disagreement between LO MadGraph and MCFM [7] calculations.

The virtual photon in the internal conversion process generally has low mass, particularly when $\gamma^* \to ee$ and $\gamma^* \to \mu\mu$. This causes the kinematic distributions for $W\gamma$ and $W\gamma^*$ leptons, jets and missing E_T to be similar. A low mass boundary cut of the γ^* decayed di-lepton invariant mass is implemented at generator level for each $W\gamma^*$ MC samples so as to avoid the duplication between $W\gamma$ and $W\gamma^*$ MC samples. Although the number of $W\gamma$ MC events passing our selection is low, we observe similar distributions for the two backgrounds after the two lepton requirement. For this reason, we consider the $W\gamma$ analysis for a check on the MCFM [7] NLO calculation. There is a 2σ discrepancy between data and MCFM [7] determinations, which after accounting for known uncertainties suggests an additional 0.24 difference. This discrepancy may be due to higher order photon emission absent in the QCD NLO calculation, and we add it in quadrature to get a total uncertainy of 0.29 on the normalization.

The potential overlaps between the Herwig $W^{\pm}Z$ sample and $W\gamma*$ with high mass photons are effectively suppressed by a gauge boson mass cut of $M_Z > 20$ GeV pre-imeplemented in $W^{\pm}Z$ samples. This can be easily checked via looking at invariant mass distribution of the two leptons ($M_{\ell\ell}$) originating from the γ^* in the MadGraph samples. For the $\gamma^* \to ee$ case, 2.6% of events in the ee channel have $M_{\ell\ell} > 20$ GeV, while 5.4% do in the $e\mu$ channel. The fraction is substantially larger for $\gamma^* \to \mu\mu$ events. A total of 8.2% are in the $\mu\mu$ channel. The distribution giving the latter is shown in Figure 3.28. We

therefore correct the event yields in each channel down by these fractions.

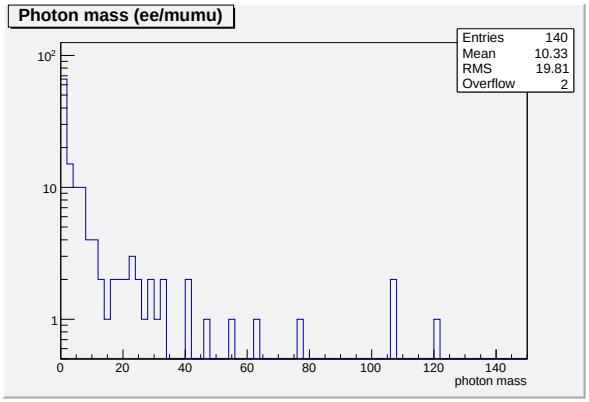

Figure 3.28 Distribution of γ^* mass in $W\gamma^* \to \ell\nu\mu\mu$ events after $\mu\mu$ kinematic selection.

The background yields and statistical uncertainties for diboson backgrounds are provided in Table 3.31. The various systematic uncertainties on these combined processes are listed in Table 3.32.

Final State	$e^+e^-E_{\mathrm{T}}^{\mathrm{miss}}$	$\mu^+\mu^-E_{\mathrm{T}}^{\mathrm{miss}}$	$e^\pm\mu^\mp E_{\mathrm{T}}^{\mathrm{miss}}$	Combined
diboson Background				
WZ	3.18±0.31	10.82±0.56	17.42±0.72	31.41±0.96
ZZ	3.43±0.32	6.93±0.48	1.17±0.26	11.53±0.63
Wγ	3.84±0.75	0±0	15.14±1.46	18.98±1.64
Wγ*	2.26±0.48	3.29±0.44	10.40±0.93	15.95±1.13
Total Background	12.70±0.99	21.04±0.86	44.12±1.89	77.87±2.30

Table 3.31 Other diboson background yields and their statistical uncertainties as determined from MC for 4.6 fb^{-1}. Scale factors for acceptance are applied.

3.6.5 Cosmic background estimation

Cosmic muons may very rarely mimic the WW signal processes in the di-muon channel by being reconstructed as one of the two different cases below:

1) two separate muons are reconstructed as if they were originating from the interaction region.

2) a single muon heading downwards, which has no good track in the upper part of the detector.

Such events with cosmic muons can fake the signal processes if a hadronic interaction overlaps with the cosmic muon.

			Uncertainties				±ΔN
	Lumi.	Cross-section*	Jets	Leptons	MET	Trigger	
ee	1.8%	8.6%	12.0%	3.5%	0.1%	0.1%	1.92
$\mu\mu$	1.8%	8.0%	7.8%	1.2%	0.4%	0.6%	2.34
$e\mu$	1.8%	9.8%	9.6%	2.3%	0.6%	0.4%	6.09
total	1.9%	9.1%	9.4%	1.9%	0.4%	0.4%	10.20

Table 3.32 Systematic uncertainties for the combined "other diboson" background processes (WZ, ZZ, $W\gamma$ and $W\gamma*$). Scale factors for acceptance are applied. * = includes seperate cross section uncertainties for WZ and ZZ (5%) vs. $W\gamma$ (7%) and $W\gamma^*$ (21%).

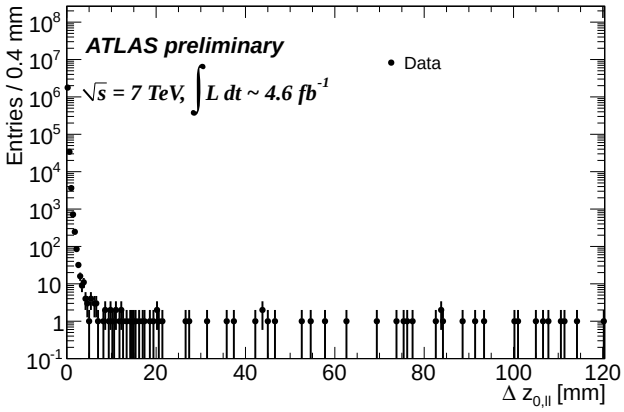

Figure 3.29 $\Delta z_0(\mu, l)$ after regular preselection in the cosmics control region with loosened vertexing cuts. The control region is in the range 20mm $< \Delta z_0(\mu, l) <$ 120mm

To estimate the cosmic muon background in signal region, a control sample is defined as events which pass the signal selection but with large difference in z-positions of the two leptons ($\Delta z_0(\mu, l) >$ 20mm). The $\Delta z_0(\mu, l)$ distribution in this control sample is show in Figure 3.29.

37 events with Δz_0 between 20mm and 120mm have been found in the control sample, And when extrapolating to $\Delta z_0 <$ 1mm, $<$ 0.4 cosmic muon events passing the the preselection is expected. Another significant reduction is expected from the stringent cut on the muon d_0.

This result shows that this type of cosmic background is marginal and can be ignored.

3.7 Systematics

3.7.1 Jet Veto Acceptance uncertainties

Due to the large Jet Energy Scale (JES) and Jet Energy Resolution (JER) uncertainties, the jet veto acceptance of the WW signal remains the biggest challenge for the precise measurement of the cross section, particularly when relying on the MC predictions. Therefore a data-driven technique has been introduced so as to reduce the uncertainty. A correction factor $\epsilon_Z^{data}/\epsilon_Z^{MC}$ ($\epsilon = N_{0\ jet}/N_{\geq 0\ jet}$) is derived from a Z-control sample by means of the formula:

$$\epsilon_{WW}^{predicted} = \epsilon_Z^{data} \frac{\epsilon_{WW}^{MC}}{\epsilon_Z^{MC}} \tag{3.16}$$

and applied to the WW signal acceptance after all selection. The Z-sample is selected in both MC and DATA by inverting the Z-veto cut in the nominal event selection. Thanks to the precise calibration of JES, large statistics and small background contamination in the Z-sample, the jet veto acceptance uncertainty is therefore expected to be reduced apart from the natural cancelation of the formula. Table 3.33 shows the numbers of events before and after the jet veto in the Z-samples and the WW MC.

Sample	$N_{0\ jet}$	$N_{\geq 0\ jet}$	ϵ^{0-jet}
$Z \to ee$ data	684941	897259	0.763
$Z \to ee$ MC	689237	864190	0.798
$Z \to \mu\mu$ data	1146369	1525398	0.752
$Z \to \mu\mu$ MC	1233586	1565715	0.788
$WW \to ee$ MC	109.667	168.154	0.652
$WW \to \mu\mu$ MC	204.956	313.015	0.655
$WW \to e\mu$ MC	676.708	1022.18	0.662

Table 3.33 The numbers of WW MC and Z data and MC events with and without the jet veto, and the corresponding jet veto acceptances ϵ^{0-jet}. The numbers correspond to an integrated luminosity of 4.6 fb^{-1}. [6]

We use the same MC generator to produce the Z samples that was used to produce the WW samples so that the jets are modelled similarly. For this reason, MC@NLO [9] Z samples were used. The ratio of WW to Z acceptances has small uncertainties from the jet energy scale due to differences

in the jet energy distributions and to the application of the missing E_T cut in WW events, which do not exist in the Z selection. Additional theoretical uncertainties on this ratio are due to the choices of factorisation and renormalisation scales, uncertainties on PDFs (Parton Density Functions) and the choice of parton showering model.

Statistical uncertainties on the veto acceptance are quite negligible(at per-mille level) benefiting from the Z-sample selection. The uncertainties due to JES and JER are determined by varying reconstructed jet energies and resolution by up and down by 1σ. Tables 3.34 and 3.35 show the corresponding $\pm 1\sigma$ acceptances of Z and WW MC respectively.

Variation	$Z \to ee$	$Z \to \mu\mu$
Nominal	0.798	0.788
JES $+1\sigma$	0.766	0.753
JES -1σ	0.824	0.816
JER $+1\sigma$	0.779	0.766

Table 3.34 The jet veto acceptances in Z MC channels due to $\pm 1\sigma$ changes in the jet energy scale (JES) and $+1\sigma$ change in the jet energy resolution (JER). [6]

Variation	$WW \to ee$	$WW \to \mu\mu$	$WW \to e\mu$
Nominal	0.652	0.655	0.662
JES $+1\sigma$	0.620	0.621	0.631
JES -1σ	0.682	0.683	0.691
JER $+1\sigma$	0.639	0.641	0.646

Table 3.35 The jet veto acceptances in WW MC channels due to $\pm 1\sigma$ changes in the jet energy scale (JES) and $+1\sigma$ change in the jet energy resolution (JER). [6]

Theoretical part of the jet veto acceptance systematic uncertainties, which are mainly due to higher order corrections of perturbation theory were accessed by varying the factorisation and renormalisation scales at truth-level study using MC@NLO. The nominal scales were multiplied by factors of 2 and 1/2 (independently in the case of WW) and the maximum deviation from the nominal result was taken as the scale uncertainty with one scale in common between WW and Z samples. These jet veto acceptances are shown in Table 3.36.

As suggested in some previous public results [51], the scale uncertainty may be underestimated

μ_R	μ_F	ϵ_{WW}^{truth}	ϵ_{Z}^{truth}
μ_0	μ_0	0.728	0.862
$\mu_0/2$	$\mu_0/2$	0.715	0.856
$\mu_0/2$	$2\mu_0$	0.727	n/a
$2\mu_0$	$\mu_0/2$	0.729	n/a
$2\mu_0$	$2\mu_0$	0.737	0.867

Table 3.36 The jet veto acceptances in WW and Z truth-level MC@NLO samples, for the ee channel. The renormalisation scale μ_R and factorisation scale μ_F were varied by a factor of 2. [6]

in a jet-binned analysis due to the accidental cancellations with log terms introduced by restricting QCD radiation. Therefore, a refined strategy has been introduced using the Stewart-Tackmann (ST) method [52] based on the assumption that the inclusive jet-binned uncertainties are uncorrelated because of the difference in the structures of these perturbative series. Hence, regarding the uncertainty estimation, we introduce:

$$\frac{\delta\epsilon^2}{\epsilon^2} = \left(\frac{1-\epsilon}{\epsilon}\right)^2 \left(\frac{\delta\sigma_{total}^2}{\sigma_{total}^2} + \frac{\delta\sigma_{\geq 1}^2}{\sigma_{\geq 1}^2}\right) \tag{3.17}$$

ϵ stands for the jet veto acceptance while σ_{total} and $\sigma_{\geq 1}$ denote the inclusive and ≥ 1 jet binned cross sections, respectively.

To proceed the methodology, the MC@NLO generator is customized so that the renormalisation and factorisation scales can be varied independently in the Drell-Yan samples to guarantee the consistency when making the ratios between WW and Z samples as well as to avoid the case when the opposite variations of the two scales occur simultaneously, which may cause a large mismatch in the scales. The results summarized in Table 3.37 compares the three different approaches with the old and the new method. The itemized scale uncertainties are documented in Table 3.38.

The PDF uncertainty is quoted from the difference between the estimations using the CT10 samples and MSTW2008NLO samples The final results of it are shown in Table 3.39 and the combined PDF uncertainty has a contribution of 0.93% to the ratio of jet veto acceptances.

The Parton Showering (PS) uncertainty was measured as the difference between POWHEG-BOX samples showered by Herwig and those by Pythia 6. The results of this study are shown in Table 3.40.

Method	$\delta\epsilon_{WW}^{truth}$	$\delta\epsilon_{Z}^{truth}$	$\delta(\epsilon_{WW}^{truth}/\epsilon_{Z}^{truth})$
Previous	1.8%	0.8%	1.0%
Naive	1.9%	0.8%	1.1%
ST	5.3%	2.4%	3.4%

Table 3.37 The scale uncertainty in the jet veto acceptances in WW and Z truth-level MC@NLO samples, for the ee channel. The renormalisation scale μ_R and factorisation scale μ_F were varied by a factor of 2. The previous method uses the old samples and method (see Table 3.36). The naive method uses the new samples, but the old method. And the ST method uses the new samples and the Stewart-Tackmann method. [6]

μ_R	μ_F	$\delta\sigma_{\geq 0\ jet}^{WW}$	$\delta\sigma_{\geq 1\ jet}^{WW}$	$\delta\epsilon^{WW}$	$\delta\sigma_{\geq 0\ jet}^{Z}$	$\delta\sigma_{\geq 1\ jet}^{Z}$	$\delta\epsilon^{Z}$	$\delta(\epsilon^{WW}/\epsilon^{Z})$
$\mu_0/2$	$\mu_0/2$	6.3%	11.4%	-4.9%	6.6%	11.7%	-2.2%	-2.7%
$\mu_0/2$	μ_0	-1.5%	0.6%	-0.6%	-4.0%	-1.4%	-0.7%	0.1%
μ_0	$\mu_0/2$	8.4%	11.3%	-5.3%	10.4%	11.1%	-2.4%	-2.8%
$2\mu_0$	$2\mu_0$	-7.3%	-10.3%	4.7%	-4.1%	-7.2%	1.3%	3.4%
$2\mu_0$	μ_0	2.0%	0.5%	0.8%	3.1%	0.6%	0.5%	0.3%
μ_0	$2\mu_0$	-9.2%	-10.9%	5.3%	-7.7%	-9.3%	1.9%	3.4%

Table 3.38 The scale uncertainties in the inclusive jet cross sections in WW and Z truth-level MC@NLO samples. The scale uncertainties in the jet veto acceptances (ϵ) in WW and Z were calculated using Equation 3.17. The scale uncertainties in WW and Z production were assumed correlated in order to calculate the scale uncertainty in the ratio of their jet veto acceptances ($\delta(\epsilon^{WW}/\epsilon^{Z})$). The largest scale uncertainty in each quantity is what is used in Table 3.37. [6]

The PS uncertainty in the ratio of acceptances was found to be 0.14%.

Finally, the theoretical uncertainties in the jet veto acceptances for WW and Z production, and their ratio, are shown in Table 3.41.

The scale factor and predicted WW jet veto acceptance for each channel are summarized in Table 3.42 with corresponding uncertainties presented as well.

The contributions to C_{WW} and A_{WW} associated with the jet veto are

$$A_{WW}^{jet} = \frac{N_{0\ jet}^{WW}\,(\mathrm{MC,truth})}{N_{\geq 0\ jet}^{WW}\,(\mathrm{MC,truth})} \tag{3.18}$$

$$C_{WW}^{jet} = \frac{N_{0\ jet}^{WW}\,(\mathrm{MC,reco})}{N_{0\ jet}^{WW}\,(\mathrm{MC,truth})} \times \frac{\epsilon^{Z}\,(\mathrm{data,reco})}{\epsilon^{Z}\,(\mathrm{MC,reco})} \tag{3.19}$$

Variation	ϵ_{WW}^{truth}	ϵ_{Z}^{truth}	$\epsilon_{WW}^{truth}/\epsilon_{Z}^{truth}$
Nominal (CT10)	0.728	0.862	0.844
CT10 error sets	$0.728^{+0.004}_{-0.005}$	$0.862^{+0.0013}_{-0.0015}$	$0.844^{+0.003}_{-0.005}$
MSTW2008NLO	0.717	0.855	0.838

Table 3.39 The jet veto acceptances in WW and Z truth-level MC@NLO samples, for the ee channel. Acceptances are shown for CT10 and MSTW2008NLO PDF sets and uncertainties calculated using the CT10 PDF error sets are shown. [6]

Sample	ϵ_{WW}^{truth}	ϵ_{Z}^{truth}	$\epsilon_{WW}^{truth}/\epsilon_{Z}^{truth}$
POWHEG+Herwig	0.697	0.833	0.837
POWHEG+Pythia 6	0.701	0.836	0.838

Table 3.40 The jet veto acceptances in WW and Z truth-level POWHEG-BOX samples (matched to Herwig and Pythia 6), for the ee channel. [6]

Now quantities with (MC, truth) contain theoretical uncertainties, whilst quantities with (MC, reco) contain both JES/JER and theoretical uncertainties. It is clear from these two equations that C_{WW}^{jet} and A_{WW}^{jet} will contain the uncertainties described in Table 3.43. The theoretical uncertainties in each quantity are 2.6% (C_{WW}^{jet}), 5.6% (A_{WW}^{jet}) and 3.5% ($C_{WW}^{jet}A_{WW}^{jet}$). The quantitative values of the uncertainties for each channel are shown in Table 3.44. [6]

3.7.2 Lepton Systematics

The following systematic effects are accounted in lepton systematic studies:

- energy scale and resolution uncertaintues
- particle reconstruction and identification (e.g. 'loose++', 'medium++', 'tight++' for electrons)

Process	Scale	PDF	PS	Total
$\delta\epsilon_{WW}^{truth}$	5.3%	1.6%	0.5%	5.6%
$\delta\epsilon_{Z}^{truth}$	2.4%	0.8%	0.4%	2.6%
$\delta(\epsilon_{WW}^{truth}/\epsilon_{Z})$	3.4%	0.9%	0.14%	3.5%

Table 3.41 The composition of the theoretical uncertainties on the jet veto acceptance for WW and Z production, and their ratio. [6]

ee	SF	0.957 ± 0.04 (JES) ± 0.02 (JER) ± 0.02 (theory)
$\mu\mu$	SF	0.954 ± 0.04 (JES) ± 0.03 (JER) ± 0.02 (theory)
$e\mu$	SF	0.956 ± 0.04 (JES) ± 0.02 (JER) ± 0.02 (theory)
ee	$\epsilon_{WW}^{predicted}$	0.624 ± 0.007 (JES) ± 0.0016 (JER) ± 0.02 (theory)
$\mu\mu$	$\epsilon_{WW}^{predicted}$	0.625 ± 0.004 (JES) ± 0.003 (JER) ± 0.02 (theory)
$e\mu$	$\epsilon_{WW}^{predicted}$	0.633 ± 0.004 (JES) ± 0.002 (JER) ± 0.02 (theory)

Table 3.42 The scale factor and predicted WW jet veto acceptance (including scale factor) for each channel, with accompanying uncertainties. The $e\mu$ scale factor is calculated as the average of the two same-flavour scale factors. [6]

	JES/JER unc.	Theoretical unc.
C_{WW}^{jet}	$\delta(\epsilon_{WW}/\epsilon_Z)$	$\delta\epsilon_Z$
A_{WW}^{jet}	–	$\delta\epsilon_{WW}$
$C_{WW}^{jet}A_{WW}$	$\delta(\epsilon_{WW}/\epsilon_Z)$	$\delta(\epsilon_{WW}/\epsilon_Z)$

Table 3.43 The sources of uncertainty in the jet veto contributions to C_{WW}^{jet} and A_{WW}^{jet}. Note that due to correlations in the uncertainties, there will be partial cancellations when a ratio of WW to Z is taken. [6]

uncertainties

- electron trigger uncertainties

The systematics are quoted by varying independently the corresponding systematic term up and down by one σ, which is officially provided by combined performance (CP) groups of ATLAS. The energy related variations are propagated to $E_{\mathrm{T}}^{\mathrm{miss}}$.

3.7.3 Jet Systematics

The jet energy scale and resolution uncertainty estimation is based on the combined performance group recommendations. For the jet energy scale uncertainty estimation is similar to lepton scale systematic uncertainties, which is obtained by varying the nominal scaling parameters by $\pm 1\sigma$ (provided by CP groups). Jet energy resolution is usually different between data and MC due to the possible mismodeling. Following the performance group recommendation, no nominal smearing is applied. Instead, a gaussian-like oversmearing factor is introduced to implement an oversmearing on the original

ee channel	Reco.	Theory	Total	(Naive Values)
C_{WW}^{jet}	1.1%	2.6%	2.8%	(1.7%)
A_{WW}^{jet}	–	5.6%	5.6%	(2.5%)
$C_{WW}^{jet} A_{WW}^{jet}$	1.1%	3.5%	3.7%	(1.8%)
$\mu\mu$ channel	Reco.	Theory	Total	(Naive Values)
C_{WW}^{jet}	1.0%	2.6%	2.8%	(1.4%)
A_{WW}^{jet}	–	5.6%	5.6%	(2.5%)
$C_{WW}^{jet} A_{WW}^{jet}$	1.0%	3.5%	3.6%	(1.6%)
$e\mu$ channel	Reco.	Theory	Total	(Naive Values)
C_{WW}^{jet}	0.7%	2.6%	2.7%	(1.4%)
A_{WW}^{jet}	–	5.6%	5.6%	(2.5%)
$C_{WW}^{jet} A_{WW}^{jet}$	0.7%	3.5%	3.6%	(1.6%)

Table 3.44 The uncertainties in the jet veto contributions to C_{WW}^{jet} and A_{WW}^{jet}. We also show the values which would be obtained without following the Stewart-Tackman procedure under (Naive Values). [6]

jet energy as:

$$\sigma\pm, Jet_{MC} = \sqrt{(\sigma_{Data}^{Jet} \pm \Delta\sigma_{Data}^{Jet})^2 - (\sigma_{MC,Nominal}^{Jet})^2}.$$

All the jet-related systematic variations are propagated to $E_{\mathrm{T}}^{\mathrm{miss}}$ and thus lead to a recalculation of the $E_{\mathrm{T}}^{\mathrm{miss}}$ in order to account for the change of the quantity, from which $E_{\mathrm{T}}^{\mathrm{miss}}$ is supposed to be reconstructed.

The resulting relative uncertainties vs. jet-multiplicity-distribution is shown in Figure 3.30. The data-driven method for the estimation of the jet-veto acceptance (introduced in section 3.7.1) is used to calculate the central value in this analysis.

3.7.4 $E_{\mathrm{T}}^{\mathrm{miss}}$ Systematics

The $E_{\mathrm{T}}^{\mathrm{miss}}$ systematic uncertainties have 100% correlation with the lepton and jet energy related uncertainties as elaborated in the previous sections. In addition to this, there are two more inportant points that need to be noted carefully.

The $E_{\mathrm{T}}^{\mathrm{miss}}$ has its hard jet (jet with $p_T > 20$ GeV) term 100% correlated with the jet energy uncertainty variations but also has the soft term which has separate treatment using official soft term

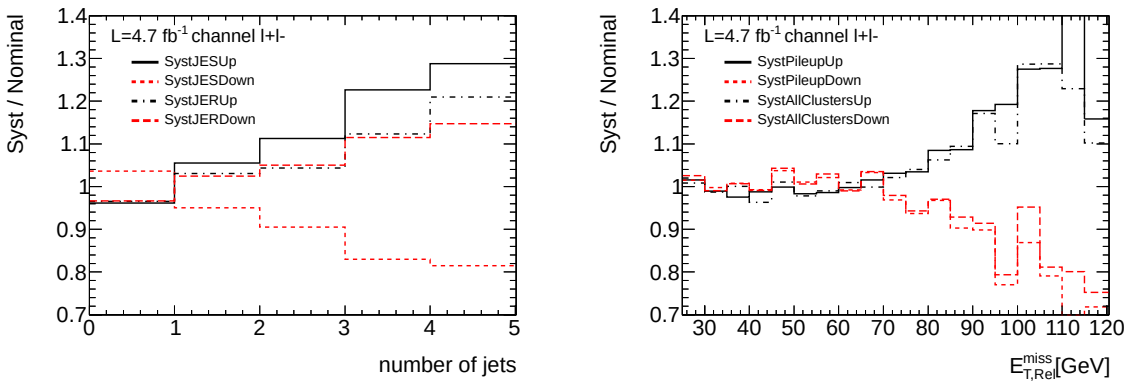

Figure 3.30 Relative systematic uncertainties vs. jet-multiplicity after cut on missing energy (left) and $E_{\mathrm{T}}^{\mathrm{miss}}$ (right) for jet-related and $E_{\mathrm{T}}^{\mathrm{miss}}$-related systematic effects. [6]

uncertainty to be added independently with the hard term uncertainties.

The $E_{\mathrm{T}}^{\mathrm{miss}}$ term in this analysis is based on the MET_RefFinal algorithm, which uses the AntiKt4LCTopo jets for $E_{\mathrm{T}}^{\mathrm{miss}}$ reconstruction but is therefore inconsistent with the jet category (AntiKt4TopoEM) used in the analysis. Hence, a compromised prescription is introduced to variate the quantities of AntiKt4LCTopo jets and propagate the correction quantities to $E_{\mathrm{T}}^{\mathrm{miss}}$ while keeping the AntiKt4TopoEM jets variate in the same direction when accessing the systematics. This is based on the assumption that the jet energy scale and resolution uncertainties are fully correlated and all the systematic variations of jets from two different categories should be variated up and down simultaneously.

3.7.5 Acceptance Uncertainties Due To PDF And Scale

The calculation of the total cross-section relies on the acceptance restricted by the phase-space definition. The nominal values of A_{WW}, C_{WW} and $\epsilon\mathcal{A}$ are calculated using the MC samples generated with MC@NLO generator and CT10 [8] NLO parton distribution function (PDF). In order to access the systematic uncertainties of the acceptance, the CT10 error matrices and the differences of the acceptance central value between CTEQ [8] and MSTW [23] are considered in the systematic variations. NNLO PDF uncertainties are not desired because of consistency of the NLO Parton Shower kernel of CT10 PDF set and NLO Matrix Element used in WW acceptance calculation.

The detailed strategies are broken down and elaborated as following:

- The uncertainty of the CT10 PDF set is obtained by following a standard procedure (recommended in the CTEQ manual). The symmetric uncertainty is favored after averaging the positive and negative uncertainties.

$$\sigma^{+} = \sigma^{-} = \frac{\sqrt{\sum_{i=0}^{N}[max(A_i - A_0, 0)]^2} + \sqrt{\sum_{i=0}^{N}[max(A_0 - A_i, 0)]^2}}{2A_0}, \tag{3.20}$$

  where A_0 is the WW acceptance evaluated at the central value of CT10 while A_i correspond to deviated central values with ± 1 *sigma* variations of the CTEQ eigen vectors applied. The acceptance of the other PDF set is evaluated by applying event-by-event PDF reweighting technique to

the 9 WW signal samples listed in Table 3.1. The gg fusion production is not accounted because of the negligible $\sim 3\%$ contribution to the total WW signal cross-section.

- The uncertainty between different PDF sets is estimated by comparing CT10 with the central MSTW 2008 NLO 68% CL PDF set.

For the inclusive channel, the uncertainty calculated from 52 CT10 error eigenvectors is 0.8%. The central value deviation from MSTW2008 NLO is 0.9%.The combined systematic uncertainty with quadratic sum is 1.2%. [6]

Additionally, some other systematic sources may come from the renormalisation (μ_R) and factorisation (μ_F) scale factor. The two scales are varied both "up" and "down" by a factor of 2 to so as to access the corresponding contributions to the acceptance uncertainties.

The PDF and scale factor uncertainties on A_{WW} and C_{WW} of each dilepton channel are summarised in Table 3.45 and 3.46, respectively. [6]

Channel	PDF	Scale	Combined
$e\nu e\nu$	0.85%	0.48%	0.98%
$\mu\nu\mu\nu$	0.93%	0.48%	1.05%
$e\nu\mu\nu$	0.88%	0.63%	1.08%

Table 3.45 Summary of the fractional theoretical uncertainties on A_{WW} due to PDF and scale of WW acceptance in each dilepton channels in MC@NLO samples. [6]

Channel	PDF	Scale	Combined
$e\nu e\nu$	0.17%	0.70%	0.72%
$\mu\nu\mu\nu$	0.17%	0.65%	0.67%
$e\nu\mu\nu$	0.14%	0.25%	0.29%

Table 3.46 Summary of the fractional theoretical uncertainties on C_{WW} due to PDF and scale of WW acceptance in each dilepton channels in MC@NLO samples. [6]

3.7.6 Summary of systematic uncertainties

The WW signal acceptance systematic uncertainty is given in Table 3.47 broken down into different the sources and each channel. The listed uncertainties with their values $\leq 0.1\%$ are labeled without

providing explicit value because the precision of the current statistical uncertainty is $\approx 0.1\%$.

The Jet-Veto has two components, one theoretical contribution affecting A_{WW} and one experimental contribution affecting C_{WW}. For the Jet-Veto uncertainty on the product $A_{WW}C_{WW}$, a reduced uncertainty applies due to cancellation (see Table 3.44).

The systematic error for the total cross-section measurement is calculated using error propagation:

$$\left(\frac{\Delta\epsilon\mathcal{A}}{\epsilon\mathcal{A}}\right)_{syst} = \sqrt{(\Delta A/A)^2 + (\Delta N_b/(N_{obs} - N_b))^2}.$$

Table 3.48 gives the systematical uncertainties in cross section measurements for three dilepton channels.

Sources	$e^+e^-E_{\mathrm{T}}^{\mathrm{miss}}$	$\mu^+\mu^-E_{\mathrm{T}}^{\mathrm{miss}}$	$e^\pm\mu^\mp E_{\mathrm{T}}^{\mathrm{miss}}$	Combined
Luminosity	1.8%	1.8%	1.8%	1.8%
A_{WW} uncertainties				
PDF	0.85%	0.93%	0.88%	0.88%
Scale (μ_R, μ_F)	0.48%	0.48%	0.63%	0.41%
Jet veto	5.60%	5.60%	5.60%	5.60%
$\Delta A_{WW}/A_{WW}$	5.68%	5.69%	5.70%	5.69%
C_{WW} uncertainties				
Trigger	0.1%	0.6%	0.3%	0.4%
Electron Scale	0.8%	$\leq$0.1%	0.4%	0.3%
Electron Resolution	0.2%	$\leq$0.1%	$\leq$0.1%	$\leq$0.1%
Muon Scale	$\leq$0.1%	0.5%	0.2%	0.2%
ID Muon Resolution	$\leq$0.1%	0.1%	$\leq$0.1%	$\leq$0.1%
MS Muon Resolution	$\leq$0.1%	0.1%	$\leq$0.1%	$\leq$0.1%
Electron recon. SF	1.6%	$\leq$0.1%	0.8%	0.7%
Electron ID SF	2.3%	$\leq$0.1%	1.1%	1.0%
Muon ID SF	$\leq$0.1%	0.5%	0.3%	0.3%
Electron IsoIP	0.7%	$\leq$0.1%	0.3%	0.3%
Muon IsoIP	$\leq$0.1%	0.4%	0.2%	0.2%
Scale Soft Terms	0.4%	0.2%	0.4%	0.2%
Reso Soft Terms	0.3%	0.1%	$\leq$0.1%	$\leq$0.1%
JES & JER	0.6%	0.5%	0.5%	0.5%
Jet veto scale factor	2.8%	2.8%	2.7%	2.8%
PDF and Scale	0.7%	0.7%	0.3%	0.3%
$\Delta C_{WW}/C_{WW}$	4.2%	3.1%	3.2%	3.2%
$A_{WW}C_{WW}$ uncertainties				
Jet veto scale factor	3.7%	3.6%	3.6%	3.6%
$\Delta C_{WW}A_{WW}/C_{WW}A_{WW}$	4.9%	4.0%	4.1%	4.0%
$\sigma(WW)$ theoretic uncertainty	6.2%	6.2%	6.2%	6.2%
Full WW signal estimation uncertainty	8.1%	7.6%	7.6%	7.6%

Table 3.47 Uncertainty sources and associated relative uncertainties for WW signal acceptance estimations for ee, $e\mu$ and $\mu\mu$ channels. The overall WW signal estimation uncertainties include additonal luminosity (1.8%) and total cross-section (6.2%) uncertainties. [6]

Sources	$e^+e^-E_{\mathrm{T}}^{\mathrm{miss}}$	$\mu^+\mu^-E_{\mathrm{T}}^{\mathrm{miss}}$	$e^{\pm}\mu^{\mp}E_{\mathrm{T}}^{\mathrm{miss}}$	Combined
Overall signal acceptence $\epsilon\mathcal{A}$	0.030	0.056	0.080	0.062
Fiducial acceptence A_{WW}	0.075	0.081	0.159	0.119
Acceptance correction factor C_{WW}	0.403	0.687	0.505	0.520
Signal acceptance uncertainty $(\Delta\epsilon\mathcal{A}/\epsilon\mathcal{A})$	4.9%	4.0%	4.1%	4.0%
Background uncertainty $\Delta N_b/(N_{obs} - N_b)$	16.8%	8.8%	7.2%	6.5%
$(\Delta\sigma/\sigma)_{syst}$	17.5%	9.7%	8.2%	7.6%

Table 3.48 Fractional systematic errors for three dilepton channels on total cross section measurements calculated from the signal acceptance uncertainties and background estimation uncertainties. [6]

3.8 Cross Section measurement results

After all the detailed studies and estimations in the previous sections, the WW production cross section is extracted from the observed WW candidates and signal and background estimates which have been presented. [6]

Once the fiducial phase space is defined in three channels, the coefficients A_{WW} and C_{WW} are defined as follows:

- A_{WW} denotes the acceptance for the WW decays under consideration, defined as the fraction of decays satisfying the geometrical and kinematic constraints at the generator level (fiducial acceptance). This quantity can only be determined from Monte-Carlo simulations. It is defined here after the decay leptons emit photons via QED final state radiation; photons within a $\Delta R < 0.1$ cone are added back to the decay leptons ("dressed" leptons).

- C_{WW} denotes the ratios between the total number of generated events which pass the final selection requirements after reconstruction and the total number of generated events within the fiducial acceptance. This corrections factor includes the efficiencies for triggering, reconstructing, and identifying the WW decays falling within the acceptance.

The fiducial cross-section is calculated by

$$\sigma_{WW}^{fiducial} = \frac{N_{obs} - N_{bkg}}{C_{WW}\,\mathcal{L}}$$

where N_{obs} is the number of observed events, N_{bkg} denotes the number of estimated background contributions in the signal region.

With those notations, the total cross-section can be presented as following:

$$\sigma_{WW}^{total} = \frac{N_{obs} - N_{bkg}}{\epsilon\mathcal{A}\,\mathcal{L}\;Br} = \frac{\sigma_{WW}^{fiducial}}{A_{WW}\;Br}$$

where $\epsilon\mathcal{A}$ was defined as the product of C_{WW} and A_{WW} and is discussed in Section 3.8.3. The final values and associated uncertainties of all the three variables are shown in Table 3.49.

	$e\nu e\nu$	$\mu\nu\mu\nu$	$e\nu\mu\nu$	Combined
A_{WW}	$0.075 \pm 0.001 \pm 0.0020$	$0.081 \pm 0.001 \pm 0.0022$	$0.159 \pm 0.001 \pm 0.0043$	$0.119 \pm 0.001 \pm 0.0032$
PDF (uncertainty)	0.85%	0.93%	0.88%	0.88%
Scale (uncertainty)	0.48%	0.48%	0.63%	0.41%
Jet-Veto	5.60%	5.60%	5.60%	5.60%
Combined $\Delta A_{WW}/A_{WW}$	5.68%	5.69%	5.70%	5.69%
C_{WW}	$0.403 \pm 0.005 \pm 0.017$	$0.687 \pm 0.005 \pm 0.021$	$0.505 \pm 0.002 \pm 0.016$	$0.520 \pm 0.002 \pm 0.017$
Combined $\Delta C_{WW}/C_{WW}$	4.2%	3.1%	3.2%	3.2%
$A_{WW} \times C_{WW} = \epsilon\mathcal{A}$	$0.030 \pm 0.001 \pm 0.001$	$0.056 \pm 0.001 \pm 0.002$	$0.080 \pm 0.001 \pm 0.003$	$0.062 \pm 0.001 \pm 0.002$
$\Delta\epsilon\mathcal{A}/\epsilon\mathcal{A}$	4.9%	4.0%	4.1%	4.0%

Table 3.49 The WW overall acceptance $A_{WW} \times C_{WW}$, fiducial phase space acceptance A_{WW} and correction factor C_{WW} and their uncertainties. The first errors are statistical and the second errors represent systematic uncertainties.

3.8.1 Observed WW candidates and MC expectations

As elaborated in Section 3.5.8 and 3.6.4, WW signal and other diboson backgrounds are estimated from MC predictions. The normalization is done according to the SM cross-section and total integrated luminosity of 4.6 fb^{-1}. The overall WW signal acceptance ($\epsilon = A_{WW} \times C_{WW}$) is written as:

$$\epsilon = \frac{N_{MC\ WW\to\ell^+\nu\ell^-\nu}(pass\ all\ the\ selection\ cuts)}{N_{MC\ WW\to\ell^+\nu\ell^-\nu}(Total)}, \quad \ell = e,\ \mu, \tau.$$

The Top, the Drell-Yan and W+jets background processes are estimated using data-driven methods. The detailed procedures are elaborated in Section 3.6.

The number of WW candidate observed in data and the yields of signal and background events estimated after applying all the selections in three pure leptonic decay channels are shown in Table 3.50 with the associated statistical (first) and systematic (second) uncertainties shown accordingly. The overall systematic uncertainties of WW signal are estimated using MC simulation. The combined top background systematic uncertainty is the linear sum of the three dilepton channel top systematics because the major uncertainties due to JES/JER and b-tagging are correlated. The combined systematic uncertainty for W+jets is the linear sum of $\sqrt{\sigma_{ee}^2 + \sigma_{\mu\mu}^2}$ and $\sigma_{e\mu}$, since the e and μ fake rates used to estimate the W+jet background were determined independently. The same combination approach applies to the Drell-Yan systematic uncertainties. The total "other diboson" systematic uncertainty is the linear sum of uncertainties from the three dilepton channels. Finally, the total systematic uncertainty is determined by the quadratic sum of top, W+jet and the linear sum of Drell-Yan and other

diboson background uncertainties.

Final State	$e^+e^-E_{\mathrm{T}}^{\mathrm{miss}}$	$\mu^+\mu^-E_{\mathrm{T}}^{\mathrm{miss}}$	$e^\pm\mu^\mp E_{\mathrm{T}}^{\mathrm{miss}}$	Combined
Observed Events	174	330	821	1325
Total expected events (S+B)	168.7±12.3±15.0	279.8±15.5±19.5	743.6±23.7±53.6	1192.1±30.9±82.2
MC WW Signal	100.3±1.5±8.1	185.5±2.0±14.1	537.8±3.4±40.9	823.6±4.2±63.1
Background estimations				
Top(data-driven)	22.4±11.8±3.4	32.3±14.2±4.9	86.5±23.3±13.1	141.2±29.7±21.5
W+jets(data-driven)	21.38±0.53±11.34	6.56±0.96±2.77	70.0±1.7±31.3	98.0±2.0±42.9
Z+jets (data-driven)	11.9±3.0±2.5	34.4±5.8±9.8	5.2±1.6±1.1	51.4±6.8±11.5
Other dibosons (MC)	12.70±0.99±1.92	21.04±0.86±2.33	44.14±1.89±6.09	77.88±2.30±10.20
Total Background	68.4±12.2±12.6	94.3±15.4±13.4	205.8±23.5±34.7	368.5±30.6±52.7
Significance (S / $\sqrt{B}$)	12.1	19.1	37.5	42.9

Table 3.50 Summary of observed events and expected signal and background contributions in three di-lepton and combined channels. The first error is statistical, the second systematic.

Given the current uncertainties, The observed data are consistent with the signal predicted by MC plus estimated backgrounds.

3.8.2 Measurement of the fiducial $WW \to \ell^+\nu\ell^-\nu$ production cross sections

WW fiducial cross-sections in all the three the three dilepton channels ($WW \to e\nu e\nu$, $\mu\nu\mu\nu$ and $e\nu\mu\nu$) are extracted by maximising the log-likelihood functions in Equation 3.21:

$$L(\sigma_{WW}^{fid}) = \ln \prod_{i=1}^{3} \frac{e^{-(N_s^i+N_b^i)} \times (N_s^i + N_b^i)^{N_{obs}^i}}{N_{obs}^i!},\ N_s^i = \sigma_{WW\to\ell\nu\ell\nu}^i \times \mathcal{L} \times C_{WW}^i \tag{3.21}$$

The indices $i = 1, 2, 3$ refer to each of the three dilepton channels. N_s^i, N_b^i and N_{obs}^i denote the expected signal, estimated backgrounds and observed candidates respectively for the i-th dilepton channel. $\mathcal{L}$ is the total integrated luminosity.

The detector resolution, efficiency and background corrections are accounted in the C_{WW} correction factor, which relate the WW event selection at reconstruction level to the truth-level phase space and hence can evaluate the fiducial cross-sections. Together with the fiducial phase space acceptance A_{WW}, the overall WW selection efficiency can be defined as:

$$\epsilon_{WW} \ = \ A_{WW} \ \times \ C_{WW}.$$

The definition of the WW fiducial phase space is driven by the motivation of minimising the extrapolation from the measured cross section to the theoretical cross section and meant to mimic the WW event selection at reconstruction level and hence accessible experimentally. The detailed definition is listed below:

- muon cuts: $p_{\mathrm{T}} > 20$ GeV, $|\eta| < 2.4$
- electron cuts: $p_{\mathrm{T}} > 20$ GeV, $|\eta| < 1.37$ or $1.52 < |\eta| < 2.47$
- jet cuts: $p_{\mathrm{T}} > 25$ GeV, $|y| < 4.5$, $\Delta R(e, \mathrm{jet}) > 0.3$, define with an Anti-KT-Algorithm (cone-size 0.4) on MCTruth level
- event cuts:
  - leading lepton $p_{\mathrm{T}} > 25$ GeV
  - $\mu\mu$ channel: $p_{\mathrm{T,Rel}}^{\nu+\bar{\nu}} > 45$ GeV, $m_{\mu\mu} > 15$ GeV and $|m_{\mu\mu} - m_{\mathrm{Z}}| > 15$ GeV
  - ee channel: $p_{\mathrm{T,Rel}}^{\nu+\bar{\nu}} > 45$ GeV, $m_{ee} > 15$ GeV and $|m_{ee} - m_{\mathrm{Z}}| > 15$ GeV
  - $e\mu$ channel: $p_{\mathrm{T,Rel}}^{\nu+\bar{\nu}} > 25$ GeV, $m_{e\mu} > 10$ GeV
  - $p_{\mathrm{T}}^{\ell\ell} > 30$ GeV

Events are required to contain two leptons and no jets satisfying the cuts defined above, in addition to satisfying the cuts on leptons and on neutrinos. $m_{\mathrm{Z}} = 91.187$ GeV and $p_{\mathrm{T,Rel}}^{\nu+\bar{\nu}}$ is defined similarly to $E_{\mathrm{T,\ Rel}}^{\mathrm{miss}}$, introduced in Section 3.4.4.

The total systematic uncertainties of A_{WW} are 2.7% in all three dilepton channels. The overall uncertainties include the PDF uncertainty (1.04% for ee, 1.08% for $\mu\mu$, and 1.04% for $e\mu$), the renormalisation and factorisation scale uncertainty (1.70% for ee, 2.22% for $\mu\mu$ and 1.30% for $e\mu$), and the parton shower/fragmentation modelling uncertainty of 1.4%. The MC scale uncertainty is accessed using MC simulation where the normalisation and the factorisation scales were changed to one half and twice of their nominal value. The systematic uncertainties are categorized and presented in Table 3.49 for each dilepton channel. [6]

The overall WW event selection efficiency can be written as $A_{WW} \times C_{WW}$. C_{WW} can be calculated once A_{WW} and the overall efficiencies are in place (see Table 3.49). The systematic uncertainties of C_{WW} are itemized and shown in Table 3.47. [6]

The remaining MC-based uncertainty affects dominantly to extrapolation from the fiducial to the full phase-space, i.e. the C_{WW} factor. The systematic uncertainty on C_{WW} related with changes in the normalisation and factorisation scales is 0.8% in the ee channel, 1.0% in the $\mu\mu$ channel, and 0.2% in the $e\mu$ channel. Taking all these uncertainties into account, the C_{WW} uncertainties are 3.4%, 1.8% and 1.8% for ee, $\mu\mu$ and $e\mu$ channels, respectively. [6]

As for the total cross section measurement, the evaluation of the systematic on $A_{WW} \times C_{WW}$ is demanded while the systematics on A_{WW} and C_{WW} partially overlap with each other.

Finally, the measured WW fiducial cross sections with associated uncertainties from C_{WW} and estimated backgrounds in three dilepton channels are summarized in Table 3.51 and compared with the MC predictions.

Channels	expected σ^{fid} (fb)	measured σ^{fid} (fb)	$\Delta\sigma_{stat}$ (fb)	$\Delta\sigma_{syst}$ (fb)	$\Delta\sigma_{lumi}$ (fb)
$e\nu e\nu$	54.6±4.1	56.4	± 6.8	± 9.8	± 1.0
$\mu\nu\mu\nu$	58.9±4.5	73.9	± 5.9	± 6.9	± 1.3
$e\nu\mu\nu$	231.4±19.9	262.3	± 12.3	± 20.7	± 4.7

Table 3.51 The predicted and measured fiducial WW production cross sections in three dilepton channels.

3.8.3 Measurement of the total WW production cross section

The total cross-section of the WW production is measured for all the three dilepton channels ($WW \to e\nu e\nu$, $\mu\nu\mu\nu$ and $e\nu\mu\nu$) by maximising the log-likelihood functions (Equation 3.22) :

$$L(\sigma_{WW}^{total}) = \ln \prod_{i=1}^{3} \frac{e^{-(N_s^i+N_b^i)} \times (N_s^i + N_b^i)^{N_{obs}^i}}{N_{obs}^i!}, \qquad N_s^i = \sigma_{WW}^{total} \times Br \times \mathcal{L} \times \epsilon_{WW}^i \tag{3.22}$$

The notations are same as Equation 3.21 while Br is the branching ratio of $WW \to \ell\nu\ell\nu$ (for each lepton flavor, which equals 0.108×0.108), The overall acceptance for each channel is represented by ϵ_{WW}^i, which is listed in Table 3.49 including the geometric and kinematic acceptances A_{WW} and the particle identification and event selection efficiencies C_{WW} in each channel. The overall efficiency in each of the three pure leptonic channels is shown in Table 3.14. [6]

By means of all the information of data and signal/background estimation shown in Table 3.50 and the overall acceptances ϵ^{i}_{WW} in all three purely leptonic decay channels, The measured total WW production cross sections [6] are determined after maximising the log-likelihood function shown in Equation 3.22 and finally the fitted results are summarized in Table 3.52. The mean values of the WW cross sections obtained from the likelihood fits are statistically consistent with the SM NLO prediction for WW production of $44.7^{+2.1}_{-1.9}$ pb. Combining the three dilepton channels, the measured total WW cross section is

$$51.9 \ \pm \ 2.0(stat) \ \pm \ 3.9(syst) \ \pm \ 0.93(lumi)pb.$$

The statistical uncertainty (3.9%) is determined from the likelihood fit, and the systematic uncertainty on the measurement is $\sim$ 7.6% including the signal acceptance uncertainty ($\sqrt{(\Delta A/A)^2 + (\Delta C/C)^2}$) of 4.0% and uncertainty of the background estimation ($\Delta N_{bkg}/(N_{obs} - N_{bkg})$) of 6.4%. The systematic error is calculated using error propagation as follows:

$$(\Delta\sigma/\sigma)_{syst} = \sqrt{((\Delta\epsilon_{WW}/\epsilon_{WW})^2 + (\Delta N_{bkg}/(N_{obs} - N_{bkg}))^2}.$$

To cross check the systematic uncertainties, the signal and background uncertainties are also included in the likelihood fitting program. The results obtained from the fitting program are within a few percent of the results obtained by error propagation described above. [6]

The luminosity uncertainty is 1.8%, which is officially recommended by the ATLAS collaboration and listed separately in the Table. Currently the overall uncertainty is dominated by the systematic uncertainty of 7.6% compared with the statistical uncertainty of 3.9%. [6]

Channels	Total cross-section (pb)	$\Delta\sigma_{stat}$(pb)	$\Delta\sigma_{syst}$(pb)	$\Delta\sigma_{lumi}$(pb)
$e\nu e\nu$	46.85	$\pm$ 5.65	$\pm$ 8.21	$\pm$ 0.84
$\mu\nu\mu\nu$	56.65	$\pm$ 4.52	$\pm$ 5.46	$\pm$ 1.02
$e\nu\mu\nu$	51.13	$\pm$ 2.41	$\pm$ 4.24	$\pm$ 0.92
Combined	51.91	$\pm$ 2.0	$\pm$ 3.92	$\pm$ 0.93

Table 3.52 The measured total WW production cross sections in three dilepton channels and in the combined channel.

Given the latest results of the discovery of a neutral Higgs-like boson with the mass 125 GeV, we estimated the SM Higgs event yields in our event selection to be 2.67±0.05, 6.72±0.07 and 16.22±0.11 for the $ee E_{\mathrm{T}}^{\mathrm{miss}}$, $\mu\mu E_{\mathrm{T}}^{\mathrm{miss}}$ and $e\mu E_{\mathrm{T}}^{\mathrm{miss}}$ channels, respectively. Conservatively for document purpose and a future reference, the total SM non-resonance WW production cross-section is measured to be 50.52±1.95±3.85±0.91 pb after subtracting the possible Higgs events in our data samples.

3.9 Differential cross section measurement

3.9.1 Motivation to measure differential distributions

To measure the differential distributions in WW leptonic decay channels is not only essential for the MC tuning in t- and s- channel but also gives the possibility for setting the limits of anomalous triple-gauge boson couplings on unfolded distributions in the future. As a result, the electroweak interactions of SM can be tested without detector effects such like limited resolution, efficiency and acceptance in the measurement. In this section, a first result of the differential distribution is obtained for the p_T spectrum of the leading lepton.

3.9.2 Generic methodology

The measured quantities are all subject to distortion and smearing effects due to detector coverage and resolutions. An unfolding technique can be used to derive the truth distributions based on the measured spectrum and known detector effects. Given the $f(x)$-distrubuted actual observable x and its corresponding experimental variable y distrubuted according to $g(y)$, Equation 3.23 shows the a generic relation between the two in a convolutional form by introducing a kernel $A(y,x)$ in the Fredholm integration.

$$\int A(y,x)f(x)\mathrm{d}x = g(y) \tag{3.23}$$

, where $f(x)$ and $g(y)$ stand for the probability density functions (p.d.f.) for x and y, respectively while $A(y,x)$ represents the detector response in the measurement. In reality, one would not possibly or necessarily know the the analytically paraterized form of $g(y)$ and $A(y,x)$. However, by means of the discrete distribution measured experimentally, one can transform the equation 3.23 into matrix form,

$$\mathbf{Ax} = \mathbf{y}. \tag{3.24}$$

The vector elements of $\mathbf{y}$ and $\mathbf{x}$ represent the histograms of measured quantities and true quantities respectively, which are connected by the response matrix elements a_{ij} interperated as the probability that a true value x_j is experimentally measured as y_i. $\mathbf{A}$ matrix can be possibly obtained using either

Monte Carlo simulations with particle-matter interactions and other detector responses accounted or directly the control regions defined in data.

There are in principle two typical methodologies to derive the true distribution out from a given spectrum measured in reality:

- *Smearing*: One may vary the true observable vector $\mathbf{x}$, while smearing the physics model parameters according actual detector effects, in order to approach the measured distribution which can match with the actual measured distribution $\mathbf{y}$ with the resoponse matrix $\mathbf{A}$.
- *Unfolding*: One can choose to invert the response matrix to get the measured true distribution using MC determined detector smearing by means of the formula $\mathbf{x} = \mathbf{A}^{-1}\mathbf{y}$.

Compared to smearing, unfolding method can not only help to test existing theory but also be flexible for the comparisons between various experiments and future theoretical models let alone, smearing will be potentially challenging a lot the computing resources resulting from the complexity of the detector systems and underlying theories which may evolve rapidly while smearing method generally requires additional MC productions in addtion to the nominal one and hence the detector simulation and event reconstruction of each MC phase space point would be unrealistically desired. We eventually favor the unfolding method for the differential distribution extraction with the following notations to be emphasized first:

- 1-D histograms and vectors in lower-case letters (e.g. $\mathbf{x}$, $\mathbf{y}$)
- 2-D histograms and matrices in upper-case letters (e.g. $\mathbf{A}$)
- Vectors and matrices both in Bold letters (e.g. $\mathbf{x}$, $\mathbf{A}$)
- Non-bold letters refer to scalars (e.g. τ)
- Letters with indices refer to either vector or matrix elements (e.g. x_j, A_{ij})
- Summation is indicated explicitly in the form such like $\sum_j A_{ij}x_j$ but not for regular repeated indices
- Covariance matrices shown as in the form of $\mathbf{V}(\mathbf{y})$ or $\mathbf{V}_y$) where $\mathbf{y}$ refers to a certain variable

The general methodologies of unfolding are elaborated literally in [53,54,55,56] while the actual strategy used in this analysis is illustrated in a brief and simplified way.

The simplest way to carry out this technique is to do the bin-by-bin unfolding. Given a measured vector from data $\mathbf{y^{data}}$, the corresponding unfolded results $\mathbf{x^{data}}$ is derived with the help a set of correction factors c_i as:

$$x_i^{data} = y_i^{data}/c_i \tag{3.25}$$

, where c_i is calculated using a control sample from data or MC simulation to represent the ratio between the observations and true values of a specific variable:

$$c_i = y_i^{sim}/x_i^{sim} \tag{3.26}$$

The simple bin-by-bin unfolding in principle works fine when the purity of each bin exceeds 80% so that the majority of reconstructed events correspond well to its true binning and the bin-to-bin migrations are mandatorily desired. Otherwise the unfolded results will be biased to the control sample from which the bin-by-bin corrections are derived. Therefore, in this analysis, we introduce the Bayesian unfolding technique [56] to provide the nominal value. Bayesian unfolding, as an iterative unfolding algorithm based on Bayes theorem, treat the response matrix as the probability of measuring a given the true distribution as a reconstructed observable. The corresponding probability distribution based on Bayesian theorem can be interpreted as:

$$P(\mathbf{x} \mid \mathbf{y}, \mathbf{A}, I) \propto P(\mathbf{y} \mid \mathbf{x}, \mathbf{A}, I) \cdot P(\mathbf{x} \mid I) \tag{3.27}$$

where, $\mathbf{x}$ refers to the true distribution, $\mathbf{y}$ stands for the observation, $\mathbf{A}$ represents the response matrix, I stands for the implicit underlying assumptions of the analysis. The probability distribution in Bayesian unfolding is broken down into two terms on the right, the first of which is the likelihood of observation from data while the second term represents the prior on the underlying truth distribution.

The first iteration consists of solving equation 3.27 above using the supplied Monte Carlo truth distribution as the prior distribution. For subsequent iterations, the result from the previous iteration is used as the prior. The more iterations that are run, the less the bias from the Monte Carlo truth

distribution becomes. However, at the same time, as the bias decreases, the statistical uncertainty increases, as statistical fluctuations are amplified due to the positive feedback nature of the system. Thus, the number of iterations serves to balance the strength of the bias with the size of the oscillations. In general, the number of iterations taken is small (roughly 10), as otherwise the statistical errors become very large.

The Bayesian unfolding technique has several advantages:

1) It only has one parameter, the number of iterations.

2) The machinery is fast enough for uncertainty estimation using toy MC and pseudo-experiments.

3) The prior distribution does not affect the results much, particularly for unfolding those rapidly falling distributions.

4) Already integrated with ROOT in the RooUnfold package and hence, technically very easy to use.

To proceed the methodology in reality, the following sets of parameters are extracted from MC signal samples:

- The response matrix **A** defined for the reconstructed events within the fiducial phase space at truth level so as to account for bin-to-bin migrations between the reconstructed and the truth distribution.

- The correction factors $c_i = \frac{N_i^{reco}}{N_i^{truth}}|_{\text{in fid.}}$ is defined as the ratio between of the number of reconstructed events N_i^{reco} and the number of MC truth events N_i^{truth} within the fiducial phase space at truth level to correct for the acceptance and selection efficiency losses due to reconstrution and binned based on the truth distribution.

- the fiducial factors $f_i = \frac{N_i^{\text{in fid.}}}{N_i}|_{\text{is reco.}}$ is introduced to represent and correct for the acceptance of fully reconstructed and selected events in truth fiducial region and binned based on the reconstructed distribution.

Taking all these parameters above into account, the unfolded distribution is then derived in the flowchart 3.31 and the formula below:

$$y_i = (d_i - b_i) \cdot f_i$$

$$x_i = (A^{-1}_{i,j} y_i) \cdot c_i$$

, where y_i and x_i stand for elements of the observed signal distribution and unfolded distribution connected by the response matrix $A_{i,j}$ and the correction factor c_i. Experimentally, the y_i is derived from the measured data d_i and estimated background b_i.

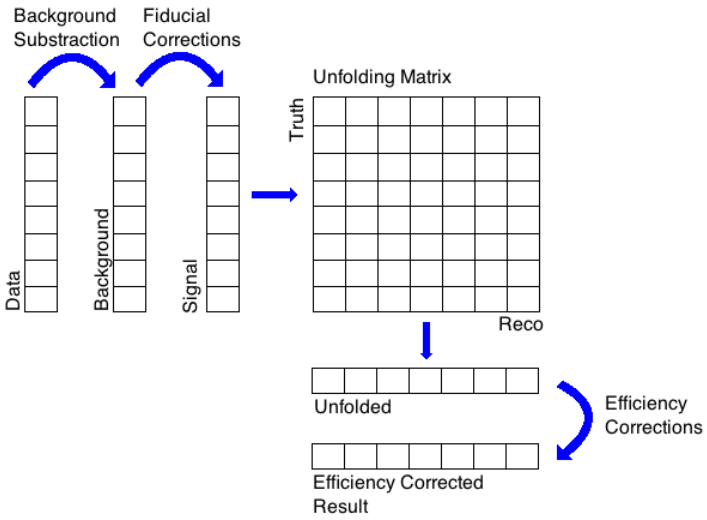

Figure 3.31 Pictoral description of the unfolding method for a distribution in a fiducial volume. [6]

3.9.3 Uncertainty estimation strategy

To access the statistical uncertainty of the unfolded distribution, a Toy-MC test is introduced. For each bin of the measured data distribution, the entry is varied with poisson fluctuation and the unfolding treatment elaborated aboved is implemented. The entire test is performed for 200 times and eventually the statistical uncertainty is taken from the RMS of the unfolded values x_i in each bin.

The systematic uncertainties are estimated from both the signal and background input distribution with the corresponding sytematic variations applied individually. i.e. for each systematic variation

(documented in 3.7.6), which can be further splitted into upwards and downwards variations of 1σ off its nominal value, such like the energy scale and resolution of jets and leptons and identification efficiencies, etc., the input MC distribution is remade and then used for the full unfolding process. The difference $\delta_i^{sys} = x_i - x_i^{sys}$ is then taken as the systematic uncertainty in each bin. The corresponding covariance matrix for bins i and j is defined by

$$\mathrm{Cov}_{i,j} = \delta_i^{sys} \times \delta_j^{sys}.$$

The several covariance matrices of all systematic uncertainties can be linearly added, which enables the definition of the global bin-by-bin correlation matrix $C_{i,j}$ via

$$C_{i,j} = \frac{\mathrm{Cov}_{i,j}}{\sqrt{\mathrm{Cov}_{i,i}}\sqrt{\mathrm{Cov}_{j,j}}}.$$

Additionally, in order to test the stability of unfolding, different iteration numbers, two (nominal) Vs three, are tested for the same Bayesian unfolding algorithm. The corresponding difference is then taken as the intrinsic systematic uncertainty of the unfolding stability.

3.9.4 Specific Situation in the WW analysis

To proceed the WWdifferential measurement of the leading lepton transverse momentum spectrum, the similar binning is chosen as the aTGC limit setting does:
$[0.0, 25., 40., 60., 80., 100., 120., 140., 350]$ GeV and the last bin has included all the candidates measured from real collision data without any extrapolation to larger phase-spaces. The major difference of binning is to merge the last three bins so as to reduce the the statistical uncertainties in the tail. The unfolded distributions are then normalzed to the unity, i.e. the measured quantities are $(1/\sigma_{fid})d\sigma_{fid}/dp_T^{lead}$.

As suggested by the normalization, the detector corrections do not impact the final result as long as they are independent from the unfolded variable, which is very much comprehensible taking 2-bin case for instance. And as a result of the normalization, the bin-by-bin correlation for the statistical uncertainties is therefore under control because the upwards fluctuation and downward fluctuation in

the other bin are always simultaneous. Hence, only shape-dependent systematic effects will impact the final results.

The purity, the response matrix and the corrections factors c_i of the p_T^{lead}distribution are shown in Figure 3.32 using the nominal SIGNAL NTUPLE. The bin-to-bin migration are restricted due to the high purities in all bins which are in general around 80%. The correction factors c_i ranging from 0.5 to 0.6 are flat w.r.t p_T^{lead}.

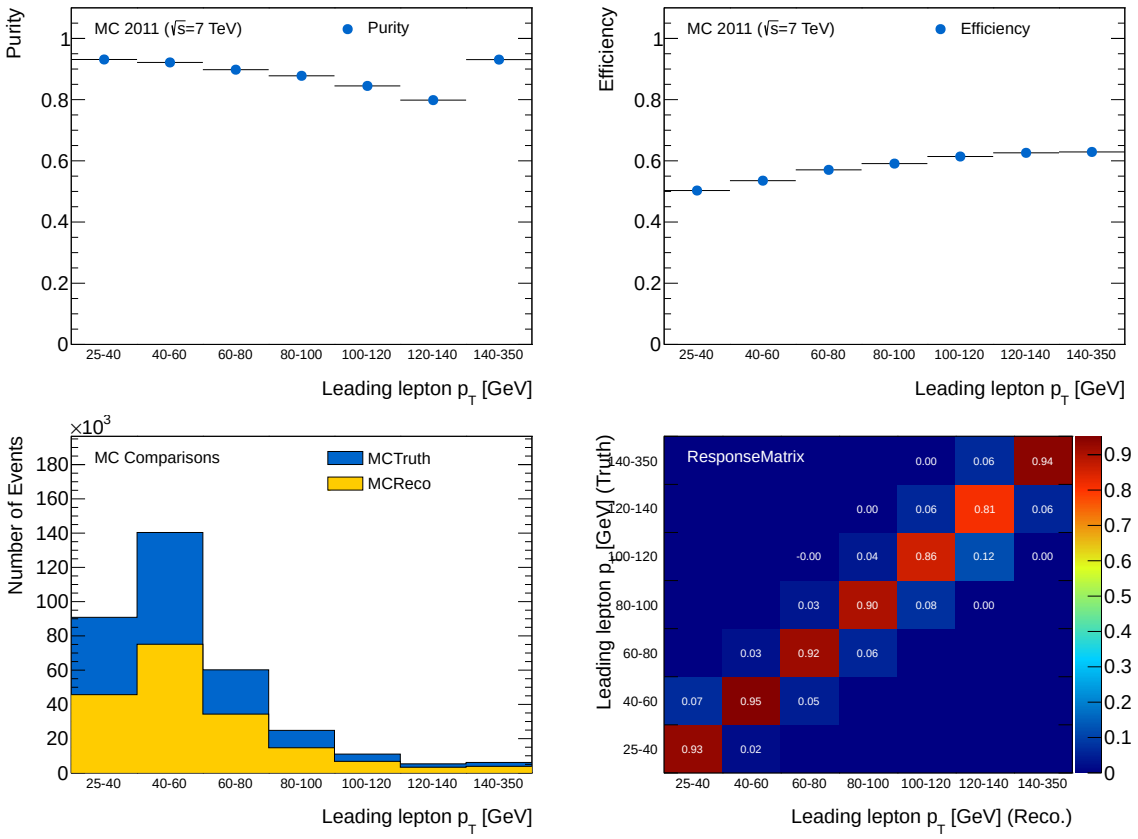

Figure 3.32 Shown are the purity distribution (upper left), the correction factors c_i (upper right), the truth and reconstruction MC distributions (bottom left) and the response matrix (bottom right) for the p_T^{lead}distribution. [6]

There are two MC closure tests performed so as to demonstrate the robustness of the unfolding procedure:

- The nominal SIGNAL NTUPLE is not only used to define the unfolding procedure but also chosen as the input signal distribution. The results shown in the distribution in Figure 3.33 are indicating

a good enough closure and certify that the unfolding is robust.

- A different MC generator file (HERWIG) is used as the signal Monte Carlo and the same procedure as for the nominal one is then applied in turn. An additional systematic uncertainty is quoted from the difference, which are summarized in Table 3.53.

The background systematics are treated as following:
The Monte Carlo predicted background shape had been smoothed with Function 3.28.

$$p_0 \times (1 + \sqrt{e^{\frac{-100}{x-25}} \times log(1 + e^{p_1 \times x})}) \tag{3.28}$$

The shape-uncertainties related to scale and resolution of leptons are based on MC studies. The total uncertainty of the predicted number of background events, which are mostly data-driven, has been used to scale the background-distribution up and down accordingly.
The similar procedure will also be used for the anomalous triple gauge coupling study.

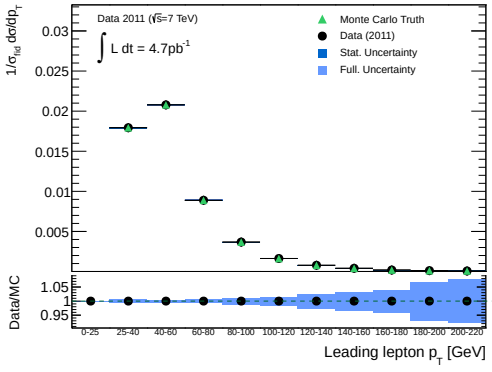

Figure 3.33 Result of closure test with nominal MC used as input for the p_T^{lead}distribution. [6]

3.9.5 Results

The input p_T^{lead} distributions of both data and background expectations used in the unfolding procedure are shown in Figure 3.34. The final unfolded distribution is shown and compared with the MC prediction with the nominal generator and the corresponding uncertainties are estimated in each bin. An additional comparison is also shown in Figure 3.35 with normalized reconstructed distribution prediced by MC and unfolding results so as to test the consistency. The good agreement of the shape distribution is verified, which is guaranteed by the small migration effects.

The corresponding numerical values and correlation matrices are shown in Tables 3.53 – 3.57. [6]

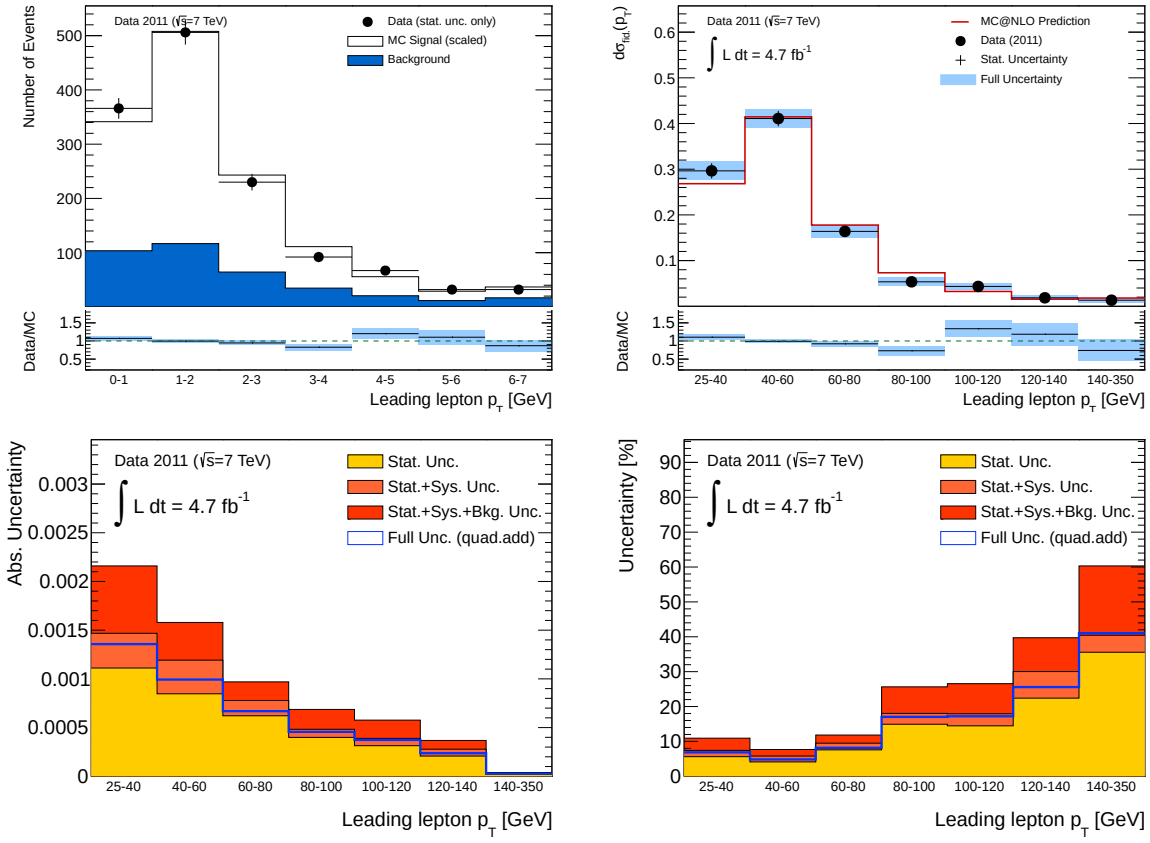

Figure 3.34 Data and background distributions which are unfolded (upper left), unfolded distribution and comparison with MC prediction (upper right), absolute errors (lower left), relative errors (lower right) for the p_T^{lead} distribution. [6]

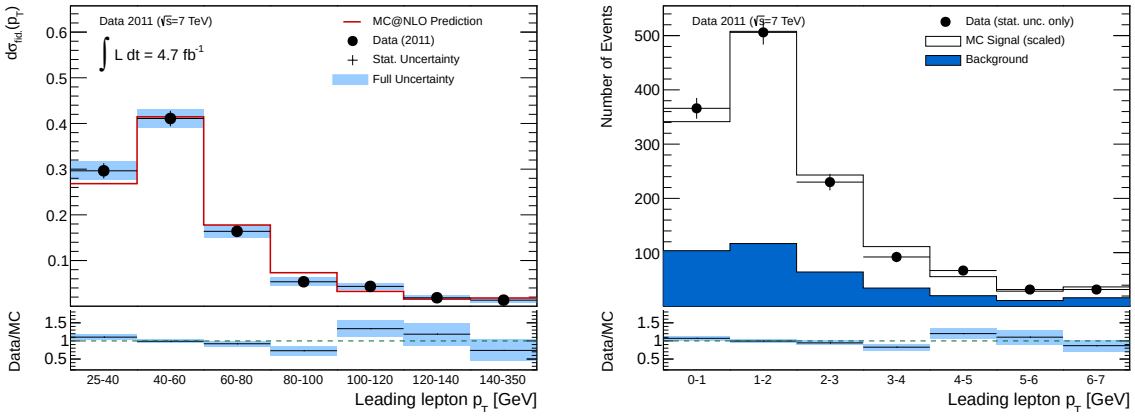

Figure 3.35 Unfolded distribution with all uncertainties (left) and comparison of MC prediction and data-signal distribution normalized (right) for the p_T^{lead} distribution. [6]

p_T^{lead} [GeV]	25 - 40	40 - 60	60 - 80	80 - 100	100 - 120	120 - 140	140 - 350
Bin	25 - 40	40 - 60	60 - 80	80 - 100	100 - 120	120 - 140	140 - 350
Bin Center	33.4586	50.1607	70.2366	89.1422	107.051	127.542	180.42
Results	0.2964	0.4109	0.163907	0.0535292	0.0434283	0.0185259	0.0133096
Results (div. by BinWidth)	0.01976	0.020545	0.00819533	0.00267646	0.00217142	0.000926297	6.33789e-05
Comb. Unc.	6.86%	4.83%	8.15%	17.0%	17.1%	25.5%	41.0%
Stat. Unc.	5.62%	4.12%	7.58%	14.9%	14.4%	22.4%	35.5%
Sys. Unc.	1.80%	1.68%	1.91%	3.11%	3.44%	7.62%	4.87%
Bkg. Unc.	3.50%	1.88%	2.33%	7.61%	8.63%	9.69%	19.8%
Stat. Unc. (MC)	0.40%	0.29%	0.50%	0.87%	1.13%	1.80%	1.75%
AlternativeUnfolding	0.11%	0.08%	0.31%	2.15%	1.92%	0.19%	1.08%
UniformPrior	1.14%	1.45%	1.06%	1.08%	1.45%	6.58%	2.50%
JES	0.41%	0.10%	0.64%	0.88%	0.28%	0.17%	0.20%
EScale	0.71%	0.06%	0.60%	0.44%	0.96%	1.99%	2.75%
ERes	0.07%	0.00%	0.39%	0.42%	1.02%	1.92%	0.55%
MEff	0.00%	0.00%	0.00%	0.00%	0.00%	0.00%	0.05%
MSSmear	0.00%	0.08%	0.40%	0.37%	0.58%	0.55%	1.30%
IDSmear	0.00%	0.06%	0.32%	0.32%	0.47%	0.42%	1.27%
METCluster	0.95%	0.74%	0.51%	0.78%	0.85%	1.68%	0.23%
JER	0.16%	0.07%	0.39%	0.63%	0.38%	0.16%	0.00%
METTool	0.00%	0.00%	0.29%	0.28%	0.54%	0.30%	0.91%
EEff	0.09%	0.00%	0.00%	0.08%	0.06%	0.11%	0.11%
EEffTrkID	0.00%	0.00%	0.00%	0.00%	0.05%	0.00%	0.06%
Trigger	0.00%	0.00%	0.00%	0.00%	0.00%	0.00%	0.00%
EIso	0.07%	0.00%	0.10%	0.12%	0.16%	0.15%	0.17%
METPileUp	0.22%	0.14%	0.34%	0.36%	0.63%	0.47%	0.54%
ResSoftTerms	0.09%	0.00%	0.43%	0.60%	0.28%	0.11%	0.70%
ScaleSoftTerms	0.23%	0.11%	0.37%	0.23%	0.67%	0.32%	0.49%
BkgTop	2.27%	1.09%	1.19%	6.09%	4.78%	7.62%	19.0%
BkgWJets	2.44%	0.84%	0.90%	0.48%	2.70%	1.93%	3.77%
BkgDrellYan	0.81%	0.11%	0.50%	0.33%	1.18%	1.49%	1.05%
Bkg	0.23%	0.28%	0.00%	0.44%	0.22%	0.17%	2.36%
BkgElectronScale	0.11%	0.38%	0.11%	1.80%	1.47%	2.48%	2.00%
BkgElectronRes	0.20%	0.43%	1.47%	2.96%	0.57%	1.40%	2.59%
BkgElectronEff	0.06%	0.00%	0.00%	0.10%	0.00%	0.14%	0.23%
BkgMuonScale	0.47%	0.39%	0.27%	0.00%	0.74%	3.02%	0.00%
BkgMuonRes	0.00%	0.06%	0.00%	1.09%	0.96%	0.22%	0.00%
BkgMuonEff	0.00%	0.00%	0.00%	0.00%	0.00%	0.00%	0.00%
BkgOthers	0.28%	1.01%	0.82%	2.63%	6.23%	3.52%	0.50%
Bayesian3	0.11%	0.08%	0.31%	2.15%	1.92%	0.19%	1.08%

Table 3.53 Unfolded results including uncertainties for the p_T^{lead} distribution, showing the central unfolded values and statistical, systematic and background uncertainties in summary as well as a detailed list of signal and background systematics. Also shown are uncertainties from applying the Bayesian unfolding algorithm with an additional iteration and the uncertainties from a closure test using a SM reweighed aTGC MC sample, rather than a SM MC sample. [6]

1						
-0.51	1					
-0.32	-0.32	1				
-0.22	-0.22	-0.04	1			
-0.18	-0.20	-0.07	0.085	1		
-0.07	-0.17	-0.09	-0.06	0.154	1	
-0.12	-0.10	-0.09	-0.02	-0.03	0.160	1

Table 3.54 Correlation matrix of statistical uncertainties for the p_T^{lead} distribution. Only half the elements are shown due to the symmetry of the matrix. [6]

1						
-0.72	1					
-0.02	-0.36	1				
0.275	-0.35	0.106	1			
-0.07	0.269	-0.26	-0.19	1		
0.617	-0.83	0.616	0.422	-0.25	1	
-0.58	0.498	0.210	0.020	0.165	-0.15	1

Table 3.55 Correlation matrix of systematic uncertainties for the p_T^{lead} distribution. Only half the elements are shown due to the symmetry of the matrix. [6]

1						
-0.05	1					
-0.62	-0.10	1				
-0.55	-0.59	0.088	1			
-0.55	-0.52	0.138	0.687	1		
-0.68	-0.57	0.451	0.775	0.703	1	
-0.75	-0.52	0.671	0.753	0.550	0.838	1

Table 3.56 Correlation matrix of Background uncertainties for the p_T^{lead} distribution. Only half the elements are shown due to the symmetry of the matrix. [6]

1						
-0.43	1					
-0.33	-0.29	1				
-0.27	-0.29	-0.01	1			
-0.27	-0.23	-0.04	0.210	1		
-0.13	-0.30	0.017	0.105	0.232	1	
-0.29	-0.15	0.025	0.143	0.113	0.269	1

Table 3.57 Correlation matrix of the combined uncertainties for the p_T^{lead} distribution. Only half the elements are shown due to the symmetry of the matrix. [6]

3.10 Anomalous TGC

The s-channel process of SM WW production includes the triple gauge boson couplings resulting from the non-Abelian nature of the $SU(2)_{\rm L} \times U(1)_{\rm Y}$ group symmetry of the SM. As introduced in 1.2, any anomalous triple-gauge boson couplings(aTGCs) will result in enhancing the WW production cross sections particularly at the high transverse momentum and high transverse mass regions. Therefore, by comparing the shape of these distributions with SM predictions will potentially provide a first sight of new physics signatures through aTGC. Therefore, precise measurements of the TGCs will not only provide a stringent test of the SM, but also a sensitive probe to new physics through anomalous couplings.

As an extension of the cross-section measurement of WW production, we probe the anomalous TGCs by examining the leading lepton transverse momentum spectrum with the selected $WW \rightarrow \ell\nu\ell\nu$ events. Technical details of how to extract the experimental constraints on anomalous TGCs are presented in this section.

3.10.1 Effective Lagrangian for charged TGCs

As mentioned in Section 1.2, The most general effective Lagrangian, that conserves C and P separately, for charged triple gauge boson interactions in 1.13 has included the TGC parameter as: g_1^V, k_V and λ_V and the SM triple gauge boson vertices can be recovered by requiring: $g_1^V = k_V = 1$ and $\lambda_V = 0$.

With non-SM coupling parameters, the amplitudes for gauge boson pair production grow with energy, eventually violating tree-level unitarity. The unitarity violation is avoided by introducing an effective cutoff scale,Λ. For charged anomalous TGCs we have used dipole form factors with a cutoff scale Λ. The anomalous couplings take a form, for example,

$$\Delta k(\hat{s}) = \frac{\Delta k}{(1 + \hat{s}/\Lambda^2)^2},$$

where $\sqrt{\hat{s}}$ is the invariant mass of the vector-boson pair and Δk is the coupling value in the low energy limit. Λ is the mass scale, above which the new phenomenon could be directly observed.

The effective Lagrangian could be interpreted depending on specified symmetry and the particle content of the low energy theory. There are three senarios, in which the effective Lagrangian is

interpreted conventionally, concerned in the following study.

- The LEP scenario (three free parameters)

  $\Delta k_\gamma = (\cos^2\theta_W / \sin^2\theta_W)(\Delta g_1^Z - \Delta k_Z), \quad \lambda_Z = \lambda_\gamma$

- The HISZ scenario [57] (two free parameters)

  $\Delta g_1^Z = \Delta k_Z/(\cos^2\theta_W - \sin^2\theta_W), \quad \Delta k_\gamma = 2\Delta k_Z \ \cos^2\theta_W/(\cos^2\theta_W - \sin^2\theta_W), \quad \lambda_Z = \lambda_\gamma$

- The equal couplings scenario (two free parameters)

  $\Delta k_Z = \Delta k_\gamma, \quad \lambda_Z = \lambda_\gamma, \quad \Delta g_1^Z = \Delta g_1^\gamma = 0$

In addition, one should note that different diboson final states of W^+W^-, $W^\pm Z$, and $W^\pm\gamma$ may have different sensitivities to different charged aTGC parameters which can be complementary to each other [58,59,60]. For example, W^+W^- production is supposedly more sensitive to Δk_V than $W^\pm Z$ and $W^\pm\gamma$ production are because the corresponding terms are proportional to $\hat{s}$ only in WW production. Likewise, $W^\pm Z$ production is expected to be more sensitive to Δg_1^Z due to the same reason. The λ-type anomalous couplings have a strong $\hat{s}$ dependence in all three cases. By combining different channels, the limits of all these parameters are prospectively getting more restrictive at the high centre-of-mass energy of the LHC than all the previous experiments.

3.10.2 Probing the Anomalous TGC Parameter Space Using A Re-weighting Method

BHO [58, 59, 60] is chosen to model the WW production cross sections with programmable input parameters and kinematics with the SM and anomalous couplings. The aTGC parameter space is probed using a re-weighting method, which is used to avoid generating overwhelmingly enormous MC samples in multi-dimentional anomalous coupling space.

For example, the MC event re-weighting factor is determined by differential cross section ratio (see the right plot of Figure 3.36):

$$Weight \quad = \quad \frac{d\sigma(non-SM)/dM_T(WW)}{d\sigma(SM)/dM_T(WW)}. \tag{3.29}$$

given the differential cross section of the WW transverse mass distribution in Figure 3.36 with the anomalous TGCs compared to the SM couplings in the same plot.

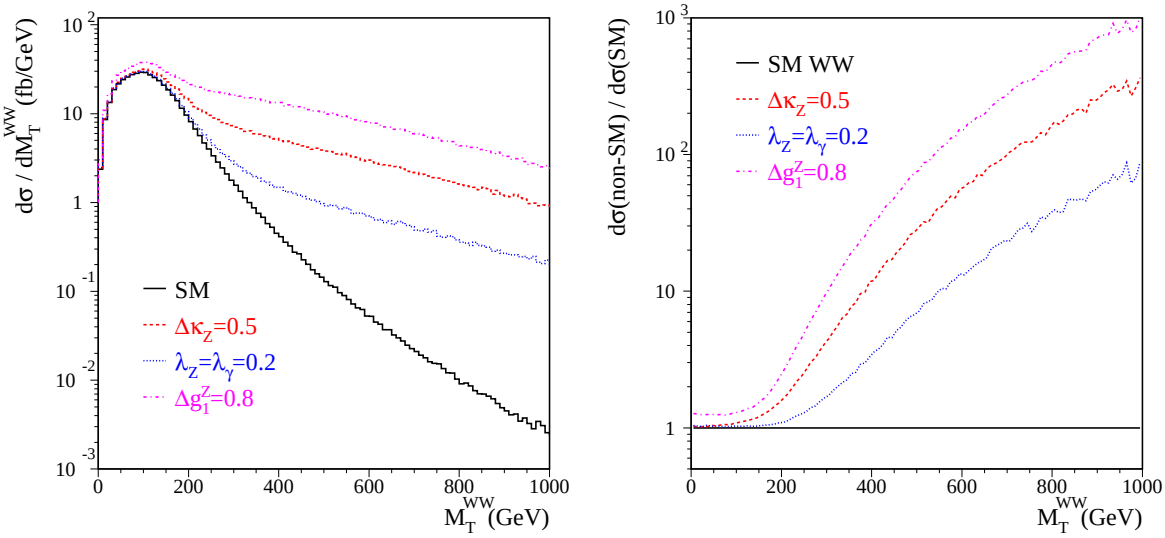

Figure 3.36 Left: WW transverse mass distribution, events are generated with the SM couplings(black) and the anomalous couplings(colour); Right: the corresponding differential cross section ratio, $d\sigma(non-SM)/d\sigma(SM)$. [6]

In this study a "Parametrised Re-weighting" method based on a small set of anomalous TGCs points is used.

WW cross sections have quadratic dependence on the anomalous couplings since the effective Lagrangian is a linear function of anomalous TGC parameters. Thus, only a few selected TGC points have to be used to determine the re-weighting functions to access all the anomalous TGCs by using these functions. Equation 3.30 shows the relation between the differential cross section with anomalous TGCs and the SM differential cross section:

$$d\sigma(non-SM) = const \times |M|^2_{SM} \frac{|M|^2}{|M|^2_{SM}} d\overrightarrow{X} = d\sigma(SM) \times R(\overrightarrow{X}; \Delta k_Z, \lambda_Z, \Delta g_1^Z, \Delta k_\gamma, \lambda_\gamma) \qquad (3.30)$$

where $d\sigma(non-SM)$ is the differential cross section which includes the anomalous couplings contribution, $d\sigma(SM)$ is the SM differential cross section. $\overrightarrow{X}$ is a set of kinematic variables sensitive to the anomalous couplings. $|M|^2$ and $|M|^2_{SM}$ are squared matrix elements with and without the anomalous couplings. The weight R represents the ratio of squared matrix elements $|M|^2/|M|^2_{SM}$ [61].

The LEP scenario contains three independent coupling parameters, and thus it has 9 re-weighting coefficients based on Eq. 3.30 as shown in Eq. 3.31, where A_1, B_1, C_1, D_1, E_1, F_1, G_1, H_1, I_1 are

coefficients to be determined in our TGC function. Similarly, the Equal Couplings and HISZ scenarios contain 5 re-weighting coefficients as shown in Eq. 3.32 and 3.33, respectively. Similar strategy is used to determine the coefficients from Equal Couplings scenario and for the HISZ scenario.

LEP scenario:

$$\begin{aligned} R(\overrightarrow{X};\Delta k,\lambda,\Delta g_1) =& 1 + A_1(\overrightarrow{X})\Delta k + B_1(\overrightarrow{X})\Delta k^2 + C_1(\overrightarrow{X})\lambda + D_1(\overrightarrow{X})\lambda^2 + \\ & E_1(\overrightarrow{X})\Delta g_1 + F_1(\overrightarrow{X})\Delta g_1^2 + G_1(\overrightarrow{X})\Delta k\lambda + H_1(\overrightarrow{X})\Delta k\Delta g_1 + I_1(\overrightarrow{X})\lambda\Delta g_1 \end{aligned} \tag{3.31}$$

Equal couplings scenario:

$$R(\overrightarrow{X};\Delta k,\lambda) = 1 + A_2(\overrightarrow{X})\Delta k + B_2(\overrightarrow{X})\Delta k^2 + C_2(\overrightarrow{X})\lambda + D_2(\overrightarrow{X})\lambda^2 + E_2(\overrightarrow{X})\Delta k\lambda \tag{3.32}$$

HISZ scenario:

$$R(\overrightarrow{X};\Delta k,\lambda) = 1 + A_3(\overrightarrow{X})\Delta k + B_3(\overrightarrow{X})\Delta k^2 + C_3(\overrightarrow{X})\lambda + D_3(\overrightarrow{X})\lambda^2 + E_3(\overrightarrow{X})\Delta k\lambda \tag{3.33}$$

Five Million MC events are generated for each TGC point to have smooth differential cross section spectra in determination of the ratio (R). The re-weighting coefficients are determined for each bin of kinematic distributions such as transverse momentum of the leading lepton from W decay, transverse momentum of the dilepton and transverse mass of WW.

We use 3-Dimensional re-weighting based on transverse momenta of leptons, $p_T^{\ell^+}$, $p_T^{\ell^-}$, and relative transverse missing energy, $E_{\mathrm{T,\ Rel}}^{\mathrm{miss}}$. A set of kinematic distributions, which have been used for WW event selection, are validated by comparing the distributions from the 3D re-weighting (black histograms) and from MC simulation with anomalous couplings (red histograms), as shown in Figure 3.37, in which the comparison results indicate that the 3D re-weighting method works well.

3.10.3 Probing the Anomalous TGC Sensitivity with Data

The measured leading lepton p_{T} spectrum is compared between the experimental observations and the expectations as shown in Fig. 3.38. Note that we effectively cut the p_{T} spectrum with anomalous TGCs with $p_{\mathrm{T}} < 500$ GeV for this analysis due to no events are predicted by the SM WW production at that region given the current 4.6 fb^{-1} integrated luminosity.

To probe the anomalous TGCs, the following strategy is carried out:

- the signal and background uncertainties are determined as a function of the leading lepton p_{T}.

- a binned log-likelihood function is constructed based on the sources and nature of these uncertainties
- to fit data to the expectations in coupling parameter space.
- The 95% CL anomalous coupling limits can be determined in the fitting procedure.

3.10.3.1 WW Signal uncertainties as a function of lepton p_{T}

The global systematic uncertainties of signal estimated in Section 3.7 include 1.8% on luminosity, 5% on total cross section, 1.8% on overall acceptance due to PDF and the variations of renormalization and factorization scales. In order to extract the anomalous TGCs from the leading lepton p_{T}, the leading lepton p_{T} dependent signal systematic uncertainties are desired. Hence, all the list theoretical and experimental uncertainties in 3.7 are examined on the leading lepton p_{T} spectrum by varying $\pm 1\sigma$ of all the sources considered to see the bin-by-bin behavior. And the uncertainties are classified as two different types:

- **type-1** uncertainties are treated as fully correlated across all p_{T} bins: all bins vary up and down coherently for a given uncertainty source. Examples are PDF and scale uncertainties, lepton and trigger scale factors uncertainties or jet energy scale and jet energy resolution uncertainties. Eventually, these uncertainties are all added up quadratically in each leading lepton p_{T} bin as they are uncorrelated with each other.
- **type-2** uncertainties include the sign of bin-by-bin correlations to account for bin migration effects: while one bin may vary upwards due to a given uncertainty, another bin may vary downwards. Examples are lepton energy/momentum scale and resolution uncertainties, $E_{\mathrm{T}}^{\mathrm{miss}}$ soft term uncertainty, which all have p_T^{lead}dependence.

The theoretical and experimental combined p_{T} dependent uncertainties for signal are given in Table 3.58. These type-1 uncertainties in different p_{T} bins vary fully coherently in a flat way when fitting the likelihood function and therefore, It means only one nuisance parameter is used to describe all the type-1 systematic uncertainties in each bin. The seven sets of "type-2" systematic uncertainties are treated individually with 8 nuisance parameters in the leading lepton p_{T} fitting. The uncertainties

are assigned signs, determined by upwards variations, in different p_{T} bins to account for the bin-by-bin migration effects.

p_{T} (GeV)	Total "type-1"	e res.	e scale	mu scale	mu (ID)	mu (MS)	$E_{\mathrm{T}}^{\mathrm{miss}}$ res.	$E_{\mathrm{T}}^{\mathrm{miss}}$ scale
25-40	8.42%	-0.24%	0.04%	-0.23%	-0.06%	-0.02%	0.06%	-0.10%
40-60	8.54%	0.23%	-0.01%	0.37%	0.03%	0.04%	-0.04%	-0.33%
60-80	9.14%	0.70%	-0.02%	0.36%	0.01%	-0.09%	-0.05%	-0.20%
80-100	10.44%	0.77%	0.14%	0.45%	0.07%	0.14%	0.01%	-0.14%
100-120	9.72%	0.51%	0.13%	0.83%	-0.33%	-0.03%	-0.14%	-0.28%
120-140	9.61%	-2.84%	-0.23%	0.75%	0.22%	-0.13%	-0.37%	0.30%
140-160	12.20%	1.70%	1.52%	-0.23%	-0.81%	1.10%	-0.05%	0.29%
160-180	13.32%	-1.59%	0.41%	0.22%	0.78%	-1.77%	0.26%	0.08%
≥180	13.58%	1.58%	-0.94%	2.26%	0.29%	0.84%	-0.25%	-0.28%

Table 3.58 Summary of the leading lepton p_{T} spectrum bin-by-bin systematic uncertainties for expected WW signals. The "overall type-1" systematic uncertainty includes overall cross section uncertainty 5%, overall acceptance uncertainty due to PDF and scale 1.8% and theoretical and "type-1" experimental uncertainties as a function of leading lepton p_{T}. These p_{T} dependent uncertainties arise from PDF/scale, electron reconstruction and identification scale factors, muon identification scale factors, jet energy scale and jet energy resolution, lepton isolation and impact parameter cut efficiency scale factors . The p_{T} dependent "type-2" p_{T} dependent uncertainties due to lepton resolution and scales and $E_{\mathrm{T}}^{\mathrm{miss}}$ soft term scale and resolution are treated separately in the leading lepton p_{T} fitting. [6]

3.10.3.2 Background uncertainties as a function of leading lepton p_{T}

The overall systematical uncertainty of each background has been estimated in the total cross section measurement and summarized in Table 3.50 and independent if lepton p_{T}. The shape uncertainties of each different background, there are two different ways to proceed depending on the background characteristics and its estimation techniques.

The shape uncertainties of W+jet background leading lepton p_{T} distribution is estimated with help of the shape provided by the data-driven technique itself. To access the shape uncertainty, the absolute differential spectrum is fit to Equation 3.34 so as to smooth the statistical fluctuation. The shape uncertainty in each p_{T} bin is then estimated as the fit value at the p_{T} bin. To further cover statistical fluctuations, the fit error in each p_{T} bin is added to the fit value. The shape using a second data-driven technique using matrix method for W+jets background estimation is cross-checked and verified to be well covered by the shape systematic uncertainties as shown in 3.39.

$$p_0 \times (1 + \sqrt{e^{\frac{-100}{x-25}} \times log(1 + e^{p_1 \times x})}) \tag{3.34}$$

The shape uncertainties of top, Drell-Yan (Z+jets) and other diboson processes are derived based on MC simulations by varying each of the systematic uncertainty sources that were mentioned in Section 3.10.3.1. All the shape variations due to different systematic uncertainty sources summed up in quadrature in each p_{T} bin as the shape difference in the p_{T} bin, then plot the shape difference as a function of leading lepton p_{T} as shown in 3.40 (right, blue dots) to be fit to Equation 3.34. To be more conservative, the fit error is added to the fit value in each p_{T} bin, and take the the sum of the two as the final shape uncertainty in the p_{T} bin. The fitting results and final shape systematic error bands are shown in 3.40.

The global and p_{T} dependent shape systematic uncertainties for each background are given in Table 3.59.

	Wjets	Di-boson	Drell-Yan	Top
Global	43.82%	13.33%	25.99%	25.43%
p_{T} (GeV)				
25-40	15.55%	9.44 %	21.32 %	4.00 %
40-60	17.64%	9.66 %	26.25 %	4.18 %
60-80	26.24%	9.86 %	44.50 %	4.91 %
80-100	38.33%	10.95%	69.03 %	6.15 %
100-120	50.27%	13.07%	92.89 %	7.81 %
120-140	61.29%	15.52%	114.79%	09.55%
140-160	71.39%	17.94%	134.82%	11.23%
160-180	80.69%	20.25%	153.24%	12.81%
$\geq$180	89.32%	22.43%	170.33%	14.30%

Table 3.59 Global systematic uncertainties and bin-by-bin shape uncertainties for all backgrounds. "Global" uncertainties mean the overall systematic uncertainties used for the cross section measurement. The bin-by-bin shape uncertainties are treated independently because the uncertainties mainly come from the limited statistics. [6]

3.10.3.3 Binned Log-Likelihood Function

A binned likelihood function is constructed given the signal and background leading p_{T} spectra and corresponding uncertainty. The formula is shown in Eq. 3.36. The number of events from different sources are shown in Table 3.60 with the overflow bin included as it is in the high p_{T} region which is sensitive to aTGCs.

In each p_{T} bin the MC expected signal plus the estimated background are compared to the observed

p_{T} (GeV)	Data	WW	Wjets	Di-boson	Drell-Yan	Top	Total Background
25-40	366	204.80	40.29	25.56	22.18	15.20	103.24
40-60	506	337.01	33.76	23.61	19.94	39.14	116.44
60-80	230	153.64	14.09	13.46	6.14	30.51	64.20
80-100	92	65.64	5.27	6.45	2.39	20.55	34.66
100-120	67	30.17	2.16	3.09	0.51	14.83	20.60
120-140	32	14.90	1.26	1.94	0.00	8.54	11.75
140-160	12	7.41	0.38	1.66	0.00	6.25	8.28
160-180	6	4.24	0.41	0.57	0.23	3.14	4.35
$\geq$180	14	5.82	0.37	1.55	0.00	3.05	4.96

Table 3.60 Number of events in each leading lepton p_{T} bin for Data, SM expected signal and estimated background. [6]

data based on Poisson statistics:

$$p(N_{obs}; N_{exp}) = \frac{N_{exp}^{N_{obs}}\ e^{-N_{exp}}}{N_{obs}!}, \quad \text{with } N_{exp} = N_s + N_b \tag{3.35}$$

where N_{exp} is the predicted mean value of the number of events, which is determined by the signal N_s and the background N_b together. The predicted signal N_s is determined from the standard equation, $N_s = \mathcal{L} \times \epsilon \times \sigma_{SM} \times R(\Delta k_Z, \lambda_Z, \Delta g_1^Z, \Delta k_\gamma, \lambda_\gamma)$. Here $\mathcal{L}$ is the total integrated luminosity, ϵ is the acceptance in the p_{T} bin, and σ_{SM} is the cross section with the SM couplings, R is the re-weighting ratio which is a function of the anomalous coupling parameters determined in section 3.10.2.

The systematic uncertainties used for the anomalous TGC fit include luminosity uncertainty (1.8%), "type 1" and "type 2"signal systematic uncertainties, global and bin-by-bin uncertainties in each background. And all the exact uncertainties are presented in Table 3.58 and Table 3.59. The likelihood function is convolved with a set of Gaussian distributions with the Poisson distribution to account for

all the systematic uncertainties as shown in Equation 3.36:

$$
\begin{aligned}
L &= \int_{1-3\sigma_c}^{1+3\sigma_c} g_c \; df_c \; \int_{1-3\sigma_s}^{1+3\sigma_s} g_s \; df_s \; \Big[\prod_{n=1}^{4} \int_{1-3\sigma_{bn}}^{1+3\sigma_{bn}} g_{bn} \; df_{bn}\Big] \; \Big(\prod_{i=1}^{6} P^i_{shape}\Big) \\
P^i_{shape} &= \int_{1-3\sigma_{si}}^{1+3\sigma_{si}} g_{si} \; df_{si} \; \Big(\prod_{j=1}^{7} \int_{1-3\sigma_{sij}}^{1+3\sigma_{sij}} g_{sj} df_{sij}\Big) \; \Big(\prod_{m=1}^{4} \int_{1-3\sigma_{bim}}^{1+3\sigma_{bim}} g_{bim} \; df_{bim}\Big) \; \frac{{N^i_{exp}}^{N^i_{obs}} \; e^{-N^i_{exp}}}{N^i_{obs}!} \\
N^i_{exp} &= f_c f_s f_{si} (\prod_{j=1}^{4} f_{sij}) \; N^i_s + f_{b1} f_{bi1} N^i_{b1} + f_c f_{b2} f_{bi2} N^i_{b2} + f_{b3} f_{bi3} N^i_{b3} + f_{b4} f_{bi4} N^i_{b4} \\
g_l &= \frac{e^{-(1-f_l)^2/2\sigma_l^2}}{\sqrt{2\pi}\sigma_l}, \quad l = c, s, [si \; (i = 1, 6), sj \; (j = 1, 4)], bn \; (n = 1, 4), bim \; (i = 1, 6; m = 1, 4) \\
N_s &= \mathcal{L} \times \epsilon \times \sigma_{SM} \times R(\Delta k_Z, \lambda_Z, \Delta g_1^Z, \Delta k_\gamma, \lambda_\gamma)
\end{aligned}
\tag{3.36}
$$

3.10.4 Determination of 95% Confidence-Level Interval Limits

The 95% Confidence-Level Interval Limits are obtained by fitting the negative Log-likelihood function so as to compare the measured leading lepton to the MC predicted signal and estimated background.

One should note that when fitting only one anomalous triple coupling (aTGC) parameter, a 95% confidence-level (C.L.) interval of the anomalous triple coupling is defined by: Log(L) > (Log(L0)-1.92), in which L0 is the maximum likelihood. When fitting two aTGC parameters, a two-dimensional 95% C.L. interval of the two parameters is defined by the constraint of Log(L) > (Log(L0)-2.99).

Limits on the aTGC parameters then can be set with the fit. The aTGC limits are derived for the three TGC parameter constraints (LEP, EQUAL, HISZ) and without any constraint.

Table 3.61 shows the 95% CL limits on anomalous TGCs in the LEP constraint scenario. There are only three free parameters in the LEP scenario. Limits are given on the three parameters in the table for cutoff $\Lambda = 6$ TeV and ∞ respectively.

The 2D contour limits at 95% CL in the LEP scenario with cutoff $\Lambda = \infty$ are shown in Figure 3.41 for any two of the three free parameters. The 2D limit for Δg_1^Z vs. Δk_γ is also presented.

There are only 2 independent parameters in both HISZ and EQUAL scenarios. Limits in each of the two constraint scenarios are also derived on the two independent parameters for cutoff $\Lambda = 6$ TeV and ∞, respectively.

LEP constraint	Δk_Z	$\lambda_Z = \lambda_\gamma$	Δg_1^Z
Cutoff scale $\Lambda = 6$ TeV			
DATA	[-0.045,0.044]	[-0.062,0.065]	[-0.036,0.066]
MC	[-0.043,0.040]	[-0.060,0.062]	[-0.034,0.062]
Cutoff scale $\Lambda = \infty$			
DATA	[-0.043,0.043]	[-0.062,0.059]	[-0.039,0.052]
MC	[-0.039,0.039]	[-0.060,0.056]	[-0.038,0.047]

Table 3.61 One-dimensional limits of the anomalous TGCs with LEP constraint by fitting leading lepton p_{T} spectrum (9 bins) with systematic errors included. [6]

Figure 3.42 shows the Log-likelihood function value F versus Δk_Z (left plot) and λ_Z (right plot) in the HISZ scenario. Table 3.62 gives the 95% CL limits on aTGC parameters in the HISZ scenario. A tighter limit on Δk_Z is obtaied in the HISZ scenario than in the LEP scenario due to an additional constraint applied in the HISZ scenario.

The log-likelihood function value F versus Δk_Z (left plot) and λ_Z (right plot) in the EQUAL scenario are shown in Figure 3.43. And the 95% CL limits on aTGC parameters in the Equal scenario are presented in Table 3.63.

The 95% CL limits on anomalous TGCs are also derived without any constraints for cutoff $\Lambda = \infty$. The results are given in Table 3.64. As expected, the limits without constraints are weaker than those with some constraints.

Cutoff scale $\Lambda = 6$ TeV		
DATA	[-0.039,0.057]	[-0.066,0.065]
MC	[-0.040,0.054]	[-0.064,0.062]
Cutoff scale $\Lambda = \infty$		
DATA	[-0.036,0.057]	[-0.063,0.063]
MC	[-0.037,0.054]	[-0.061,0.060]

Table 3.62 One-dimensional limits of the anomalous TGCs for Δk_Z (left) and λ_Z(right) with HISZ constraint by fitting leading lepton p_{T} spectrum (9 bins) with systematic errors included. [6]

Finally, we compare our anomalous TGC limits with LEP scenario with the limits obtained from CMS, CDF, DØ and LEP experiments [62, 63, 64, 65] in Figure 3.44. The current limits are already more restrictive than Tevatron while getting competitive with LEP.

Cutoff scale Λ = 6 TeV		
DATA	[-0.061,0.093]	[-0.062,0.065]
MC	[-0.058,0.089]	[-0.060,0.062]
Cutoff scale $\Lambda = \infty$		
DATA	[-0.061,0.083]	[-0.062,0.059]
MC	[-0.057,0.080]	[-0.060,0.056]

Table 3.63 One-dimensional limits of the anomalous TGCs for Δk_Z (left) and λ_Z(right) (EQUAL Coupling constraint) by fitting leading lepton p_{T} spectrum (9 bins) with systematic errors included. [6]

Cutoff scale $\Lambda = \infty$					
No constraint	Δk_Z	λ_Z	λ_γ	Δg_1^Z	Δk_γ
DATA	[-0.078,0.092]	[-0.074,0.073]	[-0.152,0.146]	[-0.373,0.562]	[-0.135,0.190]
MC	[-0.077,0.086]	[-0.071,0.069]	[-0.144,0.135]	[-0.449,0.546]	[-0.128,0.176]

Table 3.64 One-dimensional limits of the anomalous TGCs without constraint by fitting leading lepton p_{T} spectrum (9 bins) with systematic errors included. [6]

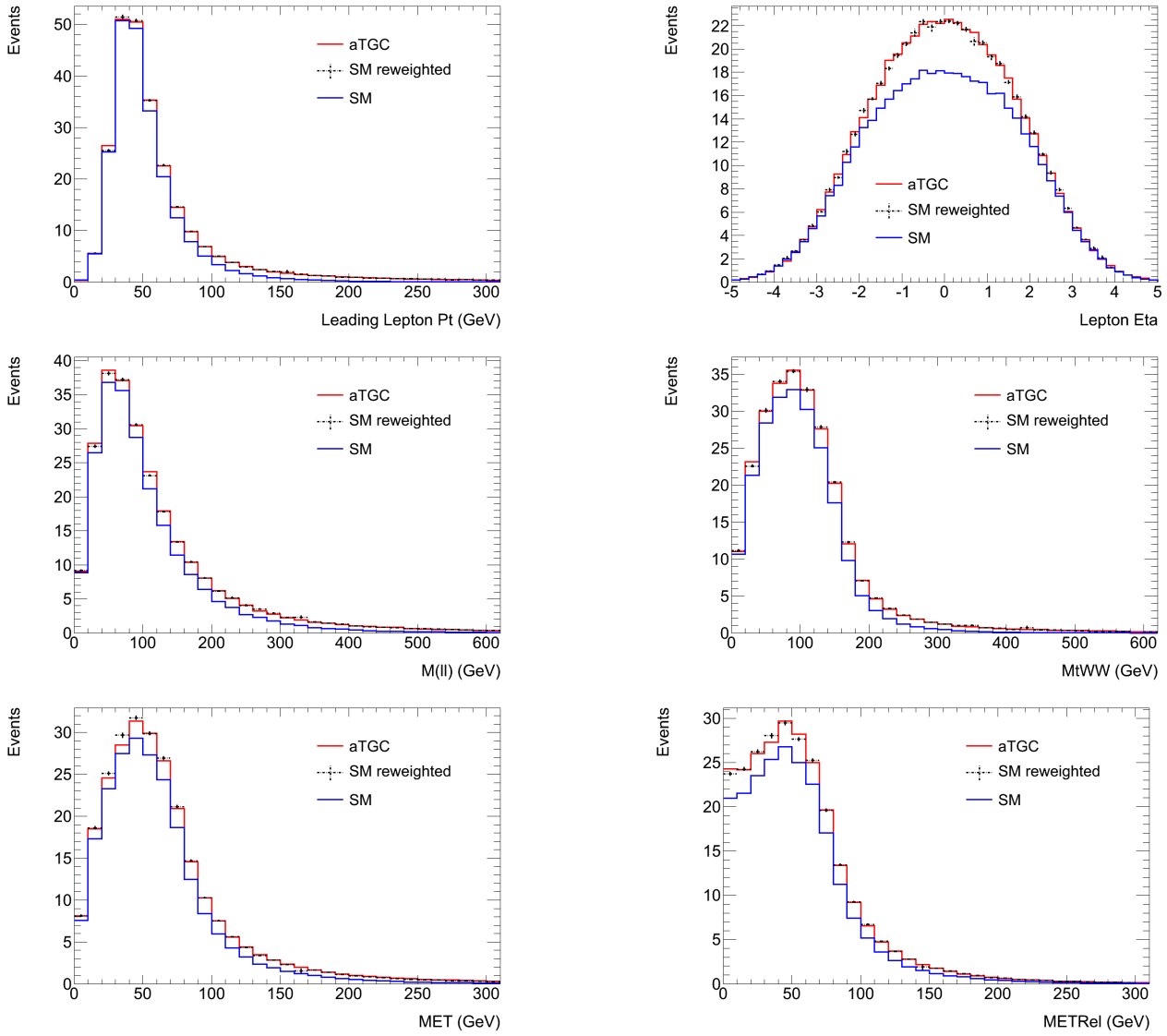

Figure 3.37 Distributions of the leading lepton p_T (top left), eta (top right), dilepton mass (middle left) and transverse mass of WW (middle right). $E_{\mathrm{T}}^{\mathrm{miss}}$ (bottom left) and relative $E_{\mathrm{T}}^{\mathrm{miss}}$ (bottom right). Blue histograms are for SM distributions, red histograms are MC distributions with anomalous couplings, black histograms are for 3D re-weighted distributions. The anomalous couplings for the test point are $\Delta k_Z = 0.1$, $\lambda_Z = 0$ and $\Delta g_1^Z = -0.1$. [6]

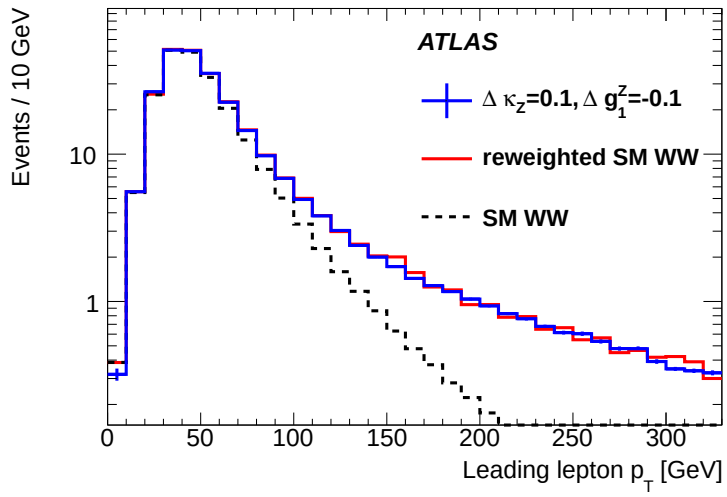

Figure 3.38 Distribution of the leading lepton p_{T}. The dots with error-bars indicate the measured data points, the green histogram presents the estimated total background, the black histogram shows the overall MC expected SM WW events plus estimated background and histograms with different other colours show MC expectations for different anomalous couplings. The last bin in the plot is an overflow bin. [6]

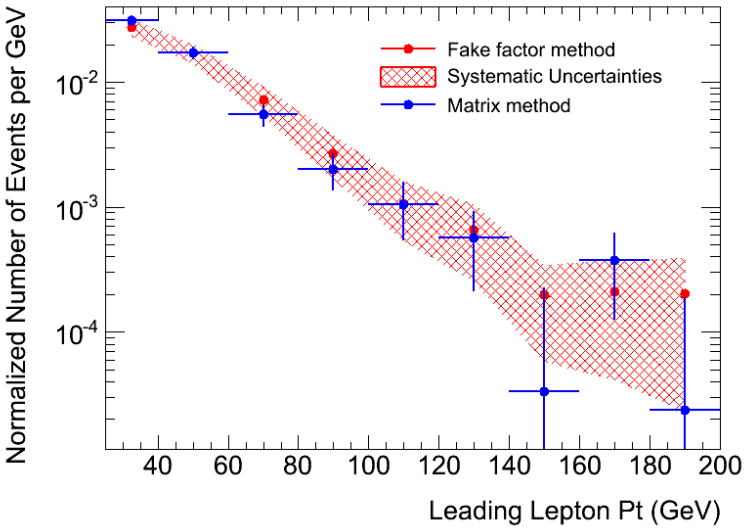

Figure 3.39 The W+jet background p_{T} spectra estimated by two data-driven methods and the systematic error band of the p_{T} spectrum. [6]

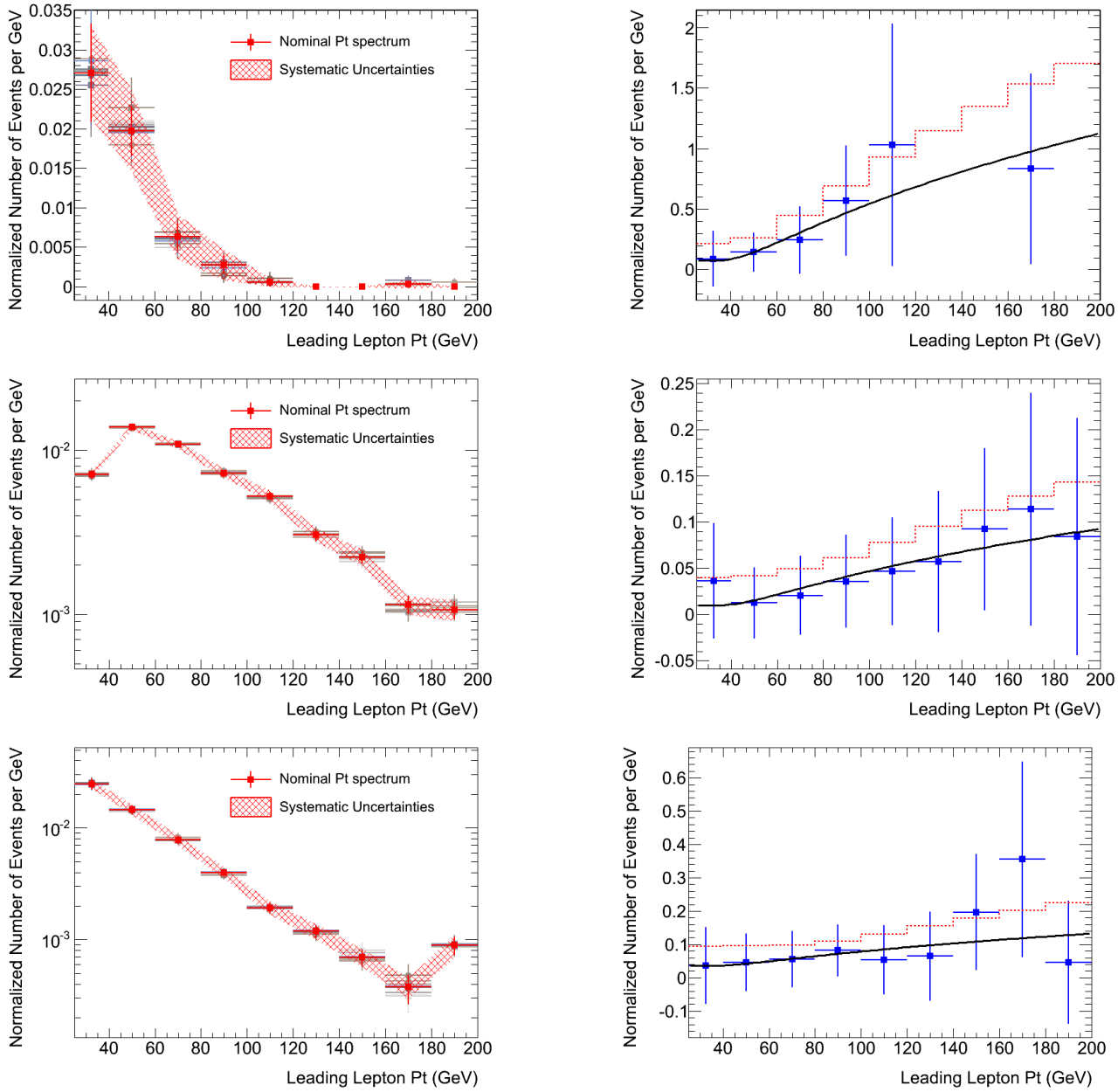

Figure 3.40 From top to bottom: Drell-yan, Top and other diboson backgrounds. Left: the normalized p_{T} spectra with different systematic effect variations and the final shape uncertainty bands. Right: the fitting results of shape uncertainty estimation and the final shape uncertainties (red dash lines). [6]

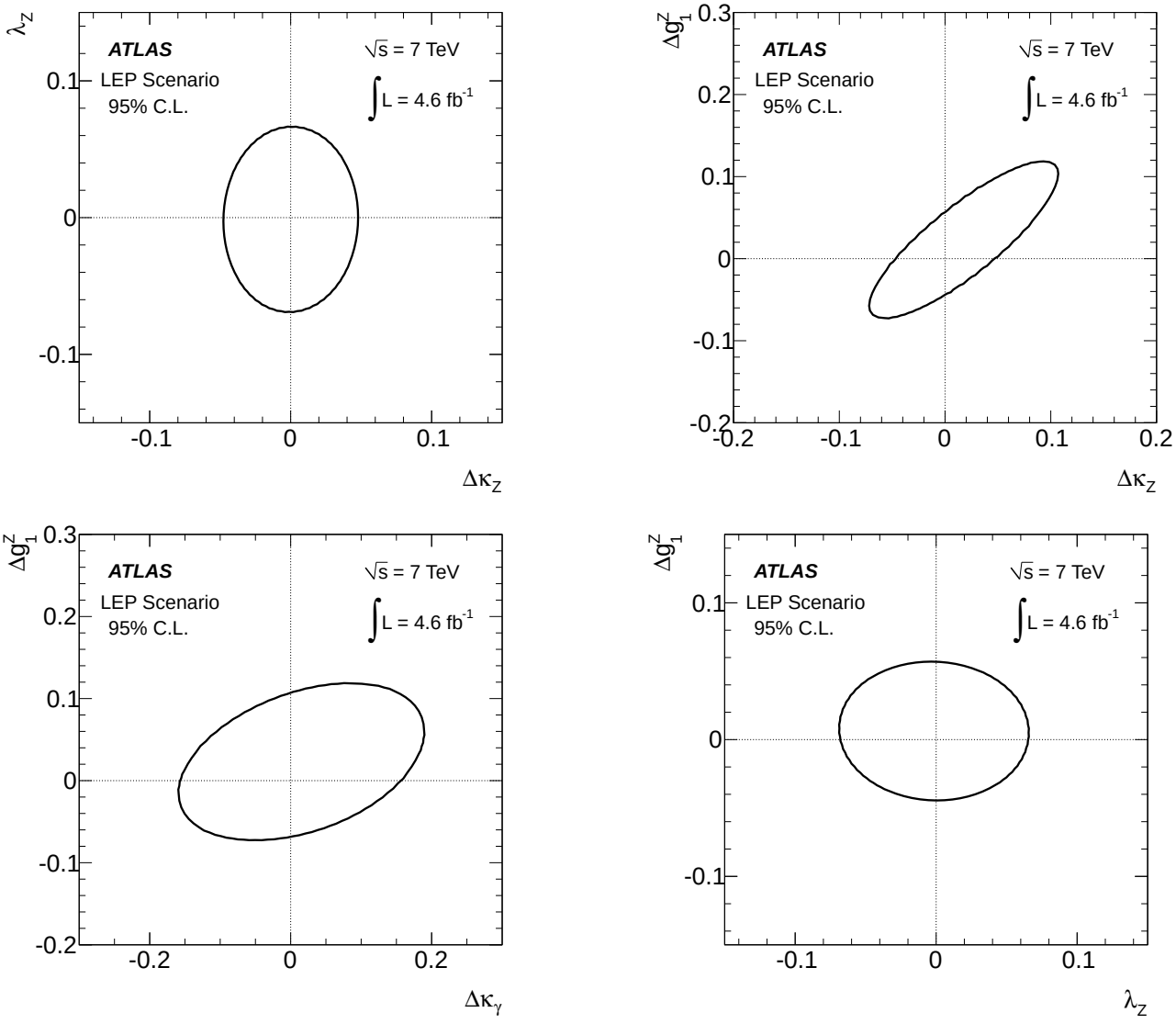

Figure 3.41 The 95% CL 2D limits of Δk_Z vs λ_Z (top left), Δk_Z vs Δg_1^Z (top right), Δk_γ vs Δg_1^Z (bottom left) and λ_Z vs Δg_1^Z (right) for LEP scenario with $\Lambda = \infty$ using 9-bin fit with systematic uncertainties included. [6]

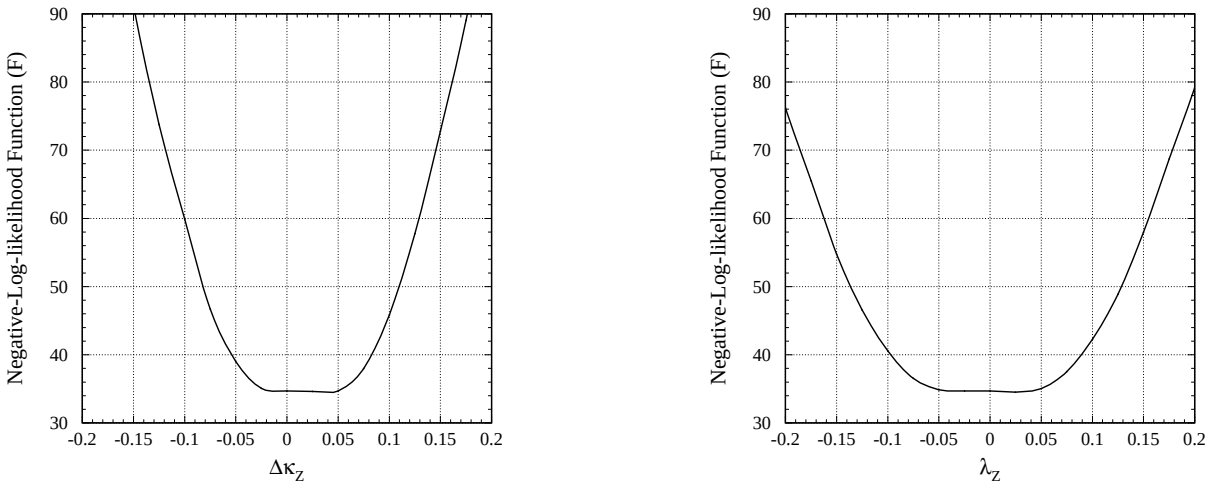

Figure 3.42 The log-likelihood function value F versus Δk_Z (left plot) λ_Z (right plot) for HISZ scenario. The limits of the given anomalous coupling with 95% C.L. is taken to be at the $F_{min} + 1.92$ of the log-likelihood function curve. [6]

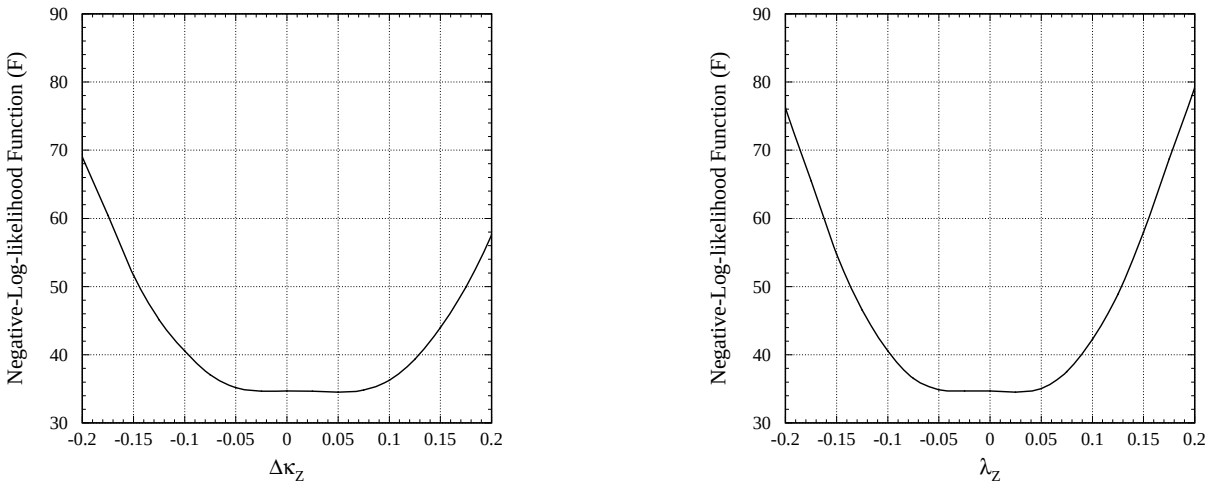

Figure 3.43 The log-likelihood function value F versus Δk_Z (left plot) λ_Z (right plot) for EQUAL scenario. The limits of the given anomalous coupling with 95% C.L. is taken to be at the $F_{min} + 1.92$ of the log-likelihood function curve. [6]

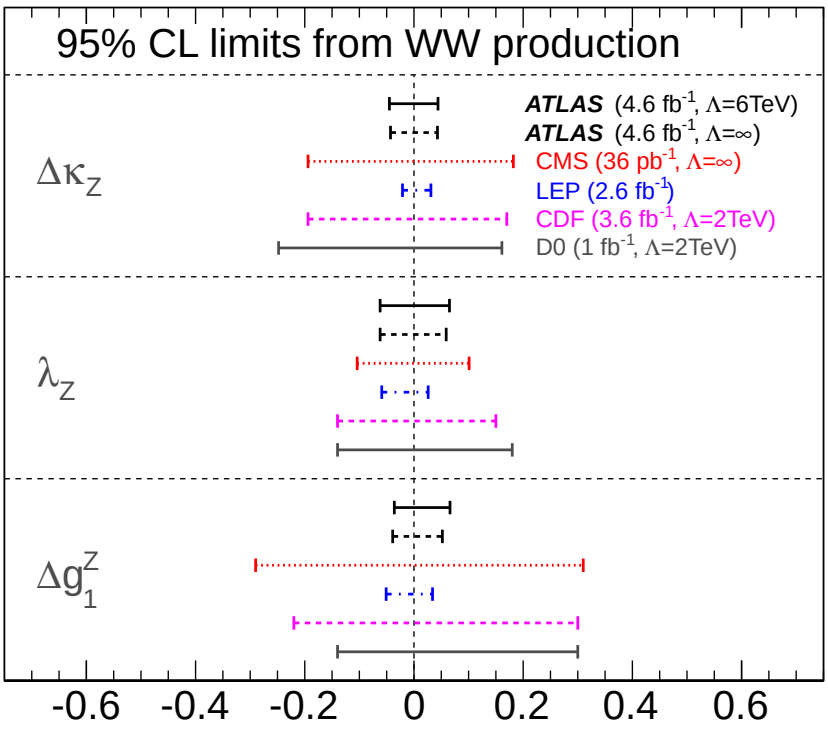

Figure 3.44 Comparison of anomalous TGC limits from ATLAS, CMS, CDF, D0 and LEP using WW events. [6]

CHAPTER 4. CONCLUSIONS

The ATLAS experiment at the LHC has had a successful year of data taking at the center-mass-energy $\sqrt{s} = 7$ TeV. Over the full year, 4.6 fb^{-1} pp high quality collision data were collected, with which the measurement of Standard Model WW production cross section is performed.

The total cross section of Standard Model WW production is measured in three fully leptonic decay channels. Overall, 1325 candidates are selected with an estimated background of 368.5 ± 60.9. The cut-based selection was tuned based on Monte Carlo aiming for an improved signal to background significance $S/\sqrt{S+B}$. Most of the major backgrounds (Z+jets, top and W+jets) are estimated using dedicated data-driven techniques to avoid Monte Carlo mismodeling and large uncertainties. The measured total cross section of $\sigma(pp \to W^+W^-)$ is 51.9 $\pm$ 2.0 (stat) $\pm$ 3.9 (syst) $\pm$ 0.9 (lumi) pb, which is compatible with the Standard Model NLO prediction of $44.7^{+2.1}_{-1.9}$ pb. The uncertainties are now dominated by the systematics. The fiducial cross sections of all three channels, which is less theory-dependent, are measured as well within the fiducial phase space defined to match closely the offline signal selection. The unfolded shape of the leading p_T spectrum is measured for the first time.

Limits on anomalous triple-gauge-boson couplings ($WW\gamma$ and WWZ) are set using the selected WW events by fitting the leading lepton transverse momentum spectrum. With the *equal coupling assumption* ($\Delta k_Z = \Delta k_\gamma$, $\lambda_Z = \lambda_\gamma$, $\Delta g_1^Z = \Delta g_1^\gamma = 0$) we set 95% CL limits on Δk_Z and λ_Z in the intervals $[-0.061, 0.093]$ and $[-0.062, 0.065]$, respectively, for a cutoff scale of $\Lambda = 6$ TeV. Other one-dimensional and 2-dimensional triple-gauge-boson coupling limits are also obtained within various coupling scenarios. The current limits are the best out from all the hadron collider experiments.

The LHC is now running at an even higher center-mass-energy of $\sqrt{s} = 8$ TeV in 2012 with the total integrated luminosity of $\sim$25 fb^{-1} expected by the end of this year. It will provide both a potential improvement and a big challenge to the WW cross measurement due to the worse pileup conditions. The aTGC limits will be combined with other diboson measurements and the gauge couplings will be

measured with unprecedented precision.

APPENDIX A. Kinematic distributions of selected events for each channel

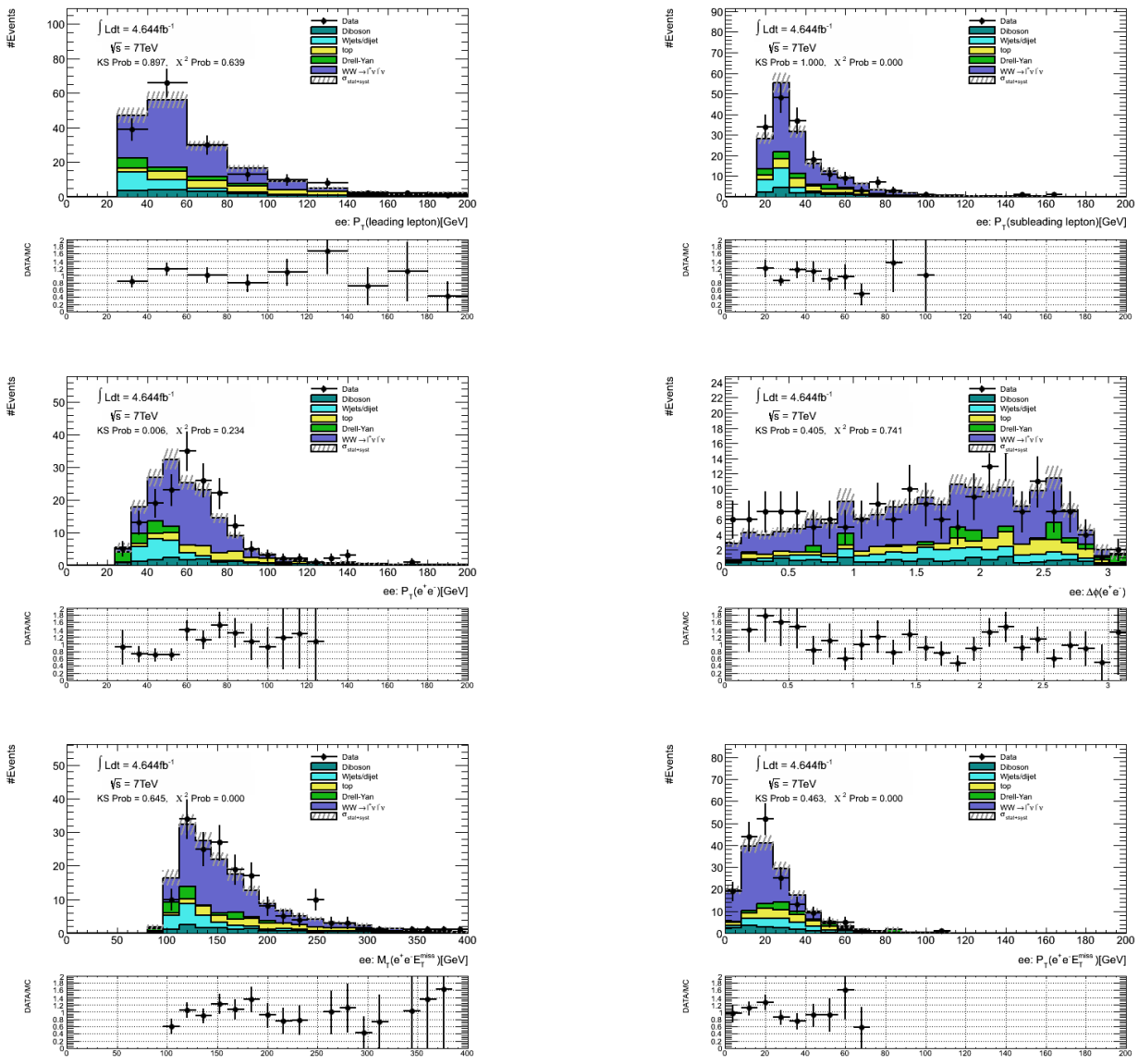

Figure A.1 Distributions for WW candidates after the final event selection for the ee channel: the first row is the p_{T} of leading lepton (left) and the p_{T} of trailing lepton (right); the second row is the $p_T(\ell\ell)$ (left) and the ϕ angle difference between two leptons (right); the third row is the M_T for di-lepton+$E_{\mathrm{T}}^{\mathrm{miss}}$ system (left) and p_{T} for di-lepton+$E_{\mathrm{T}}^{\mathrm{miss}}$ (right). The points represent data and stacked histograms are from MC predictions except W+jets/Dijet background, obtained from a data-driven method. Scale factors as outlined in Section 3.3.2 are applied to MC.

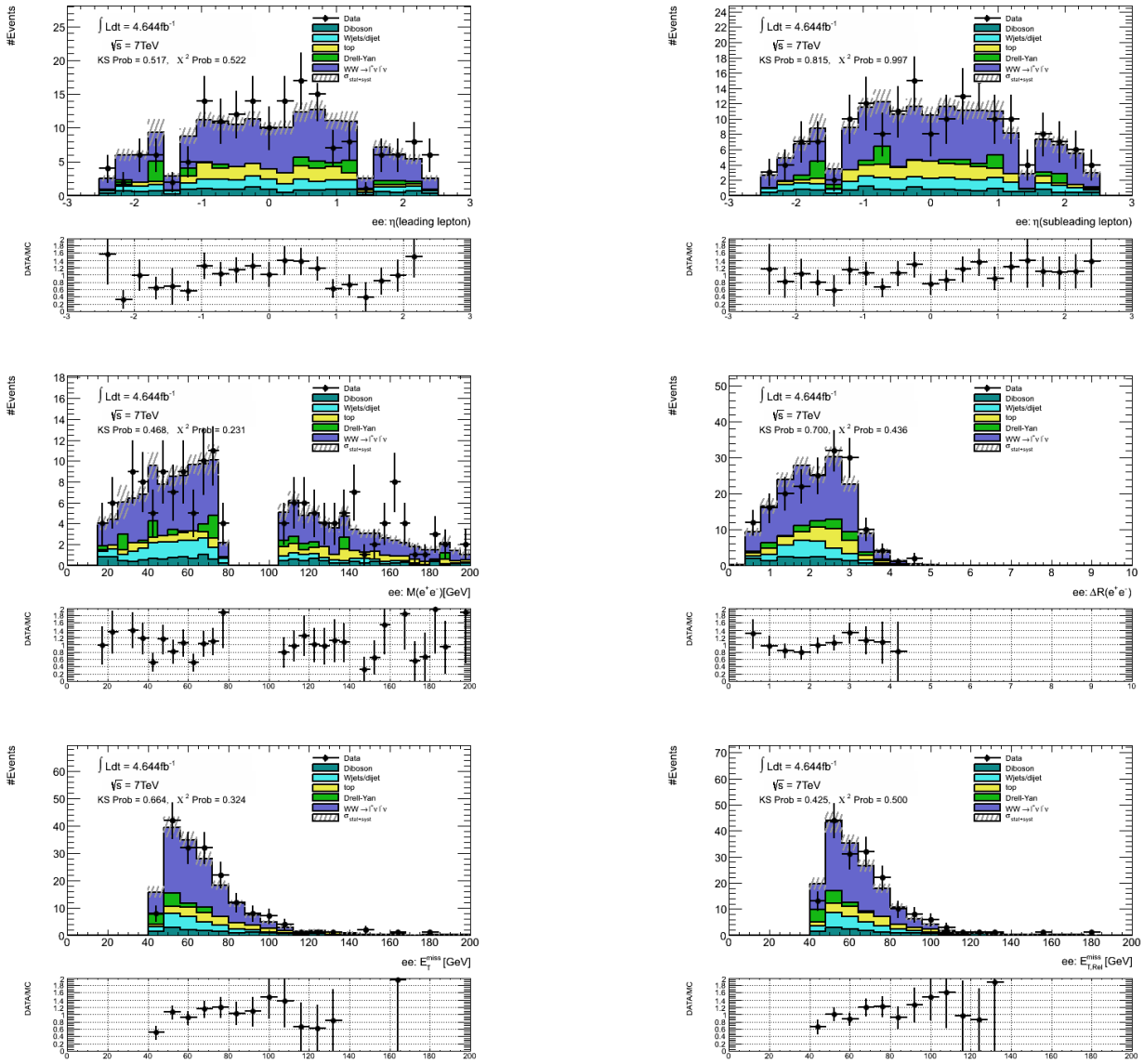

Figure A.2 Distributions for WW candidates after the final event selection for the *ee* channel: the first row is the η of the leading lepton (left) and the η of the trailing lepton (right); the second row is the $M(\ell\ell)$ (left) and the ΔR between the leptons (right); the third row is the $E_{\mathrm{T}}^{\mathrm{miss}}$ (left) and $E_{\mathrm{T,\,Rel}}^{\mathrm{miss}}$ (right). The points represent data and stacked histograms are from MC predictions except W+jets/Dijet background, obtained from a data-driven method. Scale factors as outlined in Section 3.3.2 are applied to MC.

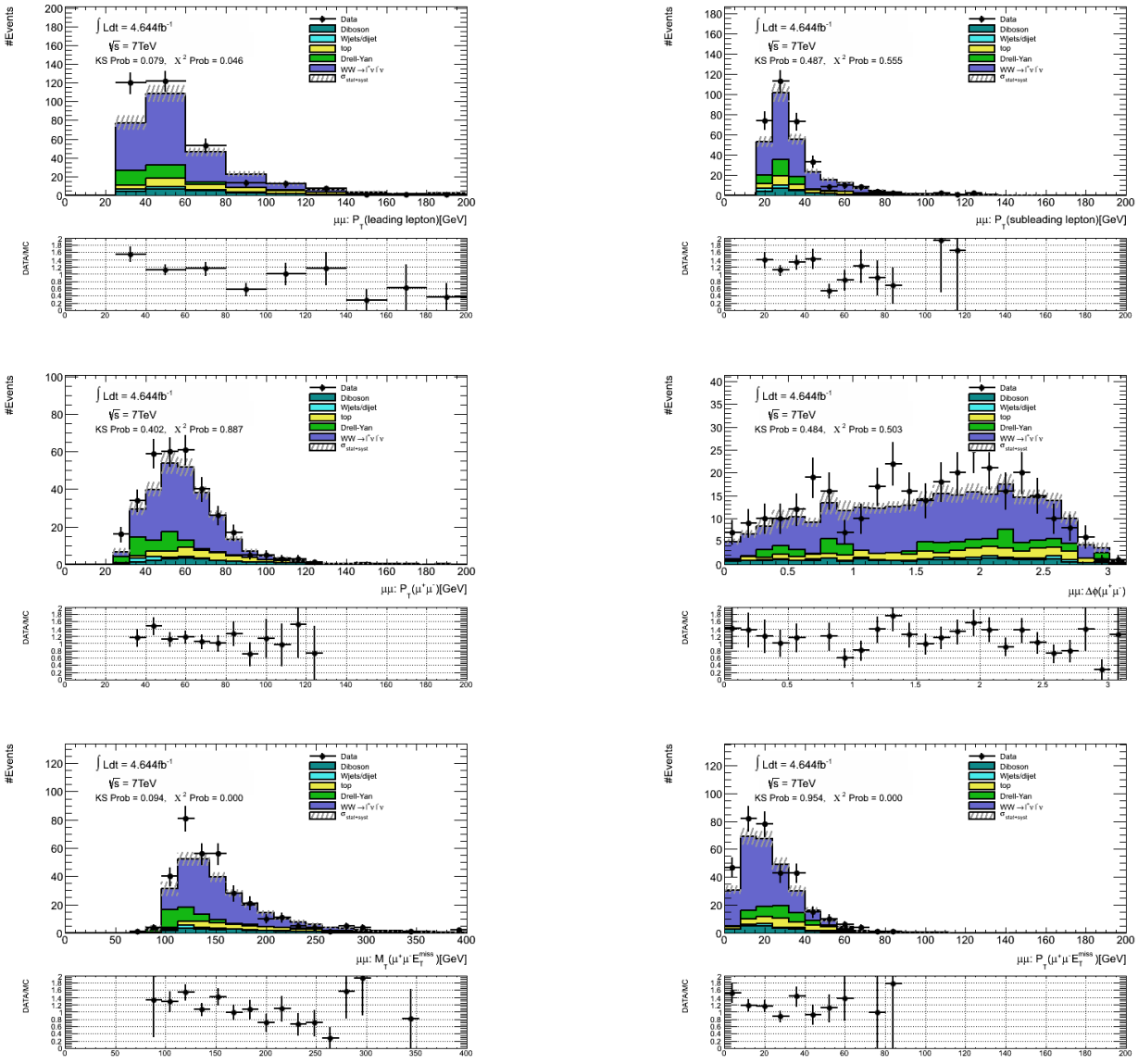

Figure A.3 Distributions for WW candidates after the final event selection for the $\mu\mu$ channel: the first row is the p_{T} of leading lepton (left) and the p_{T} of trailing lepton (right); the second row is the $p_T(\ell\ell)$ (left) and the ϕ angle difference between two leptons (right); the third row is the M_T for di-lepton+$E_{\mathrm{T}}^{\mathrm{miss}}$ system (left) and p_{T} for di-lepton+$E_{\mathrm{T}}^{\mathrm{miss}}$ (right). The points represent data and stacked histograms are from MC predictions except W+jets/Dijet background, obtained from a data-driven method. Scale factors as outlined in Section 3.3.2 are applied to MC.

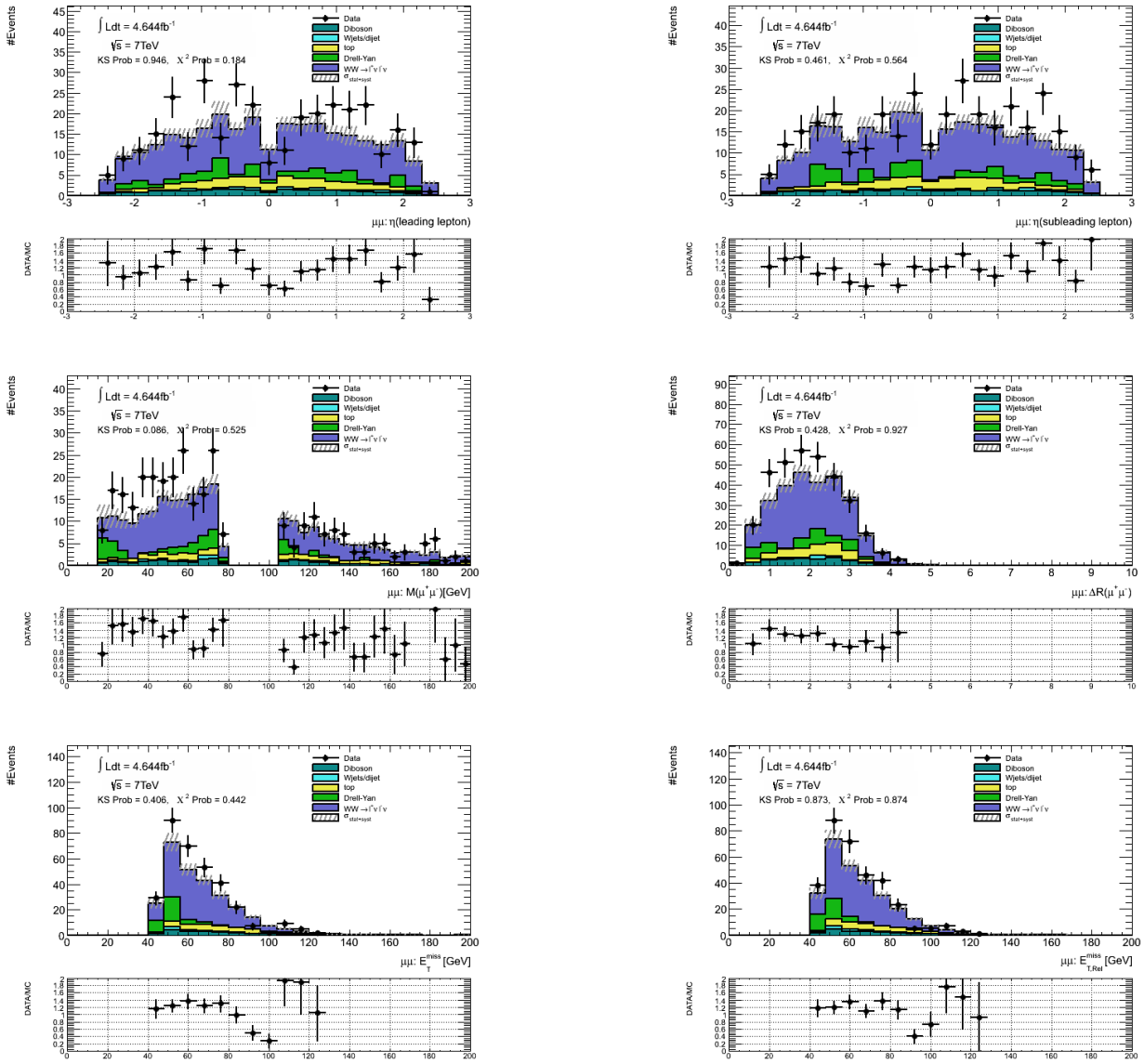

Figure A.4 Distributions for WW candidates after the final event selection for the $\mu\mu$ channel: the first row is the η of the leading lepton (left) and the η of the trailing lepton (right); the second row is the $M(\ell\ell)$ (left) and the ΔR between the leptons (right); the third row is the $E_{\mathrm{T}}^{\mathrm{miss}}$ (left) and $E_{\mathrm{T,\,Rel}}^{\mathrm{miss}}$ (right). The points represent data and stacked histograms are from MC predictions except W+jets/Dijet background, obtained from a data-driven method. Scale factors as outlined in Section 3.3.2 are applied to MC.

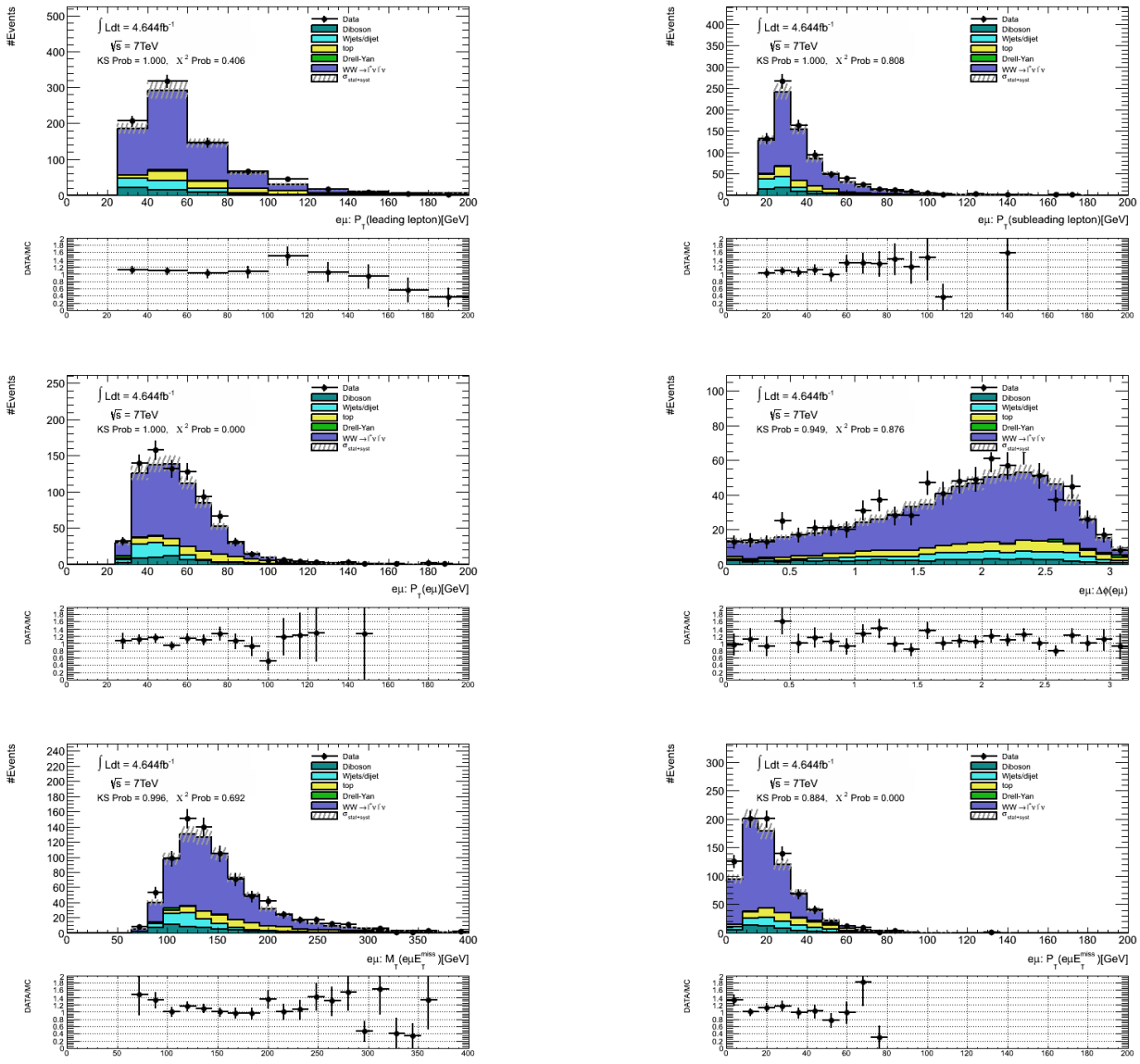

Figure A.5 Distributions for WW candidates after the final event selection for the $e\mu$ channel: the first row is the p_{T} of leading lepton (left) and the p_{T} of trailing lepton (right); the second row is the $p_T(\ell\ell)$ (left) and the ϕ angle difference between two leptons (right); the third row is the M_T for di-lepton+$E_{\mathrm{T}}^{\mathrm{miss}}$ system (left) and p_{T} for di-lepton+$E_{\mathrm{T}}^{\mathrm{miss}}$ (right). The points represent data and stacked histograms are from MC predictions except W+jets/Dijet background, obtained from a data-driven method. Scale factors as outlined in Section 3.3.2 are applied to MC.

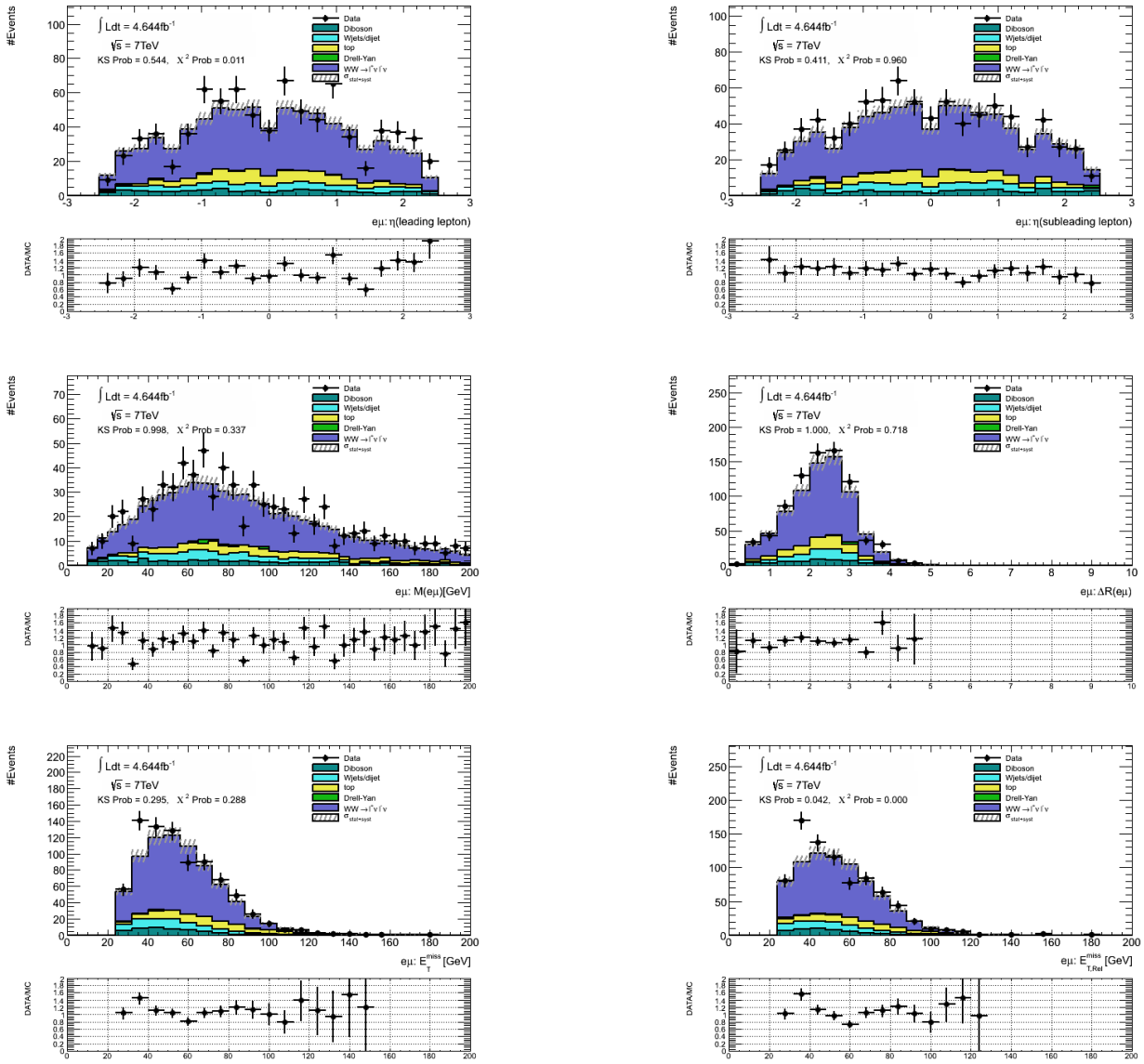

Figure A.6 Distributions for WW candidates after the final event selection for the $e\mu$ channel: the first row is the η of the leading lepton (left) and the η of the trailing lepton (right); the second row is the $M(\ell\ell)$ (left) and the ΔR between the leptons (right); the third row is the $E_{\mathrm{T}}^{\mathrm{miss}}$ (left) and $E_{\mathrm{T,\,Rel}}^{\mathrm{miss}}$ (right). The points represent data and stacked histograms are from MC predictions except W+jets/Dijet background, obtained from a data-driven method. Scale factors as outlined in Section 3.3.2 are applied to MC.

LIST OF TABLES

LIST OF FIGURES

BIBLIOGRAPHY

[1] http://en.wikipedia.org/wiki/Standard_Model.

[2] Particle Data Group Collaboration, K. Nakamura et al., *PARTICLE PHYSICS BOOKLET*, Journal of Physics G **075021** (2010) 37.

[3] R. Brout et al., *Broken Symmetry and the Mass of Gauge Vector Mesons*, Phys. Rev. Lett. **13** (1964) no. 321, .

[4] S. Weinberg et al., *A Model of Leptons*, Phys. Rev. Lett. **19** (1967) no. 1264, 12641266.

[5] J. Campbell et al., *Vector boson pair production at the LHC*, arXiv:1105.0020 [hep-ex].

[6] The ATLAS Collaboration, *Measurement of the WW Production Cross Section in Proton-Proton Collisions at* $\sqrt{s} = 7$ *TeV with the ATLAS Detector and Limits on the Anomalous Triple-Gauge-Boson Couplings*, ATL-COM-PHYS-2012-189.

[7] J. Campbell, R. Ellis, and D. Rainwater Phys. Rev. **D68** (2003) no. 094021, .

[8] P. Nadolsky et al. Phys. Rev. **D78** (2008) no. 013004, .

[9] S. Frixione and B. Webber http://www.hep.phy.cam.ac.uk/theory/webber/MCatNLO/.

[10] CERN LHC Collaboration, *LHC Design Report*, http://lhc.web.cern.ch/lhc/lhc-designreport.html.

[11] https://twiki.cern.ch/twiki/bin/view/AtlasPublic/LuminosityPublicResults.

[12] The ATLAS Collaboration, *Expected Performance of the ATLAS Experiment - Detector, Trigger and Physics*, . CERN-OPEN-2008-020.

[13] The ATLAS Collaboration, *The ATLAS Experiment at the CERN Large Hadron Collider*, Jinst (2008) .

[14] The ATLAS Collaboration, *ATLAS run stats public results*, https://twiki.cern.ch/twiki/bin/view/AtlasPublic/RunStatsPublicResults2010.

[15] J. Levêque and B. Trocmé, *LAr Data Quality: What CP groups need to know about the data*, https://indico.cern.ch/getFile.py/access?contribId=2&resId=0&materialId=slides&confId=132011.

[16] B. Jager, C. Oleari, and D. Zeppenfeld, *Next-to-leading order QCD corrections to W+W-production via vector-boson fusion*, hep-ph/0603177.

[17] K. Arnold, J. Bellm, G. Bozzi, M. Brieg, F. Campanario, et al., *VBFNLO: A parton level Monte Carlo for processes with electroweak bosons – Manual for Version 2.5.0*, arXiv:1107.4038 [hep-ph].

[18] K. Arnold, M. Bahr, G. Bozzi, F. Campanario, C. Englert, et al., *VBFNLO: A Parton level Monte Carlo for processes with electroweak bosons*, Comput.Phys.Commun. **180** (2009) 1661–1670, arXiv:0811.4559 [hep-ph].

[19] J. R. Gaunt, C.-H. Kom, A. Kulesza, and W. J. Stirling, *Same-sign W pair production as a probe of double parton scattering at the LHC*, Eur. Phys. J. **C69** (2010) 53–65, arXiv:1003.3953 [hep-ph].

[20] https://atlas-datasummary.cern.ch/lumicalc/.

[21] G. Corcella et al., *HERWIG 6.5: an event generator for Hadron Emission Reactions With Interfering Gluons (including supersymmetric processes)*, JHEP **0101** (2001) 010, arXiv:hep-ph/0011363.

[22] T. Binoth, M. Ciccolini, N. Kauer, and M. Kramer, *Gluon-induced W-boson pair production at the LHC*, JHEP **12** (2006) 046, arXiv:hep-ph/0611170.

[23] A. D. Martin, W. J. Stirling, R. S. Thorne, and G. Watt Eur. Phys. J. **C63** (2009) no. 189, .

[24] https://twiki.cern.ch/twiki/bin/view/AtlasProtected/HforTool.

[25] R. Cray et al., *Backgrounds To Higgs Boson Searches from Asymmetric Internal Conversion*, arXiv:1110.1368 [hep-ph].

[26] J.M. Butterworth et al., *Single Boson and Diboson Production Cross Sections in pp Collisions at* $\sqrt{s} = 7$ *TeV*, ATL-COM-PHYS-2010-695.

[27] http://root.cern.ch/drupal.

[28] The ATLAS Collaboration, *Expected electron performance in the ATLAS experiment*, ATL-PHYS-PUB-2011-006.

[29] https://twiki.cern.ch/twiki/bin/view/AtlasPublic/ElectronGammaPublicCollisionResults.

[30] https://twiki.cern.ch/twiki/bin/viewauth/AtlasProtected/EnergyScaleResolutionRecommendations.

[31] https://twiki.cern.ch/twiki/bin/view/AtlasProtected/EfficiencyMeasurements.

[32] https://twiki.cern.ch/twiki/bin/view/AtlasProtected/MCPAnalysisGuidelinesEPS2011.

[33] M. Cacciari, G. P. Salam, and G. Soyez, *The anti-kt jet clustering algorithm*, JHEP **04** (2008) 063, arXiv:0802.1189 [hep-ph].

[34] M. Cacciari and G. P. Salam, *Dispelling the* N^3 *myth for the* k_t *jet-finder*, Phys. Lett. **B641** (2006) 57–61, arXiv:hep-ph/0512210.

[35] *Jet energy scale and its systematic uncertainty for jets produced in proton-proton collisions at* $\sqrt{s} = 7$ *TeV and measured with the ATLAS detector*, ATLAS-CONF-2010-056.

[36] https://svnweb.cern.ch/trac/atlasgrp/browser/CombPerf/JetETMiss/JetUserGuide/tags/JetUserGuide-00-01-02/AtlasJetUserGuide.pdf.

[37] https://twiki.cern.ch/twiki/bin/view/AtlasProtected/HowToCleanJets#Bad_jets_rel16_data.

[38] *Commissioning of the ATLAS high-performance b-tagging algorithms in the 7 TeV collision data*, Tech. Rep. ATLAS-CONF-2011-102, CERN, Geneva, July, 2011.

[39] https://twiki.cern.ch/twiki/bin/view/AtlasProtected/PileupReweighting.

[40] S. Grinstein, M. Martinez, E. Meoni, C. Ochando, and E. Perez, *Study on the impact of lepton-jet overlap removal in Z ($\rightarrow l^+ l^-$)+jets final states*, ATL-COM-PHYS-2010-021 (2010) .

[41] https://twiki.cern.ch/twiki/bin/view/AtlasProtected/HowToCleanJets#Guideline_for_LAr_Hole_treatment.

[42] https://twiki.cern.ch/twiki/pub/Atlas/MuonTriggerPhysicsTriggerRecommendations2011/trigger.pdf.

[43] https://twiki.cern.ch/twiki/bin/view/AtlasProtected/WZElectroweakCommonTopics2011.

[44] http://tmva.sourceforge.net/docu/TMVAUsersGuide.pdf.

[45] Aben, R et al., *Background estimates in the HWWlnulnu analysis with 4.7* fb^{-1} *of data collected with the ATLAS detector at* $\sqrt{s} = 7$ *TeV*, Tech. Rep. ATL-COM-PHYS-2011-1728, CERN, Geneva, Dec, 2011.

[46] *Higgs Boson Searches using the* $H \rightarrow WW(^*) \rightarrow \ell\nu\ell\nu$ *Decay Mode with the ATLAS Detector at 7 TeV*, Tech. Rep. ATLAS-CONF-2011-005, CERN, Geneva, Feb, 2011.

[47] B. Mellado, X. Ruan, and Z. Zhang, *Extraction of Top Backgrounds in the Higgs Boson Search with the* $H \rightarrow WW^\star \rightarrow \ell\ell + E_{\text{T}}^{\text{miss}}$ *Decay with a Full-Jet Veto at the LHC*, Phys. Rev. **D84** (2011) 096005, arXiv:1101.1383 [hep-ph].

[48] A. Belloni, G. Conti, J. Guimaraes da Costa, J. Huth, and C. Mills, *Top Background Estimation Using Jet Multiplicity Distributions*, ATL-COM-PHYS-2012-856, June, 2012.

[49] The ATLAS Collaboration, *Commissioning of the ATLAS high-performance b-tagging algorithms in the 7 TeV collision data*, ATLAS-CONF-2011-102, 2011.

[50] ATLAS Collaboration Collaboration, G. Aad et al., *Measurement of W gamma and Z gamma production cross sections in pp collisions at sqrt(s) = 7 TeV and limits on anomalous triple gauge couplings with the ATLAS detector*, arXiv:1205.2531 [hep-ex].

[51] Carola F. Berger et al., *Higgs Production with a Central Jet Veto at NNLL+NNLO*, MIT-CTP **4122** (2011) .

[52] I. W. Stewart and F. J. Tackmann, *Theory Uncertainties for Higgs and Other Searches Using Jet Bins*, arXiv:1107.2117 [hep-ph].

[53] V. Blobel, *An Unfolding Method For High Energy Physics Experiments*, arXiv:0208.022 [hep-ex].

[54] A. Hocker and V. Kartvelishvili, *SVD Approach to Data Unfolding*, arXiv:9509.307 [hep-ph].

[55] B. Malaescu, *An Iterative, Dynamically Stabilized Method of Data Unfolding*, arXiv:0907.3791 [physics.data-an].

[56] G. D'Agostini, *Improved Iterative Bayesian Unfolding*, arXiv:1010.0632 [physics.data-an].

[57] K. Hagiwara, S. Ishihara, R. Szalapski, and D. Zeppenfeld, *Low energy effects of new interactions in the electroweak boson sector*, Phys. Rev. **D48** (1993) no. 5, 2182.

[58] U. Baur, T. Han, and J. Ohnemus, *QCD corrections and nonstandard three vector boson couplings in W^+W^- production at hadron colliders*, Phys. Rev. **D53** (1996) 1098–1123, arXiv:hep-ph/9507336.

[59] U. Baur, S. Errede, and G. Landsberg, *Rapidity correlations in $W\gamma$ production at hadron colliders*, Phys. Rev. **D50** (1994) no. 3, 1917.

[60] U. Baur, T. Han, and J. Ohnemus, *WZ production at hadron colliders: Effects of nonstandard WWZ couplings and QCD corrections*, Phys. Rev. **D51** (1995) no. 7, 3381.

[61] V. M. Abazov, *Measurement of trilinear gauge boson couplings from $WW + WZ \to e\nu\ jj$ events in $p\bar{p}$ collisions at $\sqrt{s} = 1.96\ TeV$*, Phys. Rev. **D80** (2009) no. 053012, .

[62] V. M. Abazov, *Measurement of the WW Production Cross Section with Dilepton Final States in $p\bar{p}$ Collisions at $\sqrt{s} = 1.96\ TeV$ and Limits on Anomalous Trilinear Gauge Couplings*, Phys. Rev. Lett. **103** (2009) no. 191801, .

[63] T. Aaltonen, *Measurement of the WW and WZ Production Cross Section Using the lepton+ jets Final State at CDF II*, Phys. Rev. Lett. **104** (2010) no. 101801, .

[64] C. Collaboration, *Measurement of the WW Production and Search for the Higgs Boson in pp Collisions at* $\sqrt{s} = 7\ TeV$, Phys. Lett. **B699** (2011) .

[65] L. Collaboration, *A Combination of Preliminary Electroweak Measurements and Constraints on the Standard Model*, CERN-PH-EP/2006-042, hep-ex/0612034 (2006) .